Universitätsklinikum
Hamburg-Eppendorf

Universität Hamburg
DER FORSCHUNG | DER LEHRE | DER BILDUNG

DISSERTATION

with the aim of achieving a doctoral degree at
the Faculty of Mathematics, Informatics and Natural Sciences/
Department of Biology of the University of Hamburg

MULTIMODAL PERSPECTIVES ON THE UPPER-LAYER NEUROGENESIS IN THE MURINE CEREBRAL CORTEX

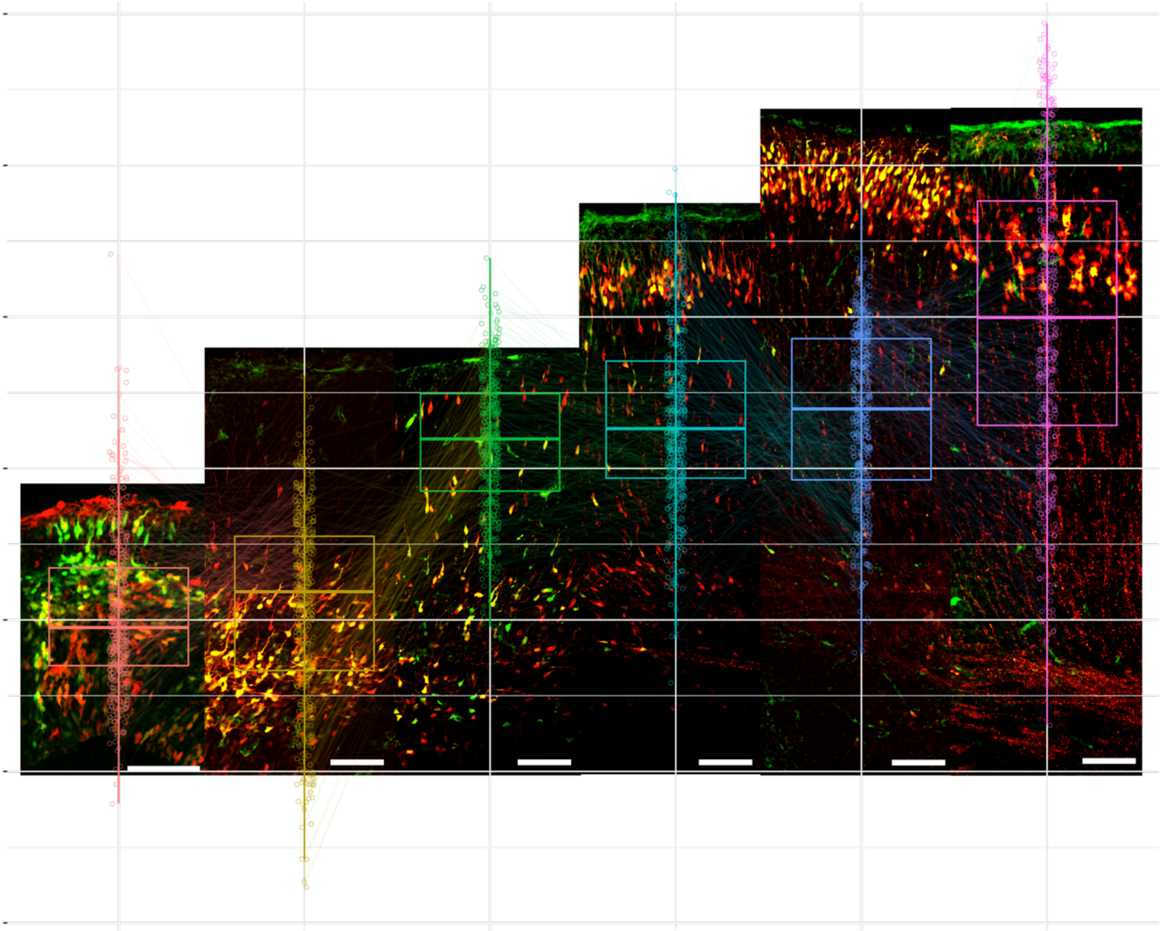

Tabitha Marie Rücker

born in Hagen, Germany

Matriculation number: 6649606

Dissertation submission date: 17.11.2023

Persistent identifier: urn:nbn:de:gbv:18-ediss-123996

PhD defense date: 22.11.2024

Preliminaries

Evaluators

PROJECT LEADER (LAB WORK)
AND FIRST REVIEWER:

Froylan Calderón de Anda, PhD

Center for Molecular Neurobiology
Hamburg (ZMNH)

Institute of Developmental Neurophysiology
R. 2.20
Falkenried 94
20251 Hamburg

Phone: +49 (0) 40 7410 - 56817
E-mail: froylan.calderon@zmnh.uni-hamburg.de

SECOND REVIEWER:

Prof. Dr. Christian Lohr

Universität Hamburg
Fakultät für Mathematik,
Informatik und Naturwissenschaften
Fachbereich Biologie

Institut für Zell- und Systembiologie der Tiere/
Neurophysiologie
R. 423
Martin-Luther-King-Platz 3
20146 Hamburg

Phone: +49 40 42838-5924
E-Mail: christian.lohr@uni-hamburg.de

THIRD REVIEWER:

Dr. Patrick Varga-Weisz

University of Essex
School of Biological Sciences
3SW.3.04, Colchester Campus
Phone: +44 (0) 1206 872318
Email: patrick.varga-weisz@essex.ac.uk

Additional committee members:

Prof. Dr. med. Julia Neumann

Prof. Dr. Thomas Oertner

Declaration on oath – Eidesstattliche Erklärung

I hereby declare, on oath, that I have written the present dissertation by my own and have not used other than the acknowledged resources and aids. I further affirm that the printed version of the dissertation corresponds to the electronically deposited version.

Hiermit erkläre ich an Eides statt, dass ich die vorliegende Dissertationsschrift selbst verfasst und keine anderen als die angegebenen Quellen und Hilfsmittel benutzt habe. Außerdem versichere ich, dass die gedruckte mit der elektronisch hinterlegten Version der Dissertationsschrift übereinstimmt.

Hamburg, the 17th of November 2023

T. Rücker

Tabitha Rücker

Personal contributions to coauthorships

During my PhD journey, I contributed to several publications by my colleagues:

1st Article

Durga Praveen Meka#, Melanie Richter#, **Tabitha Rücker**#,*, Hannah Voss, Anne Rissiek, Christoph Krisp, Nisha Hemandhar Kumar, Birgit Schwanke, Eugenio F Fornasiero, Hartmut Schlüter*, and Froylan Calderon de Anda§,*
# These authors contributed equally
* Corresponding authors
§ Lead Contact

Preaccepted in STAR protocols.

Personal contribution:

- I harvested, cryo cut, stained, and imaged around 50 mice with different test promoters (IUE at E12, harvested at E14, see Suppl. Fig. 1). The best images of the constructs pGlast1-dsRed2/pCAG-Venus and pNeuroD1-eGFP/pCAG-tDimer went for publication.
- I provided the resulting FACS gates from my experiments used in this dissertation with pGlast1-dsRed2/pCAG-Venus and pNeuroD1-eGFP/pCAG-tDimer constructs and the accompanying statistics.

  For the revision:
    - Provided all RNA-seq results.
    - Replaced all the FACS schemes and generated FlowJo matrices.
    - Corrected and rewrote several versions of the manuscript. Wrote rebuttal letter and cover letter.

2nd Article

Henis, Melad, **Tabitha Rücker**, Robin Scharrenberg, Melanie Richter, Lucas Baltussen, Durga Praveen Meka, Birgit Schwanke, Nagammal Neelagandan, Danie Daaboul, Nadeem Murtaza, Christoph Krisp, Sönke Harder, Hartmut Schlüter, Matthias Kneussel, Irm Hermans-Borgmeyer, Joris De Wit, Karun K. Singh, Kent E. Duncan, Froylan Calderón De Anda, and Kent Duncan. 2022. "TAOK2β Represses Translation via Phosphorylation of EEF2 and Ameliorates Exaggerated Protein Synthesis in a Mouse Model of 16p11.2 Microdeletion-Driven Autism." BioRxiv 2022.08.22.504812. DOI: https://doi.org/10.1101/2022.08.22.504812.

In revision at ScienceAdvanced.

Personal contribution:

I performed bioinformatic analyses of the generated mass spectrometry data set from start to finish. We went through several trials as the experiment had to be repeated. In the end, we selected a cnetplot and an overrepresentation analysis for publication.

3rd Article

Scharrenberg, Robin, Melanie Richter, Ole Johanns, Durga Praveen Meka, **Tabitha Rücker**, Nadeem Murtaza, Zsuzsa Lindenmaier, Jacob Ellegood, Anne Naumann, Bing Zhao, Birgit Schwanke, Jan Sedlacik, Jens Fiehler, Ileana L. Hanganu-Opatz, Jason P. Lerch, Karun K. Singh, and Froylan Calderon de Anda. 2022. "TAOK2 Rescues Autism-Linked Developmental Deficits in a 16p11.2 Microdeletion Mouse Model." Molecular Psychiatry.

Personal contribution:

- I cryo cut part of the harvested brains, stained against DAPI, and imaged them for publication.
- I performed PCRs for distinguishing experimental genotypes (16p11.2, TaoK2).
- For the revision: I performed all the AMAXA experiments for (live) imaging on problematic 16p11.2 and TaoK2 knockout organotypic slice cultures, and maintained the accompanying cell cultures until fixing. Both imaged slices and cells were all used for later publication.

4th Article

Meka, Durga Praveen, Oliver Kobler, Shuai Hong, Carina Meta Friedrich, Souhaila Wuesthoff, Melad Henis, Birgit Schwanke, Christoph Krisp, Nessa Schmuelling, René Rueter, **Tabitha Ruecker**, Ewelina Betleja, Tao Cheng, Moe R. Mahjoub, Peter Soba, Hartmut Schlüter, Eugenio F. Fornasiero, and Froylan Calderon de Anda. 2022. "Centrosome-Dependent Microtubule Modifications Set the Conditions for Axon Formation." Cell Reports 39(3). Doi: https://doi.org/10.1016/j.celrep.2022.110686.

Personal contribution:

- I helped establish the communication and the gates for FACS experiments.
- I analysed the generated mass spectrometry data set towards a heatmap for publication.

Acknowledgements

The path to a doctorate was the culmination of the skills and mindsets I had previously acquired during my time in the GoycooLab, in Udo Schumacher's research group, and in Patrick’s group at the Babraham. The PhD project itself was a huge playground where I could develop and grow. I am sincerely grateful for the trust and support I have received on this journey.

Firstly, I thank Froy for entrusting me with such an extensive project and for allowing me to learn whole new things along the way. I had no prior knowledge of neurodevelopmental processes, nor did I have NGS or coding skills that were fundamental to advancing the original question. I learned the importance of asking tailored questions and seeking the most elegant solutions from him. This boosted my confidence to keep up my curiosity and motivation.

Thank you, Francisco, for your confidence when ten years ago I was "just" a student asking you about mycelium as potential drug carrier. You cannot imagine how honoured I am to now be part of the Goycoo family and one of your "scientific offspring". Every time I have encountered difficulties on my path so far, I have thought back to this time and gained new hope and strength. There is simply nothing like the GoycooLab, and that is what makes it difficult at times. Thank you from the bottom of my heart.

Speaking of people who have awakened my scientific interest – thank you, Mrs Heinrichs, for recognising my biological interest at school and subsequently giving me this old edition of the Stryer (1996), the only book that accompanied me on my journey to Hamburg, to Britain and back. The following night I read the first chapters, and it gave me such a satisfaction that for the first time I seriously considered embarking on a scientific rather than a linguistic journey. Well, here is my dissertation :)

Many thanks also to Prof. Udo Schumacher who sparked my interest in epigenetics. Based on my question about the proinflammatory behaviour of cancer, this was the right path for me to take. Thank you, Patrick, for reinforcing my view of holistic approaches; that biology is complex, often redundant, and interconnected.

Thank you also to my co-workers. Especially the people at the LIV, including the receptionist, who passed on the samples to the sequencing facility, sometimes weekly, even in the midst of the Corona pandemics. Kerstin, thank you for handling all my samples with such care and passion. That really means a lot to me. During the time at the ZMNH I also received valuable tips from Sabine and Marcel. Thank you for the many conversations about Evo-Devo and the encouraging words! I additionally would like to thank the cleaning staff at the ZMNH. You always made me feel welcome when I once again entered the institute at 4am to harvest the

E19 embryos that had not yet been born. You are the foundation for us to do our work well. I thank you for that.

I am sincerely grateful for the encouragement of the above-mentioned people, who have all contributed to this dissertation in their own unique ways.

I also want to thank my dissertation examiners Prof. Dr. Christian Lohr and Dr. Froylan Calderón de Anda.

Thank you, Robin, for ensuring my energy level throughout the PhD phase with the most delicious creations of my favourite food such as “Grießpuddings”, melanzane alla parmigiana, and lentil soups. Thank you for always pulling me out to gain new perspectives and for keeping my curiosity alive. I have learned to care for both my physical AND my mental health, I have learned to acknowledge my demands, and I have learned to stand up and to not let stereotypes hold me back. Thank you for always being there for me.

Last but not least, I would like to thank my family. My siblings, who have opened my mind to new perspectives, my sisters, who have shown me that a woman is capable of anything she wants, and my brother, who always makes my mental boundaries disappear as surely as if it was a matter of course. Thank you, mum and dad, for helping me mature my values and for teaching that I can set my own standards. Thank you for answering my endless questions, not only in childhood days, but still today. Thank you for understanding and supporting me in every way possible.

I am looking forward to the next steps and I feel well prepared!

FOR MY FAMILY,

AND THE GOYCOO FAMILY.

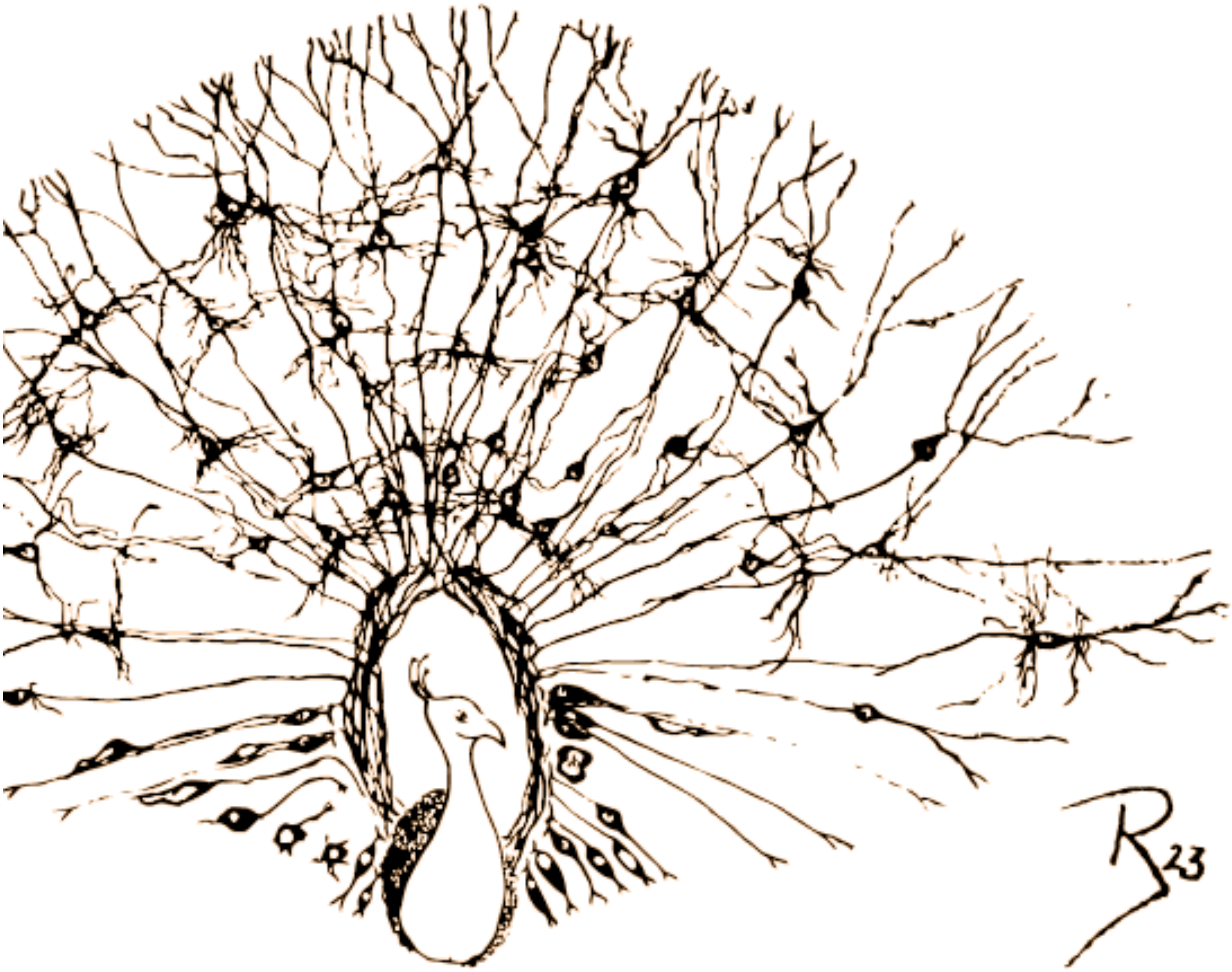

►Table of Contents

Materials and Methods 42

Results 73

Tables

Abbreviations

ABBREVIATION	DEFINITION
5-(h)mC	5-(Hydroxy-)methylcytosine
ACN	Acetonitrile
AD	Alzheimer’s disease
AMPAR	Alpha-Amino-3-Hydroxy-5-Methyl-4-Isoxazole Propionic Acid receptor
ASD	Autism spectrum disorders
BDNF	Brain-derived neurotrophic factor
BH	Benjamini-Hochberg
BHLH TFs	Basic helix–loop–helix transcription factors
bp	Base pair(s)
BP	Biological process
cDNA	Complementary DNA
CP	Cortical plate
DEGs	Differentially expressed genes
DEPs	Differentially detected proteins
DIABLO	Data Integration Analysis for Biomarker discovery using Latent variable approaches for Omics studies
E(14, 16, …)	Embryonic day 14, 16, etc.
ECM	Extracellular matrix
EDTA	Ethylenediaminetetraacetic acid
eGFP	Enhanced green fluorescent protein
EM-seq	Enzymatic methyl sequencing
EOMES	Eomesodermin protein, also called: Tbr2
eYFP	Enhanced yellow fluorescent protein
FA	Formic acid
FAC(S)	Fluorescence-activated cell (sorting)
FDR	False discovery rate
FMO	Fluorescence minus one
GABA	Gamma-aminobutyric acid
gDNA	Genomic DNA
GO	Gene ontology
GPCR	G protein-coupled receptor
HB	Holm-Bonferroni
HPA	Hypothalamic-Pituitary-Adrenal axis
i.p.	Intraperitoneal
IGV	Integrative Genomics Viewer
IKNM	Interkinetic nuclear migration

IPC	Intermediate progenitor cell
L I, L II, L III, …	Layer 1, Layer 2, Layer 3, etc.
LC-MS/MS	Liquid chromatography-tandem mass spectrometry
LFQ	Label-free quantification
LRT	Likelihood ratio test
MIA	Maternal immune activation
MNAR	Missing not at random
ms	Milliseconds
MS	Mass spectrometry
MTOC	Microtubule organization center
MZ	Marginal zone
NA	Not available
NB	Negative binomial
NES	Normalised enrichment score
NMDAR	N-methyl-D-aspartate receptor
P(3, 5, 7)	Postnatal day 3, 5, 7
p.adj.	Adjusted p-value
PC	Principle component
PCA	Principle component analysis
PCM	Pericentriolar material
PFKFB3	6-phosphofructo-2-kinase/fructose-2,6-biphosphatase 3
RGC	Radial glia cell
RIN	RNA integrity
RNA-seq	RNA sequencing
RQ	Relative quantification
RT	Room temperature
RTK	Receptor-tyrosine kinase
SDC	Sodium deoxycholate
Shh	Sonic hedgehog
SVZ	Subventricular zone
TBR2	T-box brain protein 2, also called: Eomesodermin
TEAB	Triethylammonium bicarbonate
TF	Transcription factor
ULN	Upper-layer neuron
v.	Version
VZ	Ventricular zone
WGCNA	Weighted gene co-expression network analysis
Wnt	Wingless-related integration site

List of Figures

List of Supplementary Figures

List of Tables

List of Supplementary Tables

List of Equations

Introduction

The neocortex evolved about 250 million years ago [1–3] in an amniotic ancestor that gave rise to the present mammalian species. Neocortical structures exhibit new functional circuits resulting from the division of the cerebral cortex into several layers.

During the third trimester of mammalian gestation, neuronal stem cells start structuring the neocortex through a direct and an indirect form of neuron production. Initially, the stem cell population directly transforms from the progenitor state into differentiated neurons for the later deep layers. Then, the neurogenic phase is prolonged by a second phase of neuron production through indirect neurogenesis. In this process, the neuronal progenitor population amplifies the neuronal output exponentially by an additional symmetric cell division. The transformation of these progenitor cells into an intermediate state, so-called "**i**ntermediate **p**rogenitor **c**ells" (**IPC**s), enables this expansion. Ultimately, the neurons produced by IPCs migrate into the upper cortical plate, forming two more layers. Unlike the deep-layer neurons, these **u**pper-**l**ayer **n**eurons (**ULN**s) project into the other hemisphere via the *corpus callosum* [2]. The order in which cortical layers and their unique connections evolved during evolution is consistent with the sequence of neuronal development in mammals, reflecting a congruence between evolutionary history and the timing of embryogenesis.

This combination of biphasic neurogenesis together with the differential connection endows us mammals with a wealth of additional cognitive circuitry that not only has contributed to a new evolutionary niche, but also appears to be prone to neurodevelopmental disorders such as **a**utism **s**pectrum **d**isorders (**ASD**) [4,5] and schizophrenia [6,7]. These psychological variations can be attributed to cortico-architectural disturbances affecting callosal projection neurons, but the molecular basis of the morphological dysfunctions remains vaguely defined.

In the introductory section, I frame the steps required to fine-tune corticogenesis in the upper layers and merge this information with known perturbations that affect this landscape.

For the experimental part, I collected multimodal information about the corticogenesis of the upper layers. First, I analysed how the ULNs go through which developmental milestones to determine their cell fate and created a developmental map. Second, I interrogated this map with a maternal immune activation, employing the null hypothesis that the externally applied "stress" has no effect on the development of ULNs.

The results reveal a shift of intrinsic neurodevelopmental processes upon immune activation, specific to ULNs.

Highlights

- Acute **m**aternal **i**mmune **a**ctivation (**MIA**) signatures implicated disturbed synaptic processes and elevated canonical Wnt signalling at the transcriptomic level.
- Developing neurons evoked immune responses at the post-migratory stage; thus, ULN developed along intrinsic **and** extrinsic factors.
- The transcriptomic and proteomic levels mirrored each other with a time delay.

Conclusion

With this work, I aim to provide a profound description of the untreated and immune-activated upper-layer corticogenesis in a murine model system. I hope to enhance our understanding of how external stress affects this susceptible yet robust system.

Abstract

Upper-layer corticogenesis endows us mammals with a variety of additional cognitive circuits. Via indirect neurogenesis, neuronal progenitor cells transform from a radial glia cell to an intermediate stage where they exponentially amplify neuronal output, migrate into the upper parts of the neocortex, and settle there as excitatory projection neurons. Along the way, *Glast1*+ (Glutamate aspartate transporter 1) progenitor cells exit the cell cycle, begin to express *NeuroD1* (Neuronal Differentiation 1), and terminally commit to the neuronal fate.

Urgent questions emerged, such as,

How do neurons gradually enter and maintain the "post-mitotic" state?

What regulatory landscape mediates the explicit formation of the upper layers?

Do prenatal stressors influence upper-layer corticogenesis?

These questions required the creation of a multimodal map in a mouse model to answer them holistically. The mapped untreated and immune-activated indirect neurogenesis allowed me to infer subtle imprints that could explain the sporadic aetiology of neurodevelopmental disorders. With the introduction of a fluorescent dye driven by the *Glast1* or *NeuroD1* promoter into the embryonic brain at the peak of neurogenesis, this study tracked untreated neurogenesis at different levels of biological complexity (mass spectrometry, bulk RNA-seq, and DNA methylation assays) at a daily interval. In addition, maternal immune activation (MIA) was provoked with PolyI:C (immune activation) and PBS (control) injections twice during acute neurogenesis to challenge the plasticity of the naïve landscape.

It is now possible to derive interdependent components between all three modalities over developmental time. Additionally, it emphasised the functional embedding of Wnt signalling and the underrepresentation of synaptic translation in MIA animals, indicating a link to autism spectrum disorders. Integrating all this information will provide the scientific community with a rich data set that enables the design of tailored experiments about the neurogenic fate acquisition of the upper-layer neurons.

KEYWORDS: Corticogenesis, lamination, maternal immune activation, multimodal analysis, cell fate acquisition, two-hit hypothesis

Deutscher Überblick über das Projekt

Die Entwicklung der äußeren Schichten der Großhirnrinde ist uns Säugetieren eigen – sie statten uns mit zusätzlichen, einzigartigen neuronalen Vernetzungen aus, die uns von Reptilien und Vögeln unterscheiden. Die pyramidenförmigen Neurone der äußeren Großhirnschicht werden während der „indirekten Neurogenese“ gebildet. Dabei unterlaufen neuronale Vorläuferzellen einen Zwischenzustand, in dem sie sich noch einmal symmetrisch teilen und somit ihre Produktion von ausgereiften Neuronen exponentiell steigern. Danach migrieren diese inzwischen jungen Neurone nach außen, an schon älteren Neuronen vorbei, hin zur *Pia mater* und verknüpfen sich schließlich mit der jeweils anderen Gehirnhälfte. Auf ihrem Weg exprimieren diese Zellen zunächst *Glast1* (ein Glutamattransporter) und anschließend *NeuroD1* (ein neurogener Transkriptionsfaktor). Die *NeuroD1* Expression ist an ihre Eigenschaft gebunden, sich nach der Migration nicht mehr zu teilen, sondern sich für den Rest des Lebens des Säugers lokal in den neuronalen Schaltkreis einzubinden.

Was ist für diesen „post-mitotischen“ Zustand der Neurone verantwortlich?

Was reguliert die Bildung der äußeren Großhirnschicht explizit in Säugern?

Haben pränatale Faktoren Einfluss auf die Entwicklung der äußeren Großhirnschicht?

Ziel der Arbeit ist es, eine multimodale Karte zu erstellen, an der sich zukünftige Entwicklungsforscher orientieren können. Die Karte berücksichtigt die unbehandelte und immunaktivierte neuronale Entwicklung im murinen Modellsystem, um von Abweichungen auf mögliche subtile Prägungen schließen zu können. Vielleicht erklären diese den ein oder anderen “spontanen” Auftritt von frühkindlichem Autismus, für den es keine hinreichenden genetischen Erklärungen gibt.

Die Methodik beruht auf der fluoreszenten Markierung von neuronalen Vorläuferzellen und jungen Neuronen mit den Promotoren der genannten Gene *Glast1* und *NeuroD1*. Anhand ihrer Fluoreszenz konnten die Zellen aus dem embryonalen Cortex an jedem Tag ihrer Entwicklung sortiert und auf drei verschiedenen biologischen Ebenen (Proteom, Transkriptom und DNA Methylom) untersucht werden. Zusätzlich wurde die physiologische Entwicklung der jungen Neurone mit einer maternalen Immunaktivierung gestresst und kongruent ausgewertet.

Die Ergebnisse liefern nicht nur einen großen Datensatz, der die spezielle Entwicklungsphase detailliert darstellt, sondern gewähren auch mechanistische Einblicke. Es scheint, als sei die synaptische Entwicklung bei gestressten Tieren entscheidend gestört worden und als sei die post-transkriptionelle Maschinerie ein guter Anhaltspunkt für eventuelle Interventionen. Die Verknüpfung von unterschiedlichen Methodiken über den gesamten Entwicklungszeitraum dieser Zellpopulation hinweg wirft vor allem neue Fragen über Stabilität und Plastizität dieses Entwicklungssystems auf.

► Untreated, indirect corticogenesis

The mammalian neocortical structures form via a highly orchestrated lamination process called corticogenesis. During corticogenesis, neuronal cells arrange sequentially for the deep and upper layers. In murine gestation, cortical neurogenesis occurs from around embryonic day 11 to 15, after which it is followed by gliogenesis until birth at around E19 [8]. The layering process is spatially limited; internally to the ventricular surface and externally to the pial surface and follows four key steps: (1) the neuronal progenitor cells exponentially amplify their cellular output in the "**s**ub**v**entricular **z**one" (**SVZ**), (2) the progenitors polarize, (3) after which they migrate radially towards the pial surface, and (4) lastly integrate with the already established neural circuitry built up from the deep layers (Fig. 1).

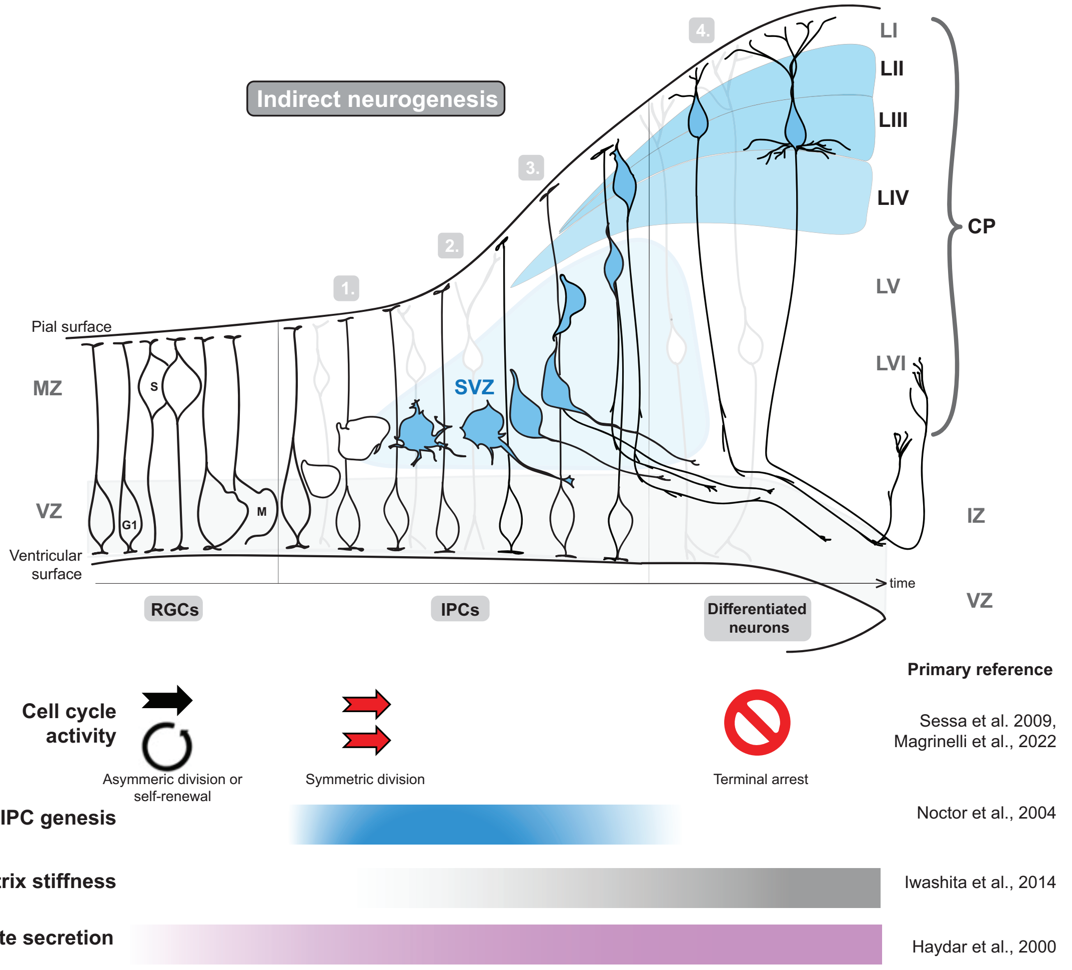

Figure 1: Mammalian indirect corticogenesis includes second phase of symmetric cell division for upper-layer formation

Late neurogenesis forms the neurons for the later upper layers II-IV (ULNs marked in turquoise). These upper-layer neurons arise from multipolar Tbr2+ intermediate progenitor cells (IPCs), which are transformed radial glia cells (RGCs) that divide again symmetrically and thus temporarily expand the neuronal output in the subventricular zone [9–11] (1). After this second cell cycle, they polarise (2) by forming an axon, and migrate into the cortical plate following in an inside-out, outside last mechanism along the radial glia fibres (3). Finally, they integrate with the neuronal circuit and project into the other hemisphere (4). Along their way, the matrix of the system stiffens as more axons outgrow [12]. The secretion of the excitatory neurotransmitter glutamate accompanies ULN genesis and is fundamental to their function [13]. Murine corticogenesis shown, numbers refer to subchapters of this introduction.

Proliferative zone – Plastic progenitor cells define neuronal output

SUMMARY: *Radial glia cells build the basis for direct and indirect neurogenesis. Initially, RGCs form long radial fibres that span the entire cortex from the apical ventricular zone and basal pial surface, and thus provide a continuous scaffold for the nascent neurons to migrate along* [14]*. They already express a glutamate transporter, called Glast1/Slc1a3, as a response to increasing glutamate accumulation.*

At the beginning of neurogenesis, neuroepithelial stem cells start shaping the neural tube into a functional, activity-dependent neuronal circuit that is ultimately able to transmit action potentials across hemispheres. For this, they initially transform into bipolar **r**adial **g**lia **c**ells (**RGC**s) by asymmetric cell division.

The bipolar shape is defined by their soma located in the ventricular zone of the developing neocortex, whilst spanning their long, radial fibre across the entire apical-basal axis, with the ventricular zone as the apical platform and the pial surface as the basal limit. This fibre provides the first scaffold along which the emerging neurons migrate [15]. As RGCs are initially both apically and basally anchored, they are particularly broadly embedded within the neurogenic niche. They receive chemoattractant or -repellent cues from the whole span of the cortex [16].

During neocortical development, RGCs are multipotent; thus, they are able to give rise to a unique set of neocortical cells – not only neurons – with distinct functions. As their name suggests, radial **glia** cells express mature glial marker genes such as the glial fibrillary acidic protein (*Gfap*) and vimentin (*Vim*) [17]. Once neurogenesis is completed, the remaining parental RGCs take on an astrocytic or oligodendrocytic character, a process known as "gliogenesis". These glial cells adapt to the originally created neuronal scaffold and provide crucial support for the mature neuronal circuit [15]. How their transcriptional landscape defines laminar positions, timing, and *vice versa* is still under debate [10,18,19].

Glast1 expression in radial glia cells

Next to the typical RGC-specific transcription factors, RGCs express high levels of glutamate receptors, such as the high-affinity L-glutamate transporter *Slc1a3*/GLAST-1 [20] and the metabotropic glutamate receptor GRM5 [21]. Glutamic acid (**glutamate**) is the most abundant excitatory neurotransmitter in the central nervous system. Glutamate mediates neurogenic cell fate acquisition by inducing a proton gradient [22–24]. Cajal-Retzius cells [25] as the earliest neuronal population [26], and the subplate neurons [27] have been suggested to be the main source of the first spontaneously released glutamate [13,28,29]. Thus, RGCs already encounter a challenging microenvironment in the VZ. Glutamate accumulation, e.g. by excessive Ca^{2+} influx, can lead to excitotoxicity in differentiated tissue [22,30], just as overstimulation of their primary receptors (NMDAR) impairs corticogenesis [31].

This way, the ‘glutamate aspartate transporter 1’/GLAST-1 helps maintain L-glutamate supply below neurotoxic levels and limits the extracellular glutamate concentration by removing L-glutamate from the synaptic cleft, indirectly mediating postsynaptic excitation. Because of its ability to protect against glutamate-induced excitotoxicity, GLAST-1 is also characteristic of the functional maturation of cortical astrocytes [32]. In human pathogenic GLAST polymorphisms (SLC1A3 variant microdeletions), the glutamate uptake is impaired and has been linked to neuropsychiatric disorders such as schizophrenia [33]. *Slc1a3* double knockout mice exhibit symptoms similar to schizophrenia [31,34], while all downstream functional roles of RGCs in neurogenesis are hindered [35]. Postnatal removal of GLAST also leads to disturbed neuronal morphology and cognitive impairment [36]. Thus, *Slc1a3* expression is indispensable for the onset of neurogenesis [35], as it regulates glutamate uptake before the mature neuronal circuit is even established.

The promoter of GLAST1 was used here to drive the expression of a fluorophore for specifically sorting radial glia cells by flow cytometry. This sorted RGC population established a direct cell lineage relationship as they represented the progenitor pool from which the mature ULN cell population was derived.

Radial glia cells begin neurogenesis

RGCs are – like every neuroepithelial cell – subject to **i**nter**k**inetic **n**uclear **m**igration (**IKNM**). They translocate their soma with the nucleus up to the pial surface for IKNM, but only for the “S”/synthesis phase. Afterwards, RGCs retranslocate their soma to the VZ for asymmetric cell division/”M” phase (Fig. 2). The mechanisms contributing to replicating and passing on the radial fibre are largely unsolved. However, the IKNM is likely triggered by spindle orientation and mitogen gradients that define polarity [37,38].

RGCs supply the upper and deep cortical layers with neuronal outputs via direct and indirect neurogenesis [11,39].

Direct neurogenesis is the standard mechanism by which RGCs produce neurons for the cortical plate, again by asymmetric cell division. In mice, direct conversion of RGCs to neurons begins at E11 [40]. Without an intermediate step, these early-born neurons build up the deep layers, which are constructed similarly to the cortical homologues of reptiles and birds [3].

Expansion phase accompanied by Tbr2 expression

At the peak of neurogenesis (at E14 in mice) the majority of basally anchored **RGCs** switch to an **indirect** form of neurogenesis: These transformed RGCs, now so-called "**i**ntermediate **p**rogenitor **c**ells" (**IPC**s), undergo another phase of symmetric cell cycle [11] to both massively expand the progenitor pool and to give rise to a pair of cortical, clonally related neurons. The IPC-derived neurons contribute 70-80% of the cortical excitatory neurons in the upper layers II-IV [41–43]. Thus, IPCs expand the cortex exponentially with two additional layers compared to e.g. reptiles [3,44–46]. Upper layer formation has also been linked to the evolutionary expansion of the neocortex and associated enhanced cognitive abilities [41,47–49].

The second, symmetrical cell division of IPCs defines their prominent role in mammalian corticogenesis. Along the way, IPCs establish a transient and mammalian-specific germinal zone, the **s**ub**v**entricular **z**one (**SVZ**) [11], between the **v**entricular **z**one (**VZ**) and the **i**ntermediate **z**one (**IZ**), where they acquire a multipolar character. In this SVZ, IPCs start to express *Tbr2*/EOMES. From the SVZ, they migrate long distances into the developing cortex and the IPC population is quickly depleted afterwards [50,51].

IPCs have overlapping profiles to RGCs and immature neurons, making them challenging to detect experimentally [52]. *Tbr2* is the only characteristic marker gene of IPCs. The expression of the **t**ranscription **f**actor (**TF**) *Tbr2* is also present in reptiles and in avian cortex, but there, an SVZ or mammalian equivalent of layer II-IV is absent [9,45,53–56]. However, IPC identity is not entirely dependent on the onset of *Tbr2* expression [53]. It is yet unknown what cues trigger the RGC population to express *Tbr2*.

EOMES is critical in enabling migration of multipolar IPCs in the SVZ. In humans, the congruent cell type to IPCs – based on EOMES – represents the population of outer radial glia cells that forms the outer SVZ [57,58]. In contrast to rodents, outer radial glia cells in humans undergo not only one but several additional rounds of the cell cycle and increasingly shorten their G1 phase during neurogenesis [59]. The human outer SVZ can be distinguished from the ventricular SVZ as early as E58 [48,60]. In contrast, the two zones are indistinguishable in the rodent brain, and harbour IPCs with a multipolar character that form more neurites in humans than their rodent counterparts [61]. Moreover, their increased abundance correlates with increased gyrification of the human neocortex [49]. Target genes of characteristic *cis*-regulatory domains (enhancers) found only in humans (and primates) controlled the development of the outer radial glia cells [62].

Transcription factors contributing to cell cycle control, migration processes, and anti-apoptotic signalling are found up- and downstream of the *Tbr2* locus [63]. For example, the IPC-characteristic expression of the Notch ligand *Dll1* is activated by *Neurog2* and *Tbr2* [64–66]. NEUROG2 and EOMES have combinatorial transcriptional function [67], which form mutually with PAX6 an activation cascade that drives the neurogenic cell identity switch [55,67–71]. EOMES acts upstream of E-cadherin and represses it upon NEUROG2 activation allowing progenitors to enter the migratory state [72,73]. NEUROG2 activates the expression of small GTP-binding protein *Rnd2*, which mediates the migration process, lamina formation [67], and generally the multipolar to bipolar transition [74,75].

Overexpression of *Tbr2* in the neurogenic context impacts the pattern of angiogenesis and results in unstable cell fate specification [76]. In addition, overexpression of *Tbr2* impedes cell cycle exit, leading to overproduction of both IPCs and descending neurons [9]. Overproduction of IPCs, in turn, leads to autism-related behavioural abnormalities, which can be attributed to an imbalance between excitatory and inhibitory output [4].

Axonogenesis – reacquisition of polarity

SUMMARY: *For cytokinesis, intermediate progenitor cells lose their bipolar character and become multipolar. This multipolar shape stands in close contact with centrosomal motility and retraction of the primary cilium, leading to active delamination* [77–79]*. To subsequently enable radial migration into the cortex, intermediate progenitor cells must resolve their multipolarity. They repolarise by stabilising one of the early neurites to become the future axon* [79]*. Especially upper-layer neurons, which will project to the other hemisphere, must establish a robust and well-defined axon.*

Axons are polarised, neuron-specific organelles that – when mature – propagate electrical “action potentials” across their apically oriented microtubule-based fibres. Axonogenesis is a highly coordinated process that breaks the symmetry of the progenitor cell [80].

During axonogenesis, *Foxg1* and *Sox2* [81] expression is superseded by *Neurod1* and *Unc5d* expression [82]. EOMES promoted efferent axon projections, while the EOMES+ lineage itself appeared to be targeted by thalamic axons [83]. Moreover, alternative splicing is key to proper axon formation [84]. At the posttranslational level, axon formation is driven by (histone) acetyltransferases, which alter the distribution of acetylated tubulin and ultimately trigger microtubule dynamics [85–87].

In culture, plated progenitor cells form several growth cones that extend and retract. Eventually, one of the growth cones becomes the single, unidirectional axon, and the other neurites form several dendrites in the differentiated, pyramidal neuron. Eventually, the axon initial segment forms during polarity reacquisition, which is later located on the axon shaft. Neuronal excitability depends on this axon initial segment, since it maintains polarity and regulates electrophysiological properties [87–89].

After the soma has regained its polarity, it begins migrating towards the CP, while translocating the centrosome together with the Golgi apparatus and other polarised cytoplasm basally. In this way, the somatic processes move upwards (leading process). Once settled in their new niche, ULNs elongate their newly formed axon (trailing process) (Fig. 2; [79]).

Mature axons are periodically ensheathed with myelin to enable a saltatory, highly efficient signal transmission [90].

Filaments scaffold axonogenesis

During polarity formation and later migration, progenitor cells undergo a drastic cytoskeleton rearrangement. Filaments such as microtubules, actin, and intermediate filaments ensure intracellular transport and plasticity of the transforming cell.

Polarised **microtubules** play a systemic role in reacquiring polarity and establishing unidirectional signal transmission. Microtubules are organelles that polymerise α- and β-tubulins into a tubule with a plus and minus end. This tubulin assembly into a microtubule is fueled by GTP hydrolysis. Thus, GTP hydrolysis by Rho-GTPases, such as Rnd2 or RhoA, influences the dynamic rearrangements of microtubules (microtubule treadmilling) during neurogenesis [15,91]. Assembled microtubules traverse the axon and are critically involved in delamination, reorganisation of the primary cilium, and intracellular polarised transport of small molecules via motor proteins [87].

In the axon, the intrinsically polarised microtubules orient towards the leading edge/growth cone as the plus end. Microtubule stability within the growth cone is crucial for singular axon formation [86]. To achieve repolarisation in multipolar IPCs, the centrosome preferentially locates close to the axon initial segment and condenses even more microtubule structures, which even predicts axonal outgrowth [79,86,92–95]. Microtubules concentrate around the centrosome (oriented by their minus ends), which plays the crucial role of the **MTOC**, the **m**icro**t**ubule **o**rganisation **c**enter of the cell. The centrosome consists of two centrioles and a surrounding protein matrix, the so-called **p**eri**c**entriolar **m**aterial (**PCM**), which divides into two opposite poles in dividing cells and forms the basis for the spindle apparatus (Fig. 2).

F-actin, as the filamentous version of actin assemblies, dynamically polarises concomitantly to microtubular treadmilling. During polarity formation, F-actin directly stabilises microtubules in the future axon, thus it is crucial to prevent multipolarity [86,96]. For reliable axon outgrowth *in* *vitro*, the dynamics of F-actin at the growth cone interact with the microtubule assemblies [96]. During migration, the F-actin flow anterogradely concentrates on the leading edge, where its contractile area encloses the centrosome [97].

Together, these mechanisms promote the radial migration that accompanies axonal growth and create the prerequisites for the expansion of the neocortex.

Radial migration into the upper cortical plate

SUMMARY: *After repolarisation, these young neurons begin radial migration into the cortical plate by pushing their soma up the radial scaffold and afterwards elongating their axon. Thus, they cross the barrier to the cortical plate and squeeze past older neurons. Early-born neurons preferentially end up in the deep layers and late-born, IPC-derived neurons end up in the upper layers due to this inside-out, outside-last mechanism* [69,98,99]*.*

Emerging neurons produced by indirect neurogenesis [54,100–102] migrate the longest distance from the VZ into the cortical plate along the radial fibres of RGCs [72,103]. IPCs first resolve their physical connections to the SVZ [104] mediated by neurogenic transcription factors such as NEUROD1 and EOMES and morphogenetic signalling gradients, and are further triggered by disintegrins such as ADAM17 [105]. Adhesion molecules then aid with repeated radial fibre attachment and detachment. N-cadherin, laminin, and vimentin mediate the radial glia-driven locomotion of young neurons [15,106–112], and are required for the stabilisation of the Wnt signalling cascade [113] and proper laminar formation [108,110,114]. Protocadherin 19 [53] and cadherin 11 [115,116], known for their role in neural tube differentiation, are important regulators in mediating radial migration of multipolar cells. Besides, this network of adhesion molecules resembles those used during epithelial-mesenchymal transition events [73,117]. The SNAIL and SCRATCH 1 and 2 proteins repress E-cadherin expression during epithelial-mesenchymal transition as well as radial migration of IPCs [77,117,118].

Radial migration follows the delamination of progenitor cells from their early cell context and occurs with a saltatory movement of the cell soma (Fig. 2; [119]). A repetitive pattern of rapid expansion and retraction of the leading process characterises this saltatory locomotion. First, the leading process displaces with the centrosome upwards the radial fibre, which is visible as a basal swelling. Subsequently, the soma shifts upwards together with its nucleus. F-actin dynamics establish protrusive forces with the contractility of motor proteins such as dynein, kinesins and myosin II to actively locomote the soma [87,97,120]. Moreover, the neurogenic transcription factors NEUROG2 and ASCL1 promote the expression of GTPases like *Rhoa* and *Rnd2* to enable dynamic microtubule stabilisation [91]. During this process, microtubule flux radiates from the centrosome anterogradely towards the leading process and retrogradely to envelop the nucleus and forms a perinuclear tubulin cage. This microtubular cage is not as clearly defined in multipolar IPCs as in bipolar RGCs (Fig. 2; [79]).

When IPCs, as developing neurons, leave the SVZ to migrate radially into the cortex, they encounter mechanical constraints within the nascent neuronal scaffold built up from the deep layer neurons. The border to the cortical plate (~subplate) is the stiffest zone in the developing neocortex, which the IPCs must pass [12,121,122]. Thus, late-born neurons not only have the longest migration distance and spend the longest in the motile state [43,123], but must also overcome this mechanical barrier to the developing cortical plate. Softening the ECM during corticogenesis could control the number and the orientation of these mechanosensitive progenitor cells, underscoring that they use durotaxis during migration [124]. Once migrating neurons reach the pial surface, they encounter stop signals. In particular, GPCRs transmit durotactic information to stop migration and integrate into the new niche, the upper cortical layers [125,126].

Depending on the neuron’s “birthday”, radial migration creates layers. Layer 1 comprises the neurons of the subplate, which still originate from splitting the neural preplate into the apical **m**arginal **z**one (**MZ**, future layer I) and the subplate, which establishes a boundary between the VZ and the developing CP [127]. Lamination of the six layers of the murine neocortex occurs between the subplate and the MZ in an inside-out, outside-last mechanism [41,58]. Layer 6 as one of the deep layers, is the first to form after the division of the preplate, and layer 2 as one of the upper layers is the last to develop during neurogenesis.

Thus, the migration phase requires a high degree of transient, concerted interplay of various organelles within the developing neuron, such as the condensed form of the Golgi apparatus [79,128]. A motile state during differentiation is likewise tightly bound to cell fate commitment in cardiac progenitor cells [129,130].

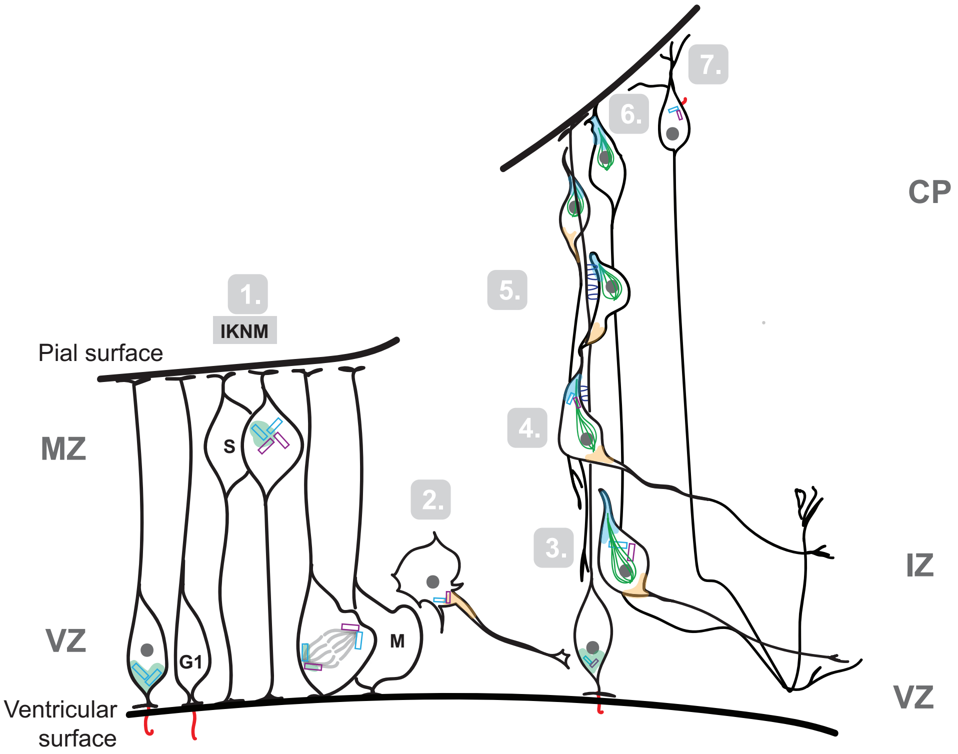

Figure 2: The reacquisition of polarity and radial migration imply major cytoplasmic rearrangements

1. In RGCs, the primary cilium points to the VZ and registers cues for cytokinesis. The two centrioles locate at the basal base of the primary cilium as part of the centrosomal complex, surrounded by the PCM. For division, RGCs undergo IKNM. During the S phase of the IKNM, the centrioles are duplicated. Once the soma returns to the VZ for cytokinesis, along with the now doubled nuclear load, the two centrioles with most of the PCM remnant remain in the RGC. The newly formed cell continues as IPC.
2. In indirect neurogenesis, amplifying divisions increase the progenitor pool followed by direct neurogenesis. Polarity is reacquired by axon formation. Axonogenesis occurs preferentially at the apical site where the centrosome is located.
3. The polarised developing neuron delaminates from the early cell context and relocates its centrosome (purple) apically/ towards the leading edge. F-actin (turquoise) is stabilised and accumulates at the future leading edge. A cage of microtubules (green) forms around the nucleus. A network of actin and myosin II (yellow) gathers at the trailing process, the axon of the developing neuron.
4. New cell-cell connections (dark blue) form between the migrating neuron and the radial fibre. The centrosome is now completely apically oriented. The interaction of the basal actin-myosin network and the apical F-actin force contract the microtubule cage and centrosome further together towards the leading edge, triggering swelling.
5. In saltatory movements, the migrating developing neuron moves upwards the radial fibres, with the centrosome always leading the way and dragging the nucleus behind it.
6. Finally, the migrating neuron meets the pial surface. Stop signals terminate the migration. The axon begins to extend into the other hemisphere.
7. The young neuron detaches from the radial fibre and orients itself in the new cell context. The primary cilium is replaced basally, and with it the centrioles. Likely, the PCM is reassembled around the centrosomal complex. The exact function of this neuronal primary cilium is still unknown.

Note: The primary cilium is highlighted in red. The parental centrioles are highlighted in turquoise, while the daughter centrioles are purple. The lightgreen represents the PCM. These are parts of the centrosome, which is closely coupled with other polarised compartments of the cytoplasm, such as the Golgi apparatus, which plays at least as important a role in controlling centrosomal motility.

Differentiated state as layer II/III neuron

SUMMARY: *Soon after reaching their final location, upper layer neurons cease cell cycle activities, coinciding with their terminal differentiation triggered by the pioneer transcription factor NeuroD1. Upper-layer neurons then orient in their new neocortical niche by projecting their axons ipsilaterally or via the corpus callosum into the contralateral hemisphere, making them unique to mammalian corticogenesis* [41,44,131,132]*. With these interhemispheric connections, these neurons integrate sensory and motor contextual information* [133,134]*. Like all neocortical layers, the upper layers are both cytoarchitecturally and functionally distinct, and none of them can be distinguished by a single marker gene. Even their axonal projections and electrophysiological properties differ* [135–137]*.*

When mature, the upper layers consist mainly of excitatory glutamatergic neurons that project to the respective other hemisphere along the *corpus callosum*. The *corpus callosum* enables lateralisation of cognitive functions unique to mammals. Neurons themselves are *elementi perenni*; after embryonic development, they remain in the same place for the rest of the organism's life. However, neurons remain plastic and can adapt to stimuli such as neuronal activity or inflammation throughout the lifespan by building or dissolving their axonal and dendritic connections.

At the peak of neurogenesis (in mice at E14), late-born neuronal progenitor cells begin to form neurons only for the upper layers [10,41–43]. After detachment from the radial fibre and due the "outside-last" mechanism of the cortical lamination process, late-born neurons settle in layer II/III of the neocortex, also called the "supergranular layer" [10,138,139]. So far, no specific, consistent marker genes for the upper layers are available. However, *Satb2* [140,141], *Sp2* [142], *Dlx1,2* [143], *Cux1* [144], and *Pou3f3* [52] are overrepresented in layer II/III neurons [51].

Moreover, no upper layers are formed in neocortical organoids, suggesting that indirect neurogenesis via IPCs has not occurred or has occurred only to a limited extent [145], indicating the importance of external cues for upper-layer neurogenesis [146]. In contrast, transplanted ESC-derived cortical neurons integrate both histologically and functionally with the upper and deep layers [147].

Pyramidal morphology refines function

The excitatory **u**pper-**l**ayer **n**euronal (**ULN**) cell body has a pyramidal shape with dendrites branching out from the soma and an axon extending away from the soma opposed to the dendrites. These cellular components are all optimised for circuit formation in the developing cortex.

Apical and basal dendrites serve as receiving ports for incoming signals from the surrounding cells, which are then processed and interpreted by the soma body. They arborise soon after settling in the layer, increasing dendritic complexity first spontaneously and then in an activity-dependent manner [148–150]. The axon shaft then transmits the integrated action potentials unidirectionally via the myelinated axon fibre to the distal synaptic terminals, where the signal is again translated by chemical and physical means.

Where layer II/III synapses project to depends on which area of the cerebral cortex their soma originates (Fig. 3). ULNs project across the rostral prefrontal to caudal somatosensory cortex. Moreover, they project callosally, i.e. their axon has an L-like shape and establishes long-range synaptic connections to the other hemisphere across the *corpus callosum* [133,134,144]. These contralateral synapses seek their targets by extending and retracting their synaptic bundles [133,134,151], similar to *in vitro* observations [104]. In this way, they can bind to a dendritic target or even to a primary cilium [152]. Callosal axons require specific neurotrophic signals to guide their search for target cells in the other hemisphere, especially in the first postnatal days. During axon outgrowth, the neuron “overextrudes” its axon and branches it to find synaptic targets. The distal residual axon remaining behind is then eliminated by “synaptic pruning” processes [151,153]. The mechanisms for this guidance are still unclear, but vascularity [76,154] and microglial support may play a chemotactic role (see section “**Microglial guidance for differentiation”**).

The morphology of ULNs is thus inextricably linked to their primary function – their excitability. Excitatory neurons of the upper layers predominantly use glutamate instead of **g**amma-**a**minο**b**utyric **a**cid (**GABA**) as neurotransmitter [155,156]. The establishment of an activity-dependent membrane potential is finely tuned and guided by both spontaneous as well as active events, and the initial discordance of ion gradients.

Initially, GABA is excitatory and shapes the nascent neuron's first circuit towards mature excitability. In immature neurons, active net chloride transport is inward, producing a high intracellular chloride concentration ($[\mathrm{Cl}^-]_i$). This ion gradient enables anions to flow out of the neuron when metabotropic GABA channels are opened, causing depolarisation. The depolarisation induces sodium and calcium action potentials and overrides the voltage-dependent magnesium blockade of **N**-**m**ethyl-**D**-**a**spartate (**NMDA**) channels. The excitatory function of GABA eventually transitions to an inhibitory function when the chloride exporter's expression and the NMDA channels' opening are delayed, resulting in a decrease in intracellular chloride concentration and activation of voltage-gated calcium channels. This so-called “GABA-shift” triggers intracellular calcium oscillations and promotes the fusion of glutamate vesicles at presynaptic membranes. Once released, glutamate induces spontaneous action potentials and synaptic currents that gradually transition to activity-dependent release [157–159]. Lastly, glutamate binds postsynaptically to ionotropic receptors to induce a first excitatory post-synaptic potential [160], dependent on sufficient glutamate and GABA synapse density [161].

Moreover, the synaptic activity itself stimulates the corresponding receptor expression that ensures the internalisation and regulation of both glutamate and calcium oscillations that accumulate intrinsically and finely balance their output [13,162,163]. The ionotropic NMDA [164] and AMPA [165] receptors change their subunits upon calcium influx following synaptic activity and even promote neuronal survival and plasticity [165–167].

Sequential expression and synergistic effects of metabotropic and ionotropic GABA, NMDA and AMPA receptors turn a neuronal precursor cell into a functional upper-layer neuron that transmits action potentials across hemispheres [168].

Once the neuron is functionally embedded in the circuit, the nucleus responds closely to synaptic input [169]. Calcium and glutamate stimuli trigger the transcription of activity-dependent immediate early genes such as *Creb* [170], *cFos* [171], and *Bdnf* [172]. Through sensory-triggered stimuli and interaction with these biochemical signals, early synaptic inputs integrate sensory and motor contextual information (Fig. 3) and regulate adaptive responses. This intrinsic function of ULNs to transmit electrical signals over long distances is the basis for a physiological neural circuit [173].

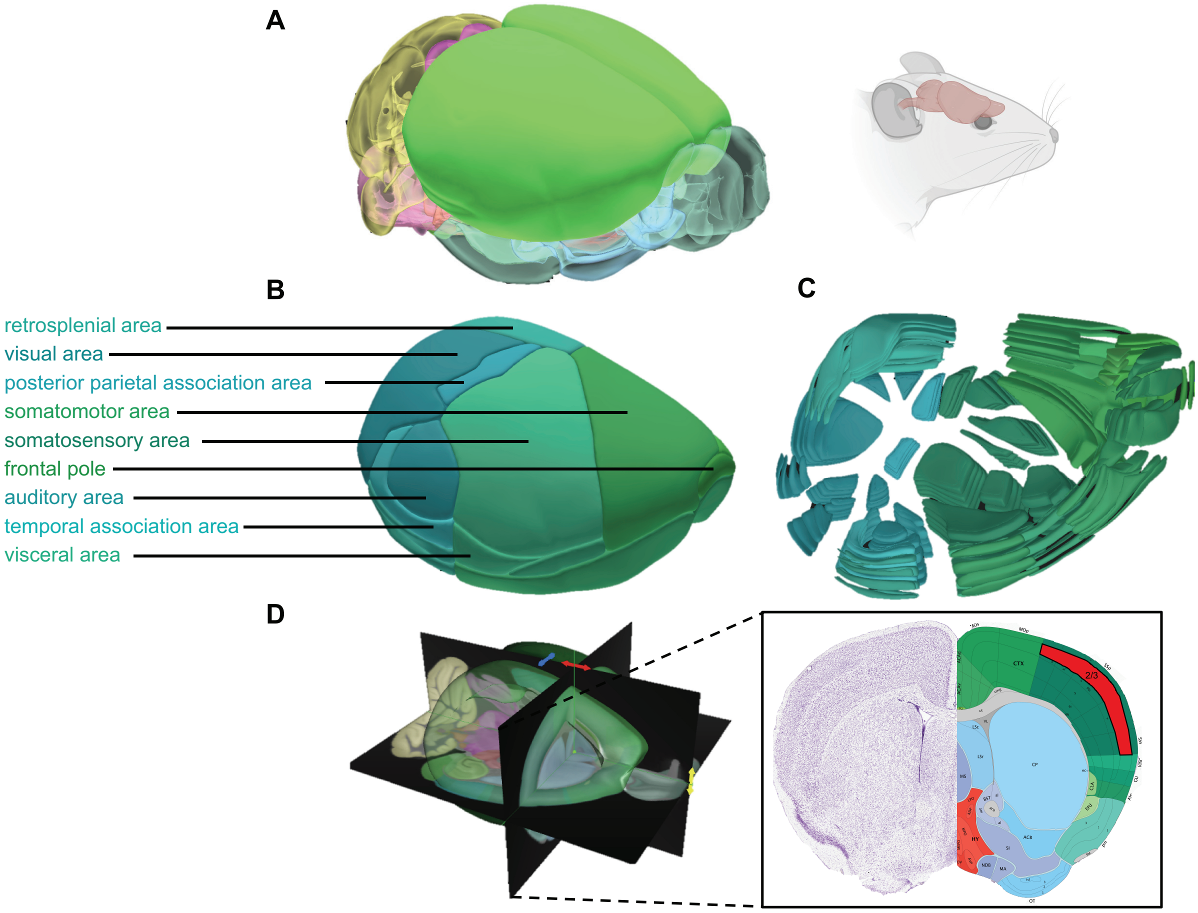

Figure 3: Spatial division of upper cortical layers in the lissencephalic isocortex of the adult mouse

A. The two cortical lobes form the largest superficial part of the mouse brain.

B. The distinction between the main areas of one cortical hemisphere is associated with their respective main known function. However, they all have heterogeneous electrophysical properties. The areas were part of the experimentally targeted cerebral cortex in this study using ***in utero*** **e**lectroporation (**IUE**).

C. The same hemisphere but turned inside out and with separated layers.

D. Cross section of the adult murine brain on the left and a coronal section with Nissl staining on the right. The area mainly targeted in the experiments described here is highlighted in red (layer 2/3 of the primary somatosensory area). Other cortical regions were also used. Since IUE was performed at E14, most of the neuronal output ended up in layers 2/3.

Depictions were generated using the AllenBrain Atlas Map and the ‘Genome-wide atlas of gene expression in the adult mouse brain’ [174].

NeuroD1 expression in differentiating post-mitotic neurons

NeuroD (Neuronal Differentiation) expression attenuates Tbr2-mediated indirect neurogenesis [163,175] towards a **neuronal post-mitotic state**. Expression of the NeuroD protein family as type II bHLH-TFs is transient in the SVZ, and declines postnatally (Fig. 16; [176–178]).

NeuroD1 encodes a pioneer transcription factor occupying bivalent loci [179,180] whose promoter is already in a poised state when β-catenin replaces SOX2 influence during neuronal differentiation [181,182]. *NeuroD1* then regulates calcium-dependent delamination as a target gene of WNT [181,183,184], NGN2 [185], and NOTCH [186], and induces the migration of multipolar neurons that accumulate in the SVZ [123]. Simultaneously, NEUROD1 has also been proposed as a terminal selector transcription factor [180,187]. The concept of terminal selector genes helps explain the precise control of a gradual maturation along inductive cues by combinatorial determinants. Terminal selector genes represent regulatory endpoints in developmental processes [188–190] and encode transcription factors that control a specific *cis*-regulatory motif (e.g. promoter) of another gene-specific cassette. Maintenance of the resulting end state is achieved through the direct autoregulatory function of these terminal selector genes.

Moreover, *NeuroD1* is even sufficient to convert different cell identities such as astrocytes [191] or mature microglia (derived from a different germ layer) [192] or even ectoderm [193] into neurons [194,195]. The NEUROD1+ glutamatergic lineage forms circuits that have been extensively studied in axonal regeneration [196], dendritic growth [150,175], and in the neurogenic niche of the hippocampus [166,197,198], where expression of *Neurod1* is a prerequisite for adult neurogenesis [156,181,199].

NeuroD2 expression also influences axonal pathfinding during neocortical lamination [200]. *NeuroD2* expression is characteristic of the post-mitotic glutamatergic neuronal lineage and initiates a critical transcriptional reprogramming for these excitatory neurons [176,180].

Thus, the promoter of *NeuroD1* as an early post-mitotic neuronal marker [180,201] was used here to isolate the neurogenic population of the upper layers by flow cytometry.

The “barrier of no return”

Elementi perenni, such as neurons, completely cease all cell cycle activities after neurogenesis. They only keep innate regenerative capacity within the first postnatal week [188,202] and can not re-enter cytokinesis thereafter [203,204]. Thus, following their genesis, ULNs enter post-mitosis, the “barrier of no return”. This state is characteristic of many somatic cell types; nevertheless, neurons remain functional and plastic for the rest of the organism’s life. Whether post-mitosis is a prerequisite for progenitor cells to transition to the differentiated state is still unknown.

Post-mitotic neurons can re-enter the cell cycle after an artificial calcium hit up to P5 [202,211]. A strong transcription factor gradient of FEZF2 can also push neurons back into a progenitor character within the first postnatal week [205,206]. So far, there is no mechanistic explanation for these artificially induced re-cycling events of neurons [202,207–210]. In cardiac progenitor cells, the precursors of cardiomyocytes, a similar post-mitotic state is established that has been predominantly explained by metabolic rearrangements [208,209,212–218]. In general, cells such as neurons and cardiomyocytes resemble each other both in excitatory function, post-mitotic acquisition [219] as well as in the onset of communication with the immune system [220]. Thus, a hint for terminal neurogenic fate commitment is the **metabolic switch** from proliferative glycolysis towards oxidative phosphorylation, accompanied by the downregulation of key enzymes such as PFKFB3 [221–223] or mitochondrial pyruvate carrier 1 (MPC1) [224,225], and the presence of neuron-specific enzymes such as Succinate-CoA Ligase ADP-Forming Subunit Beta (SUCLA2) [226].

Moreover, the replenishment of the neuronal progenitor pool in **adulthood** is naturally restricted to the hippocampal niche in mammals [66,227,228], which follows similar developmental patterns as embryonic corticogenesis [229–235]. In the presence of excitotoxic stimuli such as glutamate [236], adult neural stem cells choose the indirect route to re-enter the cell cycle through transient amplifying progenitors [237]. They express the growth factor BDNF [238,239] while attempting to resume the cell cycle, resulting in hyperploidisation instead of apoptosis. Hyperploidisation is also known, e.g. from models of **A**lzheimer's **d**isease (**AD**) [240–245].

Recent discoveries in human pluripotent stem cells attribute this "barrier of no return" to an intrinsic **epigenetic clock** [246–248] that keeps chromatin in a bivalent state during reprogramming, switching both enzymatic subunits (via alternative splicing) and modifications to a "locked" state upon fate commitment [249]. Retinal regeneration is also thought to be limited by epigenetic constraints that lock down the accessible chromatin of neurogenic genes [250].

In summary, terminal differentiation cannot yet be linked to a single factor. Efforts to enable cell cycle re-entry are still unsuccessful, indicating a complex link between cell cycle activities and the basic function of the neuron.

Birth as maturing event

SUMMARY: *Birth is a natural stressor for the foetus, triggering mainly molecular changes in organs that depend on oxygen. Organogenesis is largely completed at this point and is refined as the organism ages. Although birth sets the condition for later life, little is known about how early neurons encounter this transition at the molecular level. Furthermore, aberrant birth processes such as premature birth or caesarean section have been associated with neuropathologies.*

The birth process, with its accompanying mechanical stressors, the onset of oxygen breathing, early exposure to microorganisms, and hormonal and immunological changes [251,252], is an important transition period for the developing brain [253].

Human premature birth (< 37 weeks of gestation) can have serious long-term effects on the organism [254]; after the lungs, the brain is predominantly affected [255–257]. Reported cognitive, neuromotor [258], and behavioural abnormalities like ASD [259,260] following preterm birth point to developmental disturbances of upper-layer corticogenesis, since its interhemispheric connections are functionally correlated with these developmental diseases in the murine mouse model [4]. Distinguishing between the effects of preterm birth itself and confounding risk factors, such as viral infections, on later neurological outcomes is difficult due to their complex mutuality.

Besides, children delivered by caesarean section (C-section), which mainly bypasses stressors of vaginal birth [261–263], are more prone to developing neuropsychiatric disorders such as ASD [264],[265]. These children show decreased expression of key factors for neuronal differentiation [266] and neuroprotective mitochondrial proteins (Mitochondrial uncoupling protein 2, *UCP-2*) [267–269]. These altered stress signatures reflect in changes in DNA methylation of glucocorticoid gene promoters and generally affecting genes related to the **H**ypothalamic-**P**ituitary-**A**drenal (**HPA**) axis [270]. Moreover, questions arise about the role of microglia in the impaired perinatal clearing of the neuronal landscape in caesarean-delivered infants and their potential increased risk for neurodegenerative diseases later in life [271,272].

In summary, the mode of birth influences neuronal development. Deviations from “natural” birth modes have been correlated to a higher risk of ASD and schizophrenia, suggesting that they may be related to an altered development of the cortical upper layers.

► Neurogenesis upon immune activation

SUMMARY: *Maternal immune activation associates epidemiologically and preclinically with neurodevelopmental diseases like autism spectrum disorder and schizophrenia. A viral immune activation induces a cytokine secretion that passes through the placenta, thereby affecting the embryonic brain. Current research suggests microglia as translators of cytokine responses into neurodevelopmental disorders; however, the mechanism is unclear.*

Maternal **i**mmune **a**ctivation (**MIA**) is a specific form of embryonic hit that follows the event of invading pathogens. Recent pan- and epidemics such as COVID-19 and Zika virus have brought attention to their epidemiological significance during pregnancy. The Zika virus impinges on the EOMES+ lineage during neurogenesis, leading to microcephaly [273–275], while even the flu virus has been shown to disrupt glutamatergic synaptic transmission [276,277]. There is also mounting evidence that prenatal immune challenges can prime the developing brain for the later onset or acceleration of neurodegenerative diseases and mental disorders [278–286]. This evidence builds upon the “two-hit hypothesis”, which suggests that a first, embryonic hit sets the stage for later aberrations that are triggered by a following postnatal hit, cumulating in late-onset, sporadic diseases [287–289].

ULNs appear particularly vulnerable in development [290–292]. The mechanisms and pathways by which MIA affects the upper layers of the embryonic cortex are not entirely resolved.

Microglial guidance for differentiation

MIA is commonly thought to be translated into an embryonic response through the actions of a specialised type of brain immune cell type known as the microglia. These cells act as intermediaries, translating the extrinsic stimuli into intrinsic responses, such as complex hormonal and cytokine signalling pathways that ultimately influence the developing nervous system [293].

In the naïve state, the expansion of the neocortex is closely monitored by microglia. Like neurons, microglia are tissue-resident cells that are long-lived and not replaced by external immune cells [294,295]. Microglia are descendants of yolk sac macrophages at E9 in mice [296,297], which migrate through the developing brain vascularity [298] and eventually invade the developing cortical plate, right at the beginning of direct neurogenesis (E11 in mice) [299]. Like all immune cells, they collectively migrate along externally established, diffusible chemokine gradients [300]. They perceive these chemotactic signals primarily via superficial GPCRs and RTKs such as CXCR4, CX3CR1, CR3, and P2Y12 (Table 1; [301]). Some of these systems even promote neuronal progenitor differentiation, as microglia help co-shape the neuronal outcome.

At E14, microglia begin colonising the neocortex, interacting with neuronal precursors and being actively attracted to them through the guidance of chemokines such as IL-34 and CSF1 [302–304]. In mice and rats, a distinct layer of activated microglia forms at the border to the CP, the multipolar accumulation zone, preferentially targeting dividing PAX6+ and EOMES+ cells. Remarkably, microglia phagocytose these progenitor cells physiologically during mid-M phase and without inducing apoptotic signals [305]. Both the depletion and increase of microglia have a lasting impact on the number of intermediate progenitor cells [305] and subsequent disease susceptibility [303]. Microglia are thought to recognise and phagocytise bipolar cells rather than multipolar cells [305].

At the peak of late neurogenesis, microglia temporarily disappear from the cortical plate, attracted by the chemokine CXCL12 [306,307] secreted by IPCs. This guidance helps to regulate the production of neurogenesis and determines the ratio of neuronal subtypes [306,308-310]. Disturbances in this process can lead to behaviours reminiscent of ASD [4]. IPCs also express the purinergic receptor P2Y1R during migration, mediated by ATP signalling [311], although this somatic purinergic signalling is reversed in mature microglia-neuron contact [312,313]. Similarly, CXCL12-CXCR4 [306,308,309], FCRLS-CX3CR1 [303], CSF1-CSF1R [304], CCL2/CCL3-CCR2/CCR1 [314,315], IGFBP-IGF1 [316,317], and TRKB [318] neurotrophic systems contribute to microglial chemotaxis during IPC differentiation.

After differentiation, neurons communicate closely with microglia as brain-specific sentinel cells in a circuit-dependent manner to clear the brain of harmful cells [300] and maintain homeostasis [320-322]. Recent research classifies these different states of activity based on marker genes for scRNA-seq analyses, such as homeostatic (*P2ry12*, *P2ry13*, *Cx3cr1*, *Cd33*, *Tmem119*, *Crybb1*) and disease-associated microglia (*Spp1*, *Csf1*, *Cst7*, *Iba1*, *Cst3*, *Hexb*, *Trem2*) [300,323,324]. Conditional alteration of microglia number can be achieved e.g. using MIA models, in which an immunological challenge provokes the mother's immune system and subsequently the developing embryo.

Table 1: Common receptor-ligand interactions between microglia and developing neurons

Microglial chemotaxis is used during corticogenesis to phagocytose progenitor cells and pathogens and to prune synapses. It is generally assumed that communication is based on the microglial receptor, which recognises the ligands secreted by the (postsynaptic) neuronal component.

Receptor	Receptor type	Ligand	*References*
CXCR4	**Chemokine GPCR**	CXCL12	308, 309, 306
CX3CR1	**Chemokine GPCR**	FCRLS	303
CCR2, CCR1, CCR3, CCR5	**Chemokine GPCR**	CCL2, CCL3, CCL4, CCL5	314, 315, 319
P2X4/P2Y12R	**Purinergic GPCR**	ATP	312, 313, 311
CSF1R	**RTK**	CSF1, IL-34	304, 302, 303,
IGF1R	**RTK**	IGF1, IGFBP	316, 317
TRKB	**RTK**	BDNF	318

In MIA models, PolyI:C is commonly used to trigger immune responses [325]. PolyI:C is an artificial double-stranded RNA analogue that simulates immune responses to viral agents. When stimulated by double-stranded RNA, as artificially present in PolyI:C, or naturally in viral replication processes, the Toll-like receptor TLR3 expressed on circulating immune cells recognises structurally conserved pathogen-associated molecular patterns. TLR3 then cytoplasmically activates proinflammatory cascades such as NF-κB [326], which initiate the nuclear transcription of cytokines such as IL-6 and TNF-α [334]. These cytokines are prominently detectable in the serum of infected animals a few hours post infection/administration [286]. TLR3 for instance is also required for limiting axon outgrowth in neuronal progenitor cells by colocalising and likely also interacting with F-actin [327].

However, the underlying molecular mechanisms of MIA on the cortical upper layers have been varying and highly dependent on study outlines. Therefore, MIA was used here as a model to compare the molecular landscape previously defined in the untreated state versus the state of additional introduction of maternal PolyI:C injection shortly before the onset of upper layer corticogenesis.

Materials and Methods

All methods NOT performed by the author Tabitha Rücker herself have a grey background.

► Animal experiments

Ethical approval

The inbred strain animals were reared and housed according to the standard procedures of the Central Animal Facility at the University Medical Centre Hamburg-Eppendorf, Hamburg (**UKE**). All C57BL/6J mouse experiments were conducted in accordance with the German and European Animal Welfare Act. The experimental procedures used were approved by the Animal Research Ethics Board, the Hamburg Authority (TVA N051/2020 and N109/2020) and the Animal Welfare Commission of UKE.

All female mice imported from Charles River were allowed to adapt for at least 6 weeks, as transcriptional and epigenetic heterogeneity of the microbiome was expected when kept at different conditions [328]. All mice received a normal diet with Altromin (#1311P) *ad libitum*. After the adaptation phase, they were bred in-house with male C57BL/6J mice up to one year old. After overnight mating, a vaginal plug marked embryonic day 0.5 (E0.5). Plug checks were mostly taken over by the animal care takers. In the following, the ".5" has been removed from all IUE and harvest dates in the manuscript for improved clarity.

In utero electroporations

Technically, ***in utero*** **e**lectroporations (**IUE**s) were performed as described in Govindan et al., 2018 [329] and in the STAR protocol to subject similarly electroporated cell populations to downstream experiments.

The surgeries were mainly conducted by Birgit Schwanke as well as the preparation of the DNA mixes for IUE with an EndoFree Plasmid MaxiPrep Kit (Qiagen, #12362) according to the manufacturer's instructions.

Essentially, different constructs, shown in figure 4, were used to target different cell populations: The constructs differed in their promoter sequence that tailored different cell identities or a mixed population to regulate the expression of different fluorophores. Among different tested constructs to target developmentally active cell populations, the promoters of specific marker genes for radial glia cells and post-mitotic neurons were selected to answer the questions posed in the introduction (Suppl. Fig. 1).

These constructs together with a translation initiation cassette were then used to transfect embryonic brains:

For RGC-specific [160] expression, the promoter of the 'glutamate-aspartate transporter 1' (Glast1/here also: Glast) was used with a Kozak sequence to drive the expression of the red fluorophore dsRed2 via an IUE at E12 (Fig. 4A). The vector had a total size of 5,867 bp.

For the expression specifically in post-mitotic neurons [330], the promoter of the bHLH transcription factor 'neuronal differentiation 1' (NeuroD1/here also: NeuroD) was used to drive the expression of eGFP via IUE at E14 (Fig. 4C). This plasmid contained an IRES sequence in front of eGFP, which allowed for double-expression of two proteins under the same chosen promoter and provided the needed enhancer region to initiate transcription. The promoter itself had a size of 2.2 kb, which made a total vector size of 6,911 bp.

These two populations sorted by **developmentally active promoters** were called in the following analyses "special" populations.

In contrast, to target a mixed population, a plasmid including the CAG promoter was used. The promoter of CAG drives ubiquitous gene expression in mammalian vectors due to its composition of a CMV enhancer, the promoter of chicken β-actin, and a splice acceptor of rabbit β-globin gene [331]. In the case of the construct that was introduced via IUE at E12, Venus, a fusion protein of eGFP and eYFP, was expressed under the CAG promoter (Fig. 4B). The total vector size was 5,454 bp. If the construct was introduced via IUE at E14, pCAG drove the expression of the red fluorescent protein tDimer, with a total vector size of 7,012 bp. Its expression was triggered by an AAV2 ITR sequence, a promoter with inherent transcriptional activity (Fig. 4D). Generally, this expression under non-specific promoters was most similar to sophisticated approaches like FlashTag [10].

These two "mixed" populations based on the **ubiquitously active CAG promoter** were called in the following analyses "control"/ "ctrl" populations.

The constructs were injected into the embryonal ventricles via a mouth pipette. The concentration of the plasmids with developmentally active promoter was optimal at 4 µg/µL, for the plasmids carrying the CAG promoter, a concentration of 0.1 µg/µL was sufficient.

Electroporations were carried out with five current pulses of 50 ms with 950 ms interval à 35 V across the heads of embryos using the dipolar platinum tweezers-type electrode and the Electroporator ECM 830 BTX (Harvard Apparatus).

Throughout the entire dissertation, "p" stands for "promoter" (e.g.: **p**NeuroD1, …).

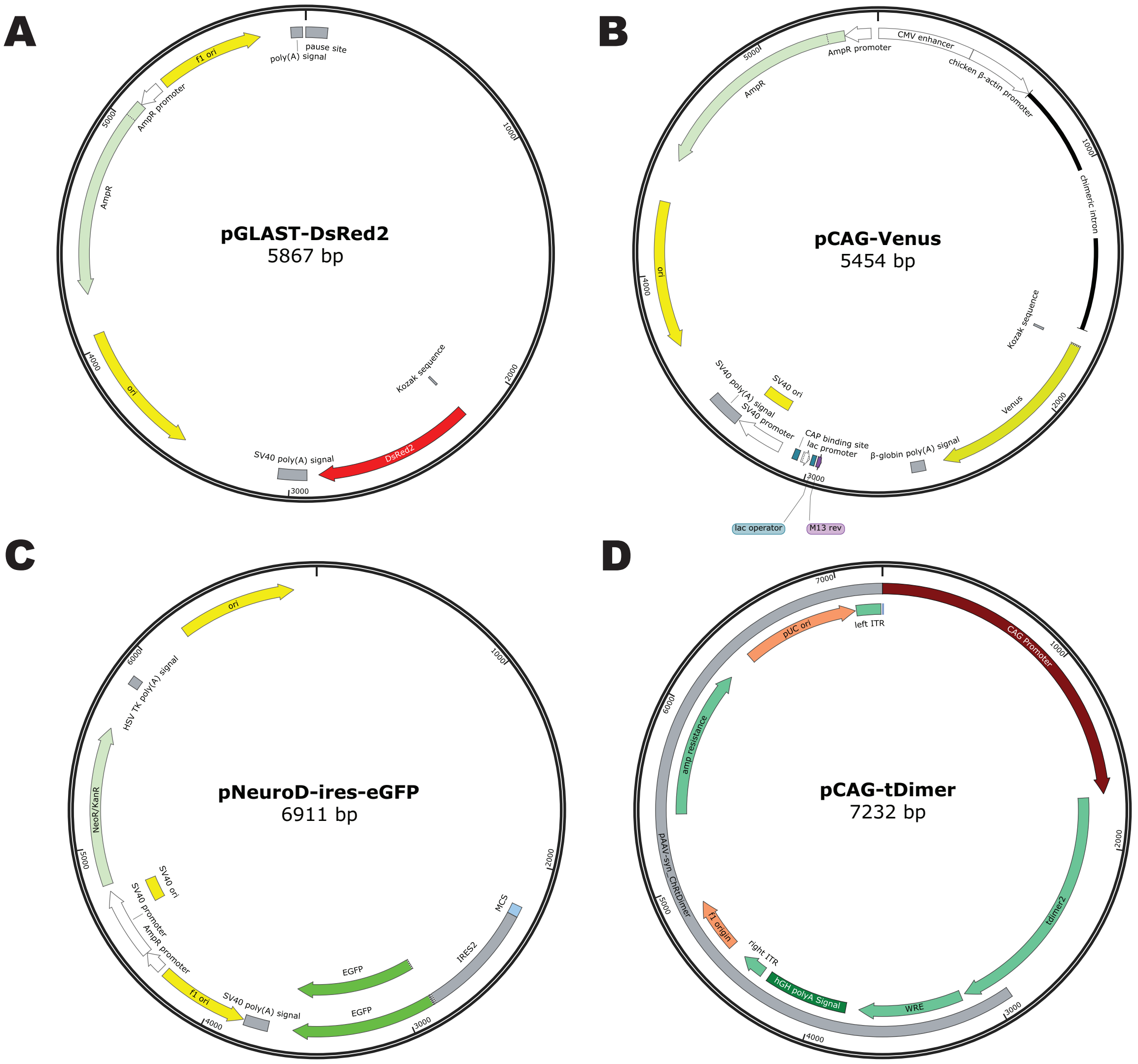

Figure 4: Vectormaps of used plasmid constructs

A. pGLAST-DsRed2 with a total size of 5,867 bp was a gift from Nicholas Gaiano (Addgene plasmid # 17706; http://n2t.net/addgene:17706 ; RRID:Addgene_17706),

B. pCAG-Venus with a total size of 5,454 bp was a gift from Phil Sharp (Addgene plasmid # 127346; http://n2t.net/addgene:127346 ; RRID:Addgene_127346),

C. pNeuroD-ires-eGFP with a total size of 6,911 bp was a gift from Franck Polleux (Addgene plasmid # 61403 ; http://n2t.net/addgene:61403 ; RRID:Addgene_61403),

D. pCAG-tDimer (pAAV Syn ChR E90R-T159C 2A tDimer) with a total size of 7,232 bp was a gift from Thomas Oertner (Addgene plasmid # 52495 ; http://n2t.net/addgene:52495 ; RRID:Addgene_52495).

Maternal immune activation

Injections

A **m**aternal **i**mmune **a**ctivation (**MIA**) was induced as a stressor, meaning that timed-pregnant mice were i.p. injected with a final administered concentration of 4 mg/kg of PolyI:C (Poly-inosinic-polycytidylic Acid Potass., Sigma, P9582-5mg, stock solution of 0.05 mg/mL in D-PBS). Repeated stimulations at E10 and E12 were performed to enhance the immune response in the mother mice right at the beginning of neurogenesis.

The administered PolyI:C concentration was determined as sublethal (>99% survival rate) in previous experiments performed by Jacobsen et al., 2021 [286] and calculated according to the respective weight of each mouse to a final volume of <200 µL i.p.. The control group was injected with the respective amount of D-PBS. Suppl. Fig. 10 shows detailed information on maternal weight of both cohorts. According to the score sheet attached to TVA N109/2020, a weight loss of >25 % of the average weight at the respective time was defined as the humane endpoint. Both PolyI:C and PBS were administered to mice mostly in parallel cohorts.

Transcriptomic and proteomic analyses were performed congruently with the untreated samples. For MIA, time points E18, E19, and P3 were selected for the transcriptome and proteome experiments, while E18 was additionally subjected to DNA methylome experiments.

Cytokine measurements

Sera and placenta were collected in parallel with E18 embryonic brains. First, the decapitated mother mice were cut open across the midline to expose the internal organs. Blood was then drained from the *inferior vena cava* (ca. 1 mL in total). After blood collection, the embryos were immediately released from the amniotic sac and their brains processed for flow cytometry experiments in 4°C Hibernate_E medium. The blood was allowed to settle in a 1.5 mL Eppendorf tube for 30 minutes at room temperature and then spun at 3,000 rpm for 10 minutes at 4°C and the serum transferred to a fresh Eppendorf tube. The blood sera were stored at -80°C.

Placental tissue and other organs were removed from the mother mice immediately after embryo removal, snap-frozen in liquid nitrogen, and stored in 1.5 mL Eppendorf tubes at -80°C.

Sera, placentae, and embryonic brains from naïve and treated conditions were tested for cytokine levels in collaboration with the RG led by Prof. Dr. Guelsah Gabriel. Note: The ELISA itself was carried out by the Leibniz-Institut für Virologie (*LIV*, Hamburg, Germany, Prof. Dr. Guelsah Gabriel, Dr. Stephanie Stanelle-Bertram, Hanna Jania), whereas downstream data analyses of the acquired observed concentrations were again performed by the author Tabitha Rücker.

For testing the cytokine levels of the collected tissue and sera, a custom-made Bio-Plex Pro Mouse Cytokine multiplex assay (Bio-Rad, ELISA) was designed and measured in a Bio-Plex 200 system following the manufacturer's instructions. The selected cytokines were interferon-γ (IFN-γ), interleukin-1β (IL-1b) [332], interleukin-2 (IL-2) [333], interleukin-6 (IL-6) [334], interleukin-10 (IL-10), interleukin-17α (IL-17a) [335], monocyte chemoattractant protein-1 (MCP-1), and tumour necrosis factor α (TNF-α) [332], mostly congruent to Jacobsen et al., 2021 [286].

Four untreated mice, six PBS-treated, and six PolyI:C-treated mice were randomly selected with their respective sera for this assay. In addition, one embryonic brain at E18 and thirteen placentae distributed among the four mother mice were measured in the untreated group, and eighteen placentae for the PBS- and PolyI:C-treated groups. In the PBS group, nine embryonic brains were measured from three different PBS mothers and three embryonic brains from one PolyI:C mother (Suppl. Table 1).
The organs of these mice weighed after freezing had similar weights under the different conditions (Suppl. Fig. 10B), so the concentration values were not normalised to organ weight. The weight of the mice themselves was more informative than the weight of the organs tested.

Technical replicates were not included. Values were normalised according to the generated standard curve of each measured cytokine with the Bio-Plex Manager software. Several values were lost due to the underrepresentation (Out of Range Below) of fluorescence calculated by the Bio-Plex Manager software. These were not replaced but treated as **n**ot **a**vailable values (**NA**). In contrast, the values extrapolated by the software were included in the analysis. These extrapolated values were estimated concentration values that are outside the range of the standards, but still within the limits of the fitted logistic eight-point standard curve (Suppl. Table 1).

► Flow cytometry experiments

Preparation of single cell suspension

The cells were taken from the embryonic cortices at the respective time point. The procedure is described in detail in the STAR protocol. Briefly, on the day of collection, the pregnant mice were euthanised with isofluorane followed by decapitation. The abdomen and uterus were opened, the embryos removed, and also decapitated. At this stage, special care was taken to act quickly so that the embryos could not breathe air, as this could potentially affect the results. From here on, the heads were stored in Hibernate™_E medium (Thermo Fisher, #A1247601) on 4°C ice. The cerebral cortex was dissected after removal from the skull, and removal of meninges and hippocampus using the classic Banker method (Goslin et al., 1998; [336]). The regions in the hemispheres with visible fluorescence were excised under a stereo microscope (Olympus SZX16) equipped with a UV light source. Here, cotransfection with a ubiquitously expressed marker protein (for E14 harvest time point: pCAG-Venus; for E16-P7 time points: pCAG-tDimer) helped identify these regions. While the isolation procedure primarily targeted cells from the prefrontal cortex, cells from the somatosensory or visual cortex could not be excluded (Fig. 3). The fluorescent regions were then pooled in a 15 mL Falcon tube and processed into a single cell suspension using an adapted protocol for primary neuronal cell cultures:

First, tissue was washed three times in cold 2 mL 1x HBSS medium (Hank's Balanced Salt Solution, Invitrogen, #14170088) and incubated in 2 mL HBSS with 25 µL of a 25 mg/mL stock solution of papain (Sigma, #P4762) and 20 µL of a 1 mg/mL stock solution of DNaseI (Sigma, #D4263) at 37°C for 10 min. Young cortices are still little myelinated and connected, so that a short enzymatic digestion is sufficient to loosen the cell context. In mature cortices, this is challenging without damaging the cells, **f**luorescence-**a**ctivated **c**ell **s**orting (**FACS**) is usually replaced by **FANS** (**f**luorescence-**a**ctivated **n**uclei **s**orting). Then 2 mL of 10% FCS (Biochrom, #S0115) in DMEM (Invitrogen, #6196526) was added to stop the digestion reaction. Cells were subsequently washed with HBSS and triturated thoroughly but gently ten times in 2 mL HBSS using a fire-polished Pasteur pipette with a 1 mm opening until suspended. Cells were then centrifuged in 4 mL HBSS buffer at 150 x g for 10 min before resuspending the cell pellets in 1 mL HBSS and passing the cell suspension through a 40 µm insert filter to remove clusters.

No more than two hours elapsed from the euthanasia of the animals to the final single cell suspension and the cells were kept continuously on ice. The single cell suspension of an average of 6×10^6 cells in total was then transferred to the Cytometry und Cell Sorting Core Unit, Dept. of Stem Cell Transplantation, University Medical Centre Hamburg-Eppendorf.

Conventional flow cytometry

A detailed version of the FACS protocol can be found in the STAR protocol mentioned above. The figures related to flow cytometry experiments were reused from the STAR protocol, as they were done by the author Tabitha Rücker.
Briefly, cells from one respective timepoint were pooled before sorting using a BD FACSAria^{TM} Fusion Cell Sorter. To ensure consistency between the FAC sorts, a template was created for the flow cytometric workflow (Fig. 5).

From the identified scatter population (Fig. 5B, leftmost plot), two doublet exclusion plots were created to exclude any remaining doublets (Fig. 5B, middle and right plot). Doublets or multiples showed increased area and width signals compared to single cells, whereas the height remains almost the same. Thus, a mismatch between height, width, and area served to identify and exclude doublets from the analysis.

Sterile conditions were maintained throughout flow cytometry experiments.

During flow cytometry, the sheath fluid hydrodynamically focused the cell suspension in the flow cell above the nozzle. It directed the cell suspension through the 100 µM nozzle suitable for sorting early neurons. Mature pyramidal neurons have been reported to have a soma diameter of 10-20 µm (Fig. 12; [337]), while all the processes, dendrites, and axon were collapsed and retracted during dissociation, if they have formed at all. Because early neurons entering the developing cortical plate are either multipolar with multiple very small processes or have transitioned to a bipolar state with a short anterior process and a short posterior process [11,329,338], they are less susceptible to cell damage during dissociation.
The nozzle separated the jet into individual droplets. The cells passed through the laser light cell by cell. Only droplets with cells of interest were charged, while those outside the sorting gates remained unaffected, even if they showed fluorescence. Deflection plates attracted or repelled cells: the charged droplets were deflected in the electric field and collected into the appropriate container. Cell pellets were collected in FACS buffer (0.2 mM EDTA in calcium- and magnesium-free PBS), centrifuged, and finally frozen and stored at -80°C until further processing.

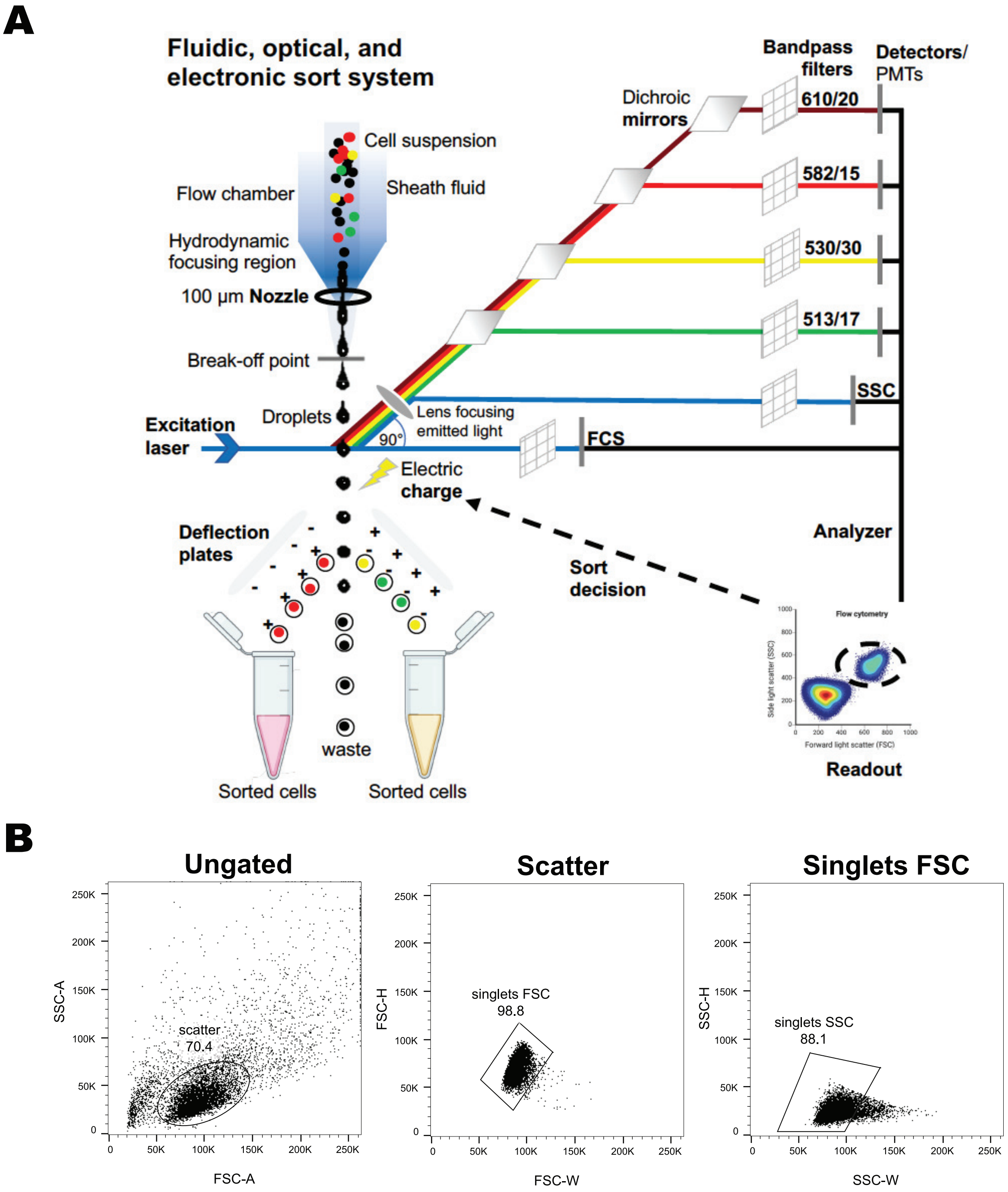

Figure 5: Principle of flow cytometry for sorting transfected developing neurons

A. The cell suspension containing transfected and non-transfected cells passes through a 100 µm nozzle and undergoes hydrodynamic focusing within the flow cell due to pressure differences between the sheath fluid and the cell suspension. After separating the stream into single droplets containing one or more cells, the excitation laser interrogates each droplet. Depending on the size (forward scatter, FSC), granularity (side scatter, SSC), and wavelength of the emitted light, a specific sorting decision is formulated. For example, the gate set for the SSC-A already helps to sort out cells that are twice the size of the cells sorted here, which could represent dividing cells or immune cells. Mirrors then deflect the incoming laser beam and filters pass a specific wavelength range to the respective detectors (PTMs). The fluorophores used here required bandpass filters of 610/20 (dsRed2), 582/15 (tDimer), 530/30 (Venus), and 513/17 (eGFP). The resulting conversion of light to an electrical charge determines the deflection of cells into their respective sorting tubes. Non-transfected cells are not charged and go into the waste container. PTM = Photomultiplier tube.

Caption continued on next page

B. Each sort decision begins with identifying the cell population of interest by plotting SSC-area (SSC-A) against FSC-A to compare the size and granularity of the scatter. Second, duplicates in this scatter were excluded by matching the width (W) against the height (H) of the FSC. These gated FSC singlets served as input for the detected cells in the SSC-H versus SSC-W plot. The resulting SSC singlet cell population served as the final input for differential fluorescence detection every time the respective transfected areas were sorted (Fig. 10 and 11).

This figure was reused from the **STAR protocol**.

► Immunofluorescence

The brains of each age were fixed with 4% paraformaldehyde at 4°C overnight. The next day, the solution was exchanged with 30% sucrose in 1x PBS until the brains fell to the bottom of the tube due to water loss. Fixed brains were frozen in Tissue-Tek® O.C.T.™ Compound (#R1180, Plano), cut with a Leica CM3050S cryostat, and mounted on Menzel-Gläser (Superfrost Ultra Plus®, Thermo Scientific, #J3800AMNZ).

For immunofluorescent staining, the slices were blocked with 10% donkey serum (**DS**, Sigma, #D9663-10ML) in 1x PBS with 0.5% Triton X-100 (Roth, #3051.2) for 3h at **r**oom **t**emperature (**RT**) to prevent non-specific binding. Primary antibody incubation in 5% DS in PBS with 0.25% Triton X-100 was performed overnight at 4°C with Iba1 (Wako, #019-19741), and SatB2 (abcam, #ab92446). After three PBS washes, the slices were incubated with the respective donkey anti-mouse or anti-rabbit Alexa Fluor 568 or 647 secondary antibodies (Invitrogen; #A10042, A-31573) at RT for 3h followed by three washing steps with PBS along with Hoechst dye (1:1,000, Invitrogen, #33258, “DAPI”) to stain for nuclei. Coverslips were mounted onto slides using Fluoromount-G® (SouthernBiotech, #0100-01). Images were taken with a Zeiss Axio Imager 2, LSM 800 with 420650-9901-000 objective (Plan-Apochromat 20x/0.8 M27) and 420660-9970-000 objective (Plan-Apochromat Korr 40x/0.95 M27), Airyscan detector and ZEN 3.1 software (blue edition), and subsequently processed with Fiji v. 2.9.0/1.54d.

► "Omic" experiments

RNA-seq sample preparation

Total RNA was extracted from frozen aliquots of 10,000 sorted cells using the RNeasy® Micro Kit (Qiagen, #74004), for which a Qiagen low input protocol was adapted (see Appendix for "**RNA extraction protocol**").

Note: The following quality assessment (1), library generation (2), and sequencing (3) was conducted in collaboration with the Leibniz-Institut für Virologie (*LIV*, Hamburg, Germany, Kerstin Reumann, Dr. Patrick Blümke, Dr. Jacqueline Nakel, Dr. Daniela Indenbirken). Downstream data analyses of the acquired base calls were again completely performed by the author Tabitha Rücker.

(1) Prior to library preparation, integrity of the extracted total RNA was assessed on an Agilent 2100 Bioanalyzer using a Eukaryote Total RNA Pico assay (Agilent Technologies, #5067-1513). The concentration was measured by the RNA HS Assay Kit on a Qubit 2.0 (Thermo Fisher Scientific, #Q32852). RNA samples below a RIN value of 7 were excluded, although exceptionally samples with a RIN of below 7 were still approved for having a sufficient level of RNA integrity for sequencing. An example of both cases was depicted in Suppl. Fig. 11.

(2) For library generation, cDNA was first synthesised, PolyA enriched, and amplified using the SMART-Seq® v4 Ultra® Low Input RNA Kit for Sequencing (Clontech Laboratories, # 634891) as per manufacturer's recommendations. Success of the cDNA generation was again verified on an Agilent Bioanalyzer. The generated cDNA was then further processed to a library using the Nextera XT DNA Library Preparation Kit (Illumina, #FC-131-1096). The fragment length distribution of each library was determined on an Agilent 2100 Bioanalyzer using the DNA High Sensitivity Chip (Agilent Technologies, #5067-4626). All samples were diluted to a concentration of 2nM, and an equimolar pool of the samples was generated.

(3) 1 x 75 bp single-end (SE) sequencing of the samples was performed on an Illumina® NextSeq™ 550 platform aiming for ~20 million reads per sample. A total of 137 samples was SE bulk sequenced in four runs.

RT-PCR

RT-PCR was performed to validate RNA-seq results. Different aliquots of 10,000 cells from the first three experiment for timepoint E14 to E19 (E and P pooled) were converted to cDNA with the SuperScript™ IV CellsDirect™ cDNA synthesis kit (ThermoFisher, #11750150) and measured on a 7900HT Real-Time PCR System.

Samples of 0.5 ng/µL were used as input for a custom designed array (Supplementary “RT-PCR protocol”) with a sample volume of 20 µL. Two custom TaqMan® Array Standard 96-well plates (Format 16, 6 plates each) were designed since conventionally used designs do not meet the requirements of a high-resolution analysis over a time course.

Twelve progenitor marker genes, [54,102,160,177,339–343], eleven neuronal marker genes [144,146,344–352] as well as seven marker genes for microglial cell identity [303,305,313,353–356] were selected for validation by RT-PCR (Table 2). The following selected assays passed the criteria of exon-spanning probes and assay availability (inventoried):

Table 2: Used TaqMan® assays for RT-PCR

One endogenous control, eleven progenitor marker genes, twelve neuronal and seven microglial marker genes were tested.

Endogenous control	**Progenitor marker genes**	**Neuronal marker genes**	**Microglia-like marker genes**
18S-Hs99999901_s1	Arx-Mm00545903_m1	Bcan-Mm00476090_m1	Aif1-Mm00479862_g1
	Eomes-Mm01351985_m1	Cops7a-Mm00488804_m1	Cd81-Mm00504870_m1
	Fezf2-Mm01320619_m1	Csf1-Mm00432686_m1	Csf1r-Mm01266652_m1
	Ndrg2-Mm00443483_m1	Cux1-Mm01195598_m1	Cx3cr1-Mm00438354_m1
	Neurod6-Mm01326464_m1	Cx3cl1-Mm00436454_m1	Fcrls-Mm00472833_m1
	Neurog2-Mm00437603_g1	Dlx1-Mm00438424_m1	Itgam-Mm00434455_m1
	Pax6-Mm00443081_m1	Grin2b-Mm00433820_m1	P2ry12-Mm00446026_m1
	Ppp2r1b-Mm01177006_m1	Map2-Mm00485231_m1	
	Rnd2-Mm00501561_m1	Ndufv1-Mm00504941_m1	
	Slc1a3-Mm00600697_m1	Satb2-Mm00507331_m1	
	Sox2-Mm03053810_s1	Syp-Mm00436850_m1	
		Timp2-Mm00441825_m1	

The assays ending in _g and _s also detected potential genomic DNA in the sample, which can lead to contaminated data. Since DNase digestion was performed during sample preparation, genomic DNA was unlikely to affect the data. Additionally, in the assays with an _s ending, both the primers and the probe were mapped within a single exon. These assays were selected because there was no similar probe available to detect non-genomic DNA (_m ending) at the time the experiment was performed (2021 and 2023).

The amplification efficiency could be considered reliable because Thermo Fisher Scientific Inc. arrays are subjected to constant quality controls.

Calculations

RT-PCR data were analysed using Cq values generated by the Applied Biosystems™ relative quantification analysis software module (v. 4.3). Well results including Cq values, which were transformed raw Ct values by the latest internal algorithm of this software can be found in the github repository https://github.com/TabithaRuecker/NeuroDev.git. Cq values above 40 were considered as NA; in case of one NA the data were replaced by the median of the other two replicates, while in case of more than one missing value the NA was kept for analysis. In particular, the genes associated with microglial character were most subject to this imputation process.

Normalisation was performed in two steps based on the ΔΔct method [357]:

First, all values were normalised against an endogenous control gene of the respective panel (here: 18S (18S-Hs99999901_s1)) as a common endogenous TaqMan® control. Secondly, the values were normalised to a control (here: E14 (pGlast-dsRed2/pCAG-Venus transfected)) to acquire **r**elative **q**uantification (**RQ**) values:

$$\Delta c_T = c_{T_{target/reference\ genes}} - c_{T_{human\ 18S}}$$

$$\Delta\Delta c_T = \Delta c_{T_{E16/E17/E18/E19}} - \Delta c_{T_{E14}}$$

$$RQ = 2^{-\Delta\Delta c_T}$$

Equation 1: Calculation of RQ values

The RQ values indicate the level of gene expression normalised to the endogenous control (here: human 18S) and relative to the E14 sample. Calculation example: Bcan has an average log2(RQ) of 4.49 at E19 for the pNeuroD+I population, i.e. it is 22.47 times more strongly expressed at E19 than at E14.

For figure 17, these RQ values were log2-transformed per replicate and used together with manually log2-transformed DESeq2-normalised RNA-seq data.

For figure 18, RQ values were averaged across the three replicates of each cell population for each gene and time point by applying the geometric mean, which was the final input for the log2 transformation. The log2 fold changes were then displayed along with the log2 fold changes of the RNA-seq data.

Mass spectrometry experiments

Note: The following preparation of frozen cell aliquots of up to 50K cells for **m**ass **s**pectrometry (**MS**) and the MS experiment itself were conducted in collaboration with the Section for Mass-Spectrometry and Proteomics, University Medical Center Hamburg-Eppendorf, Hamburg, Germany (Thomas Mair, Bente Siebels, Paula Nissen, Kilian Müller, Prof. Dr. Hartmut Schlüter). Downstream data analyses of the acquired protein hits were again completely performed by the author Tabitha Rücker.

Proteomic profiling was performed without labelling (**l**abel-**f**ree **q**uantification, **LFQ**), since tandem mass tag-based quantification resulted in technical artefacts in the spectra and proved unsuitable for the desired analysis.

Proteomics sample preparation

First, frozen cell pellets were lysed in 100 µL 0.1M **tr**i**e**thy**la**mmonium **b**icarbonate (**TEAB**) buffer containing 1% w/v **s**odium **d**eoxy**c**holate (**SDC**) and were then incubated at 95°C for 10 minutes. Additional sonication with five pulses at 35 Hz helped downsize potentially interfering DNA fragments and mechanically solubilise transmembrane proteins. Tryptic digestion was performed using the single-pot, solid-phase-enhanced sample preparation (SP3) protocol, as described by Hughes et al., 2018 [358]. SDC was removed by precipitation with 1% acetic acid, and the remaining supernatant was lyophilised using a Speedvac vacuum concentrator and stored at -20°C until further use. Immediately prior to injection, the dried peptides were resolved in water (MS grade) containing 0.1 % **f**ormic **a**cid (**FA**).

LC-MS/MS parameters

Liquid **c**hromatography-tandem **m**ass **s**pectrometry measurements (**LC-MS/MS**) were performed in a multiple-step process. Chromatographic separation of peptides was achieved with a two-buffer system (buffer A: 0.1 % FA in water (MS grade), buffer B: 0.1 % FA in **ac**eto**n**itrile (**ACN**, MS grade)). The total amount of peptides was injected into a Dionex Ultimate 3000 UPLC system. For on-line desalting and purification, a peptide trap (180 µm × 20 mm, 100 Å pore size, 5 µm particle size, Symmetry C18, Waters) was installed in front of a 25 cm C18 reversed phase column (75 µm × 200 mm, 130 Å pore size, 1.7 µm particle size, Peptide BEH C18, Waters).

Peptides were eluted in an 80-min gradient with linearly increasing concentration of buffer B from 2% to 30% in 60 min, increasing to 90% for 5 min and equilibration at 2% buffer B for 10 min. The eluted peptides were ionised and desorbed by nano-electrospray ionisation source (nano-ESI) at a spray voltage of 1.8 kV. To acquire LC-MS/MS spectra, the eluted peptides were transferred to a quadrupole-ion-trap-orbitrap mass spectrometer (Orbitrap Fusion Tribrid Mass Spectrometer, Thermo Fisher, Bremen, Germany) and further analysed in data-dependent acquisition mode.

For each MS^1 scan, ions were accumulated for a maximum of 120 **milli****s**econds (**ms**) or until a charge density of 2x105 ions (**A**utomatic **G**ain **C**ontrol target, **AGC** target) was reached. This way, the m/z ratio of the eluted and subsequently charged molecules was recorded and Fourier transformed in a mass range of 400-1200 m/z with a resolution of 120000 at m/z = 200. Peptides with charge states between 2+ - 5+ above an intensity threshold of 1,000 were isolated from each precursor scan within an isolation window of 1.6 m/z in top speed mode for 3 seconds and fragmented with a normalised collision energy of 30% using higher energy collisional dissociation.

MS^2 scans for identification of the primary sequences from the selected peak MS^1 spectra were performed using an ion trap mass analyser at a rapid scan rate covering a mass range of 120-1500 m/z and accumulated for 60 ms or to an AGC target of 1x104. Already fragmented peptides were excluded (dynamic exclusion) for 30 seconds.

EM-seq sample preparation

To distinguish between global methylation changes and local DMRs, the novel approach of **e**nzymatic **m**ethyl **s**equencing (**EM-seq**) was used here to subject four DNA samples (two PolyI:C and two PBS pNeuroD+ samples) from time point E18 to DNA methylome analysis. For EM-seq, DNA was extracted from frozen samples and scaled to 200 ng DNA, which was the lowest amount of DNA suitable for EM-seq (see Appendix "**DNA extraction**" for full protocol and Suppl. Fig. 21 for expected outcome).

Note: The library generation (1) and sequencing (2) were mainly conducted in collaboration with the Leibniz-Institut für Virologie (*LIV*, Hamburg, Germany, Dr. Patrick Blümke, Kerstin Reumann). DNA extraction and downstream data analyses were again performed by the author Tabitha Rücker.

(1) EM-seq was performed on 200 ng DNA each using a protocol adapted from [359]. The conventional NEBNext Enzymatic Methyl-seq Kit (NEB #E7120) was used for library preparation. Samples were processed according to the manufacturer's protocol, specifically the variant developed for Large Size Libraries, whereby denaturation was performed with 0.1 N sodium hydroxide (option B; [359]). After NEB library preparation, positive and negative controls (0.1 ng/µL pUC19 and 2 ng/µL λ-DNA; Table 3; Fig. 6) were diluted 1:50 and added to the samples in a volume of 1 µL per 48 µL of input DNA before fragmentation to assess the efficiency of the bisulfite conversion process and the performance of the sequencing assay. Then, the libraries were subjected to oxidation, glucosylation, and deamination to enzymatically converse 5-methylcytosines (5-mC) and 5-hydroxymethylcytosines (5-hmC) (For detailed description: [359], p.1282). DNA libraries were measured with the Agilent 2100 Bioanalyzer with a High Sensitivity DNA assay (Agilent Technologies, #5067-4626). See Suppl. Fig. 22 for Bioanalyzer results.

Table 3: Sample preparation for EM-seq libraries

NFW= Nuclease-free water.

ID	Name	Date of EM-seq run	Conc. [ng/µL]	Sample [µL]	0.1 ng/µL pUC19	2 ng/µL λ-DNA	+ NFW [µL]	Final conc. [100ng/50µL]
mr604	M16	02/08/2023	39.80	5.03	1.00	1.00	42.97	200
mr607	M19		48.80	4.10			43.90	
mr616	M28		45.80	4.37			43.63	
mr617	M29		28.20	7.09			40.91	

(2) Finally, the prepared libraries were sequenced on the Illumina NextSeq 2000 platform using the P3 sequencing reagents at 300 cycles in a paired-end configuration (2x151 bp plus 2x 10 bp for index reads). A total of 50 million read pairs per sample were generated (47.9 million, 49.7 million, 53.2 million, and 54.7 million, respectively).

SpikeIn controls

An artificially methylated pUC19 plasmid (Fig. 6A) and the unmethylated λ-DNA (Fig. 6B) were used here as positive and negative controls to verify successful sequencing.

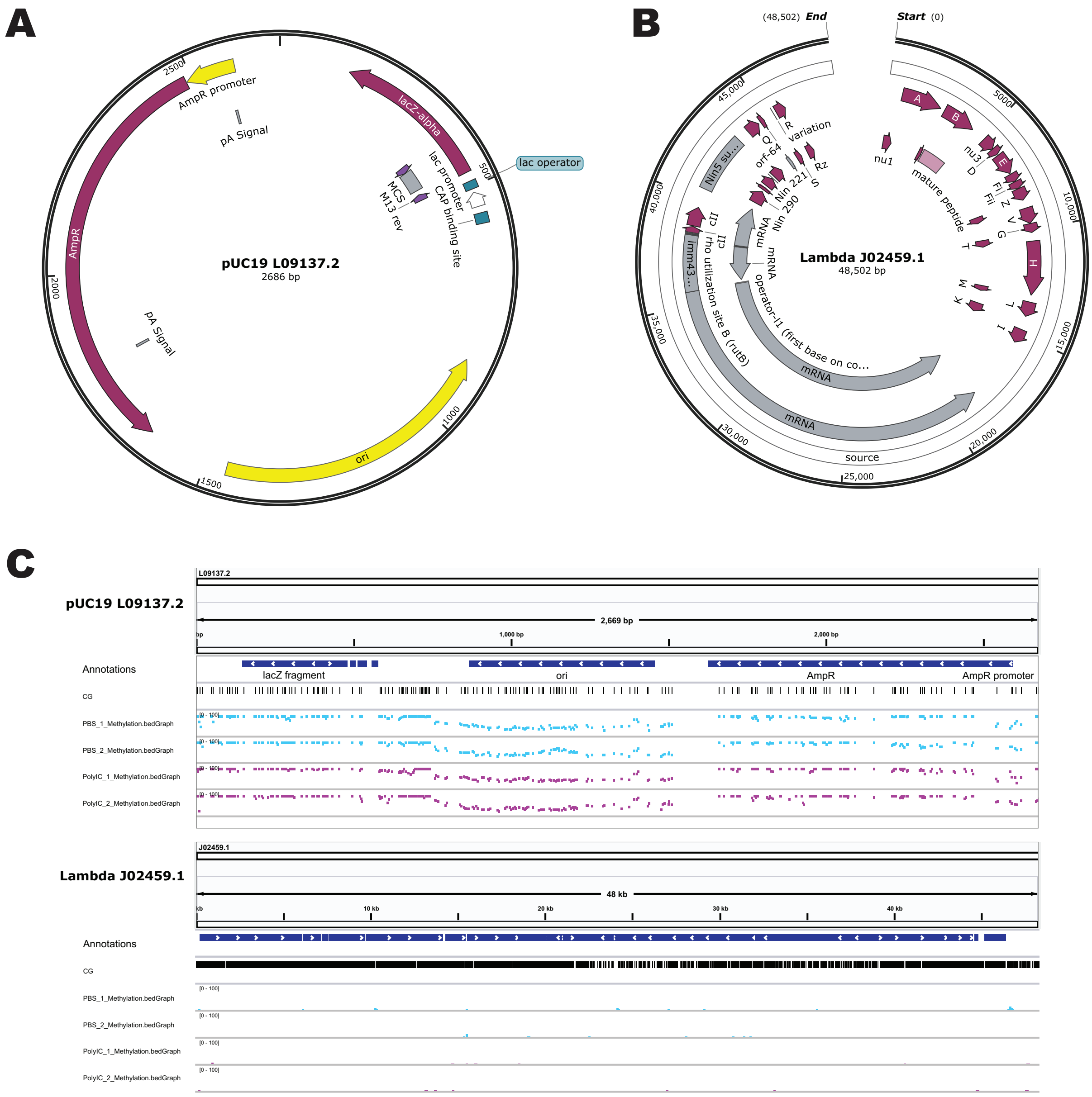

Caption continued on next page

Figure 6: SpikeIn controls verify sequencing quality and reveal pNeuroD1 usage for transfection

A. Methylated pUC19 (L09137.2) plasmid as positive control for EM-seq.

B. Unmethylated λ-DNA (J02459.1) as negative control for EM-seq.

C. Lanes visualised in the IGV of the samples annotated to the respective SpikeIn control. Upper lane: pUC19 plasmid, lower lane: λ-DNA. In the upper lanes with methylation percentages mapped to the pUC19 plasmid, the percentage of methylation partly ranges between 50-75% instead of 0 or 100%. These parts represent the “ori” and the “AmpR” region of the pUC19, but also of the pNeuroD1-ires-eGFP construct (Fig. 4C).

The base lanes of both SpikeIn controls were compared with the sample lanes using MethylDackel output files in the IGV. MethylDackel output (see section “**Raw data processing and data availability**” for DNA methylation) is a percentage measure of methylation, similar to the output of bisulfite sequencing. As expected, the λ-DNA showed almost no hits (Fig. 6C, lower IGV lane), while the pUC19 vector showed regions with 0 and 100% methylation, but also two regions with ~50-75% methylation (Fig. 6C, upper IGV lane). Likewise, the NeuroD1 promoter was unexpectedly highly covered (Suppl. Fig. 23A). These findings can be attributed to the origin of replication (ori) and the ampicillin resistance promoter (AmpR), which were parts of the pNeuroD1-ires-eGFP vector (Fig. 4C). They were transferred during DNA extraction together with the actual DNA of the neuronal cell samples. Since these parts were reintroduced by the pNeuroD1-ires-eGFP vector, they also explained the unusual coverage in the methylation analyses.

► Pipelines for bioinformatic analyses

Used software

- R version 4.3.1 (2023-06-16), open source [360]
- Fiji/ImageJ version 2.9.0/1.54d, open source [361]
- FPbase, 2023 [362]
- BD FACSDiva™ Software (BD Bioscience; https://www.bdbiosciences.com/en-us/products/software/instrument-software/bd-facsdiva-software; last accessed: 12.11.2023)
- FlowJo™ version 10 (BD Bioscience; https://www.bdbiosciences.com/en-us/products/software/flowjo-v10-software; last accessed: 12.11.2023)
- Proteome Discoverer software (version 3.0.0.757, Thermo Fisher Scientific Inc.)
- CytoScape version 3.9.1 [363]
- In Thermo Cloud (https://apps.thermofisher.com/apps/dashboard; last accessed: 12.11.2023):
  - Applied biosystems™ relative quantification analysis software module, v. 4.3.
  - Applied biosystems™ analysis software, standard curve analysis module, v. 3.9.

Where possible, all plots in this manuscript have been created using the R package ggplot2 (v. 3.4.4; [364]) with customised theme created by the author Tabitha Rücker. All annotations were made to the mm10 mouse genome (GRCm38, org.Mm.eg.db).
For data integration of protein abundances and mRNA expression, **D**ata **I**ntegration **A**nalysis for **B**iomarker discovery using **L**atent variable approaches for **O**mics studies (**DIABLO**) with a block.splsda model from the R package mixOmics (v. 6.17.12; [365]) was used.

All of the meta data and raw data (in case of RT-PCR and ELISA/Cytokine measurements) have been deposited on github: https://github.com/TabithaRuecker/NeuroDev.git (Suppl. Table 12).

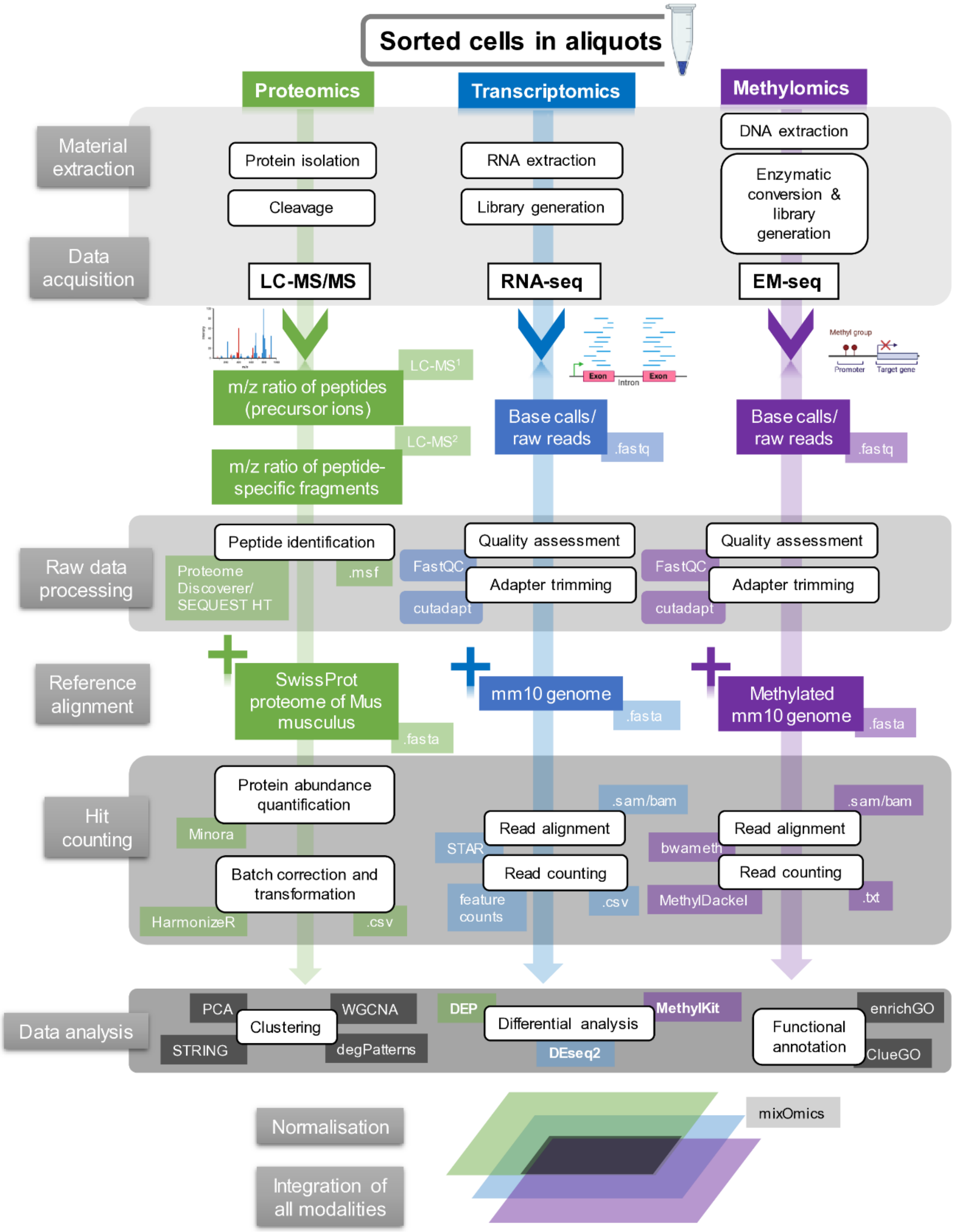

Figure 7: Pipelines applied here for analysing raw data across the three levels of biological complexity

Raw data processing and data availability

Transcriptomics

The demultiplexed base calls were available as fastq files, which will soon be deposited at the NCBI **G**ene **E**xpression **O**mnibus (**GEO**, application submitted). Before the raw reads could be used in downstream analyses, the pipeline for RNA-seq analyses shown in figure 7 was applied, consisting of quality assessment (1), adapter trimming (2), read alignment (3), and read counting (4).

1. First, FastQC (v. 0.11.8; [366]/ MultiQC; Suppl. Fig. 11) assessed the quality of the reads. Almost all measured samples passed quality criteria. Only the samples E14_c/sp_5 were excluded and replaced in the next sequencing run.
2. Illumina adapter clipping was performed using TrimGalore! with cutadapt (v. 3.1; [367]) and with the following command line parameters: -j 1 -e 0.1 -q 20 -O 1 -a CTGTCTCTTATA x.fastq
3. For spatial information, read mapping was performed using RNA STAR aligner (v. 2.7.8a; [368]) against the mm10 genome from the UCSC Genome Browser [369] with default options for SE raw data:

Example:

- runThreadN 6
- runMode genomeGenerate
- genomeDir /Users/tabitharucker/opt
- genomeFastaFiles GRCm38.primary_assembly.genome.fa
- sjdbGTFfile gencode.vM11.annotation.gtf
- readFilesIn /Users/tabitharucker/NGSdata/raw/E16_pNeuroD_3_trimmed.fq
- sjdbOverhang 100
- outSAMstrandField
- outSAMmapqUnique 255

STAR (**S**pliced **T**ranscripts **A**lignment to **R**eference) is the most widely used splice-aware aligner that maps faster and is more accurate than its alternatives TopHat or HiSAT2. The algorithm STAR is based on the search for "Maximal Mappable Prefixes", which are searched sequentially only over the not yet mapped reads, independent of isoforms, and accelerate the mapping process [368]. It indexes the genome by "features" (e.g. exons) and meta-features (e.g. genes) and assigns a feature to each read. The extension of multiple overlapping reads to features is determined by the -Q option. The output is in Sequence Alignment/Map (SAM) or Binary Alignment/Map (BAM) format, which can be visualised in the **I**ntegrative **G**enomics **V**iewer (**IGV**) or converted into a Browser Extensible Data (BED) file format for further processing.

4. Gap-aware read counting was performed using featureCounts (v. 2.0.1; Liao et al., 2014 [370]) with the options -s 0 -t -Q 12, which only consider non-stranded reads that are within an exon and have a minimum **Map**ping **Q**uality Score (**MAPQ**, column 5 of the output SAM) of 12. The primary assembly of mm10 from the database ftp://ftp.ebi.ac.uk/pub/databases/gencode/Gencode_mouse/release_M25/GRCm38.primary_assembly.genome.fa.gz and the corresponding gtf mm10_RefSeq_exon annotation file were both used as reference assemblies. As output, featureCounts generated a matrix with 27,179 unique Entrez gene identifiers for the mm10 genome, which was further used for downstream analyses.

Normalisation

RNA-seq data employ different sequencing depths for each sample and different variances for each read count. Therefore, normalisation of read counts is required when testing for **d**ifferentially **e**xpressed **g**enes (**DEGs**). The DESeq2 R package (v. 1.40.1; [371]) was used here to overcome these two inherent problems of RNA-seq data: Firstly, it calculated “size factors” for each sample to ensure that the different sequencing depths were not confounded by any condition (lowest value here: E17_c_1 with 0.58, highest value here: E19_E_c_7 with 1.68).

For purposes other than differential testing, log2 DESeq2 normalised values with a pseudocount of 0.5 were used to avoid infinite minus values due to zero counts. With these size factors, the DESeq2 algorithm accounted for variations in sample size, which was useful here to integrate reliably gene expression levels of the postnatal samples with inconsistent sample sizes. In addition, visualising particularly extreme gene expression from high count data often did not require variance-stabilised counts, making log2-transformed counts suitable.

Secondly, DESeq2 corrected for the decreasing mean dispersion with increasing gene abundance until it reached an asymptote due to biological variability, which was naturally higher in weakly expressed genes. From this inverse correlation between the mean (μ) and the gene-wise dispersion (α) resulted that for small mean counts, the dispersion was higher, leading to so-called “heteroscedasticity”. Additionally, it was assumed that similarly expressed genes have similar dispersion (maximum likelihood estimation).

Thus, given that

$$variance = \mu + \alpha * \mu^2$$

and

$$\sqrt{\alpha} = \frac{variance}{\mu} = biological\ coefficient\ of\ variation\ (BCV),$$

with α as the dispersion parameter and μ as the mean, in RNA-seq data, α>0 will always be greater than the mean, also called “overdispersion” (Fig. 8A). If α→0, then var = μ, which would apply for a Poisson model with normal distribution.

To correct this “heteroscedasticity”, the dispersion estimates were applied to the mean counts divided by the size factors to transform the normalised data with the **r**egularised **log**arithmic function (**rlog**) of the DESeq2 package.

Equation 2: Calculation of regularised transformation

rlog transformation captures high dispersions for low counts, thus these genes exhibit higher shrinkage from the rlog. Rlog is a variation of log2 transformation, where qij is proportional to the expected concentration of fragments for gene i and sample j, βi0 is an intercept that does not undergo shrinkage, and βij shrinks towards zero based on the dispersion mean over the entire data set.

$$log2(q_{ij}) = \beta_{i0} + \beta_{ij}$$

Rlog transformation is a version of a shifted log2 normalisation with an important difference: Using rlog transformation, the normalised counts were shrunken towards the average dispersion (trend line) whilst fitting a **n**egative **b**inomial model (**NB**), unless the gene-wise α was more than two SDs ($\sqrt{variance}$) above trend (these ones were excluded as outliers).

In this way, by calculating dispersion estimates (α) for each gene i, and fitting a NB model with a mean (μ) normalised to the library size, the raw counts K_{ij} could be described best:

Equation 3: Negative binomial model for adjustment of read counts

The DESeq2 negative binomial (NB) model estimates differential expression between conditions, considering biological variability and statistical dispersion. The NB distribution is fitted to model the read counts (K) in DESeq2, where μ_{ij} represents the mean expression level for a given gene (i) in an observation (j), whilst α_i models the dispersion for i.

$$K_{ij} \sim NB(\mu_{ij}, \alpha_i)$$

This significantly reduced the dependence of the variance on the mean and prevented heteroskedasticity. The appropriate sample size of six for almost every condition in the present data set also helped mitigate heteroskedasticity (Fig. 8B).

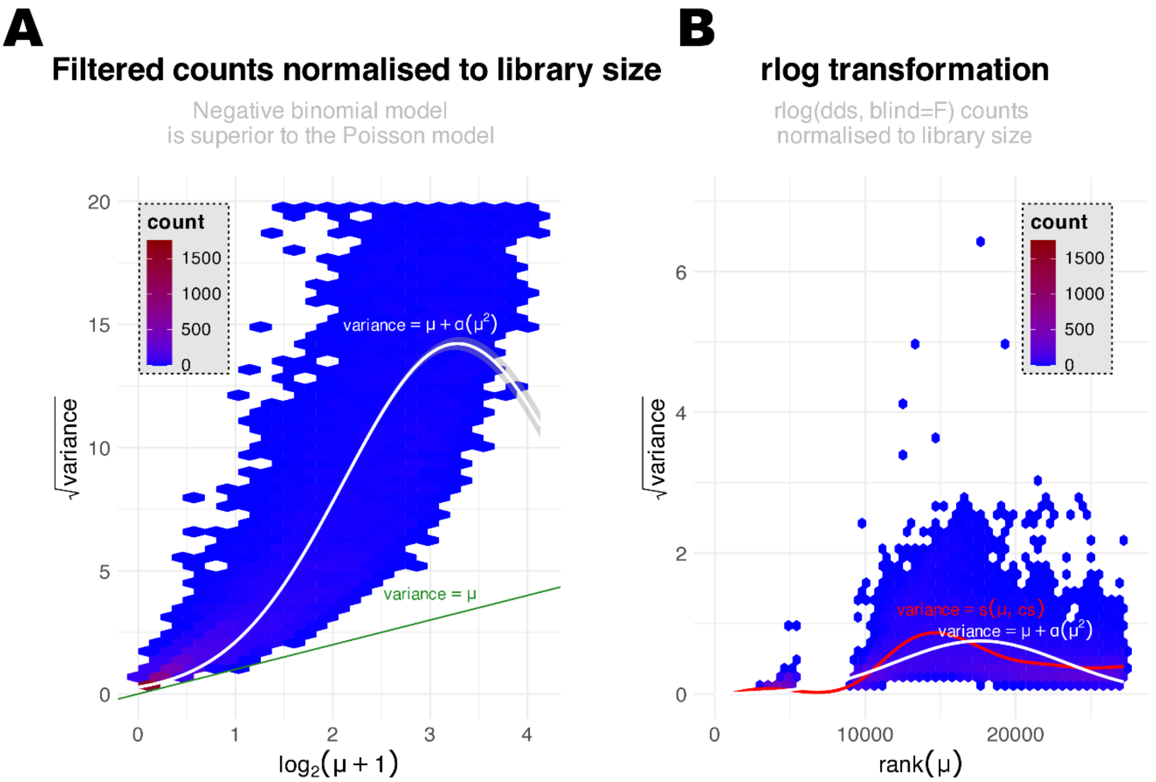

Figure 8: RNA-seq count transformation accounts for "overdispersion" and "heteroscedasticity"

A. For the raw DESeq2 counts, the Poisson model (variance = μ) is not sufficient to explain the data since the dispersion around the mean (μ) is higher in low count genes: mRNA expression is not constant for each biological replicate, which means that abundant transcripts have a larger variance than weakly expressed transcripts. A generalised linear model (GLM), where variance = $\mu + \alpha * \mu^2$, describes the distribution of read counts in the RNA-seq dataset much better. The α-parameter, the dispersion estimate, allows modelling of the extent of overdispersion.

B. Gene ranking after the shrunken rlog transformation. The rlog transformation provided by DESeq2 resolves the variance-mean dependence with respect to the previously calculated size factors. The red line shows an example of an even better fit of the average shrinkage using a cubic spline instead of a linear relationship to model overdispersion. This cubic spline is integrated into the negative binomial regression represented by the white line. Full usage of the design matrix due to blind = F.

With the new gene-specific coefficients, new normalised count data were generated and the H0 could finally be tested. For further overrepresentation analyses and visualisation purposes, gene expression was scaled (z-scored) by calculating the distance of each DEG from the mean of the rlog-transformed counts of all genes in a certain cluster divided by their standard deviation. z-scores represented the scaled transcript abundance across samples for each tested gene.

When analysing distances between samples, e.g. to derive high-dimensional similarity in a **p**rincipal **c**omponent **a**nalysis (**PCA**), "homoscedastic" data performed better when the level of gene expression did not affect the similarity measures, as would be the case for the rlog transformation with an NBM fit. PCA is a visual method for reducing large count data to a few dimensions. By calculating linear combinations of the count data, orthogonal principal components (PCs) can be extracted and visualised in 2D. The first principal component (PC1) distributes the data along its largest variation, while similar data cluster together. Thus, the first few PCs describe most of the variation in the data set, which should ideally account for up to 50% of the total variation – another reason to avoid heteroskedasticity.

Since counts with low expression levels and a low mean could have been introduced by chance, they provided little information for differential testing. Optimising mean-variance relationship by rlog-transformation for DEG analysis also prevented false positives (type I errors).

DEG analyses

Among all input genes, four conditions were analysed for **d**ifferentially **e**xpressed **g**enes (**DEGs**) in the physiological landscape: Cell population ("**ctrl**" vs. "**special**"), harvesting age (**E14-P7**), harvesting mode (***in*** vs. ***ex utero***), and MIA treatment (**naïve**, **PBS**, and **PolyI:C**).

For direct comparison between two groups, for instance between E19_E and E19_P, the Wald test was used to highlight differences. The **Wald** test performed one test per gene to test whether the estimated log2FC was significantly different from zero, i.e. whether the observed difference was statistically significant.

Capturing dynamic gene expression over time required multifactorial analyses. Either DEGs were evaluated with Wald statistics between pairs of consecutive time points, thus missing information across the temporal level. Or the entire time frame was subjected to multicomparison cluster analyses, as performed by the **l**ikelihood **r**atio **t**est (**LRT**) with reduced ~ design. The LRT between a full model and a reduced model tested whether the increased likelihood of the data using the additional terms in the full model was greater than expected when these additional terms were actually zero. With LRT, a single parameter for significance (p.adj. value) for the tested conditions was generated.

In this study, the null hypothesis/H0 (e.g. in the case of MIA: there is no difference between the treated and untreated condition) was rejected if the p-value was below the stated significance level. Unless otherwise stated, this **p**-value was often also "**adj**usted" (**p.adj.**) for multiple testing using the **B**enjamini-**H**ochberg (**BH**) approach. The BH approach aimed to limit the number of false detections in relation to the number of detections (**f**alse **d**iscovery **r**ate (**FDR**)). The q-value estimated this FDR, i.e. the expected proportion of false positives (type I errors) among the rejections.

Clustering approaches across time course

For clustering the genes, this study used two analytical tools with clustering methods – **degPatterns** and **WGCNA** – to capture the dynamic trends between different conditions over the developmental time frame of late neurogenesis.

The **degPatterns** function from the R package DEGreport (v.1.36.0; [372]) allowed for the clustering of gene expression patterns from the previously defined rlog-transformed DEGs. Unlike other time-series analysis packages, degPatterns used generalised additive models for modelling gene expression patterns, whilst allowing for linear and non-linear trends over time. Using Kendall’s correlation coefficient from pair-wise testing between all input DEGs, degPatterns clustered the genes hierarchically and intersected the resulting dendrogram in gene clusters with synergistically expressed gene profiles.

All clusters derived from DEG were generated based on strict statistical parameters for clustering the most significant 2,000 DEGs with an adjusted p-value below 0.01. Clusters must must contain at least 50 members. The remaining genes were clustered using the Kendall rank correlation coefficient as a distance measure.

For each time point, a boxplot was created with smoothed lines connecting the mean expression levels of successive time points to show a typical expression pattern for that cluster. The profiles of the DEGs were scaled with a z-score, i.e. each calculated distance from the mean log transcript count of all genes in that cluster was divided by the standard deviation of the log transcript counts in that cluster. The order of the clusters was redefined according to the course of development.

In parallel, the associated genes were functionally analysed, including overrepresentation analyses of biological processes (**G**ene **O**ntology, **GO**) using the compareCluster function of clusterProfiler (v. 4.8.2; [373]) with the parameters org.Mm.eg.db, "BP", "BH" and qvalue cut-off = 1 (Suppl. Table 2-6).

For comparing the influence of the fourth condition, MIA, on the physiological landscape, WGCNA was used here. Since degPatterns did not distinguish between significancy levels of generated clusters but was based on previously identified DEGs, **w**eighted **g**ene **c**o-expression **n**etwork **a**nalysis (**WGCNA**; v.1.72-1; [374]) was superior by assigning weights to all input genes according to their correlated expression pattern. Highly correlated genes (nodes) were stronger connected (edge weights) in this network, defined by a weighted adjacency matrix. Thus, WGCNA was a relatively unbiased approach to highlight interactions between gene modules with similar expression patterns, assuming the modules share the same signalling pathway or regulatory mechanism.

Physiological changes upon treatment were reflected in the so-called “modules”, which were clusters of gene expression that correlated to the treatment and had a high topological overlap. These modules of genes proved to be very robust and might not only be related in their expression profile but might also be involved in similar biological processes. A pairwise Pearson similarity coefficient, which was first calculated in a co-expression matrix, served as the co-expression measure. The similarity matrix was converted into a weighted adjacency matrix (signed) and only calculated for a power measure β according to their respective correlation. The weighted adjacency matrix was calculated considering the intramodular connectivity, i.e. the genes were “weighted” with a non-binary weight according to the soft threshold over a scale-free topology. The "signed" approach accounted for both negative and positive connectivity, reflecting inhibitory or activating biological processes. A corresponding adjacency function was implemented for this purpose, using power as the adjacency parameter. The power β can be defined by the probability that a gene is linked to one or more other genes, while new genes tend to associate with already established gene "hubs". This not only represented a requirement for a scale-free network, but was also close to observations of biological systems [375]. With this defined power, a factorisation of the adjacency matrix was possible. Here, factorisation meant the decomposition of the adjacency matrix into module eigenvectors and eigenvalues. Up to this point, only co-expression was considered.

In contrast to many other approaches, WGCNA also took topological similarities into account: a **t**opological **o**verlap **m**easure (**TOM**) was generated for these weighted genes, which served as a measure of centrality for the interconnectivity of genes and was generally a good predictor for the importance of genes in the respective module (Suppl. Fig. 12). TOM went beyond the initial Pearson correlation by considering the direct pairwise relationships between genes and their indirect relationships within the network (topological measure). By calculating 1-TOM, the gene **dis**similarity was defined. This weighted topological measure of overlap was highly cohesive and not inversely related to the actual connectivity of the genes. Finally, the module mapping was defined by average linkage hierarchical clustering.

For the **untreated** landscape, the transcriptome with a total of 97 samples over the time points E14, E16, E17, E18, E19_E (from embryos still *in utero* at E19), E19_P (from pups already born at E19), and P3 was sequenced in six replicates for each cell population (pCAG+ and pGlast/pNeuroD+). In addition, there were triplicates of pooled E19 *in utero* and *ex utero* samples, duplicates of P5, and one P7 sample for each cell population. Here, the multivariant analysis of DEGs was performed on raw count data with LRT using the full model ~ Age+Population implemented by the DESeq2 function compared to a reduced model that excluded the factor related to the cell population (“ctrl” vs. “special”) or the age factor with a significance threshold of p.adj. <0.01. These were input for the degPatterns clustering approach.

WGCNA was used for differential gene expression and clustering analysis of the **MIA** treated cohort in comparison with the untreated cohort. Rlog-transformed RNA-seq data of both cell populations from E18, E19_E, E19_P, and P3 samples of the non-MIA and MIA data set were used resulting in a total of 89 samples. Among them, 56 were pNeuroD+ samples and 41 were MIA (PolyI:C and PBS) treated samples. Counts with <15 hits in more than 75% of samples were rejected, ending up in 15,009 genes for WGCNA. They were computationally related to the respective categorial traits/conditions (Age: E18=0, E19_E=1, E19_P=2, P3=3; Population: tDimer+=0, pNeuroD+=1; MIA: non-MIA =0, MIA =1; Treatment: naïve =0, PBS =1, PolyI:C =2). To create gene modules with similar gene expression, modules were constructed using the signed Pearson correlation with a soft threshold power of 12. This power was chosen to achieve a scale-free model fit greater than 0.85 (Fig. 36B). In addition, a minimum module size of 30 genes per colour-coded module was enforced during the construction process.

Proteomics

Following the pipeline shown in figure 7 for mass spectrometry analyses, the primary sequences of the detected peptides were searched using the SEQUEST algorithm built into Proteome Discoverer software (v. 3.0.0.757, Thermo Fisher Scientific Inc.) against a verified murine Swissprot database (January 2023) of 17,013 entries. Since peptide modifications (e.g. post-translational modifications) alter its mass, options to consider them in the resulting .msf file were set as follows:

Carbamidomethylation was set as an artificially induced “**fixed modification**” for cysteine residues, whilst oxidation of methionine, pyroglutamate formation on glutamine residues at the N-terminus of the peptide, and acetylation of the N-terminus of the protein were allowed as biologically induced, “**variable modifications**”. Additionally, a maximum number of two missing **tryptic cleavages** was set.

Only peptides between six and 144 amino acids were considered for further analysis. A strict cut-off (FDR < 0.01) was set both for peptide and protein identification.

Quantification was performed using the Minora algorithm implemented in Proteome Discoverer v. 3.0. The obtained protein abundances were log2-transformed, followed by normalisation of the column means. As the samples were produced in three different batches, correction for the batch effect was performed using HarmonizR as described by Voss et al., 2022 [376].

Thus, further filtering or normalisation steps were obsolete. However, as the missing values were biased towards less intense proteins, indicating **m**issing **n**ot **a**t **r**andom (**MNAR**) values, the data were subtly imputed with a manual imputation with shift = 0 and scale = 0.1 (Suppl. Fig. 17) to smooth the density curves. Thus, since the dataset was already highly normalised, imputation for the statistical tests was performed on a low base to avoid artificially inflating the differences.

A total of 4,339 proteins were detected in 72 samples, of which 868 proteins were detected in all samples (for additional metrics of protein abundance: Suppl. Fig. 15, 16). The proteomic dataset comprised only a fraction of the treated replicates compared to the transcriptome dataset, mainly due to the loss of E19 samples during sample preparation.

Differential analyses were performed with the R package DEP (v. 1.22.0; [377]) using a limma-based algorithm (bayes statistics). For the following analyses of differential detected proteins (here referred to as "**DEP**s"), the timepoints (**E14-P7**), the cell populations ("**ctrl**" vs. "**special**"), and the treatment cohorts (**naïve**, **PBS**, and **PolyI:C**) were compared.

The analysis of **naïve/untreated** samples covered 41 samples of the entire time frame from E14 to P7 with both cell populations, as mentioned above.

Group differences were defined on the base of the total (MIA and naïve, E14-P7) differences between the "ctrl" population versus the "special" population.

The **treated** samples covered time points E18, E19, and P3, with a total of 49 samples. PolyI:C-induced differences were tested on both the PBS and the naïve samples.

Subsequent network analysis was performed in the CytoScape v.3.9.1 interface with ClueGO and STRING apps as a functional enrichment tools (GO:BP/ Gene ontology for biological processes) [378]. Singletons were removed from the visualisation.

The mass spectrometry proteomics data have been deposited to the ProteomeXchange Consortium via the PRIDE [379] partner repository with the dataset identifier PXD046067. The data were sorted according to the Sum **P**osterior**E**rror**P**robability (**PEP**) score, which evaluated the validity of the protein detection – a high score meant high validity.

DNA methylation

The EM-seq data in fasta format were first quality controlled using FastQC (v. 0.11.8; [366]) and were further processed according to the pipeline shown in figure 7 for EM-seq analyses. All samples met the typical criteria for EM-seq data, i.e. low C content, high T content, and average (25 %) A and G content (Suppl. Fig. 17). Subsequently, the files were subjected to adapter trimming using TrimGalore! with cutadapt (v. 3.1; [367]) and the following command line parameters: parameter: -j 6 -e 0.1 -q 20 -O 1 -a AGATCGGAAGAGC input_1.fastq.gz. The Illumina adapter-trimmed data was aligned against the built-in methylated mm10 reference genome of bwameth (v. 0.2.6; [380]) with the following parameters:

```
/usr/local/bin/python /usr/local/bin/bwameth.py c2t input_f.fastq.gz input_r.fastq.gz |bwa mem -T 40 -B 2 -L 10 - CM -U 100 -p -R '@ RG \tID:input_\tSM:input_' -t 8 /cvmfs/data.galaxyproject.org/byhand/mm10/bwameth_index/mm10.fa.bwameth.c2t /dev/stdin
```

The Picard tool MarkDuplicates (v. 2.18.2; https://github.com/broadinstitute/picard.git) was then used with the general default parameters to remove PCR duplicates. Methylation metrics per base were extracted and converted to a MethylKit-compliant format (--methylKit) using MethylDackel (v. 0.5.2; https://github.com/dpryan79/MethylDackel.git) with the mm10 reference genome. The resulting data matrix was then analysed using the R package methylKit (v. 1.26.0; [381]).

The raw sequencing data for EM-seq were available as fastq files, which will soon be deposited at the NCBI **G**ene **E**xpression **O**mnibus (**GEO**, application submitted).

Notes on experimental design

The sample size was not determined by statistical methods, but was estimated considering an average sequencing depth of 20M and similar sample sizes of Schurch et al., 2016 [382] and Ching et al., 2014 [383] for bulk RNA-seq.

With developmental maturity, expression patterns of most NeuroD protein family members declined (Fig. 16), which did not affect the flow-cytometric sorting process as the construct including the fluorescent protein was already episomally incorporated into the cell. Due to the incorporation of the fluorescent construct within the cell, the chosen cell sorting method was FACS instead of FANS. Even if only transiently expressed, the fluorophore remained stably integrated in the cytoplasmic context for at least a month (Suppl. Fig. 2).

For the transcriptomic analyses, only the P3 postnatal time point could be measured in six replicates for each cell population due to the limited availability of postnatal mice. P5 and P7 timepoints lacked most replicates but were still included in the analyses. This study focused on pNeuroD+ samples for the RNA-seq of MIA stressed samples, as the research question aimed to investigate the impact of MIA on the “pure” layer II/III neuronal population.

For the proteomic data set there were no replicates in the E19 samples. Thus, the E19_E and E19_P samples were combined for the whole analysis and not analysed separately. Unlike for the RNA-seq data set, pCAG+ samples of MIA animals were included for the proteomic data set.

Half of all samples for RNA-seq directly matched the harvesting/FACS date of the aliquots used for mass spectrometry. For EM-seq, cells needed to be pooled from two FACS dates.

Exact numbers and sample details are stored in the github repository https://github.com/TabithaRuecker/NeuroDev.git (Suppl. Table 12).

Results

► Untreated, indirect corticogenesis

The neurogenic fate acquisition of the upper-layer cell population was multimodally investigated by a flow cytometry-based sorting of different cell populations. For this approach, different developmentally active DNA constructs – that were electroporated into the developing cortex of embryonal mice – allowed for the isolation of **r**adial **g**lia **c**ells (**RGC**s) and early, post-mitotic neurons.

RGCs were isolated with an IUE at E12 via the promoter of their marker gene Glast1, which drove the expression of the red-emitting fluorophore dsRed2. This construct was electroporated together with a ubiquitously expressed construct with the CAG promoter driving the expression of the yellow/green fluorescent fusion protein Venus. These cells were harvested at E14 (Fig. 9A).

Furthermore, **post-mitotic neurons** were isolated using the NeuroD1 promoter. Cells were electroporated with pNeuroD1 at E14 and were harvested at E16, E17, E18, E19, P3, P5, and P7 (Fig. 9A). The promoter of NeuroD1 drove the expression of the fluorescent protein eGFP. Here, the CAG promoter drove the expression of the red fluorescent protein tDimer.

The cell populations that were isolated via a developmentally active promoter (pGlast1, pNeuroD1) are further called “special”, whilst the mixed cell population, which was isolated with the ubiquitous promoter CAG, was further called ”ctrl” population.

When electroporated at E14, progenitor cells physiologically contribute to the upper layers (layer II/III) of the murine cerebral cortex (Fig. 9B; [19]), which this study explicitly sought to investigate. Downstream multimodal approaches included bulk mass spectrometry, RNA-seq, and EM-seq (Fig. 9A).

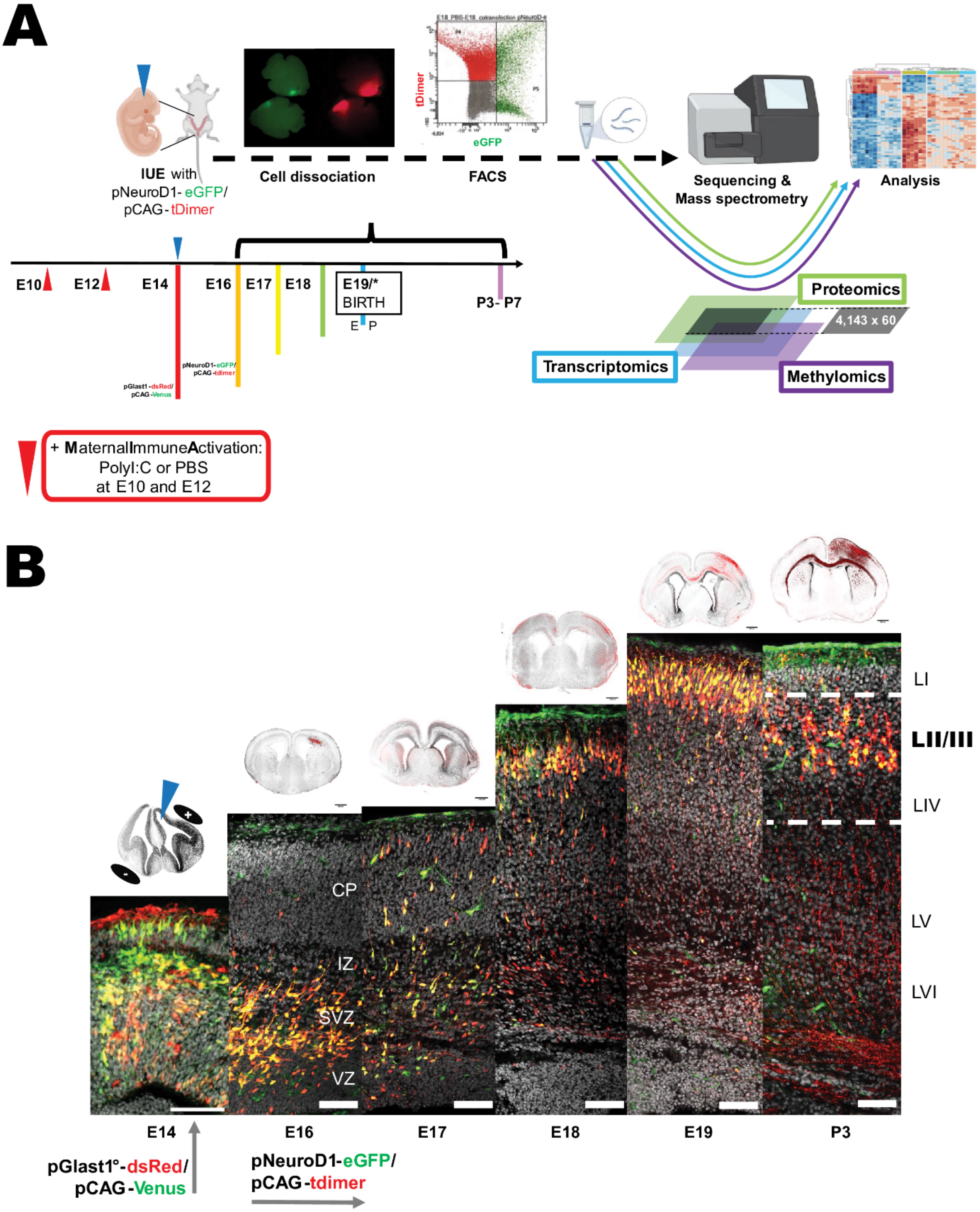

Figure 9: Experimental strategy for the temporal dissection of cortical layer II/III neurogenesis

A. After *in utero* **e**lectroporation (**IUE**) during the neurogenic timeframe, labelled cells were FAC sorted and subsequently underwent either RNA/DNA extraction for RNA-seq/EM-seq purposes or protein extraction for mass spectrometry. The resulting data was then bioinformatically analysed.

   The same process was used after **M**aternal **I**mmune **A**ctivation (**MIA**), represented by either PolyI:C or PBS i.p. injections at E10 and E12 before IUE (see section “Neurogenesis upon maternal immune activation”).

Caption continued on next page

B. Representative coronal sections of electroporated cells show the physiological upper-layer corticogenesis from the polarity formation of neuronal progenitors in the (**s**ub-)**v**entricular **z**one ((**S**)**VZ**) over the outside-last migration into the nascent **c**ortical **p**late (**CP**) until the final orientation of the neurons within the layer 2/3 (LII/III) of the neocortex. On top of each representative image, the associated 4x overview picture is displayed, showing Hoechst staining in grey and tDimer fluorescence in red. Upper-layer neuronal populations are mainly derived from intermediate progenitor cells, which divide again symmetrically in the **i**ntermediate **z**one (**IZ**). They otherwise also include layer 4 (LIV), which requires an even earlier injection to be targeted.

Cells were electroporated with the respective pull-down construct at E12 (with pGlast1°-dsRed2/pCAG-Venus, shown at E14) or E14 (with pNeuroD1°-eGFP/pCAG-tDimer, shown at E16°°, E17, E18, E19, and P3), respectively. In the following,"control"/ctrl means transfection with marker proteins such as Venus (E14) or tDimer (all other time points), while "special" means transfection with pGlast1 (E14) or pNeuroD2 (all other time points). Overlayed fluorescence of both channels results in yellow colour. For multiomic experiments, similarly electroporated cell populations were subjected to FACS and the respective analysis pipeline as required for the three modalities. Hoechst staining as background. Scale bar: 100 µm.

° “p” stands for “promoter”.

°° E15 was excluded due to sparse NeuroD1 expression after only one day of transfection.

At the peak of neurogenesis (at E14 in mice) some cell bodies of labelled pGlast1-dsRed2+ RGCs were located in the VZ (apical progenitor cells) with basal projections reaching the pial surface (Fig. 9B). Other cell bodies accumulated at the border to the CP without clear polarity, and some cell bodies were already in contact with the pial surface (basal progenitors, Fig. 9B). Two days later, at E16, the nascent CP thickened, and the radial ontogenetic columns emerged, organising neurons from the same birthplace [384,385]. From then on, the early post-mitotic neurons were labelled with pNeuroD1-eGFP for later harvesting time points. Some of these progenitor cells continued to remain multipolar. While the progenitor cells were gathering in the SVZ, more mature neuronal progenitors became bipolar again and started radial migration along the fibres of the RGCs.

At E17, almost all of these developing neurons attained the motile stage and radially migrated into the CP by crossing the subplate boundary, pushing past older neurons, and translocating along the radial fibres provided by the RGCs. By E18, most radially migrating neurons reached their final position in the upper layers, while few had not yet completed their translocation. The volume of the SVZ decreased dramatically, while the CP continued to expand, and the apically located axon bundles thickened. On the day of birth, at E19, the cortex showed an ordered laminar structure of the CP with the developed neurons all oriented in their laminar niche. From P3 onwards, the cells showed a pyramidal shape with elongated dendrites and an axon projecting in an L-shape across the *corpus callosum* to the other hemisphere (Fig. 9B; [94]).

Flow cytometry experiments

The expression of fluorescent proteins in neuronal cells of the murine embryonic cortices was driven by developmentally active and ubiquitously active promoter elements. The previously electroporated cells (Fig. 10A and 11A) were sorted based on these fluorophores via flow cytometry. For flow cytometry experiments, a template was used for compensation and gating settings every time the cotransfected samples were sorted. Gates were set from the singlets SSC population (Fig. 5B, right plot) that contained the cells to be enriched for the two channels needed to identify the fluorescent proteins of interest. **F**luorescence **M**inus **O**ne (**FMO**) controls allowed initial gate setting using cell suspensions from brains transfected with only a single fluorophore (Fig. 10A,B and 11A,B). Compensation with the FMO signals brighter than the signal in the cotransfected sample ensured correct differential fluorescence detection in the cotransfected sample (Fig. 10C and 11C). Thus, compensation accounted for spectral overlaps and prevented spillovers of emission spectra into the respective detectors (Fig. 10C, D; 11C, D) so that the transfected cell populations were consistently sorted into aliquots used for downstream analyses. Note that dsRed2+ cells might also have Venus fluorescence (double positive) and eGFP+ cells might have also tDimer fluorescence (double positive).

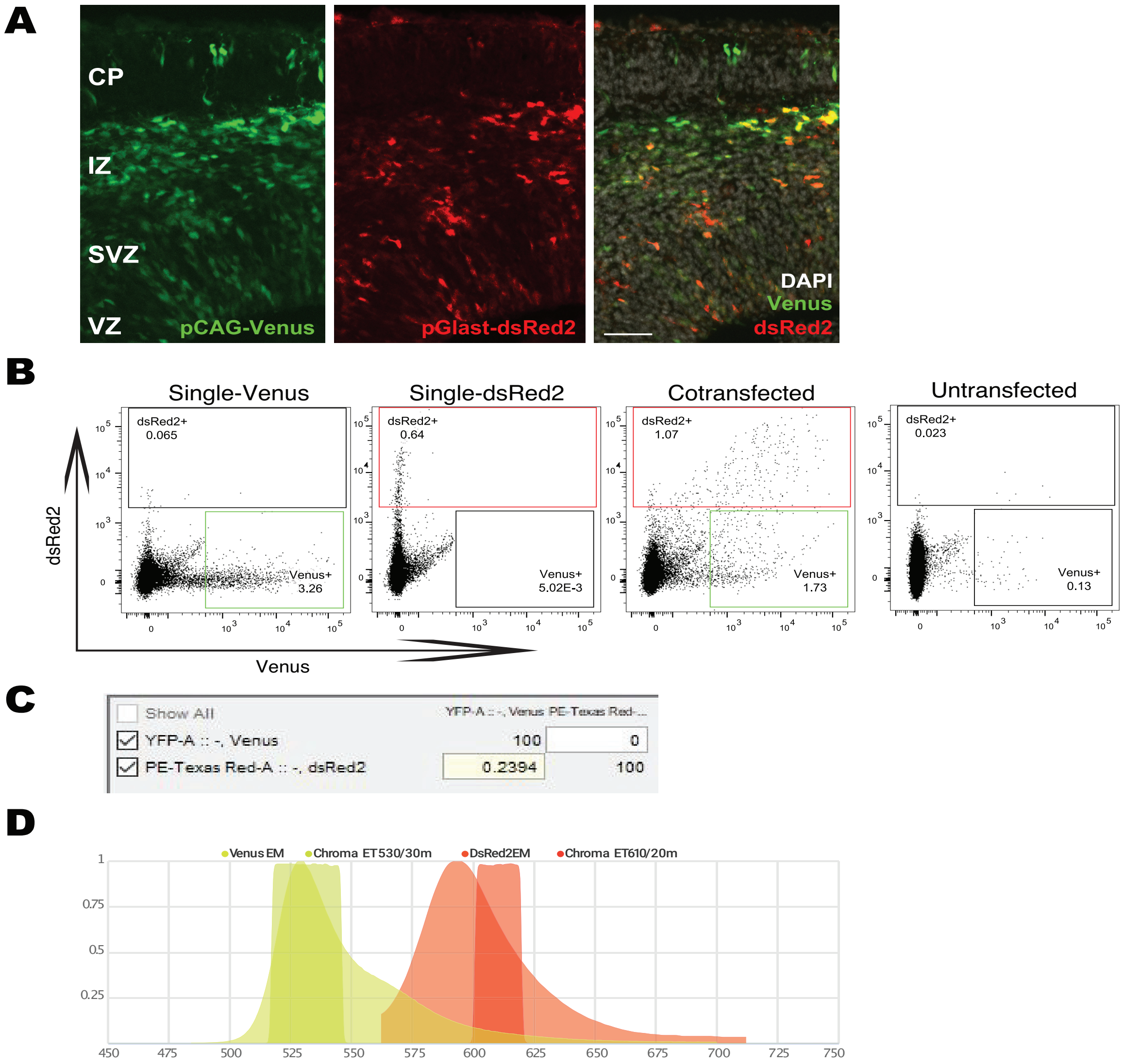

☐ Show All	YFP-A :: -, Venus	PE-Texas Red-...
☑ YFP-A :: -, Venus	100	0
☑ PE-Texas Red-A :: -, dsRed2	0.2394	100

Figure 10: Gating strategy for separating a cell population into subpopulations by flow cytometry based on the transfection of the construct pGlast1-dsRed2/pCAG-Venus

A. Coronal sections of the murine somatosensory cortex of embryonal age E14 after *in utero* electroporation at E12 show fluorescent protein expression in the target cell population: Venus expression driven by the ubiquitous promoter pCAG (left), dsRed2 expression driven by apical radial glia cell-specific promoter Glast1 (middle), and merged (right). CP: cortical plate, IZ, intermediate zone, SVZ: subventricular zone, VZ: ventricular zone. Scale bar: 50 µm.

B. The experiment performed on 20,000 cells of E14 embryonic cortices shows singlets SSC populations of both fluorescence minus one (FMO, single transfected) controls, untransfected, and cotransfected samples with the construct pCAG-Venus/pGlast1-dsRed2. The FMO control of the single Venus transfection and the FMO control of the single dsRed2 transfection, together with the untransfected control, are used to calculate the compensation. Compensation with the FMO signals brighter than the signal in the cotransfected sample ensures correct differential fluorescence detection in the cotransfected sample.

   Note: At E14, an additional low false positive signal in the Venus channel was visible already in the untransfected condition, which was excluded for sorting.

C. Computational compensation matrix (“Compensation Wizard” of BD FACS Diva software; recreated with FlowJo) defines values for compensation of spillover into the other bandpass filter.

D. The here used bandpass filter 530/30 covers the emission peak and the spread in the case of the fluorophore Venus, while the bandpass filter (610/20) covers the emission spectrum of dsRed2. The plot was generated with FPbase [362].

This figure was reused from the **STAR protocol**.

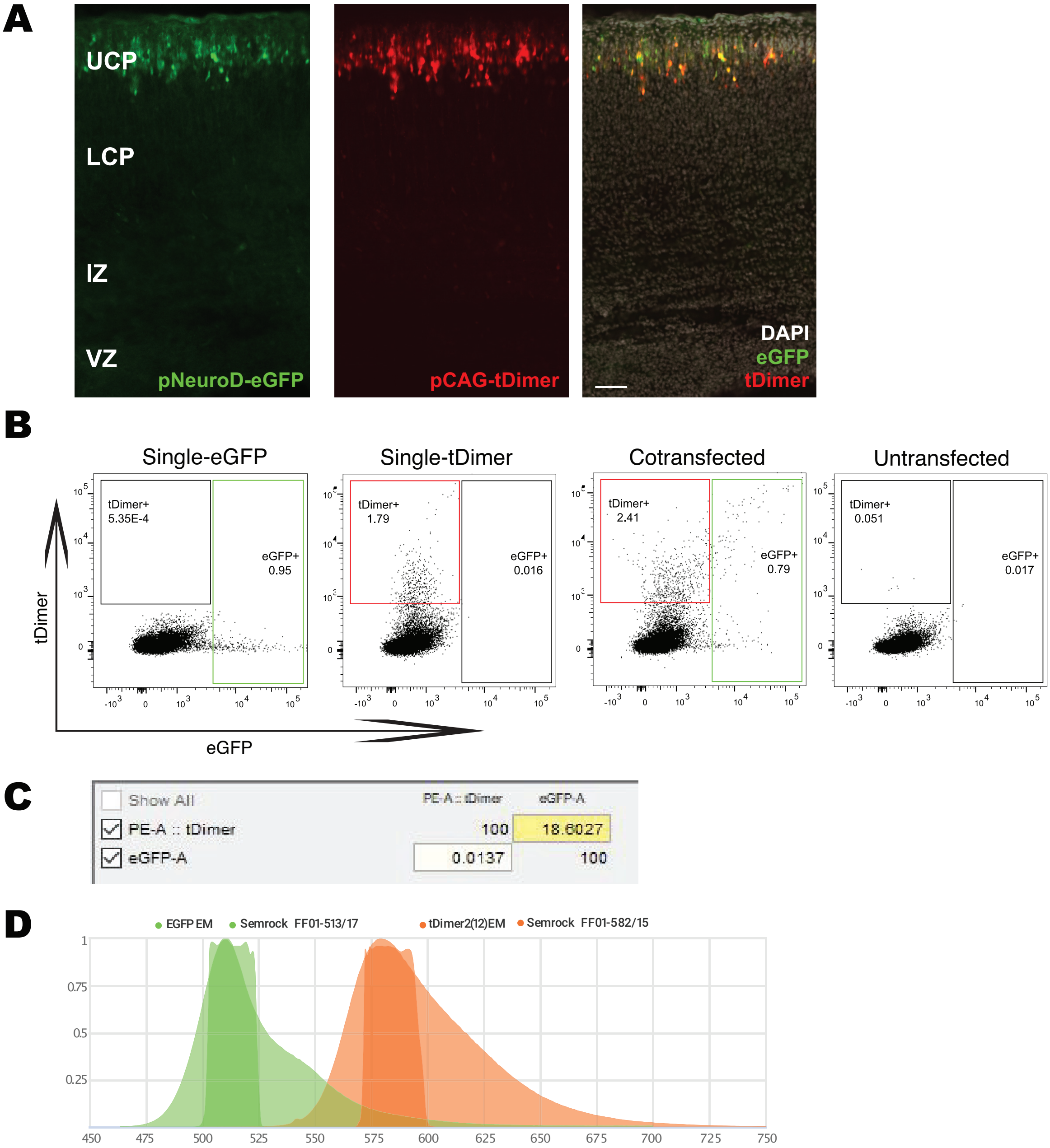

☐ Show All	PE-A :: tDimer	eGFP-A
☑ PE-A :: tDimer	100	18.6027
☑ eGFP-A	0.0137	100

Figure 11: Gating strategy for separating a cell population into subpopulations by flow cytometry based on the transfection of the construct pNeuroD1-eGFP/pCAG-tDimer

A. Coronal sections of the murine somatosensory cortex of embryonal age E18 after *in utero* electroporation at E14 show fluorescent protein expression in the target cell population: pNeuroD1-eGFP expressed in post-mitotic neurons (left), pCAG-tDimer expressed ubiquitously (middle) and merged (right). UCP: upper cortical plate, LCP: lower cortical plate, IZ, intermediate zone, VZ: ventricular zone. Scale bar: 100 µm.

B. The experiment performed on 20,000 cells of E18 embryonic cortices shows singlets SSC populations of both single transfected controls, untransfected, and cotransfected samples with the construct pNeuroD1-eGFP/pCAG-tDimer. The FMO control of the single eGFP transfection and the FMO control of the single tDimer transfection, together with the untransfected control, are used to calculate the compensation. Compensation with the FMO signals brighter than the signal in the cotransfected sample ensures correct differential fluorescence detection in the cotransfected sample.

C. Computational compensation matrix ("Compensation Wizard" of BD FACS Diva software; recreated with FlowJo) defines values for compensation of spillover into each other BP filter.

D. The bandpass filters 582/15 and 513/17 cover the peaks of the emission spectra of the fluorescent proteins used here, tDimer and eGFP, respectively. The plot was generated with FPbase [362].

This figure was reused from the **STAR protocol**.

Immunofluorescence staining confirmed upper-layer neural character of transfected cells

Immunofluorescence staining against Satb2 confirmed the upper-layer neuronal character of the pNeuroD1-eGFP+ cells and of the control (pCAG-tDimer+) cells (Fig. 12). A subset of the green fluorescent cells was not stained against Satb2. However, most of them had green autofluorescence as endothelial cells, which are not sorted by flow cytometry due to selection by size and granularity. Furthermore, a possible microglial character of this subset of cells was refuted. The eGFP+ transfected cells did not colocalise with Iba1+ cells in an additional immunofluorescence staining against Iba1, which is expressed on the surface of microglial cells [305,307] (Suppl. Fig. 3, 4).

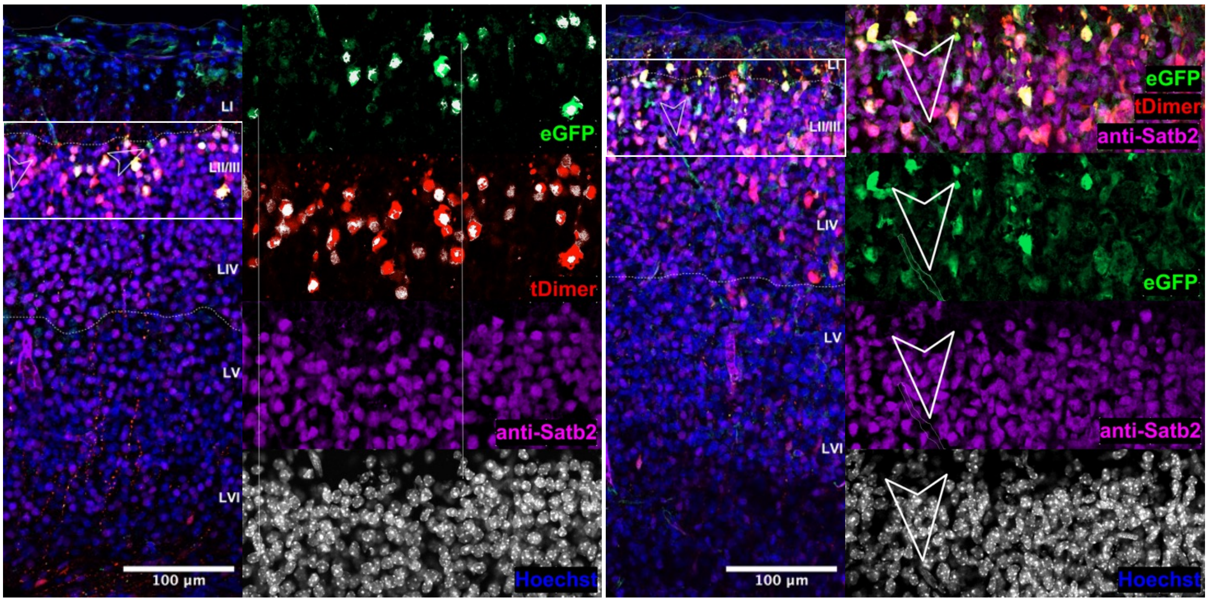

Figure 12: pNeuroD1-driven eGFP is expressed in cortical projection neurons like its pCAG-driven control tDimer

Representative coronal sections of the somatosensory cortex of E18 mice after IUE at E14 show eGFP+ cells that are also positive for the upper-layer neuronal marker Satb2. The ubiquitously expressed tDimer is also present in differentiated neurons. White frames indicate digitally enlarged regions.Lines or arrowheads indicate eGFP+ cells that are not stained for Satb2. Scale bar: 100 µm, 20x magnification.

Left panel: Digitally magnified region first shows colocalisation of eGFP+ with Satb2 staining in white, then colocalisation of tDimer+ cells with Satb2 staining. The lines highlight eGFP+ cells that are not stained for Satb2.

Right panel: The arrowhead shows an example of endothelial cells, which visually make up the majority of cells that fluoresce green but do not stain for Satb2. This is due to the autofluorescence of the endothelial cells and makes it difficult to distinguish them from eGFP+ neuronal cells. However, this is only a small proportion of the green fluorescent cells, and the proportion of eGFP+ cells that are Satb2- and also lack endothelial character, but rather have an indistinct morphology, is even smaller.

Transcriptome analyses

Validation and characterisation of RNA-seq samples

Samples reflected the gradual neurogenic cell fate commitment

PCA separated the samples along the PC1 axis by age with 44.87% variation (Fig. 13A). Postnatal samples differed most from prenatal samples (Fig. 13A, C). In particular, the progenitor stage (E14 and E16), early neuronal stage (E17, E18, and E19_E), and postnatal, differentiated stage (E19_P to P7) samples clustered among each other. Samples from time points E17 and E18 appear to have clustered farthest away from the PC2 component with 10.81% variation (Fig. 13A). The cluster of E14 samples overlapped with all of the pCAG-tDimer+ samples of the other prenatal time points. Moreover, E16 samples were transcriptionally more similar to E14 than E17 samples (Fig. 13C).

The biplot in figure 13A showed the genes that accounted for the most detected variances in the data set, which are separately depicted in figure 13B. The genes that pulled the samples most strongly along the PC2 axis were all associated with immunogenic processes. In contrast, the genes that pulled the samples in the other direction were structural elements of the maturing nervous system, mostly of oligodendrocytic or astrocytic character.

Overall, this illustrated the gradual acquisition of neurogenic cell fate from a progenitor stage (E14, pGlast1/pCAG and E16, pNeuroD1/pCAG) to a motile/migratory stage (E17, E18, pNeuroD1/pCAG) to a terminally differentiated state (E19, P3-P7, pNeuroD1/pCAG).

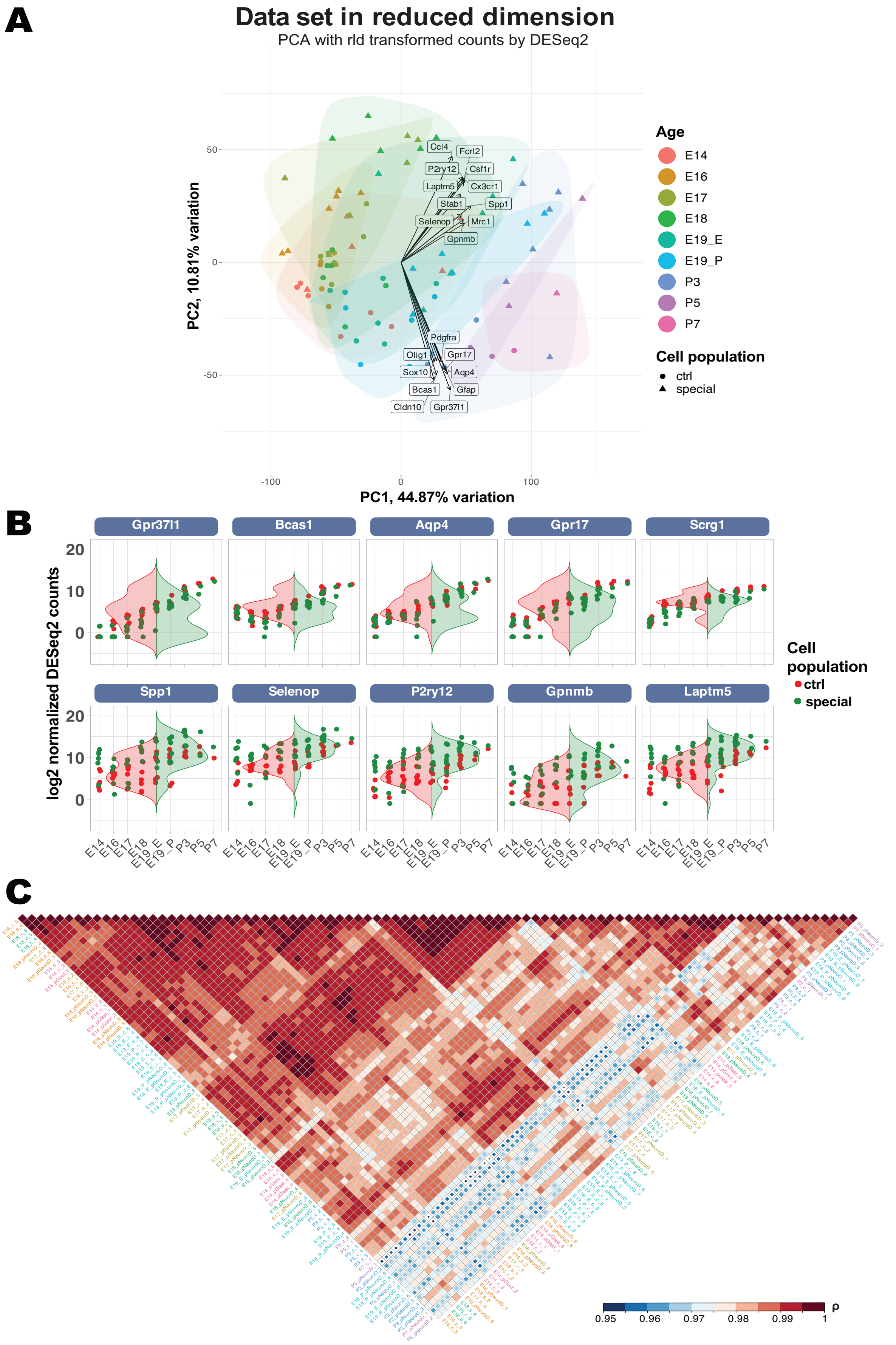

Caption continued on next page

Figure 13: Transcriptomic samples reproduce the gradual progression of indirect neurogenesis

A. RNA-seq samples intrinsically cluster by association with age and cell population. Samples with rlog-transformed counts cluster along the PC1 and PC2 axis. PC1 shows a fan-shaped clustering of consecutive harvesting time points. PC2 explains the difference in population (“ctrl” vs. “special”); while the E14 samples overlap the pCAG-tDimer+ samples of the other prenatal time points and all pNeuroD1+ samples cluster outwards. 50% of the variables were removed.

B. Top five loadings/genes show association of PCA clustering with the respective cell population and time course progression. The upper genes are increasingly expressed in both populations over time, while the bottom panel of genes shows genes that are prominently expressed by the pNeuroD+ cell population.

C. RNA-seq samples are correlated and differ mostly between the pre- and postnatal samples. Spearman’s rho (ρ) correlation coefficient greater than 0.95, with ρ represented by a colour gradient from blue (low) to red (high).

Promoters were suitable to target neuronal precursors and developing neurons

The cellular identity was additionally verified by marker gene association of pGlast1-dsRed2+ [312,386] versus pNeuroD1-eGFP+ cells [339,340,345,350,387,388] (Fig. 14C, F). Transcriptomic analyses revealed a gradual transition from a progenitor aRGCs cell character to an immature neuronal identity. Commonly used neuronal precursor marker genes were strongly expressed in E14 samples, while neuronal genes were downregulated (Fig. 14A, D). Neuronal precursor markers used here encompassed e.g. *Neurog1* [185,389,390], *Eomes* [98,391,392], *Arx* [339], *Rnd2* [388],*Sox2* [342,393–395], and *Pax6* [341,396,397] and the neuronal-specific markers e.g. *Satb2* [10,141,349,398], *Timp2* [350], *Bcan* [345,387], *Unc5d*[399,400], *Mapt*[401], *Cux1* [144,308], and *Grin2b* [402] (Fig. 14B, E). Here, neuronal progenitor genes were highly effective in excluding mature cell identity in E14 pGlast-dsRed2 samples. In contrast, some neuronal marker genes were already established in the E14 samples, even if not at high levels. In summary, the enrichment of specific marker genes in the sorted target populations by developmentally active promoters indicated a successful sorting and sequencing procedure.

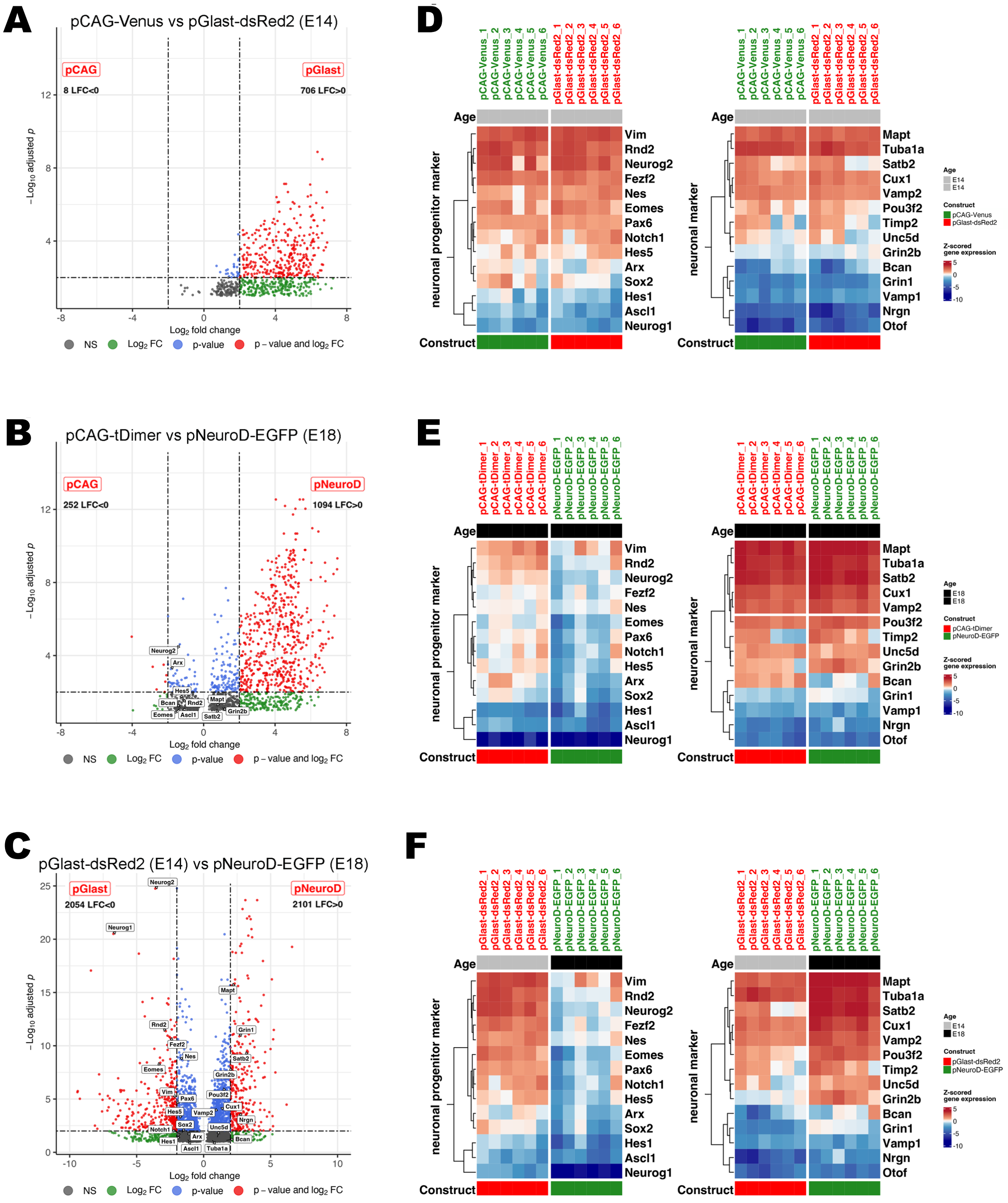

Figure 14: DEG analysis in neuronal progenitors and developing neurons reveals enrichment for developmentally-regulated marker genes

A-C: Flow cytometry-based isolation of cell populations sorted by fluorescent proteins driven by developmentally active promoters show enrichment for characteristic genes of the respective targeted cell identity after bulk RNA-seq.

Caption continued on next page

A. At E14, DEGs were detected in pGlast1-dsRed2+ progenitors compared to pCAG-Venus+ controls, but no enrichment for characteristic genes of progenitor cell identity was observed.

B. DEGs were detected in isolated pNeuroD1-eGFP+ developing neurons compared to pCAG-tDimer+ controls at E18. The volcano plot shows enrichment of multiple individual genes involved in neuronal development, indicating enrichment of characteristic genes of early neuronal cell identity (white boxes).

C. DEGs were detected in pGlast1-dsRed2+ progenitors (E14) compared to pNeuroD1-eGFP+ early neurons (E18). The volcano plot shows enrichment of multiple individual genes indicating enrichment of characteristic genes of progenitor cell identity in pGlast1-dsRed2+ cells (E14) and enrichment of multiple individual genes involved in neuronal developmental in pNeuroD1-eGFP+ early neurons (E18) validating progenitor and early neuronal cell identity, respectively (white boxes). Grey = expression not significantly altered, green = Log2 fold change (FC), blue = p-value, red = Log2 FC and p-value: Genes plotted in red passed the p.adj. cut-off of <0.01 and the log2 FC cut-off >2.00.

D-F: Commonly used marker genes for progenitor (left) and early neuronal cells (right), respectively, identified in bulk RNA-seq validate differences in cell identity of isolated cells labelled with

D. pCAG-Venus vs. pGlast1-dsRed2,

E. pNeuroD1-eGFP vs. pCAG-tDimer or

F. pGlast1-dsRed2 vs. pNeuroD1-eGFP at timepoints E14 (grey bars) and E18 (black bars). To facilitate comparison, pGlast1 (E14) and pNeuroD1 (E18) samples (in F) compare the same input from the cotransfected cell populations, which were independently scored against one another. Z-score was applied on rlog normalised counts; heatmap colours range from red (high expression), to white (moderate expression) to blue (low expression).

This figure was reused from the **STAR protocol**.

Extreme and marker gene expression of differentiating neurons

The genes most upregulated from E14 to P7 were *Gfap* [403], *Gjc3*, and *Aqp4*. In the pNeuroD1+ population, the Wnt responsive gene tensin 4 [404] (*Tns4*), the triggering receptor expressed on myeloid cells-like 4 (*Treml4*), and the proinflammatory platelet activating factor receptor *Ptafr* [405] were particularly upregulated (Fig. 15).

Neurog1 and *Neurog2* [406], *Igf2bp1* [407], and *Eomes* [98,391,392] were among the genes most down-regulated from E14 to P7 irrespective of cell population, while *Sp9* and *Dlx1,2,5* [347], and *Ascl1* [406], and *Arx* [339] were among the genes most upregulated over time in the pCAG-tDimer+ cell population (Fig. 15).

Generally, marker genes specific to neurons are commonly used in scRNA-seq analyses [408,409] to determine cell identity in deconvoluted data sets. During development, however, the expression of marker genes must be differentiated into at least three profiles with different expression dynamics, as shown in the clusters illustrated in figure 16. For example, the *Neurod* gene family stopped expression after birth (Cluster 1, Fig. 16). The expression of *Satb2* and *Cux1*, whose gene products are used in immunohistochemistry to label upper-layer neurons, peaked at E18 and declined thereafter, thus they were subject to oscillating gene expression (Cluster 3, Fig. 16). They stood in contrast to e.g. *Grin2b* (Cluster 2, Fig. 16), which is a glutamate transporter increasingly required for neuronal function.

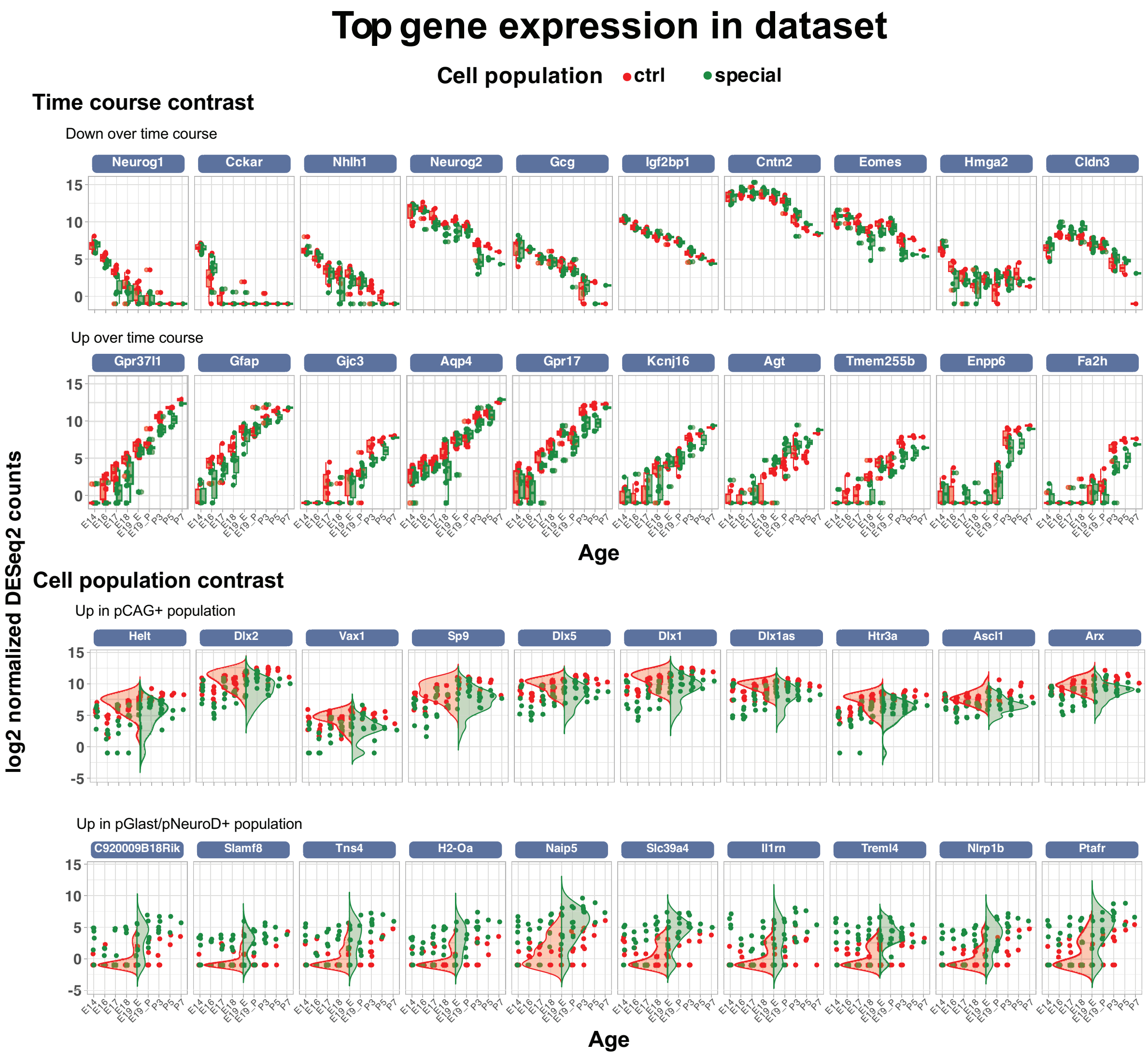

Figure 15: Representative examples of genes with extreme gene expression over time

Upper panel: DEGs with time course contrast: Top ten down-regulated (upper panels) and up-regulated (lower panel) genes during the time frame, independent of cell population.

Bottom panel: DEGs with cell population contrast show the top ten genes most upregulated in the “ctrl” population (pCAG+) compared to the “special” population, while the reverse is shown below for the “special” population (pGlast1/pNeuroD1+). Note that the DEGs that are most upregulated in the “special” population are more different from the ctrl population than *vice versa*. P.adj. sorted log2 DESeq2 normalised counts with ascending or descending l2FC.

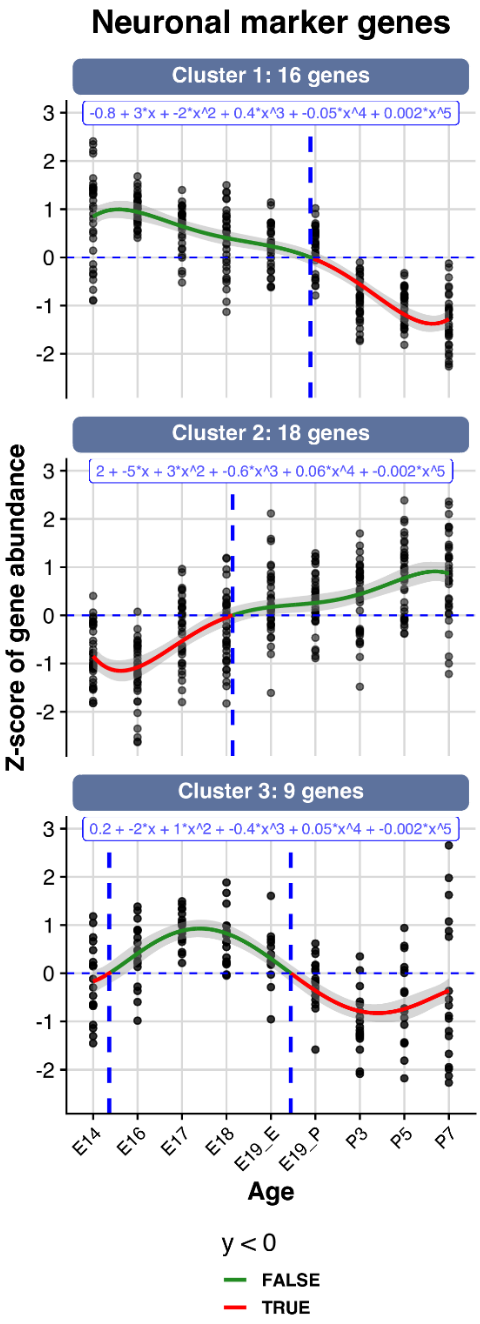

Figure 16: Commonly used neuronal marker genes are dynamically expressed during neurogenesis

Sixteen neuron-specific marker genes were expressed only at the progenitor level and then downregulated (including the NeuroD gene family) in the pNeuroD1+ cell population **after** migratory state. The expression of eighteen neuronal marker genes had an upward trend with rising gene expression above average **before** migration (including: *Mef2c*, NMDAR, Vamp, and Dlx encoding genes). Nine were initially upregulated until birth and then dropped below average expression at the postnatal stage (including *Satb2*).

RT-PCR correlated with RNA-seq counts

Two custom-made RT-PCR panels further validated the RNA-seq results, covering commonly used marker genes for neuronal progenitors, early neurons, and microglia (Fig. 17A, B, and C). Triplicate experiments of different 10K cell aliquots from the same three initial RNA-seq experiments were performed with internal plate controls, which were not included in the analyses for Fig. 17 and 18. The logarithmic data indicated a lower fit for microglia-like marker genes between RNA-seq and RT-PCR count data than for progenitor or neuronal marker genes (Fig. 17; bars: RT-PCR data, lines: RNA-seq data). The correlation analyses of monotonic relationships between RT-PCR and RNA-seq count data was expressed with a Spearman's rank correlation coefficient (ρ) and its statistical significance (p-value) for each time point tested (Fig. 18).

The **progenitor** marker genes showed similar significant trends between RNA-seq and RT-PCR data in both cell populations (highest ρ=0.95 in pNeuroD1+ population at E17; Fig. 17A, 18A). The downregulated expression dynamic captured with RNA-seq over time was detected with RT-PCR, which was evident for the *Eomes*, *Fezf2*, and *Neurog2* genes. There was a strong positive monotonic correlation between RNA-seq and RT-PCR count data, which was highly significant (lowest p-value of $<2.2e^{-16}$ in pNeuroD+ population at E17).

Neuronal marker genes also correlated significantly with both “ctrl” and “special” cell populations (highest ρ=0.81 in the pNeuroD1+ population at E19; Fig. 17B, 18B). The *Bcan* and *Timp2* amplicons particularly reflected the upregulated transcriptomic profile.

Microglia-like marker genes showed the highest variation, the lowest correlation, and significance with the RNA-seq dataset (highest ρ=0.64 in the pNeuroD1+ population at E17; Fig. 17C, 18C), especially compared to RNA-seq counts in the pCAG+ population. *Cx3cr1* showed the lowest correlation between RNA-seq and RT-PCR transcript abundance. This may be attributed to the undetectable cycle threshold for the *Cx3cr1* probe at E14, as the cycle number exceeded the maximum Ct value of 40 for all replicates. *Csf1r*, *Fcrl2* (Fcrls), *Itgam,* and *P2ry12* amplicons showed similar trends. *Itgam* had no detectable values for the internal plate controls, so the other values are also probably uncertain. Note that all microglia-like genes had the highest Ct value for time point E14, and several tested genes even exceeded the maximum Ct value of 40 in the control samples. Thus, they appeared lower expressed after subtracting from E14 (ΔΔct method).

Overall, the relatively high correlation coefficients indicated a robust detection of transcript abundance for progenitor and neuronal genes by RNA-seq, therefore, the RNA-seq data can be reliably analysed and further interpreted.

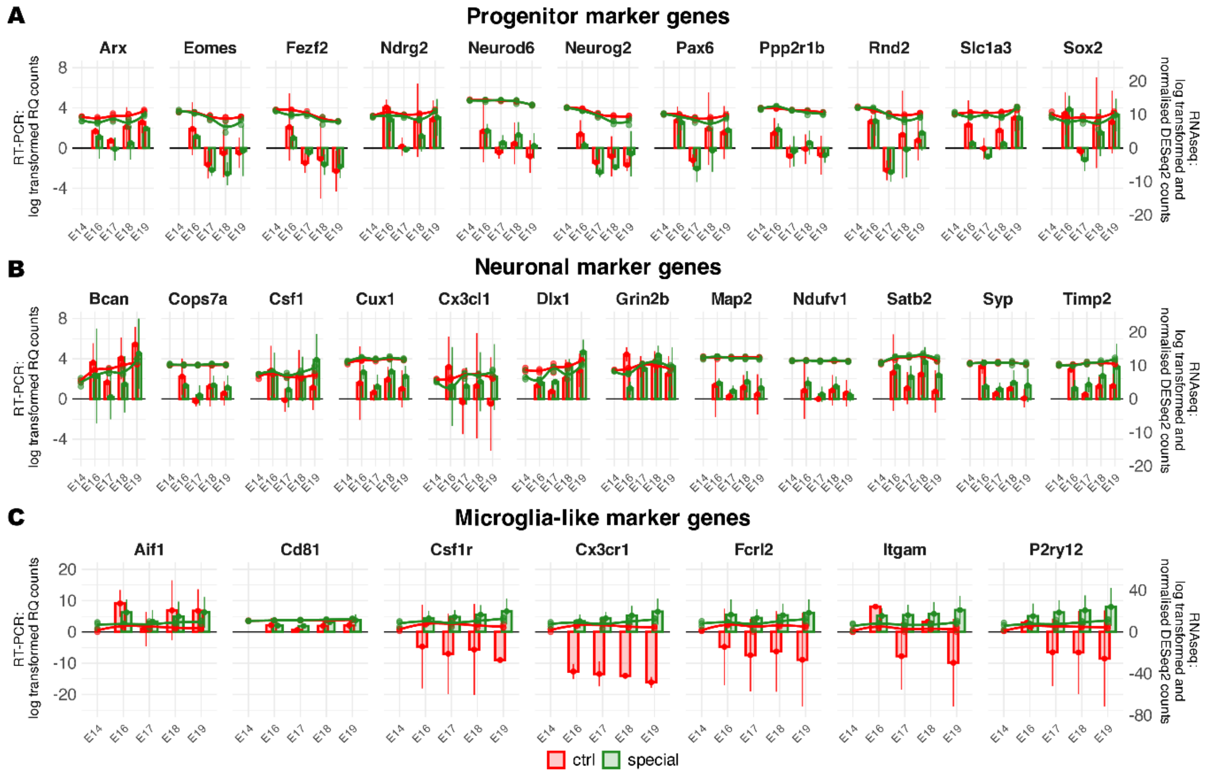

Figure 17: Expression profiles of genes detected by RT-PCR and RNA-seq over time

Log2 fold changes between RT-PCR and RNA-seq count data have similar dynamics over the chosen time frame. For RT-PCR (bars), the ΔΔCq (RQ) values were first subtracted from the respective endogenous 18S control gene and then from E14. Error bars represent the mean+/-sd of the RT-PCR values. RNA-seq data (lines) were first DESeq2-normalised and then manually log2-transformed to generate data for each replicate. Data highlighted in red represent the pCAG+ cell population, while data highlighted in green represent the pGlast1/pNeuroD1+ cell population.

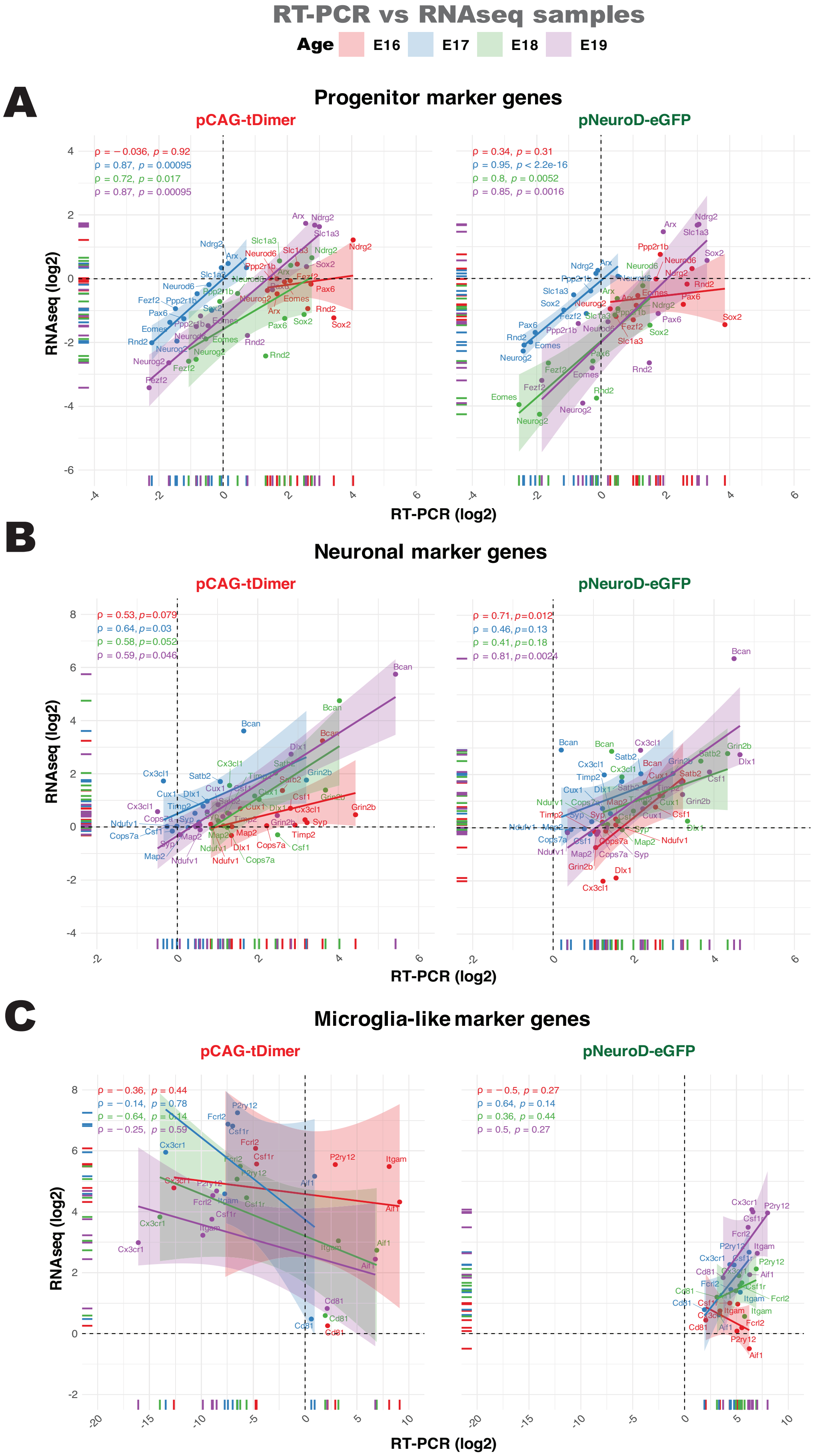

Caption continued on next page

Figure 18: RT-PCR correlates with mRNA transcript abundance detected by RNA-seq

Spearman test confirms high correlation between RT-PCR (x-axis) and RNA-seq (y-axis) mean counts for the selected genes. Consider that the RT-PCR values shown are calculated differently from the RNA-seq values. The lines for each time point show the normalised log2 fold change of the RNA-seq data calculated by DESeq2 with contrast to E14 plotted against the log2-transformed mean of the RQ values from RT-PCR. Note the wide range of RT-PCR values of the detected amplicons for microglia-like marker genes.

Meta-analysis correlated samples with LII/III neurons from scRNA-seq data set

Bioinformatic meta-analysis of samples from the untreated condition with a scRNA-seq data set of P2 mouse brains showed a positively correlated association of the upper layers (Fig. 19). With increasing age, the samples showed a prevalence for the upper layers II/III/IV; especially the E16 samples showed significant downregulation of genes associated with the highest expression in deeper layers of the Rosenberg et al., 2018 [408] data set.

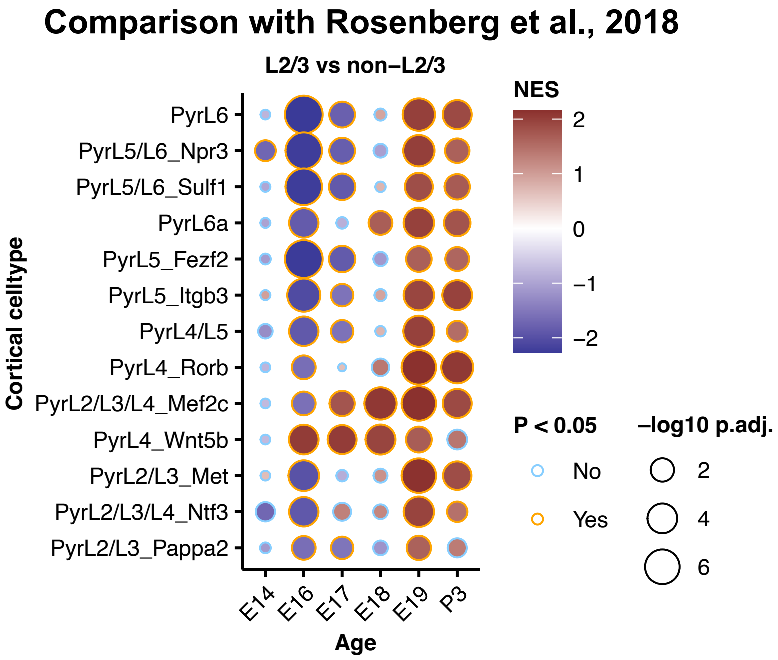

Figure 19: Meta-analysis of the physiological transcriptomic samples with a murine scRNA-seq dataset

Comparison with a dataset of the developing mouse brain by Rosenberg et al., 2018 [408] using Metacell ID 5-17. With increasing age, correlation to cortical layers other than layer 2-4 decreases, while in particular between E16 and E19, cell identity correlates with layer 2/3/4 projection neurons that express *Unc5d*, *Plxna4*, *Ptprk*, *Satb2*, *Mef2c*, *Mpped1*, and *Trpc4*. NES=normalised enrichment score. Note that e.g. *Satb2*, is also among the most expressed genes in cell cluster 14 CTX PyrL6a. Plot generated in exchange with Dr. Marcel Seungsu Woo.

Differential gene expression

The pGlast1/pNeuroD1+, “special” cell population

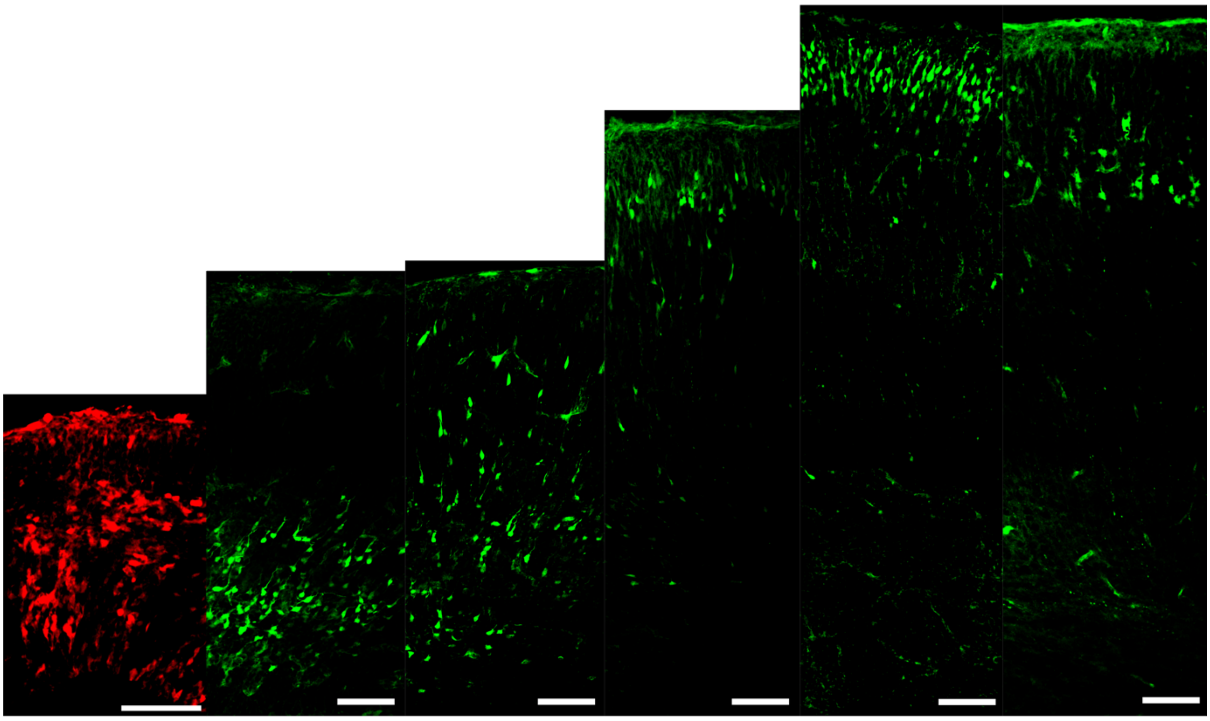

The differential gene analysis focuses first on the pGlast1/pNeuroD1+ cell populations, here the so-called “special” population.

Consecutive analysis of special population

When resolving for differential gene expression changes between consecutive time points of only the “special” cell population, the number of up- and downregulated genes was dynamically regulated, considering a statistical threshold of p.adj.<0.01 (Fig. 20; Suppl. Table 2).

A

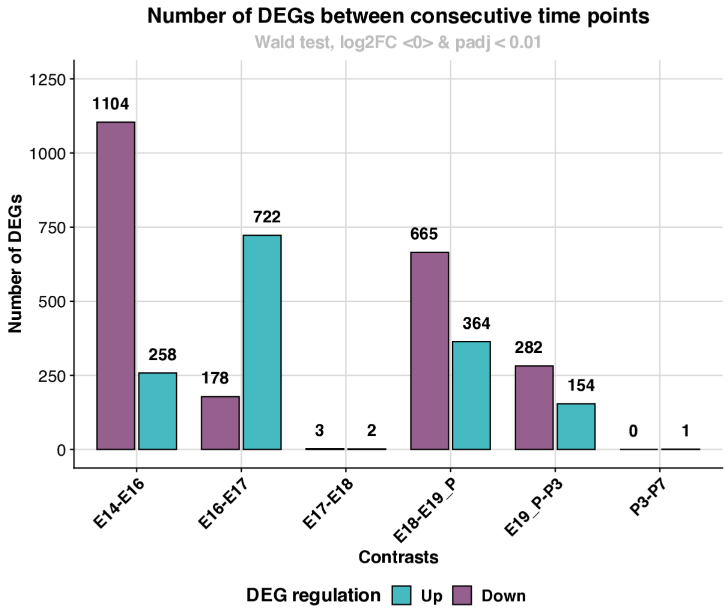

B

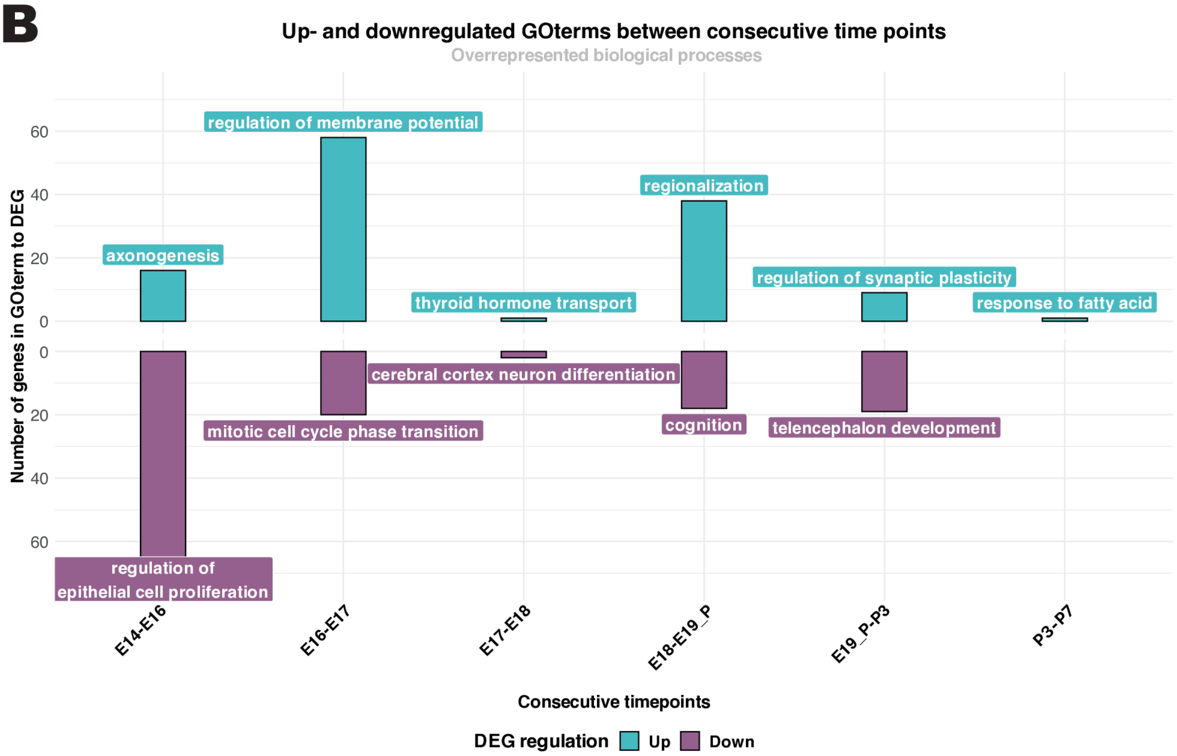

Figure 20: Consecutive analysis over the time course shows regulation of DEG at progenitor and birth stage of the special population

A. With a p.adj. of <0.01 and a log2 fold change below and above 0, most DEGs are found during the cell fate transition from a RGC to an IPC/early neuron at E14 to E16 and during birth at E19. Almost no DEG was found during migration and after P3 at this significance level.

B. One overrepresented GOterm among the first five top biological processes (GO) is shown between each of the respective consecutive time contrasts.

From E14 to E16, 1,104 genes were downregulated, while 258 genes were upregulated, thus encompassing the most prominent gene expression change compared with the other time points (Fig. 20A). “Regulation of epithelial cell proliferation” (GO:0050678) was downregulated, whereas upregulated genes were linked with “axonogenesis” (GO:0007409) (Fig. 20B, Suppl. Table 2).

From E16 to E17, most of the DEGs were upregulated, unlike all the other time points, where downregulations dominated. These 722 genes were enriched for “regulation of membrane potential” (GO:0042391). During these two developmental days, 178 genes accounting for “mitotic cell cycle phase transition” (GO:0044772) were downregulated (Fig. 20).

From E17 to E18, only *Ttr* and *S100a9* accounting for “thyroid hormone transport” (GO:0070327) were upregulated and *Tox, Cd209f,* and *Fezf2* were downregulated, which were related to “cerebral cortex neuron differentiation” (GO:0021895).

Then, from E18 to E19_P, 665 genes were repressed, mainly accounting for “regionalization” (GO:0003002). In contrast, 364 genes, which were associated with “cognition” (GO:0050890), were upregulated.

Between the postnatal time points P3 to P7, no DEGs on the here applied statistical threshold were found (Fig. 20).

Overall, the functional analysis of DEGs across consecutive timepoints indicated a cell fate transition based on the downregulation of genes linked with the progenitor stage and a highly specific upregulation of the unique neuronal transcriptomic landscape at the birth stage.

Multicomparison analysis of special population

Despite the high resolution of a DEG analysis between consecutive time points, it did not capture the dynamic changes this specific cell population underwent over time. Gene cluster analysis with likelihood-ratio tests, however, identified sets of genes with similar expression patterns that are thought to share a common functional role and were otherwise hidden in consecutive analyses.

Here, differential analysis using design = ~Age and a reduced ~1 model, revealed 10,234 DEGs over time from E14 to P7, of which 1,755 DEGs were divided into four clusters (Fig. 21; Suppl. Table 3).

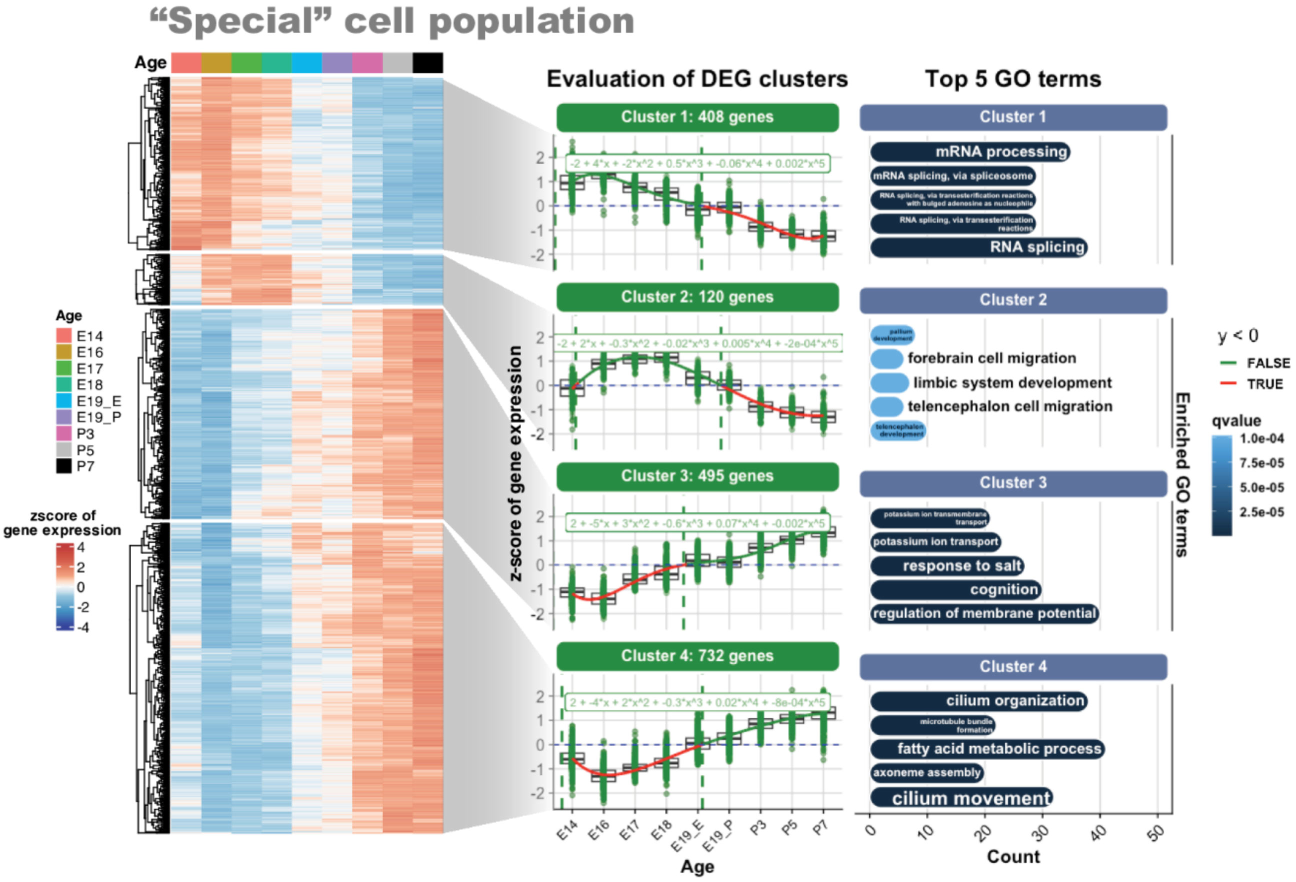

Figure 21: Cluster analysis on the pGlast1/pNeuroD1+ cell populations indicates four major gradual shifts during development

Considering only the pNeuroD1+ cell population, four clusters show gradual progression from a neuronal precursor cell (E14) towards a mature neuron (P7). Time course analysis with ~1 design identified 10,234 DEGs (after filtering: 1,755 DEGs) that passed the filters for differential analysis stated above. DEGs were derived from rlog-transformed count data with a smoothed line in red for the z-scores below average gene expression and in green for z-scores above average gene expression. The vertical dotted lines show the x-intercepts of the respective smoothed profiles, calculated by a fitted polynomial of fifth order to identify gene expression below or above average z-scores. The right adjacent plot shows the top five biological processes (GO) associated with these exact DEGs per cluster, with qvalues indicating the significance of enrichment and on the x-axis the amount of considered DEGs for this over-representation analysis.

Cluster 1 showed a downward trend from the progenitor state (E14-E16) to the mature state at P7, with gene expression falling below average in the postnatal stages. This cluster was enriched for functional GOterms such as ”mRNA processing” (GO:0006397, qvalue: 1.23E-13), and "RNA splicing" (GO:0008380, qvalue: 4.53E-17). The 408 genes belonging to this cluster were *Igf2bp1* and *Igf2bp2*, heterogeneous nuclear ribonucleoprotein genes such as *Hnrnpa1*, *Hnrnpc*, *Hnrnph1*, *Hnrnph3*, *Hnrnpl*, and *Hnrnpm*, RNA-binding protein genes such as *Rbm10*, *Rbm22*, *Rbm38*, *Rbm4*, *Rbm4b*, and *Rbmxl1*, and splicing factors such as *Sf3a1*, *Sf3b4*, *Snrnp40*, *Snrpa*, *Srpk1*, *Srrm4*, and *Srsf3* (Fig. 21).

Gene expression of the second cluster peaked during migration at E17 and then fell below average levels after birth. These 120 genes were primarily related to “telencephalon development” (GO:0021537, qvalue: 0.0001) and “forebrain cell migration” (GO:0021885, qvalue: 0.0001), such as *Bcl11a*, *Cdk5r1*, *Robo1*, *Fgfr1*, and *Unc5d*.

The gene expression profile of the third cluster had a saddle point at E19_E and otherwise increased steadily. The 495 genes belonging to this cluster were associated with “cognition” (GO:0050890, qvalue: 5.51E-10) and “regulation of membrane potential” (GO:0042391 qvalue: 1.37E-13). This cluster included, for example, the glutamate receptors *Grm5*, *Grm7* and the GABA receptors *Gabra1*, *Gabra4*, *Gabra5*, and *Gabrb1*, as well as solute carriers such as *Slc12a4*, *Slc13a5*, *Slc1a4*, *Slc1a6*, *Slc24a3,* and *Slc4a4*. In addition, *C1ql1* and *Cx3cl1* were among the genes associated with this cluster.

The fourth cluster showed a steady enhancement of gene expression. These 732 genes mainly associated with the biological functions “cilium organization” (GO:0044782, qvalue: 8.49E-10), “axoneme assembly” (GO:0035082, qvalue: 3.00E-10), and “fatty acid metabolic process” (GO:0006631, qvalue: 6.16E-10). These included many genes associated with cilia and flagella organisation, such as *Cfap126*, *Cfap161*, *Cfap43*, *Cfap44*, *Cfap45*, *Cfap54*, and *Cfap69*, but also dynein and axonemal assembly factors such as *Dnaaf3*, *Dnah12*, *Dnah2*, *Dnah5*, *Dnai1*, and again several genes belonging to the solute carrier family (Fig. 21).

Overall, pNeuroD1+ ULNs critically regulated RNA splicing, cell migration, neurotransmitters, and cilium organisation during their genesis.

What genes were co-expressed between the pNeuroD1+ and pCAG+ populations?

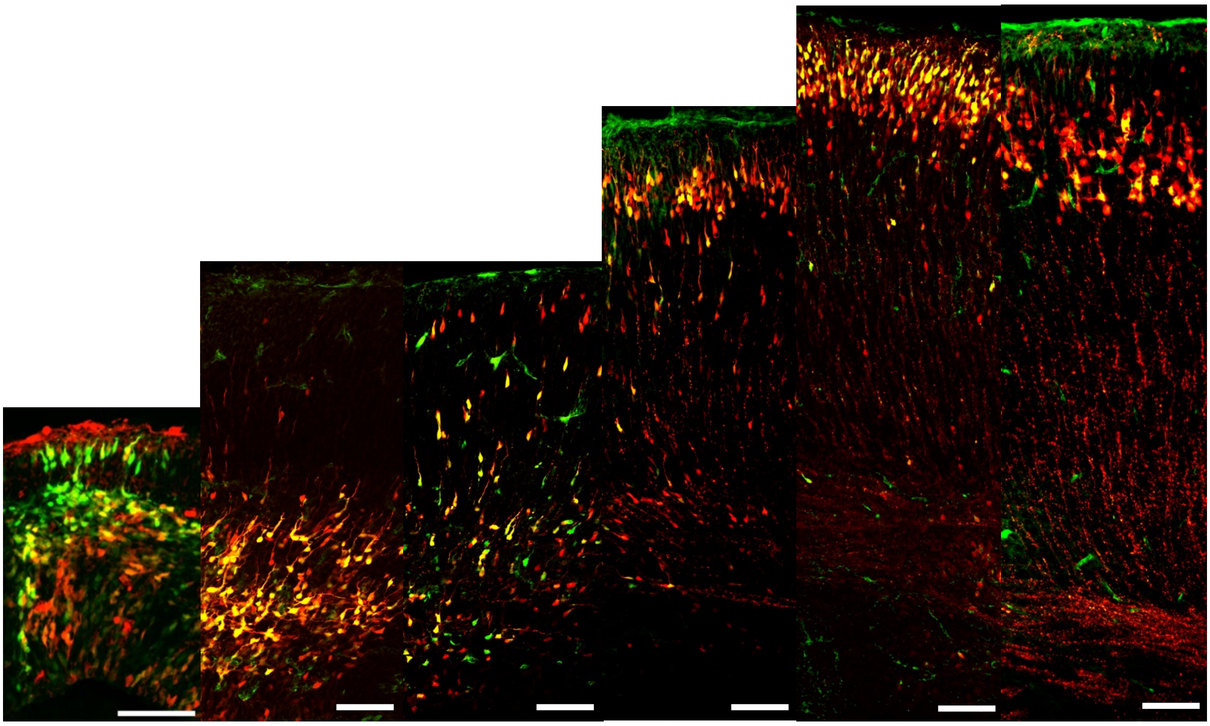

In this study, four cortical cell populations were flow cytometrically sorted; two used developmentally active promoters, and the other two used the ubiquitously expressed promoter pCAG (“ctrl” population). The so-called “special” population included the two fluorophore-labelled cell populations driven by an RGC-specific promoter (pGlast1+, E12 to E14) and a promoter specific for early post-mitotic neurons (pNeuroD1+, E14 to E16-P7).

The gradual progression of common biological functions between the sorted cell populations could be derived when including the pCAG+ population using the design ~Population+Age and a reduced ~Population model. As a result, neuron-specific functions associated with both “ctrl” and “special” populations were revealed, which were defined by the usage of the NeuroD1 promoter as a “pure” and of the CAG promoter as a partial representative identity of upper layer neurons.

Over the measured period of neurogenesis, 13,314 genes were differentially regulated in both the pGlast1/pNeuroD1+ and pCAG+ cell populations (Suppl. Table 4). When considering statistical thresholds of p.adj.<0.01 and minc=50 for the top 1,824 DE genes, the gene profiles during the developmental course were divided into six clusters (Fig. 22), which resembled those in the analysis focused on the “special” population above (Fig. 21).

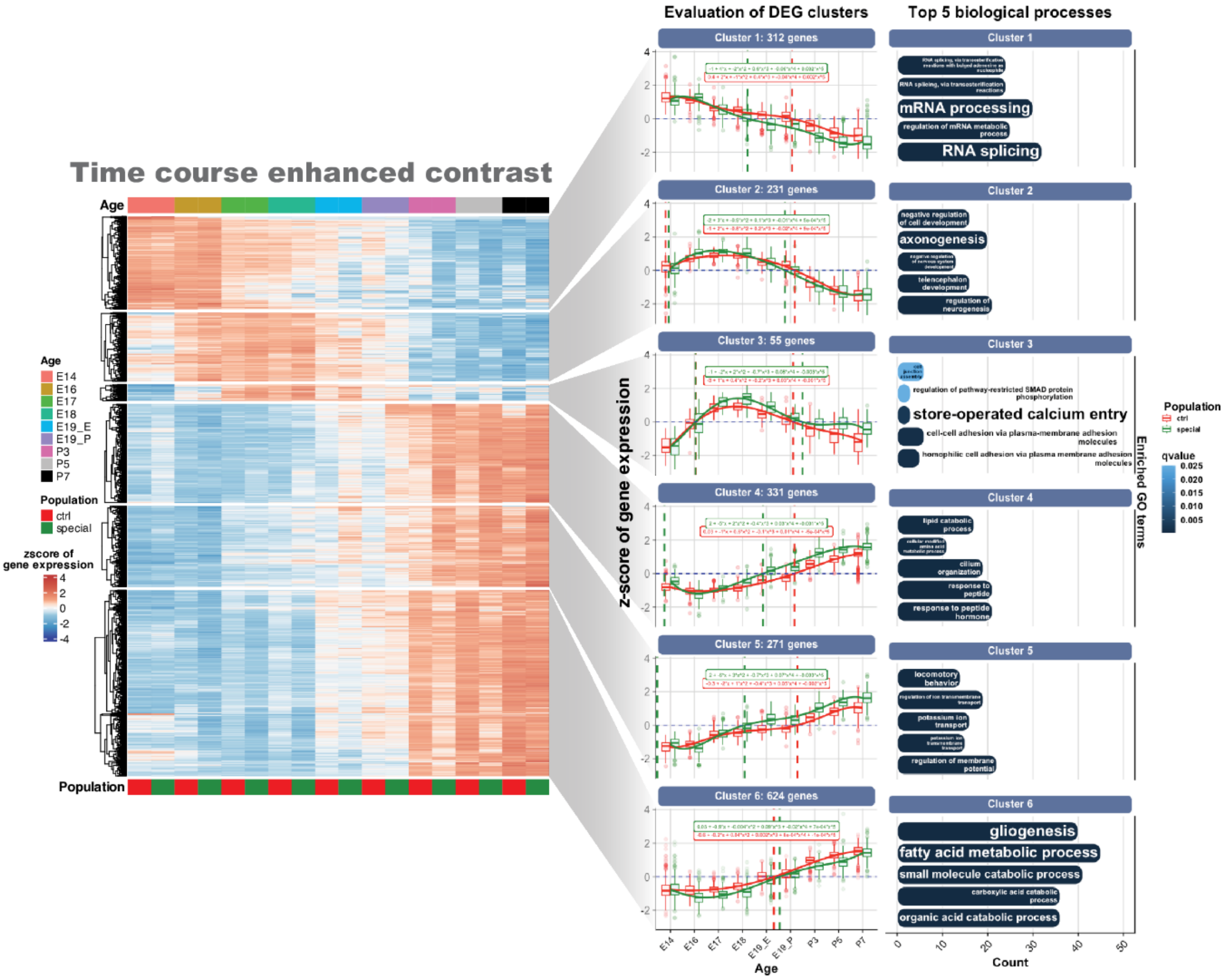

Figure 22: Evaluation of the six DEG clusters that are similarly expressed by both cell populations over the time course from E14 to P7

The panel shows the six scaled clusters with top five biological processes (GO) displayed next to them. Transcriptomic data were focused on 1,824 DEGs (LRT with ~Population+Age design and reduced Population model, p.adj.< 0.01, n = 2,000, minc = 50). DEGs were derived from rlog-transformed count data with a smoothed line in red for the "ctrl" population and in green for the "special" population. The vertical dotted lines show the x-intercepts of the respective smoothed profiles, calculated by a fitted polynomial of fifth order to identify gene expression below or above average z-scores (Suppl. Table 4). The right adjacent plot shows the top five biological processes (GO) associated with these exact DEGs per cluster, with qvalues indicating the significance of enrichment and on the x-axis the amount of considered DEGs for this over-representation analysis.

Cluster 1 comprised 312 genes that started at high expression levels and were down-regulated in a monotonic coordinated manner from E14 to P7, falling below average at E18 (see Fig. 22). Both populations ("special" vs. "ctrl") had similar expression profiles. These genes were enriched for "RNA splicing" (GO:0008380, qvalue: 4.07E-15) and "mRNA processing" (GO:0006397, qvalue: 1.35E-12) (Suppl. Table 4). These genes included, for example, members of miRISC CCR4–NOT complex (*Cnot3*, *Cnot8*), many splicing repressors (*Hnrnpa1*, *Hnrnpc*, *Hnrnph1*, *Hnrnph3*, *Hspa8*), spliceosome factors (*Sf3a2*), and several RNA-binding motif proteins (**RBM**s; *Rbm10*, *Rbm38*, *Rbm4*, *Rbm4b*, *Rbmxl1*), which control the transcription of neuronal pre-mRNA transcripts.

The second cluster, with a total of 231 genes, peaked at E17 and then steadily declined after migration until gene expression was below average. The top genes of this cluster included e.g. *Robo1*, *Neurod6*, *Tuba1a*, *Fgfr1*, *Cux1* and *2*, which were significantly enriched for the GOterm "axonogenesis" (GO:0007409, qvalue: 8.57E-07) and “regulation of neurogenesis” (GO:0050767, qvalue: 2.76E-07). This cluster was co-expressed with genes responsible for "dendrite development" (GO:0016358, qvalue: 8.16E-06), which functionally overlaps with early axon formation to promote neuronal polarisation.

The third cluster had a global peak at E18 with 55 DEGs with the lowest significance among the derived clusters that were related to “cell junction assembly” (GO:0034329, qvalue: 0.025) and “store-operated calcium entry” (GO:0002115, qvalue: 0.00268254) (Suppl. Table 4). This cluster included genes such as *Clstn2*, *Cdh12*, and *Cdh10*, all important mediators of migration and axonal outgrowth [410].

The gene expression of the fourth cluster with a total of 331 DEGs was constantly upregulated, rising above average expression levels around birth. Genes that belong to the cluster 4 such as *Camk2a*, *Cav2*, *Igf2*, and *Rhoq* were associated with the GOterms “cilium organization” (GO:0044782, qvalue: 0.000120059) and “response to peptide hormone” (GO:0043434, qvalue: 5.86E-06).

In cluster 5, the gene expression of the 271 DEGs rose, but with an inflection point around the birth stage. These genes accounted for “regulation of membrane potential” (GO:0042391, qvalue: 6.28E-07) and “locomotory behavior” (GO:0007626, qvalue: 7.85E-05). Among them, *Fgf12* and many GABA receptors (*Gabrb1*, *Gabrg3*, *Gabra5*) that also play an integral role not only to establish membrane potential, but also during neuronal migration [411],[29], and metabotropic glutamate receptors such as *Grm5* and *Egr1* as an immediate early gene [412] were differentially expressed.

The last cluster comprised 624 DEGs that were enriched for the GOterms "gliogenesis" (GO:0042063, qvalue: 9.68E-15), “small molecule catabolic process” (GO:0044282, qvalue: 2.60E-16) and "ensheathment of neurons" (GO:0007272, qvalue: 2.18E-12) (Suppl. Table 4). In this cluster, the gene expression increased with crossing average gene expression levels at birth. pCAG+ samples had a higher gene expression level than the pNeuroD1+ samples (Fig. 22). Genes belonging to this cluster encompassed e.g. *Gpr37l1*, *Olig1*, *Gfap*, *Egfr*, *Bcas1*, and *Hes5*, examples of genes that were top loadings for the PC2 axis in the PCA (Fig. 13A).

How did the pNeuroD1+ population differ from the pCAG+ cell population?

In this study, the investigated cell populations had different cell identities. The "control" population was labelled with a non-specific marker protein (Venus+ and tDimer+) driven by the ubiquitous promoter pCAG. Hence, cells electroporated at the respective time point potentially included different cell types, such as projection neurons, as well as non-neuronal cells such as microglia, macroglia, astrocytes, and oligodendrocytes. However, the pCAG-tDimer+ population colocalised with the pNeuroD1+ cells in layer II/III, which were all Satb2+ at E18 (Fig. 12). In contrast to the pCAG+ population, the subpopulation referred to here as "special" was identified by the expression of eGFP driven by the developmentally active NeuroD1 promoter and was found to target only post-mitotic projection neurons.

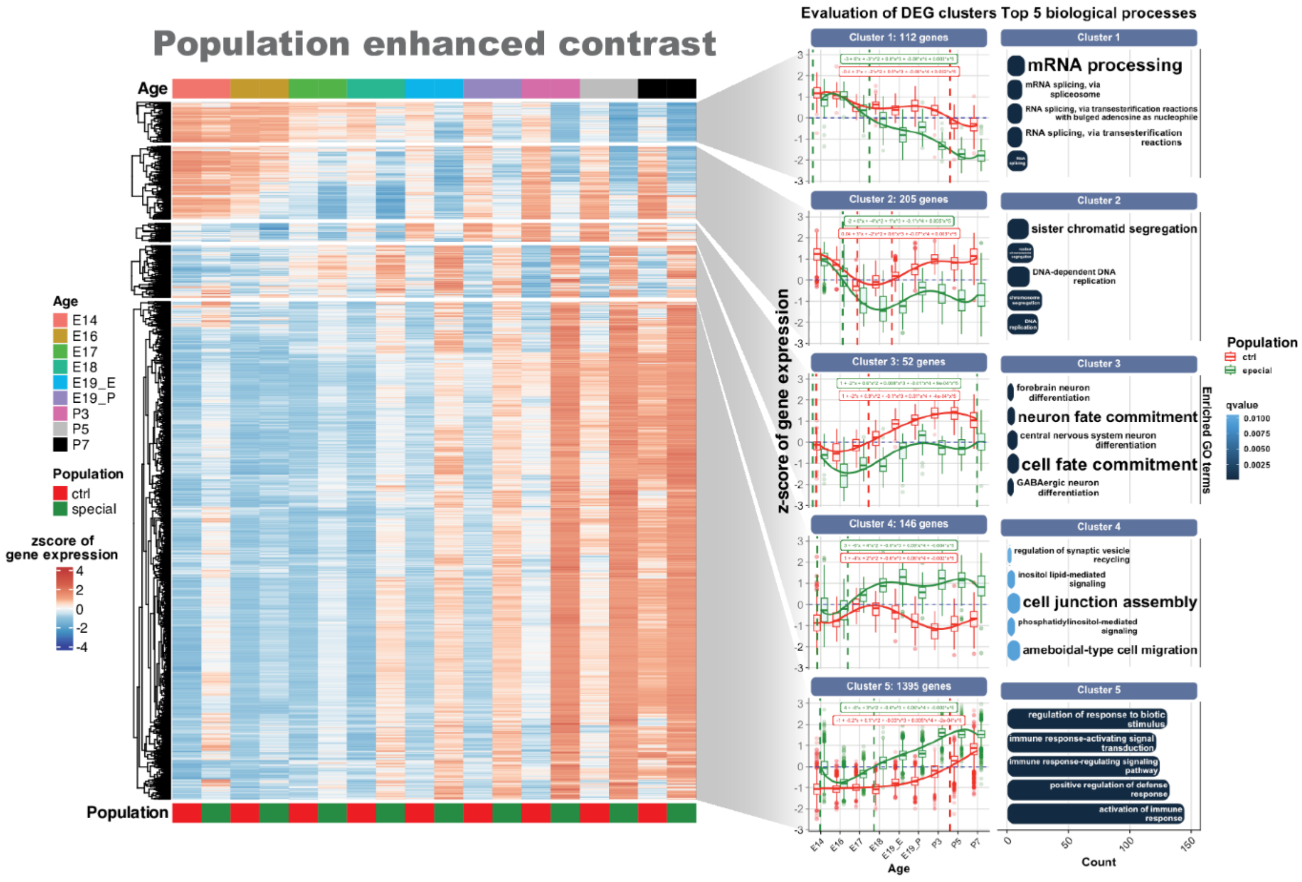

Figure 23: Evaluation of the five DEG clusters that highlight differences between "ctrl" and "special" cell populations over the time course from E14 to P7

The panel shows the five scaled clusters with top five biological processes (GO) displayed next to them. The fifth cluster showed that the most DEGs between the control ("ctrl") and "special" cell populations were associated with the GOterm "activation of immune response" (GO:0002253) over time. DEGs were derived from rlog-transformed count data with a red smoothed line for the "ctrl" samples and the green counterpart for the "special" cell population. LRT analysis with Age+Population model and reduced ~Age design from E14 to P7 with p.adj.<0.01, n=2,000, and minc=50, resulting in 1,910 DEGs as input. The vertical dotted lines show the x-intercepts of the respective smoothed profiles, calculated by a fitted polynomial of fifth order to identify gene expression below or above average values. The right adjacent plot shows the top five biological processes (GO) associated with these exact DEGs per cluster, with qvalues indicating the significance of enrichment and the amount of considered DEGs for this over-representation analysis.

To highlight the differently expressed genes between these special populations, an LRT design was again employed, using the design = ~Age+Population with a reduced ~Age parameter. This DEG analysis revealed the presence of 5,467 DEGs between E14 and P7 samples at a p.adj. level of <0.01. 1,910 DEGs were subsequently grouped into five clusters (Fig. 23; Suppl. Table 5).

In cluster 1, gene expression from E17 decreased with age in both cell populations (Fig. 23). Still, this trend was more pronounced in the pNeuroD1 samples, which started with high expression and strongly downregulated their gene expression thereafter. In contrast, the pCAG samples showed average gene expression at postnatal time points. This cluster comprised 112 genes that were enriched for the GO terms "RNA splicing" (GO:0008380, qvalue: 2.55E-10) and "mRNA processing" (GO:0006397, qvalue: 3.85E-08). Among these genes are RNA-binding proteins (*Rbm4* [413], *Rbm4b*, *Rbmx*, *Rbmxl1*, *Nono* [414]), ribonucleoproteins (*Rnps1*, *Snrnp40*), splicing repressors (*Hnrnpa1*, *Hnrnpc*, *Hnrnpk*), and spliceosome factors (*Puf60*, *Smu1*) (Fig. 23).

Starting from a high expression level at the progenitor stage, the expression level of cluster 2 gradually decreased to a low expression level in the pNeuroD1 samples. At the same time, the pCAG population showed high expression at almost every time point, especially after E18. These 205 genes were enriched for the GOterms "nuclear division" (GO:0000280, qvalue: 2.22E-11) and "DNA replication" (GO:0006260, qvalue: 4.05E-19). Among them are cell cycle-dependent factors such as Cdk-activating factor *Cdc45* [415], Cdk-inhibitors (*Cdkn2d*), cyclins (*Ccnb1*), DNA polymerases (*Pold2*, *Pole3*), spindle positioning factor *Fam83d* [416], replication factors (*Rfc3*, *Rfc4*, *Rfc5*), DNA primases (*Prim1*, *Prim2*), and the mitotic marker protein *Pcna* [417]. A broader look through a panel analysis of cell cycle-related genes (Suppl. Fig. 18) showed that members of the BAF complex (Smarc family genes) as well as *Ezh2* were negatively regulated.

In cluster 3, both cell populations exhibited similar low expression levels at the progenitor stage, but from E18 onwards, the tDimer samples showed an enrichment in "GABAergic neuron differentiation" (GO:0097154, qvalue: 5.83E-10), “cell fate commitment” (GO:0045165, qvalue: 1.76E-08), and “forebrain neuron differentiation” (GO:0021879, qvalue: 4.74E-08). This gene cluster comprised 52 genes, which mediate the transition of progenitor cells to either an excitatory neurogenic or a glial fate, such as *Gsx2* [418], *Dlx1* and *Dlx2* [143], and *Wnt7a*, as well as *Sox1*, *Sox2*, *Sox9*, and *Pou3f4* [419] redefining frontal cortex identity [420].

In the fourth cluster, gene expression was steadily upregulated above average from E16 onwards for the pNeuroD1+ population, whereas the gene expression of the tDimer population was always below average. This cluster had not a stringent significance as the other clusters and comprised 146 DEGs that accounted for GOterms such as “ameboidal-type cell migration” (GO:0001667, qvalue: 0.009), “cell junction assembly” (GO:0034329, qvalue: 0.009), and “regulation of Notch signaling pathway” (GO:0008593, qvalue: 0.015). Among them, *Tgfbr1* and *Sema4d* were differentially expressed, as well as bassoon (*Bsn*) and piccolo (*Pclo*) genes that bind presynaptic vesicles preferentially in electrophysiologically active zones [421,422].

The largest cluster 5 of a total of 1,395 genes also had the most significant expression values in the pNeuroD1+ cell population from E18 onwards compared to the pCAG+ population (Fig. 23). While this trend appeared already at E14, it disappeared in the samples from E16 and E17. Genes accounting for this cluster were enriched for “activation of immune response” (GO:0002253, qvalue: 8.82E-75), "positive regulation of defense response" (GO:0031349, qvalue: 3.33E-67), and “leukocyte mediated immunity” (GO:0002443, qvalue: 7.68E-56). The gene cluster included several members of the complement system (*C1qa*, *C1qb*, *C1qc*), the colony-stimulating factor (CSF) family, the NLR (NOD-like receptor) family, the Toll-like receptor (TLR) family, the TRIM-protein family, and the tumour necrosis factor receptor (TNFR) superfamily, as well as several chemotactic cytokines and clusters of differentiation receptors. Collectively, these genes target the activation or recruitment of inflammasomes, leading to the release of proinflammatory cytokines and chemokines. These genes, including members of the CD family (*Cd300a*, *Cd300lf*, *Cd79b*), inflammasome components (*Nlrp1a*, *Nlrp1b*, *Nlrp3*), GTPases (*Igtp*, *Irgm2*), *Arrb2*, *Dhx58*, *Dusp3*, *Havcr2*, *Ifi35*, *Irf1*, *Lcp2*, *Myo1g*, *Naglu*, and *Scimp,* have an enriched region on the mm10 genome on chromosome 11 (Suppl. Fig. 9).

Birth triggered maturation of upper-layer neurons

At E19, gestation is completed in mice, and the birth process is initiated. Significant transcriptomic restructuring occurred during this process, which was evident, for example, in the exploratory data analysis. The PCA showed a clear difference between prenatal and postnatal samples in figure parts 13A and C, with a prevalence for pNeuroD1+ samples responsible for the difference. Remarkably, birth triggered the second most frequent change in the consecutive analysis (Fig. 20). Furthermore, most of the clusters derived by the multivariate analysis DEG also had their switching points from above- to below-average gene expression or *vice versa* around birth (Fig. 21). In particular, when E19 samples were pooled, a large scatter occurred in the otherwise coordinated transcriptomic landscape (Suppl. Fig. 14), which could be resolved when *ex* and *in utero* samples were handled separately. For further transcriptomic analyses, the harvest mode was compared between E19_E (*in utero*) and E19_P (*ex utero*) samples as independent samples like a new time point (Suppl. Table 7). Aliquots of the pooled E19 timepoint were still measured by RNA-seq and validated by RT-PCR (see section "**RT-PCR correlated with RNA-seq counts"**).

Within the **E19** group itself, the expression of the serine/threonine-protein kinase TAO2 (*Taok2* with p-value of 0.001) was upregulated in the *in utero* samples. In contrast, centrosomal protein 63 (*Cep63* also with p-value of 0.001) was upregulated in the *ex utero* samples (Fig. 24A).

From E18 to **E19_E**, with a p.adj.<0.01, 666 genes were upregulated (lFC > 0) mainly related to "extracellular matrix organization" (GO:0030198, qvalue: 8.15E-16) and "regulation of membrane potential" (GO:0042391, qvalue: 5.50E-08) (Fig. 24C).

In comparison, greater differences were detectable from E18 to E19_P with a total of 1,505 upregulated genes. In the latter group, many genes related to "gliogenesis" (GO:0042063, qvalue: 6.87E-23), "cilium organisation" (GO:0044782, qvalue: 5.30E-19), and "canonical Wnt signaling pathway" (GO:0060070, qvalue: 8.53E-17) were upregulated (Fig. 24C).

From E18 to **P7**, with a p.adj.<0.01, 5,855 genes were differentially expressed, 2,022 were upregulated *in utero* (lFC > 0), and 3,833 were upregulated *ex utero*. Again, genes highly specific for central nervous system development such as "axonogenesis" (GO:0007409, qvalue: 1.19E-33), "regulation of synapse organisation" (GO:0050807, qvalue: 6.16E-19), and "methylation" (GO:0032259, qvalue: 7.26E-11) were upregulated before birth, while the "response to oxidative stress" (GO:0006979, qvalue: 6.21E-13) and "cilium movement" (GO:0003341, qvalue: 2.75E-17; GOBP_CILIUM_MOVEMENT, NES: 1.85) were enriched after birth (Fig. 24B, C). However, GOBP_MONOCYTE_CHEMOTAXIS (NES: 1.965) was the most upregulated gene set in postnatal samples (Fig. 24B, D; Suppl. Table 7).

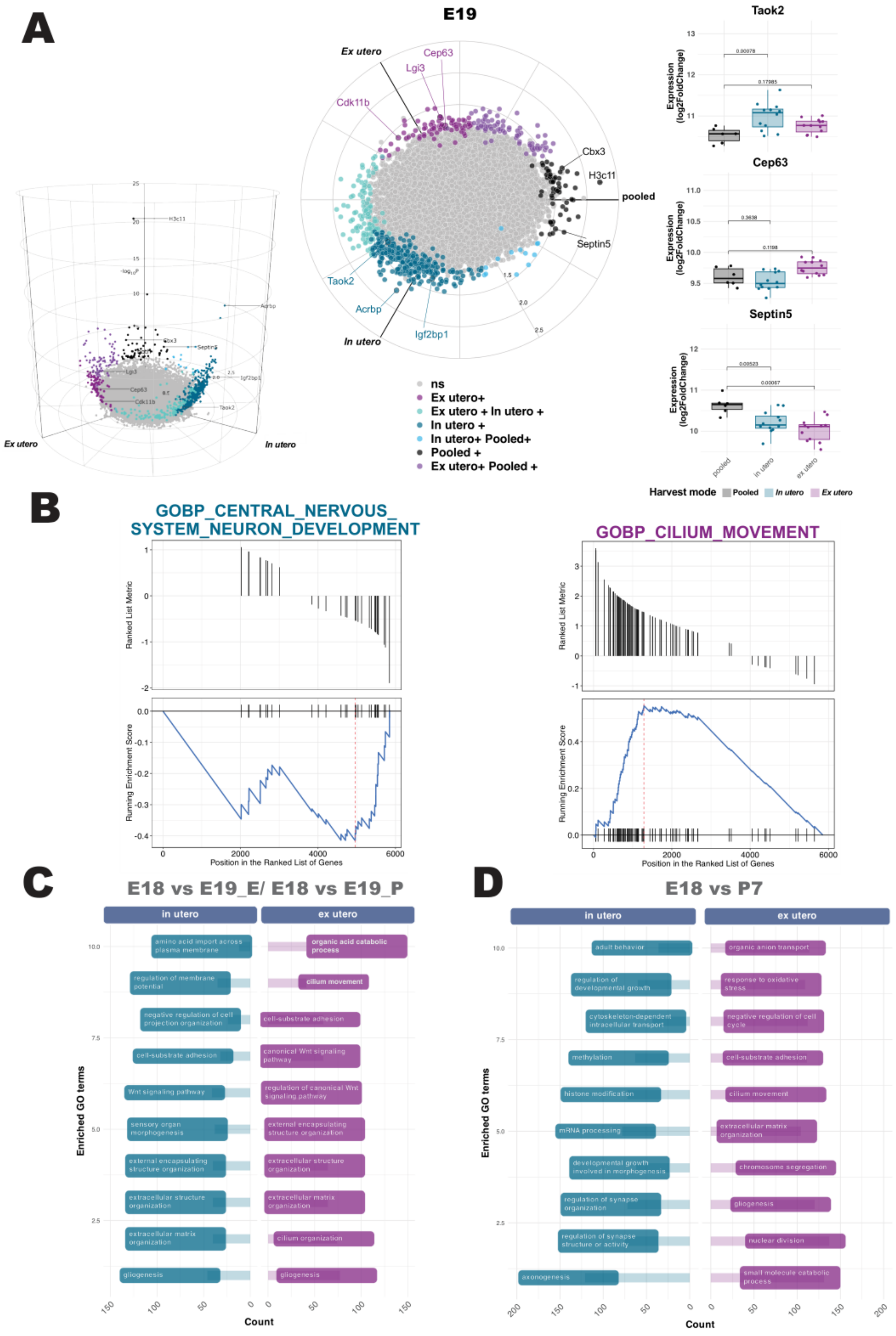

Caption continued on next page

Figure 24: Direct comparison of biological functions of DEGs between in utero versus ex utero samples

A. 3D Volcano plot of DEGs for the three intra-E19 conditions: *In utero*, *ex utero*, and pooled samples of the E19 time point, not split for cell population differences. The plot shows log2 fold changes in gene expression (x-axis) versus negative log10 p-values (y-axis). The magenta points represent upregulated genes in *ex utero* samples compared with the other groups, the blue points represent upregulated genes in *in utero* samples, the black points represent the upregulated genes in the pooled condition, and the grey points represent non-significant genes. Right panel: Representative genes for each of the mentioned conditons. Expression of the serine/threonine protein kinase *Taok2* was enriched in the prenatal samples, expression of the centrosomal protein of 63 kDa *Cep63* was enriched in the postnatal samples, while expression of the nucleotide binding protein *Septin5* was enriched in the pooled condition with a p-value cut-off of <0.05.

B. GSEA of representative enriched gene sets in *in utero* and *ex utero* conditions with E18 versus P7 contrast, with p.adj. cut-off <0.01.

   In utero: Gene set of GOBP_CENTRAL_NERVOUS_SYSTEM_NEURON_DEVELOPMENT (NES: -2.305) enriched, consisting of genes such as semaphorin 3A (*Sema3a*), forebrain embryonic zinc finger 2 (*Fezf2*), microtubule-associated protein tau (*Mapt*), and ephrin type-A receptor 4 (*Epha4*).

   Ex utero: Gene set of GOBP_CILIUM_MOVEMENT (NES: 1.850) enriched, encompassing genes such as cilia and flagella associated protein 65 (*Cfap65*), tektin-3 (*Tekt3*), and dynein axonemal intermediate chain 1 (*Dnai1*).

C. “Extracellular matrix organisation” and “Notch signalling pathway” were downregulated after birth, whilst “cilium organisation” and “microtubule-based movement” were upregulated. E19_E and E19_P samples in comparison with the E18 time point. Wald statistics with ~ Age, p.adj. cut-off <0.01.

D. Genes associated with “axonogenesis”, “histone modification”, and “regulation of synapse organization” were downregulated after birth, while genes responsible for “cilium movement” and “chromosome segregation” were upregulated upon birth. Right panel: E19_E versus all postnatal samples (P3-P7). Wald statistics with ~ Harvest mode design, p.adj. cut-off <0.01.

   For both C and D: Biological functions derived from clusterProfiler::enrichGO(OrgDb = org.Mm.eg.db, ont = "BP", pAdjustMethod = "BH", qvalueCut-off = 0.05). Removed redundant GOterms with clusterProfiler::simplify (cut-off=0.5, by="p.adjust", select_fun=min). Top 10 enriched GO terms shown.

Proteome analyses

Validation and characterisation of proteomic samples

The data set was generally clustered into treated and untreated samples (Fig. 25), so that the untreated samples were analysed separately from the treated samples. The untreated samples were further clustered by age, with E16-E18 samples clustering together and E14, as well as E19-P7 samples forming another cluster (Fig. 25, 27A). PolyI:C treated samples generally cluster away from the naïve and PBS treated samples (Fig. 25, 40A).

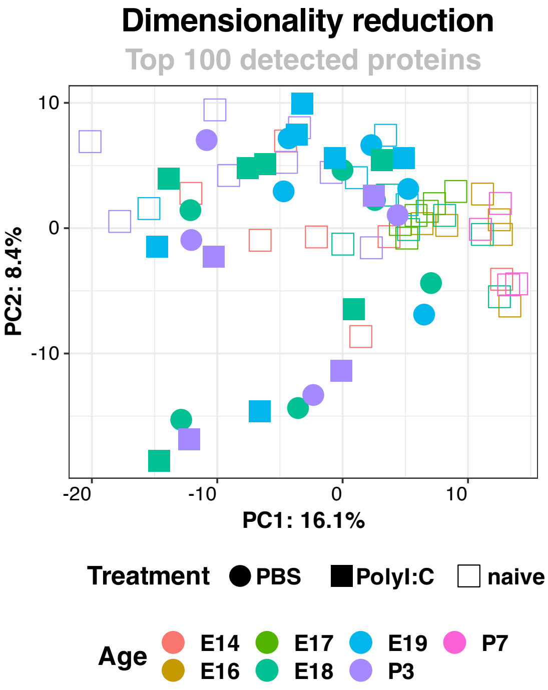

Figure 25: Treatment and age are the main contributors to differentiate the proteomic data set

The differences in the proteome dataset are treatment and age dependent. The treated samples and in general time points E18, E19, and P3 are clustered separately from the other samples. PC1 and PC2 together account for 24.5% of the difference when considering the top 100 varying proteins.

The non-significant proteins ([!significant]) in the entire data set, often referred to as "housekeeping" proteins, provided information not only about the basic biological functions of the cell populations studied, but also about cell identity. Here, 2,507 proteins were entered into the mapping, of which 467 were associated with thirteen main biological processes (GO; Fig. 26). These showed an overall neuronal character with dominant neuronal biological processes such as "regulation of axonogenesis" (GO:0050770), "neurogenesis" (GO:0022008) and "dendrite development" (GO:0016358) (Suppl. Table 10). A relatively large group of proteins was related to RNA splicing and translational regulation, while the smallest group here was related to signalling and the response to growth factors and hormones.

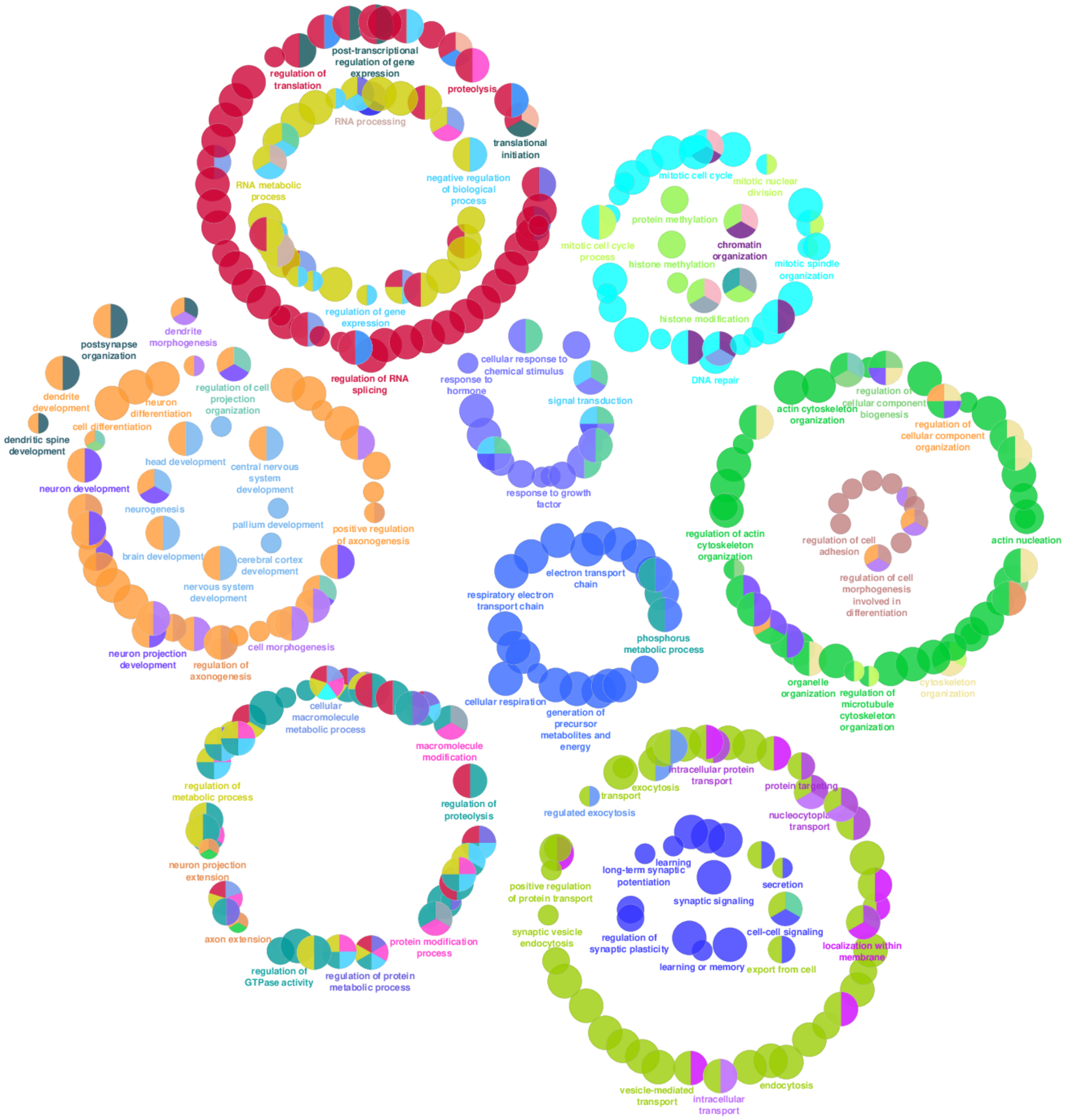

Figure 26: The proteomic landscape of all input samples has neuronal character

The Cytoscape::ClueGO network of the stably detected protein set associated with biological processes (GO) has a neuronal character (Suppl. Table 10). Protein input from both untreated cell populations (“ctrl” and “special”). Medium network specificity and connectivity (score: 0.4) with GO Term Fusion and at least five genes per cluster. Only GOterms with p-value <0.05 and GO Trees between the third and fifth level are shown.

Differential proteome analysis

Age-correlating differences

The largest component of variation in the proteomic data set was associated with age (Fig. 25). A closer look at the age-correlated differences in the untreated dataset revealed trends that shift at the birth stage.

The age-related contrast at a p-value<0.1 resulted in 258 differentially detected proteins (Suppl. Table 9). The E16, E17, and E18 samples showed similarities, and the postnatal samples (P3, P7) clustered together, while the E14 samples were additionally different from the other clusters. At the same time, samples from the “special” cell population clustered away from the “ctrl” population in E14 and the postnatal samples (Fig. 27A).

The number of DEPs peaked at birth and shifted with age from predominantly up-regulated to predominantly down-regulated DEPs (Fig. 27B).

Overall, among the 258 DEPs, the proteins were associated with biological processes (Fig. 28A; Suppl. Table 9, 11), such as “response to stress” (GO:0006950), “neurogenesis” (GO:0022008), “cell cycle” (GO:0007049), “RNA splicing” (GO:0008380), “neuron projection development” (GO:0031175), and “regulation of synapse organisation” (GO:0050807). “Transport” processes (GO:0006810) dominated the enrichment analysis. Localisations of proteins to the nucleus (GO:0034504) were downregulated over time, while membrane localisations (GO:0090150) and protein localisations to the ER (GO:0072599) were increasingly enabled (Fig. 28B).

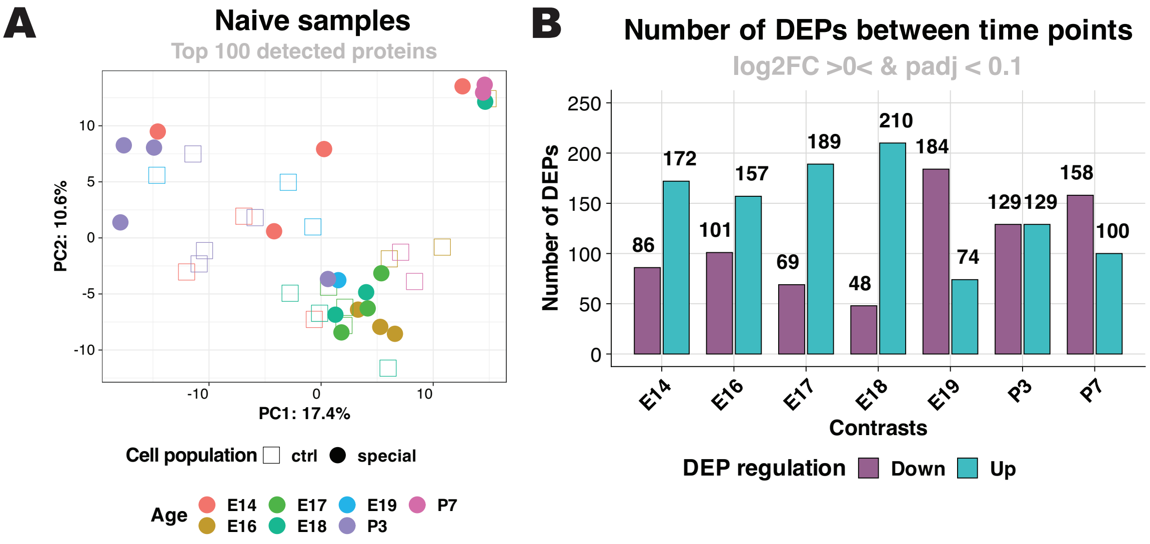

Figure 27: The postnatal proteome is most different from the progenitor stage

With the chosen log2 fold change cut-off of below and above 0 and a p-value cut-off <0.1, a total of 258 DEPs were detected.

A. PCA of the naïve proteomic landscape shows a cluster of E16 and E17 progenitor samples, while all other samples are more widely dispersed in a fan-like shape. Samples from the “special” cell population clustered away from the “control” population, in particular in those of E14 and the postnatal time points. PC1 and PC2 together account for 28% of the total variance.

B. The number of differentially detected proteins initially shows an upward trend towards birth, and thereafter more proteins are downregulated than upregulated. Consecutive differential analysis of the untreated proteomics dataset was performed.

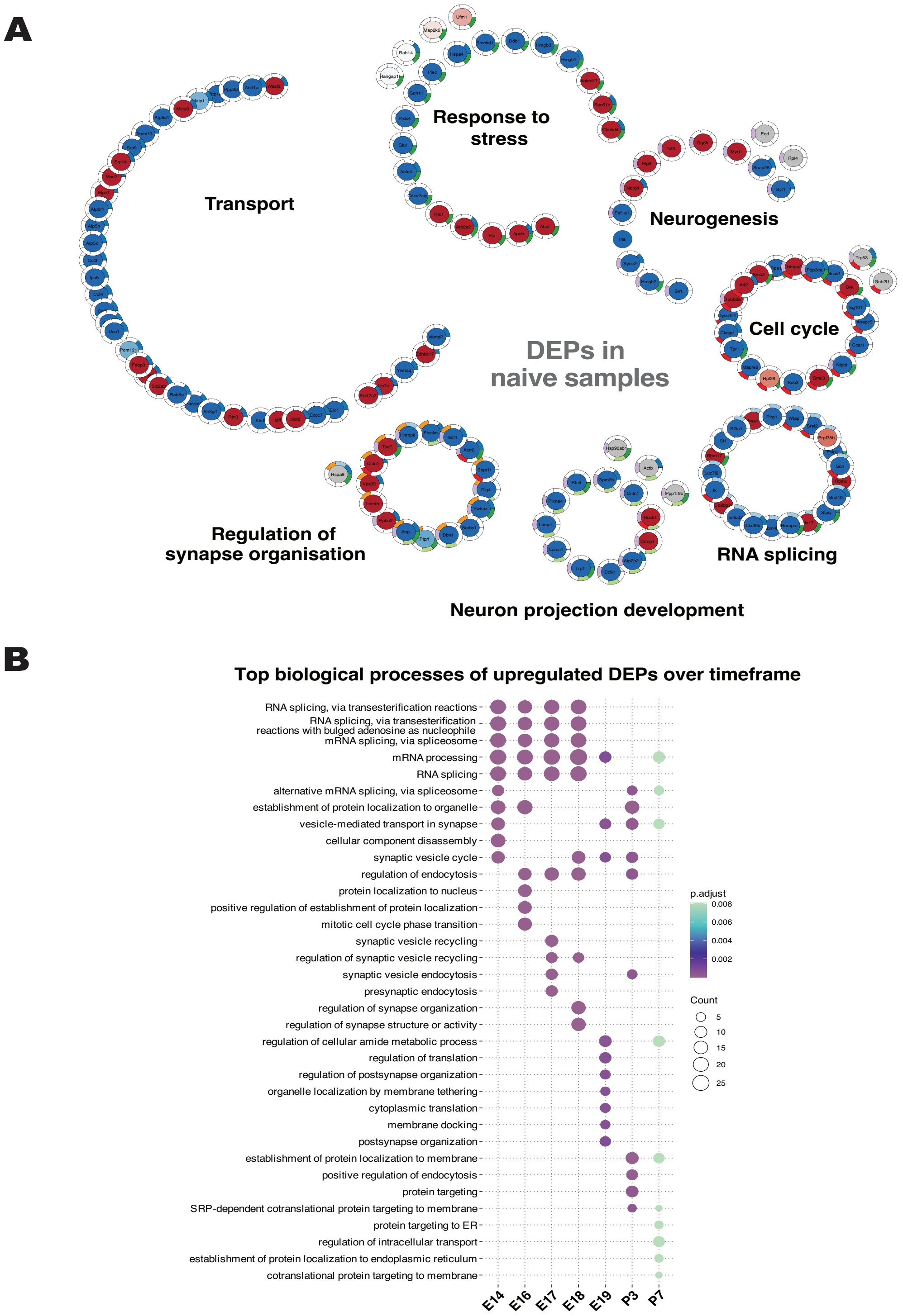

Figure 28: Overview of the biological processes (GO) of the DEPs over time

A. The proteins most different between E14 and P7 are shown as dots in circles connected to the respective GOterm derived from STRING analyses (Suppl. Table 11). Smaller circles have a continuously lower protein number and are mostly part of the next larger circle. The network represents 149 DEP, represented by nodes filled with P7-centred enrichment (blue gradient = negative ratio, red = positive ratio); nodes without GO annotation (123 DEPs) have been removed from the representation.

B. Postnatally, RNA splicing is downregulated, while translation is upregulated at synapses. GO annotation reveals biological functions of DEPs from E14 to P7 time points. Analogous to the RNA-seq dataset, “RNA splicing”, “postsynapse organization”, and “mitotic cell phase transition” are responsible for significant changes in the upper-layer neuronal proteome. The top ten GOterms were derived with clusterProfiler::compareCluster with the parameters “BP”, “BH”, and qvalue = 1.

Cell population-related differences

At a moderate alpha of 0.5, 45 possibly biologically relevant DEPs were detected between the “control”/pCAG+ and the “special”/pGlast1/pNeuroD1+ cell population (Fig. 29A; Suppl. Table 9). The associated biological processes (GO) were predominantly attributed to synaptic processes in both cell populations (Fig. 29B).

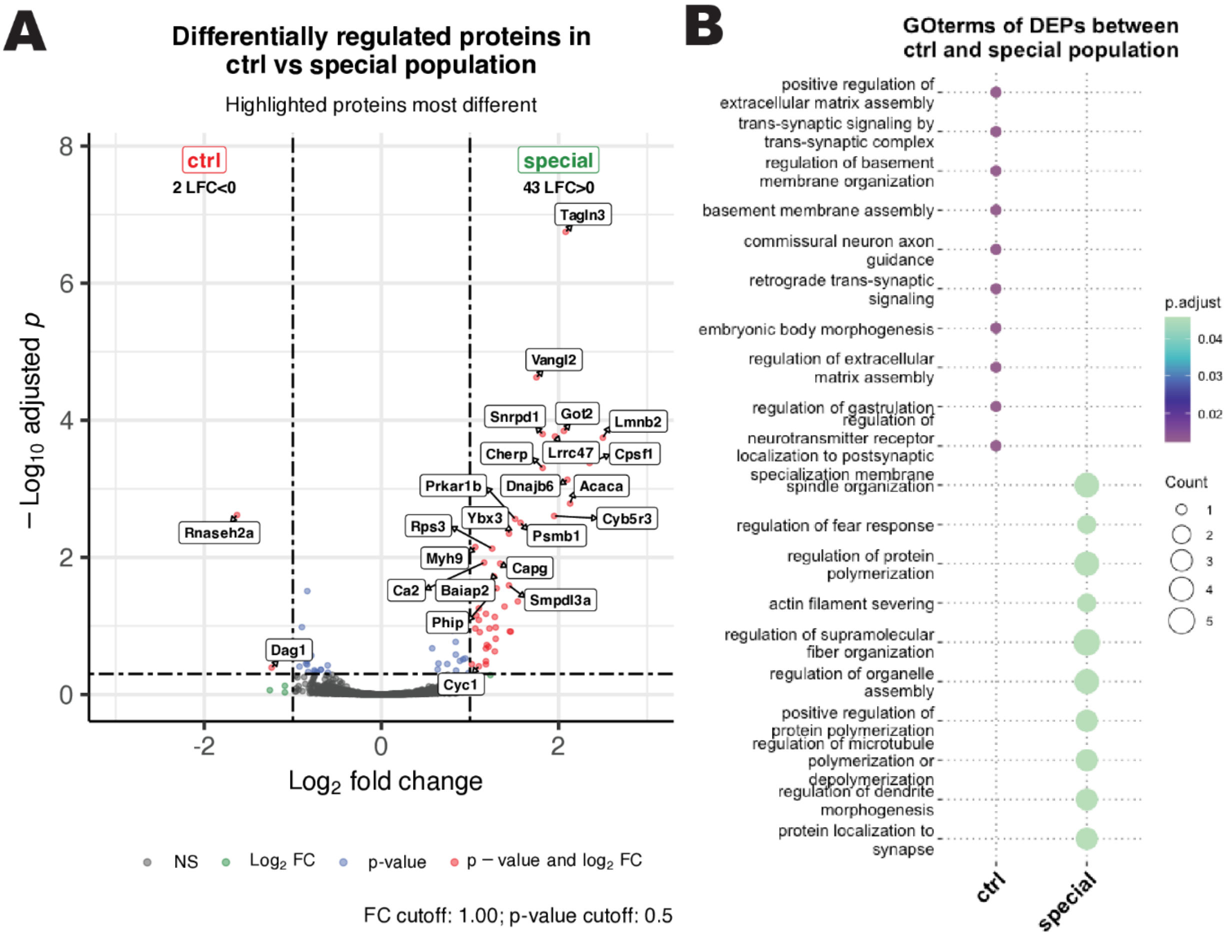

Figure 29: Sparse differences between the pCAG+ and the pGlast1/pNeuroD1+ cell populations are related to synaptic processes

A. The volcano plot compares protein detection between the “ctrl” and “special” populations. The highlighted proteins in the volcano plot represent DEPs with a p-value cut-off of 0.5. More proteins are associated with the special population.

B. The biological functions (GO) of the different proteins between the “ctrl” and “special” populations mostly relate to synaptic processes. “Spindle organisation” (GO:0007051) and “regulation of microtubule polymerization or depolymerisation” (GO:0031109) were specific for the “special” cell population.

Integration of transcriptomic with proteomic data

Here, the resolution of protein abundance was subject to the detection limit of LFQ mass spectrometry. After filtering out duplicate gene symbols and NAs, 4,295 proteins remained for alignment with the RNA-seq data. Among them, 4,147 detected proteins matched mRNA transcripts detected by RNA-seq. Twelve samples, mostly pCAG+ samples, present in the proteomics dataset were not present in the RNA-seq dataset (P7_c_2, P7_pNeuroD_2, E18_MIA_PBS_c_3, E19_MIA_PBS_Embryo_c_1, E19_MIA_PBS_Embryo_c_2, P3_MIA_PBS_c_1, P3_MIA_PBS_c_2, P3_MIA_PBS_c_3, E19_MIA_Poly_Embryo_c_2, P3_MIA_Poly_c_1, P3_MIA_Poly_c_2, P3_MIA_Poly_c_3). The proteins/genes that did not match were mainly histone variants and predicted genes.

More than half (68.68 %) of the detected proteins were predominantly mRNA transcripts with high abundance (Fig. 30A).

The up- and downregulation of differentially detected proteins over the time course primarily overlapped with the trend of the differentially expressed genes, considering the contrast between age and cell population (E14_ctrl versus P7_special, Fig. 30B). Yet, some of the upregulated proteins were down-regulated at the transcriptomic level (480 proteins). They were mainly associated with “RNA splicing”. In the opposite case, genes, which were upregulated over the measured time course but whose respective protein was downregulated (444 proteins), were predominantly associated with “actin filament organisation” (Fig. 30B, Suppl. Fig. 20).

Despite the detection limit, samples from both modalities clustered well together (Fig. 31A). The PC1 axis varied mainly along the progressing age. Age was also the discriminating component to separate the samples in the treated condition. The PC2 axis was clustered fan-wise, with the E17/E18 samples being the farthest apart. In the prenatal samples, the proteomic samples pointed to the next day cluster along the age-associated PC1 axis, indicating a delay of one day in the proteomic samples compared to the transcriptomic samples.

Both modalities had a correlation coefficient of the first component between 72% and 79 %, depending on the time frame input (Fig. 31B).

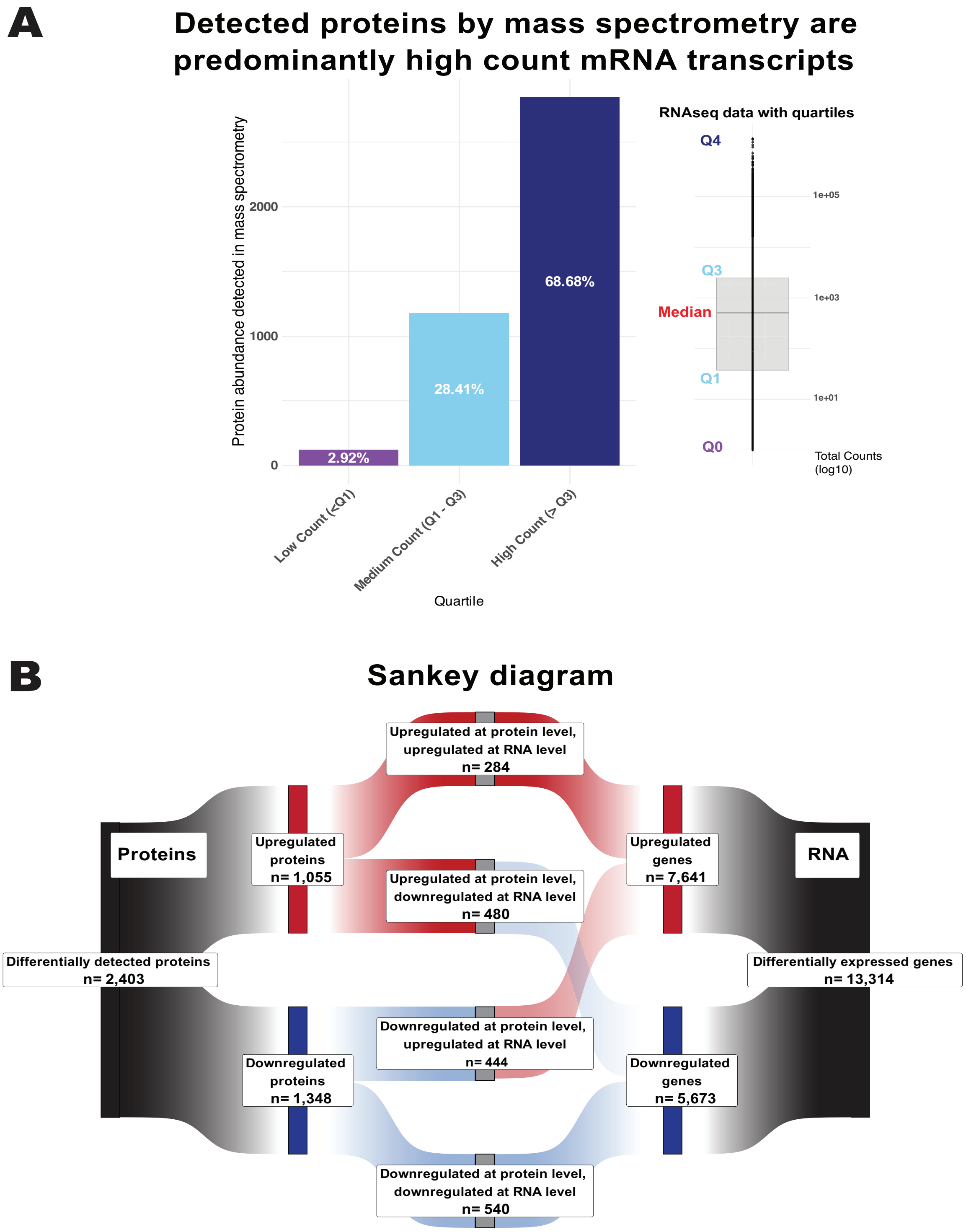

Figure 30: RNA transcript abundance overlap with the detected proteins by mass spectrometry

A. The detection limit of mass spectrometry is visible when comparing protein abundance across the quartiles of the respective sample aliquots from RNA-seq. In total, 121 proteins are detected from low count RNA transcripts, 1,178 proteins from between the 25th and 75th percentile, and 2,848 proteins represent RNA transcripts with high transcript per million (TPM) counts.

B. Among the large transcriptomic and proteomic map created here, only a part of genes and proteins are differentially detected. The Sankey diagram shows overlaps between the up- and downregulated mRNA transcripts versus detected proteins. A total of 480 proteins are generally upregulated, even if detected downregulated at transcriptomic level, while 444 proteins are downregulated, even if upregulated in the RNA-seq dataset. Based on Wald test with E14_ctrl vs P7_special contrast with a p.adj. cut-off <0.01.

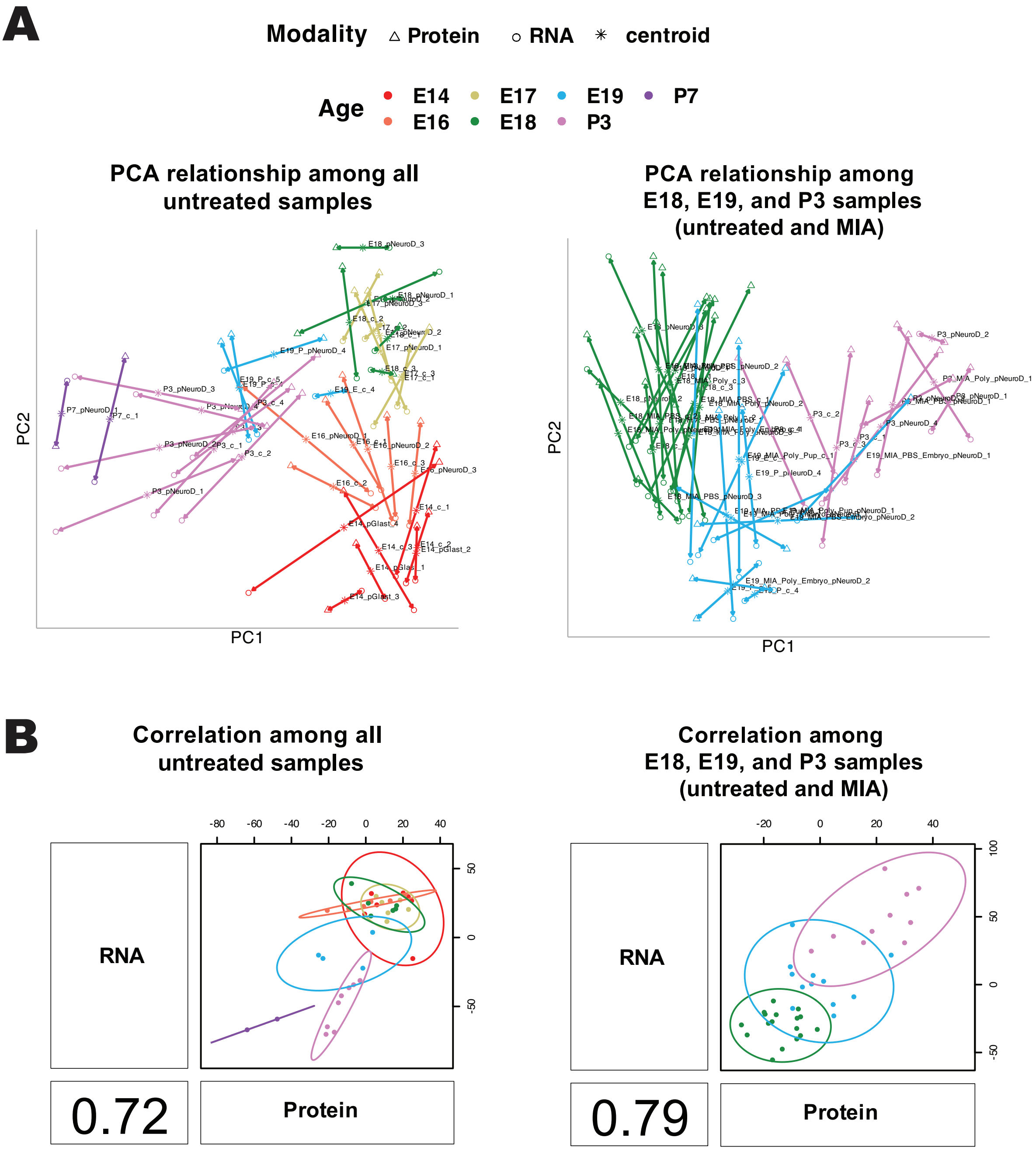

Figure 31: RNA-seq and mass spectrometry data correlate and show an age bias

A. PCA relationships of treated and untreated conditions in detail. The triangles represent protein samples, the circles the corresponding transcriptome samples and the stars are the centroids between the two modalities. Arrows further away from their centroid indicate a greater degree of inconsistency or divergence between the modalities. See Suppl. Fig. 19 for more details.

B. Despite limiting factors, both modalities correlate with each other and show similar dynamics with progressing age and among treated conditions. Mix:Omics::DIABLO Co-PCAs of RNA and protein samples with all matching 4,147 mRNA transcripts and respective proteins show a close relationship between the modalities and based on the first component.

Time course integration of transcriptomic and proteomic layer

The time frame measured here from E14 to P7 covered the course of indirect neurogenesis. During this narrow time frame, key events were derived by clustering DEGs over time. Major cellular restructuring occurred, as indicated by the number of DEGs with enhanced time contrast (Fig. 22). These clustered changes at the **mRNA transcript** level followed different **translational** timetables as suggested by the scaled log2 abundances in Fig. 32 below.

Genes of cluster 1, which were abundantly related to “RNA splicing” (GO:0008380), changed their expression between E16 and E17, while the translational response followed two days later with the same downregulation trend. This trend was in contrast to cluster 5, in which genes related to “regulation of membrane potential” (GO:0042391) showed a delay of two days at the protein level compared to the transcriptome data with an upward trend (Fig. 32).
DEGs of cluster 2 changed their translational level one day after the change at the mRNA level. Most of these genes were functionally linked to “axonogenesis” (GO:0007410).
In cluster 3, the corresponding protein levels were heterogeneous and showed a relatively uncertain trend, in contrast to the RNA-seq data. These were distinctly upregulated between E17 and E18, e.g. for the membrane-bound “store-operated calcium entry” (GO:0002115), which onset is triggered by a depletion of $[Ca^{2+}]_i$ stores in the endoplasmatic reticulum.
Contrary to all other clusters, the changes in gene expression in cluster 4 were anticipated by a change in protein detection levels one day earlier. This cluster included genes for “cilium organisation” (GO:0044782) in particular.
The translation from mRNA transcripts to protein was immediate in cluster 6. This cluster was mainly associated with the “fatty acid metabolic process” (GO:0006631) that encompasses genes responsible e.g. for the hydrolysis of fatty acids. This biological process was elevated congruent to the RNA-seq data at E19 (Fig. 32).

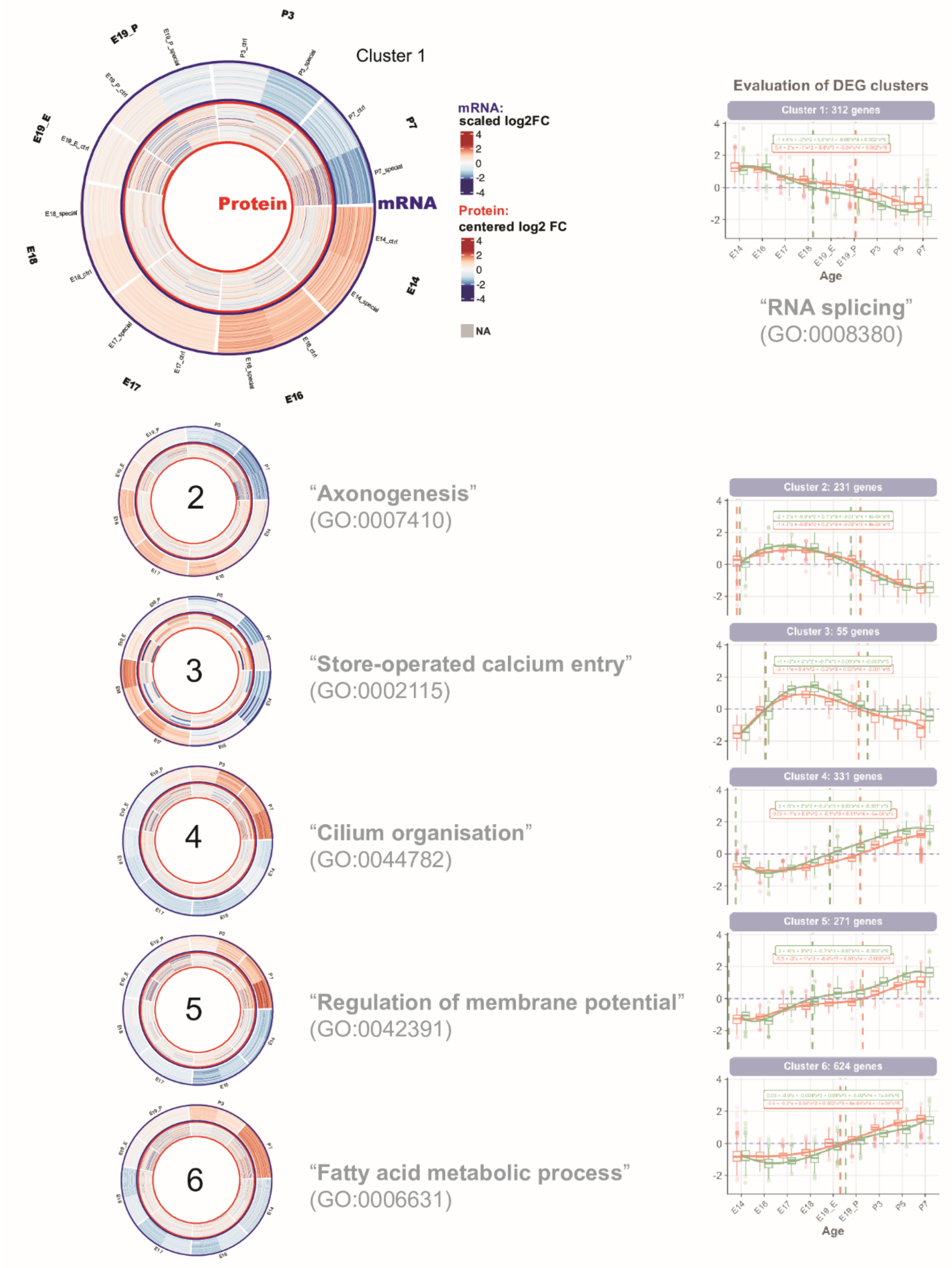

Figure 32: Proteomic response to transcriptomic changes is delayed

The circular heatmaps show scaled log2 fold changes for the transcriptomically distinct clusters (DEGs) and the respective proteomic average log2 fold changes, scaled with the protein-wise centred data by age and cell population. The transcriptomic data corresponds to figure 22. A change in proteome levels is for the second cluster e.g. noticeable a day later, whereas for the first cluster a change is visible two days later than in the transcriptomic level. The proteomic data were further filtered as gene symbols were to be matched with the RNA-seq data. For clarity, the first cluster is shown individually at the top and only one representative GO term among the five most important GO terms is annotated for each cluster on the right-hand side.

Extreme gene expression contrasted with corresponding protein levels

The Sankey plot in Figure 30B showed that not all gene expression levels could be converted into protein levels accordingly.

For example, the upper-layer neuronal marker special AT-rich sequence binding protein 2 (*Satb2*) was initially transcriptomically upregulated up to E18. Then its expression decreased but was instead consistently upregulated in the protein layer. *Satb2* as a commonly used marker of upper cortical layer identity was downregulated in the PolyI:C treated cells compared to the naïve cells at E18 in both modalities. In the transcriptomics this trend reversed during birth stage, but in the protein level it remained low in the PolyI:C samples (Fig. 33A, B, upper panels, respectively).

In contrast, the transcription factor and IPC marker *Tbr2* (Eomesodermin, EOMES) reduced its expression in two steps: just before migration (E17) and after birth (P3), which was followed at the protein level (Fig. 33A). Nestin (*Nes*), as a neuroepithelial intermediate filament, was oppositely regulated to *Satb2*. Synaptotagmin-1 (SYT1) and β-Tubulin class IIA (TUBB2A) were the proteins that were most down- and upregulated, respectively. *Tubb2a* followed this trend in the transcriptomic layer, while *Syt1* was upregulated again as mRNA transcript after birth (Fig. 33A).

The microglial marker Iba1 (Allograft inflammatory factor 1, *Aif1*) was among the 444 genes that were upregulated in the RNA layer but downregulated in the protein layer (Fig. 33B). ‘SH3 and multiple ankyrin repeat domains 2’ (*Shank2*) was among the genes most downregulated in MIA samples compared to their untreated counterpart. SHANK2 was also detected as a protein at lower levels than in the naïve state, at least in E19 and P3. Only a few samples left in the E19 cohort, so a comparison with the transcriptomic layer was inappropriate. In addition, SHANK2 had an increasing trend in the proteome but a decreasing one in the transcriptome. *Shank2* belonged to the red module identified by WGCNA analysis below (Fig. 38C), as did synaptic Ras GTPase activating protein 1 (*Syngap1*). They also showed a similar profile in both modalities. SMAD family member 4 (*Smad4*) also resembled this profile but its mRNA transcript was more highly expressed in the PolyI:C samples than in the naïve state (Fig. 33B).

Van gogh-like 2 (VANGL2) was steadily upregulated in the pNeuroD1+ cell population at the protein level over time. The corresponding mRNA transcript showed reverse regulation. Ribonuclease H2 (RNASEH2A) was the most upregulated protein in the pCAG+ population in contrast to the pNeuroD1+ population, and a similar trend was seen at the transcriptomic level (Fig. 33C).

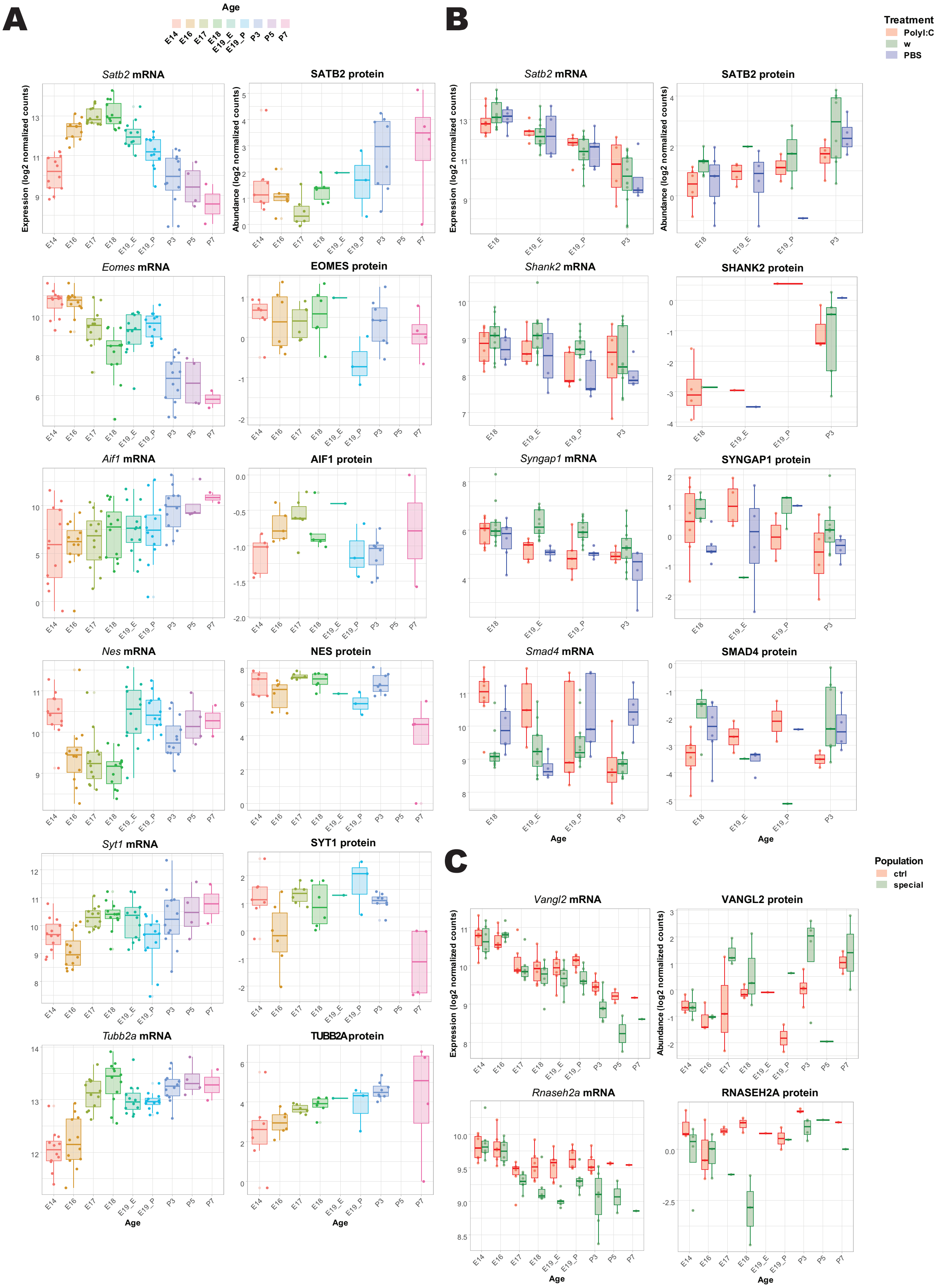

Caption continued on next page

Figure 33: mRNA expression and protein abundance profiles of selected genes and proteins

A. Satb2 has a peak at E18 in the RNA-seq data, but is steadily upregulated at the protein level over the time course of neurogenesis. Tbr2/Eomes is downregulated at transcriptomic level in two steps and is downregulated at protein level after E19. Aif1 is upregulated at the transcriptomic level, but downregulated at the protein level after birth. Nestin has a local minimum at E18 at the transcriptomic level, and has otherwise oscillatory protein levels. Syt1 was upregulated at both modalities over time, but was downregulated at P7 only at the proteomic level. Tubb2a was constantly upregulated in both modalities.

B. Profiles of Satb2, Shank2, Syngap1, and Smad4 as four representative genes/proteins differentially regulated between the MIA conditions and modalities.

C. Two representative genes/proteins differentially regulated between both cell populations: Vangl2 and Rnaseh2a.

DESeq2-normalised, log2-transformed (plus a pseudocount of 0.5), and scaled values for the transcriptomic layer and harmonised, log2-transformed, and scaled (basic R; (x - mean(x)) / sd(x)) values for the proteomic layer.

Basic upper-layer neuronal functions

During neurogenesis of the upper layers, extensive restructuring of the ECM, metabolic adaptations, and changes in the transcriptional landscape occurred. However, transcriptional output did not necessarily correspond to protein output, especially in developmental systems with an immediate need for translational adaption [423].

Typical transcription factors of neurogenesis showed a substantial decrease in expression after birth, while the protein level of SATB2 increased (Fig. 34; Suppl. Fig. 18).

Genes related to the establishment of membrane potential and excitability followed a strict sequential expression, which was also reflected at the proteomic level a day or two later. Initially, genes contributing to polarity formation and axonogenesis created the conditions for further expression of e.g. ion channels. *Robo1,2* and *Dpysl5* had the most pronounced expression change with a peak expression at E17/E18. Here, AMPA receptors such as *Gria2* were involved in the initial establishment of the membrane potential, followed by the expression of Ca^{2+}-sensitive proteins such as *Camk2b*. The expression of NMDA receptors such as *Grin2b* were the most differentially upregulated genes in this data set (Fig. 34).

Signalling factors, such as *Wnt7b*, were not detected at protein level, in contrast to growth factors (Fig. 34).

A more detailed overview can be found in supplementary figure 18.

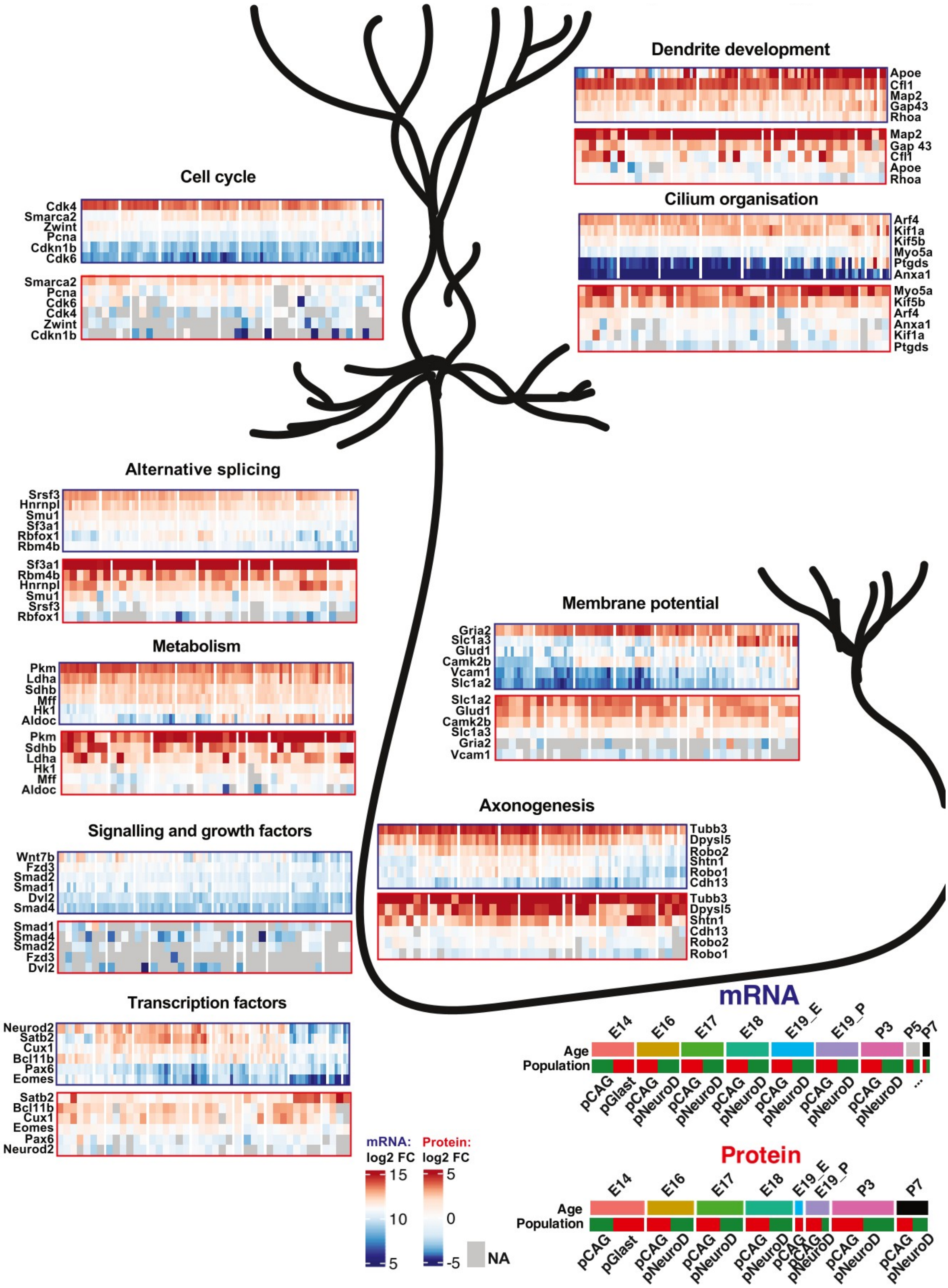

Figure 34: Selected neuron-specific biological processes compared between RNA-seq and mass spectrometry data of untreated samples over time

Six representative genes and proteins for each relevant biological process are shown as harmonised and log2-transformed values for the proteomic layer and as DESeq2-normalised and log2-transformed values plus a pseudocount of 0.5 for the transcriptomic layer. Both consistently and differentially expressed genes/proteins are included from the untreated data sets only. Heat maps are sorted from high to low abundance in the respective modality. Note that Wnt7b was not detected at protein level, representative for most of the secreted signalling factors.

► Neurogenesis upon maternal immune activation

Developing neurons showed already an enhanced response to the environment in the untreated transcriptomic landscape (see GOterm "activation of immune response" (GO:0002253) in population enhanced contrast analysis, Fig. 23), which prompted the introduction of a controlled extrinsic stimulus to compare it with the naïve acquisition of upper-layer neuronal fate.

In collaboration with Gülsah Gabriel at the LIV, the two-hit mouse model was established and applied here with slight modifications. Unlike in Jacobsen et al., 2021 [286], mice were administered PolyI:C and PBS twice directly before acute neurogenesis of the upper layers at E10 and E12 (Fig. 9A, with **M**aternal **I**mmune **A**ctivation (**MIA**)).

The aim was to gain insights into how immunogenic perturbations particularly affect the upper-layer neuronal population across three layers of biological complexity.

Cytokine levels in placental tissue indicated successful injections

The organs and sera of animals subjected to MIA were tested for elevated cytokine levels, as these are indicators of actual immune activation. The experimental mice similarly gained weight, as did their tested organs (PolyI:C, PBS, and untreated condition, Suppl. Fig. 10). For comparison, brains from thirteen embryos were also included.

The custom BioRad multiplex panel considered eight major cytokines for inflammation in maternal and embryonic tissues.

The cytokine profile showed statistical differences between the treated conditions (PBS and PolyI:C) and the untreated/naïve condition (Fig. 35). In general, the PBS condition was intermediate between the naïve and the PolyI:C conditions; it usually had cytokine levels intermediate to the other conditions. Also, the rate at which it differed from the other conditions measured was similar for all measured cytokines.

MCP-1/Ccl2 had the highest cytokine concentrations, with the highest measured value in the assay being 7,746.66 [ng/µL]. IL-1b was generally detected at low concentrations, with the highest value of 3.4 [ng/µL] in embryonic brains and placenta. In contrast, IL-1b was detected in maternal serum up to 220.29 [ng/µL] (Fig. 35A).

Two mice injected with PolyI:C showed particularly deviating values for IL-1b, IL-10, and MCP-1/Ccl2 from the other treated samples, which did not influence the overall statistical trend of the condition. These mice (#21181 and #29599; details deposited on github) were the heaviest among the PolyI:C-treated mice and had the most embryos. The concentrations of the samples (embryonic brain and placentae) from the same mother mice were otherwise within the range of the other samples for the respective cytokines and not statistically different.

Moreover, the cytokine profile showed increased levels in sera for all measured cytokines in the PolyI:C condition (Fig. 35A). However, the confidence interval was higher than in the other conditions. IFN-γ was detected significantly more frequently in the sera of PBS samples than in those of the naïve counterpart (*, after multiple-testing correction with **H**olm-**B**onferroni (**HB**) method: p.adj.: 0.087), and IL-2 was detected significantly more frequently in the PolyI:C samples than in the naïve samples (*, p.adj.: 0.039). Even the difference between PBS and PolyI:C was significant with a p-value of 0.0167 and an adjusted p-value with HB of 0.05 (Fig. 35).

Placental tissue showed a more stable cytokine profile with a significantly lower level of IL-1b in the PolyI:C placentas than in the naïve placentas (**, p.adj.: 0.023), similar to IL-10 (*, p.adj.: 0.13) and TNF-α (*, p.adj.: 0.12). IL-6 was the lowest cytokine detected in PBS placentae (*, p.adj.: 0.11).

No statistical test could be performed for the embryonic brains, as only one observation was left in the naïve state. However, the PolyI:C samples mostly had the lowest cytokine levels.

The gene expression levels for the cytokines tested here did not differ between conditions (Fig. 35B). The samples yielding the RNA-seq data did not directly match the mother mice tested for the cytokine panel.

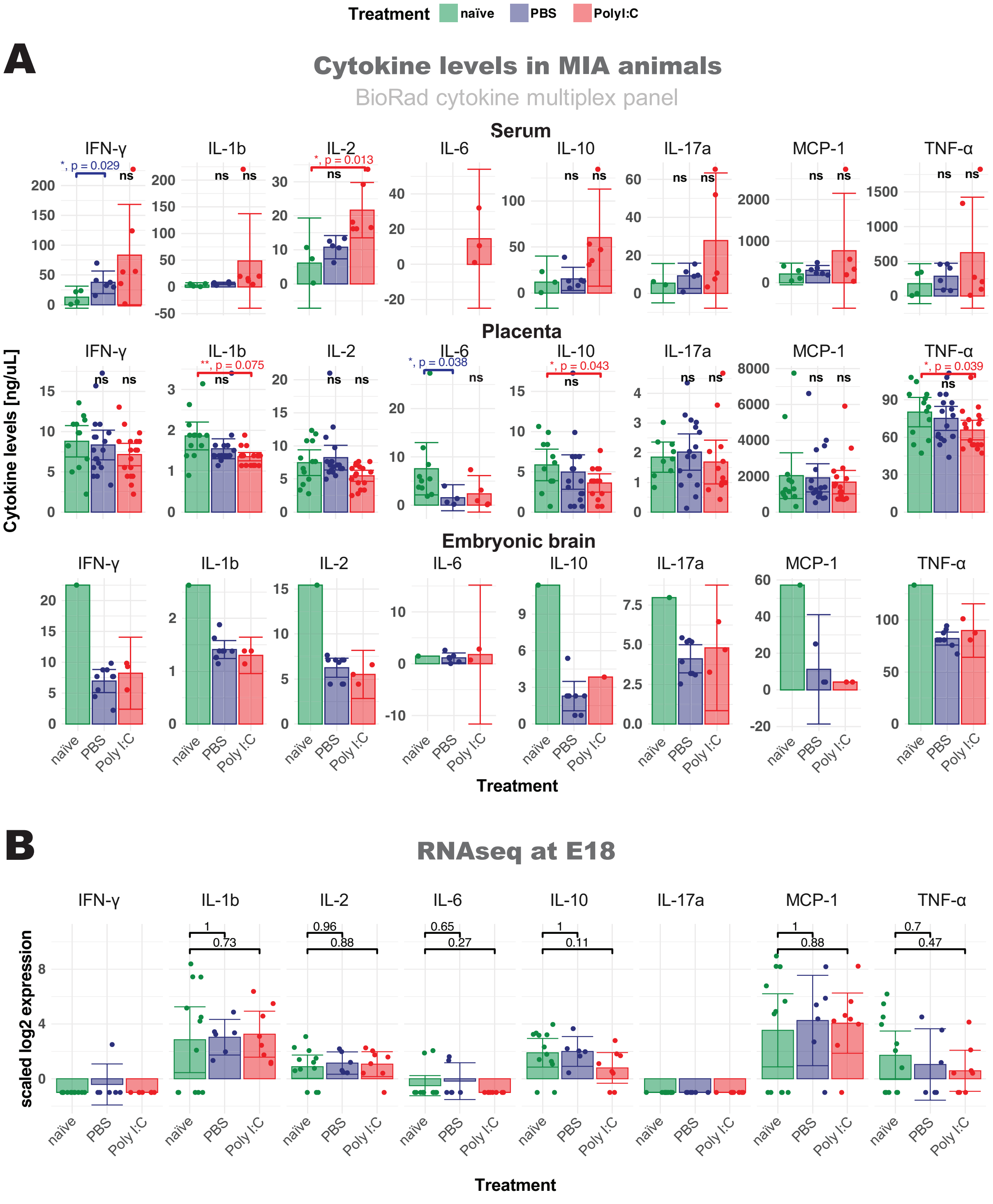

Figure 35: Maternal Immune Activated (MIA) mice show elevated cytokines in maternal sera

A. Tissues (Maternal sera, placentae, and embryonic brains) were collected from MIA mother mice with E18 FACSed offspring.The cytokine profile of the samples examined shows maternal immune activation, especially in the sera of the mother mice. Stars report p-values and indicate statistical significance according to a Welch's t test with the naïve condition as reference group (*p < 0.05, **p < 0.01, ***p < 0.001). Error bars are confidence intervals calculated with "smean.cl.normal" from the R package Hmisc. It calculates the sample mean together with lower and upper Gaussian confidence limits (quantiles) based on the t-distribution.

B. The RNA expression levels of all cytokines studied are comparable among the treated and untreated conditions. RNA-seq values as DESeq2 normalised log2 counts. Same Welch's test used as in A.

Transcriptomic treatment-based differences

WGCN analysis of the entire dataset filtered for E18, E19_E, E19_P, and P3 time points allowed the identification of regulatory signalling pathways with a particular contrast to the MIA treatment. Samples were hierarchically clustered (Fig. 36A). The identified gene expression clusters, so-called “modules”, correlated functionally and dynamically to the developmental stages and different conditions (Fig. 36B, 37A). With this, WGCNA provided valuable insights beyond the degPatterns approach.

With the statistical thresholds chosen, WGCNA identified fourteen colour-coded modules statistically differentially associated with the four conditions (Age, cell population, harvest mode, and MIA/Treatment).

Overall, almost all modules, except the yellow, pink, and greenyellow ones, were significantly different regarding **age**. The samples collected *in utero* significantly differed from those collected *ex utero*. In general, harvest mode and age were the most correlated conditions (Fig. 37A). The turquoise and brown modules contained the most positively correlated genes, while the green and purple modules contained the most negatively correlated genes. The turquoise module was the second largest module containing 3,933 genes. It was significantly enriched for “positive regulation of defense response” (GO:0031349, qvalue: 3.89E-46) and “activation of immune response” (GO:0002253, qvalue: 9.65E-46). The brown module was enriched for “chromosome segregation” (GO:0007059, qvalue: 4.10E-44) and “mitotic nuclear division” (GO:0140014, qvalue: 1.10E-34) (Fig. 37B; Suppl. Table 6).

The grey module, the largest module, consisting of 4,132 genes, included all genes that could not be integrated into any other module (Fig. 37A). This module showed a significant positive correlation with *in utero* and the pNeuroD1+ population, but not as strong a correlation as other modules with the conditions tested here. The genes in the grey module were enriched in functional categories related to nuclear cellular functions such as “mRNA processing” (GO:0006397, qvalue: 9.61E-25) (Fig. 37B; Suppl. Table 6). This suggested the identified module mainly comprised genes involved in basic molecular processes essential for cellular homeostasis (Fig. 37B).

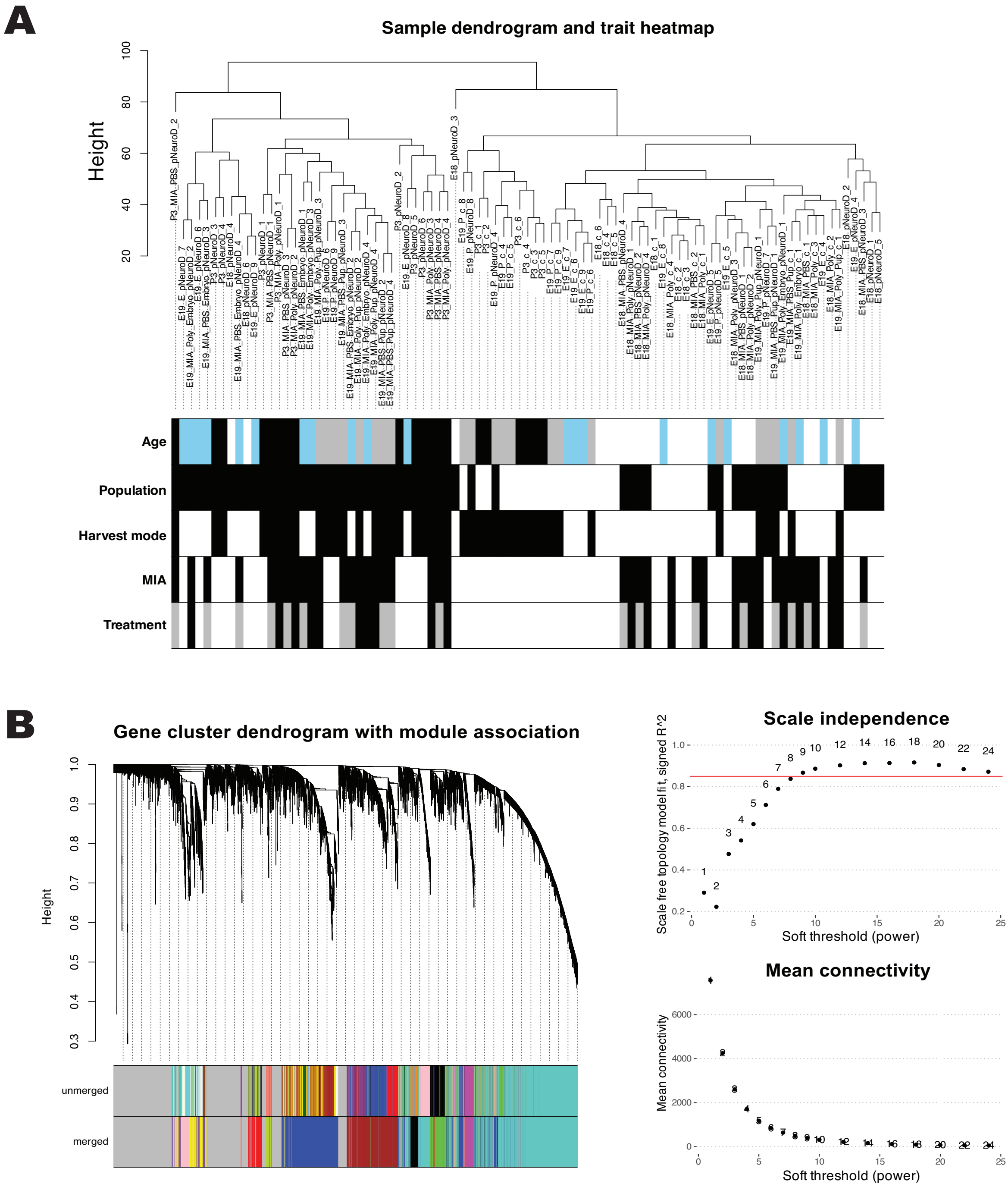

Figure 36: Overview of WGCNA metrics for the here associated conditions

A. In this WGCNA, ages of E18 (white, *in utero*), E19_E (blue, *in utero*), E19_P (grey, *ex utero*), and P3 (black, *ex utero*) are covered in both cell populations (pCAG+/white, pNeuroD1+/black). The treatment is the extended version of the MIA treatment with PolyI:C (PolyI:C/black, PBS/grey, untreated/white). The initial classification of the dendrogram primarily corresponds to cell population association, but the clustering is also age-biased.

B. The cluster dendrogram shows the association of gene expression to specific modules (more detailed presentation of TOM plot in the Suppl. Fig. 12). After clustering, modules whose eigengenes correlated above the soft threshold of 12 are merged (mergingHeight: 0.25). This way, gene modules are neither over- nor underclustered. Right panels: Power metrics – The arbitrary soft threshold is set here at the power of 12 with a scale-free index R^2 of above 0.85 as WGCNA authors suggested [374], where the R^2 values firstly reaches an inflection point and the mean connectivity enters a stationary phase. The two plots mirror the natural trade-off of the maximised fit (R^2) and the maintenance of a high mean number of connections.

Cell population differences were revealed by the contrasting green-yellow and magenta modules, which were positively correlated with the pCAG+ population and the pNeuroD1+ population, respectively. The green-yellow module was enriched for “cell fate commitment” (GO:0045165, qvalue: 3.52E-07), which was inversely correlated with age, while the magenta module was overrepresented for biological processes, such as “ameboidal-type cell migration” (GO:0001667, qvalue: 6.66E-21) (Fig. 37B; Suppl. Table 6).

Treatment was here the more specific version of the binary “MIA” (FALSE or TRUE) condition; it encompassed all three conditions (PolyI:C, PBS, and naïve). This way, the construction of a WGCNA identified modules associated with specific developmental regulation processes under treatment (Suppl. Table 6).

The MIA condition, especially the PolyI:C treatment, correlated mainly positively with the pink module and negatively with the red module. In particular, the pink module consisting of 312 genes was significantly positively correlated with MIA treatment. In contrast, the red module with 426 genes was positively correlated to the untreated cohort, particularly negatively correlated to the PolyI:C treatment. Both modules were also positively correlated with the pNeuroD1+ cell population (Fig. 37A).

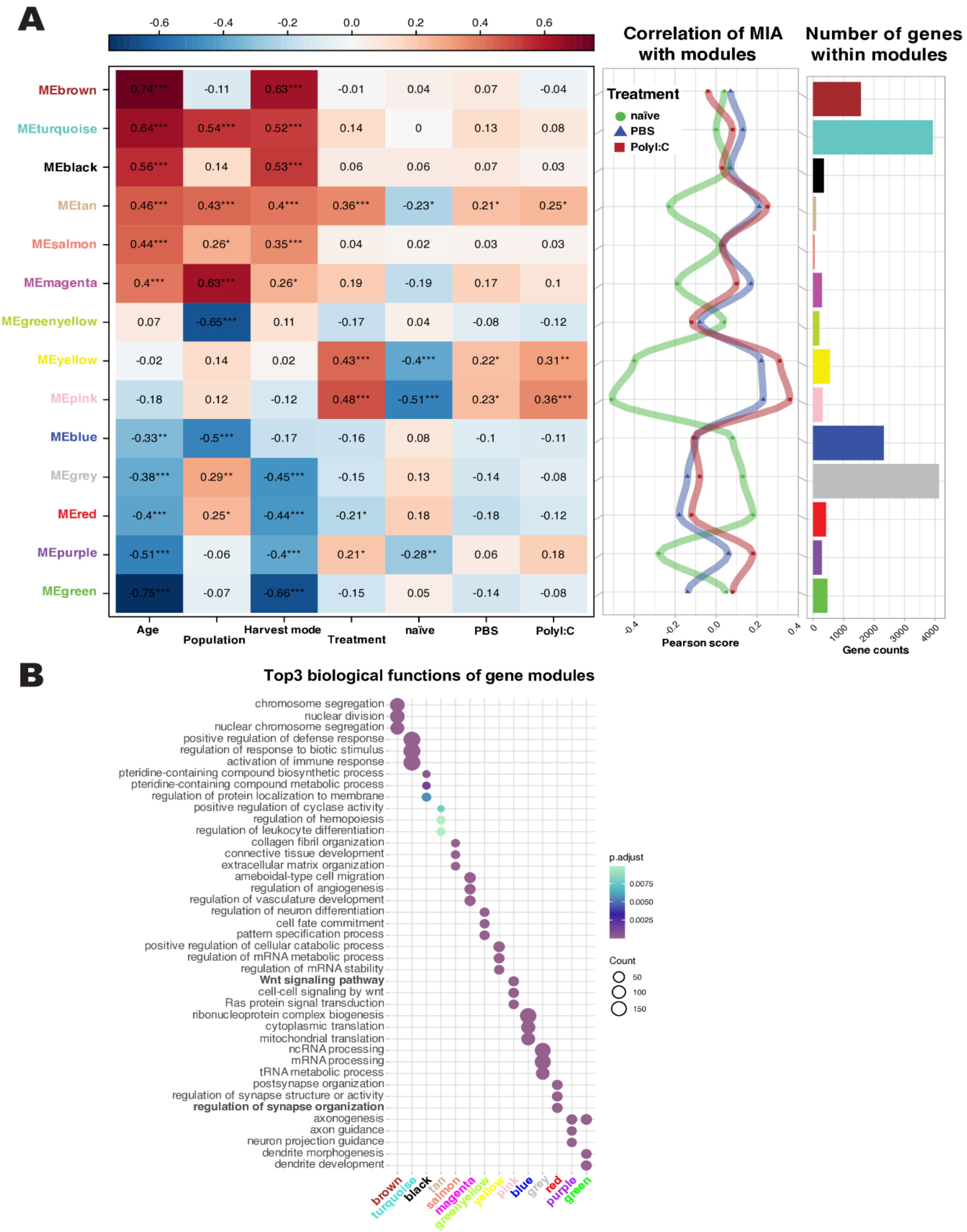

Caption continued on next page

Figure 37: Module-condition relationships shows a positive correlation of MIA treatment with the pNeuroD1+ cell population

A. At a power of 12, the heat map shows WGCNA derived and Pearson correlated gene modules at the respective time points, while the modules have highly significant Pearson scores that correlated with age (*p < 0.05, **p < 0.01, ***p < 0.001). Modules are sorted by module pseudo-age, while a positive age correlation/Pearson score represents increasing gene expression with progressing age. The green module included the most negative Pearson score of -0.75*** and the brown module included the most positive Pearson score of 0.74***. Along this pseudo-age, the MIA conditions showed significant positive and negative correlation with the **pink** and **red** module, which were analysed in detail below. Additionally, MIA treatment correlates positively with the pNeuroD1+ cell population. The respective overrepresented biological functions for each module are shown in figure part B. Apart from the unassigned gene module (grey), the turquoise module gathered most of the clustered genes (3,933 genes).

B. Dot plot shows the top three overrepresented biological functions of the fourteen WGCNA derived gene modules.

The **pink** module was functionally associated with "cell-cell signaling by Wnt” (GO:0198738, qvalue: 2.13E-07), "Ras protein signal transduction" (GO:0007265, qvalue: 3.28E-06), and "proteasome-mediated ubiquitin-dependent protein catabolic process" (GO:0043161, qvalue: 3.93E-06) (Fig. 38C, 39). Among these genes were the activity-dependent neuroprotective protein (*Adnp*), the tumour suppressor SMAD family member 4 (*Smad4*), and its SMAD specific E3 ubiquitin protein ligase 2 (*Smurf2*), and the histone deacetylase sirtuin 1 (*Sirt1*). Besides, typical neurogenic differentiation factors, such as neuregulin 2 (*Nrg2*), insulin-like growth factor-binding protein 3 (*Igfbp3*), protein kinase B (*Akt1*), guanine nucleotide-binding proteins (*Gna 12* and *q*), calsyntenin 1 (*Clstn1*), several F-box proteins (*Fbxo33, 45, Fbxl14*, *17*), and the Rho-associated coiled-coil containing protein kinase 2 (*Rock2*) were upregulated in the MIA cohort. Furthermore, typical Wnt pathway associated genes, such as the dishevelled segment polarity protein 1 (*Dvl1*), frizzled class receptor 8 (*Fzd8*), catenin delta 2 (*Ctnnd2*), and transcription factor 7 (*Tcf7*) had elevated gene expression in PolyI:C treated animals (Fig. 38C).

The genes of the **red** module were functionally related to “regulation of membrane potential” (GO:0042391, qvalue: 6.05E-08), “dendritic spine organization” (GO:0097061, qvalue: 5.35E-08), and “postsynapse organization” (GO:0099173, qvalue: 4.08E-12) (Fig. 38C, 39A). They encompassed genes encoding the ASD-associated gene ‘SH3 and multiple ankyrin repeat domains’ *Shank1, 2, 3*, as well as typical synaptic proteins such as piccolo presynaptic cytomatrix protein (*Pclo*), bassoon (*Bsn*), and postsynaptic density protein (*Psd*), and synaptojanin 1 (*Synj1*), synaptotagmin 7 (*Syt7*), and the synaptic Ras GTPase activating protein 1 (*Syngap1*). Many ionotropic channels such as calcium voltage-gated channels (*Cacna1a, Cacna1b, Cacna1e, Cacnb4*) and glutamate ionotropic receptors (*Grin1, Grin2b, Grip2*), were also downregulated in the MIA cohort. Additionally, adhesion molecules such as adhesion g protein-coupled receptors (*Adgrb2, Adgrl1, Adgrl3*), nectin1 (nectin cell adhesion molecule 1) and *Nlgn2* (neuroligin 2), were less expressed in the PolyI:C treated samples than in their naïve counterpart. Lastly, cyclin-dependent kinase-like 5 (*Cdkl5*), insulin-like growth factor 1 receptor (*Igf1r*), and kinesin family member 1A (*Kif1a*) were downregulated in MIA samples (Fig. 38C).

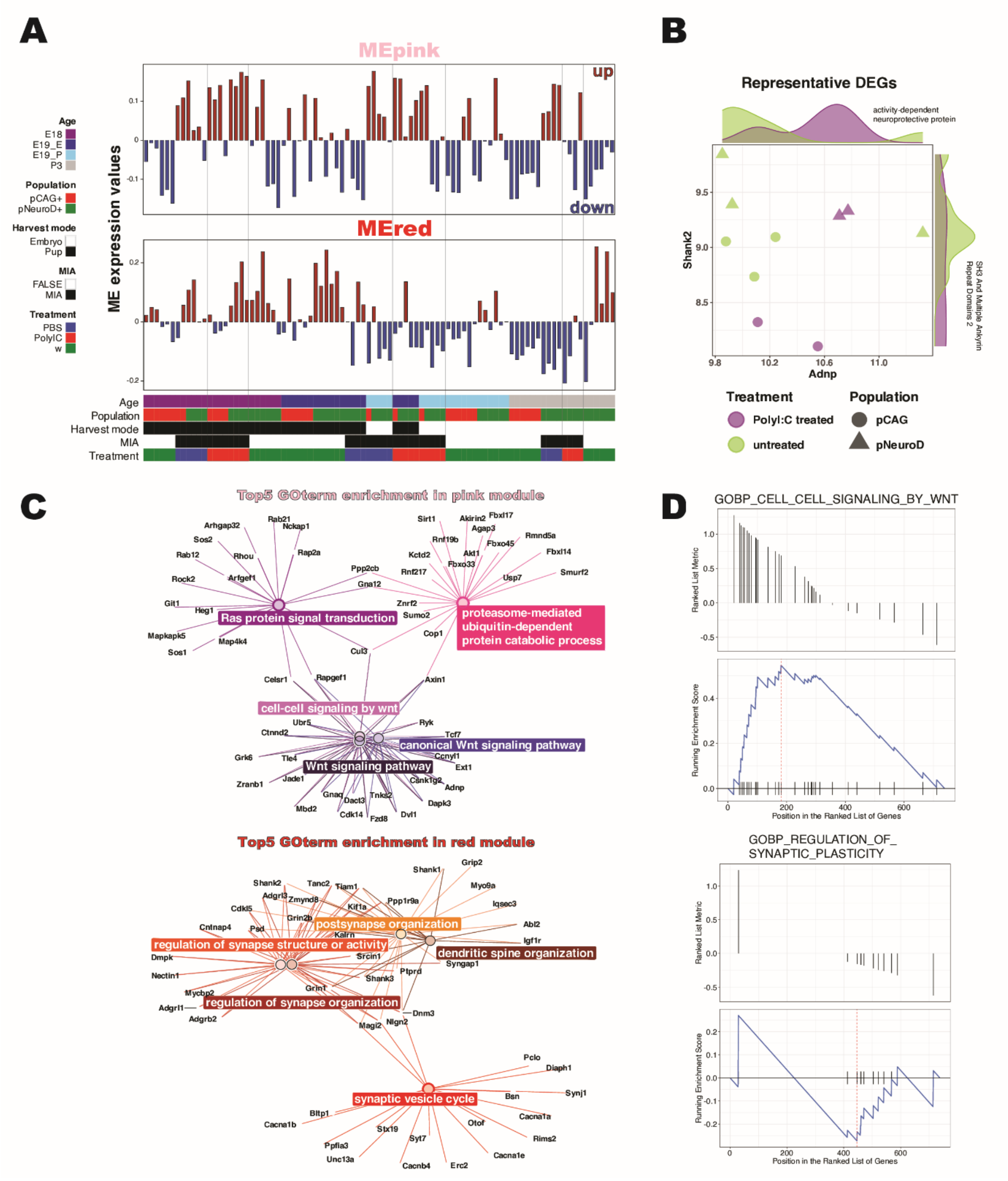

Figure 38: MIA samples differ in Wnt pathways and synaptic processes from their untreated counterparts at the transcriptomic level

A. Differential gene expression profiles show the two modules with the highest anticorrelating significance among all MIA-associated WGCNA modules. Both profiles indicate an age-dependence, biased to E18, of the differential dynamic.

Caption continued on next page

B. Two representative genes for the pink module (*Adnp*, activity-dependent neuroprotective protein) and for the red module (*Shank2*, 'SH3 and multiple ankyrin repeat domains 2') demonstrate characteristic gene expression for the PolyI:C treated and untreated conditions at E18. *Adnp*, and similarly all genes in the pink module, shows quantitatively distinct expression between both conditions, while *Shank2*, like all genes in the red module, is more widely dispersed in gene expression than its naïve counterpart, which is significantly highly expressed.

C. Cnetplots show overrepresentation of the five major biological processes (GO) together with the enriched genes associated with the pink and red module, respectively. The top ten biological processes are shown in Suppl. Fig. 13.

D. Likewise, GSEA shows two representative enriched gene sets, which were up- and downregulated in the stimulated condition, with p.adj.<0.01. Upregulated: Gene set of GOBP_CELL_CELL_SIGNALING_BY_WNT (NES: 1.584), consisting of genes such as the activity-dependent neuroprotective protein (*Adnp*), dishevelled segment polarity protein 1 (*Dvl1*), frizzled class receptor 8 (*Fzd8*), and T cell specific transcription factor 7 (*Tcf7*). Downregulated: Gene set of GOBP_REGULATION_OF_SYNAPTIC_PLASTICITY (NES: -0.882) enriched, containing genes such as the glutamate receptor, ionotropic, NMDA1 (zeta 1) and NMDA2B (epsilon 2) (*Grin1,2b*), 'SH3 and multiple ankyrin repeat domains' 1, 2 and 3 (*Shank1,2,3*), Synaptotagmin-7 (*Syt7*), and synaptic Ras GTPase activating protein 1 homolog (*Syngap1*).

Overall, the enriched gene expression of the pink module that responded to the PolyI:C treatment showed a remarkable increase in gene expression within the Wnt pathway (Fig. 38D; Fig. 39) and thereby showed a substantial increase in log2 fold change levels (Fig. 38A, B). In contrast, the expression of the red module was reduced in synaptic genes. These synaptically associated genes showed a wider range of log2 fold change values than their untreated counterparts (Fig. 38A, B, D). Note that no Wnt gene directly was differentially expressed, and both pink and red modules were enriched for different biological functions, but also overlapped in "regulation of synapse organization" (GO:0050807) with each other (Suppl. Fig. 13). *Igf1r* and *Igfbp3* were oppositely expressed.

In addition, the yellow, purple, and tan modules significantly correlated with MIA, while the red module was the only significantly negatively correlated module. The modules enriched for MIA showed an inverse trend with age/harvest mode. That correlated with cell population, suggesting that gene expression dynamics were biased towards *in utero* pNeuroD1+ samples rather than *ex utero* pCAG+ samples (Fig. 37A).

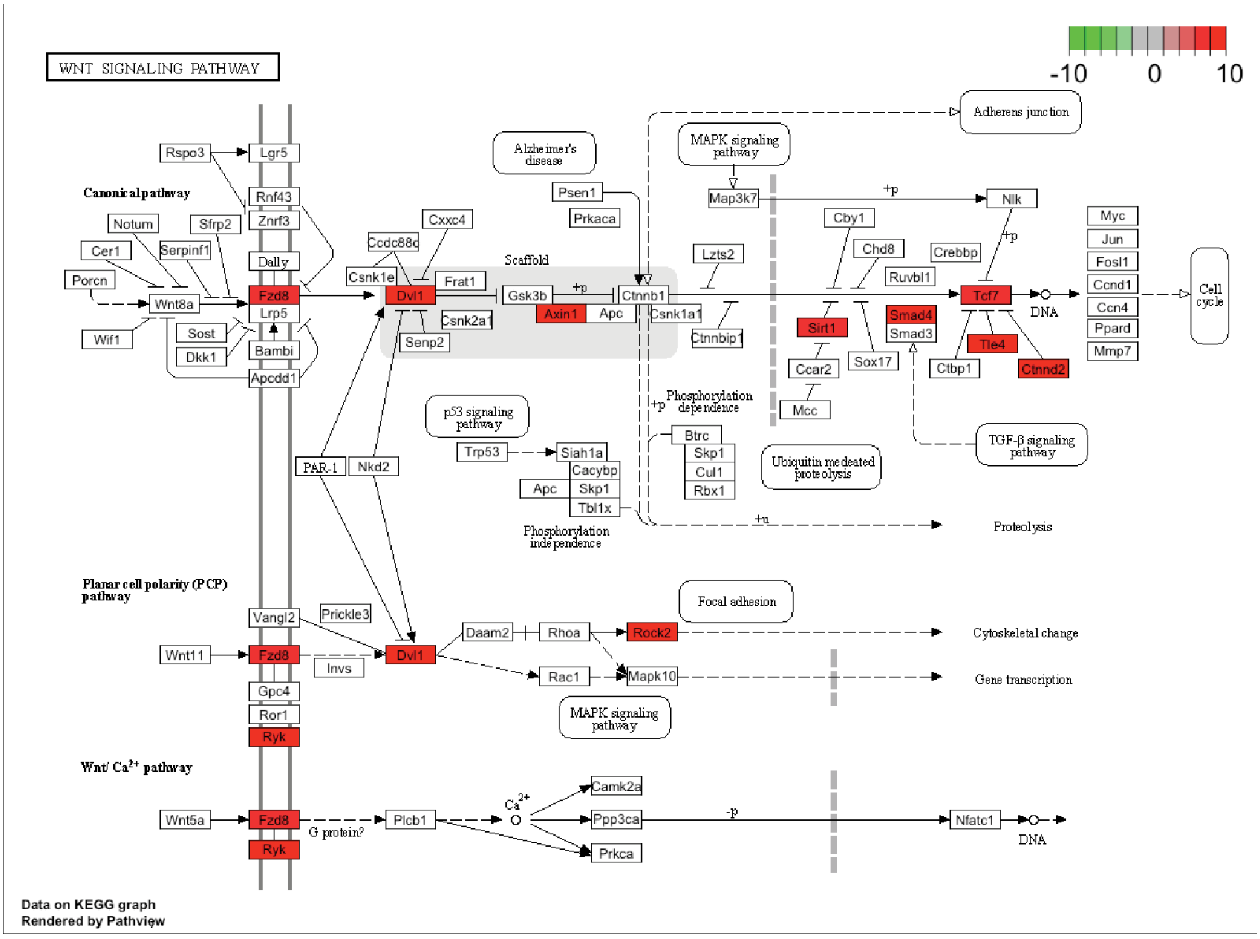

Figure 39: Canonical Wnt pathway is enriched for MIA treated developing neurons

The enriched KEGG pathway "Wnt signalling" (mmu04310) shows the enriched rlog-transformed RNA-seq counts in the MIA transcriptomic dataset contrasted for PolyI:C versus the naïve state.

Proteomic treatment-based differences

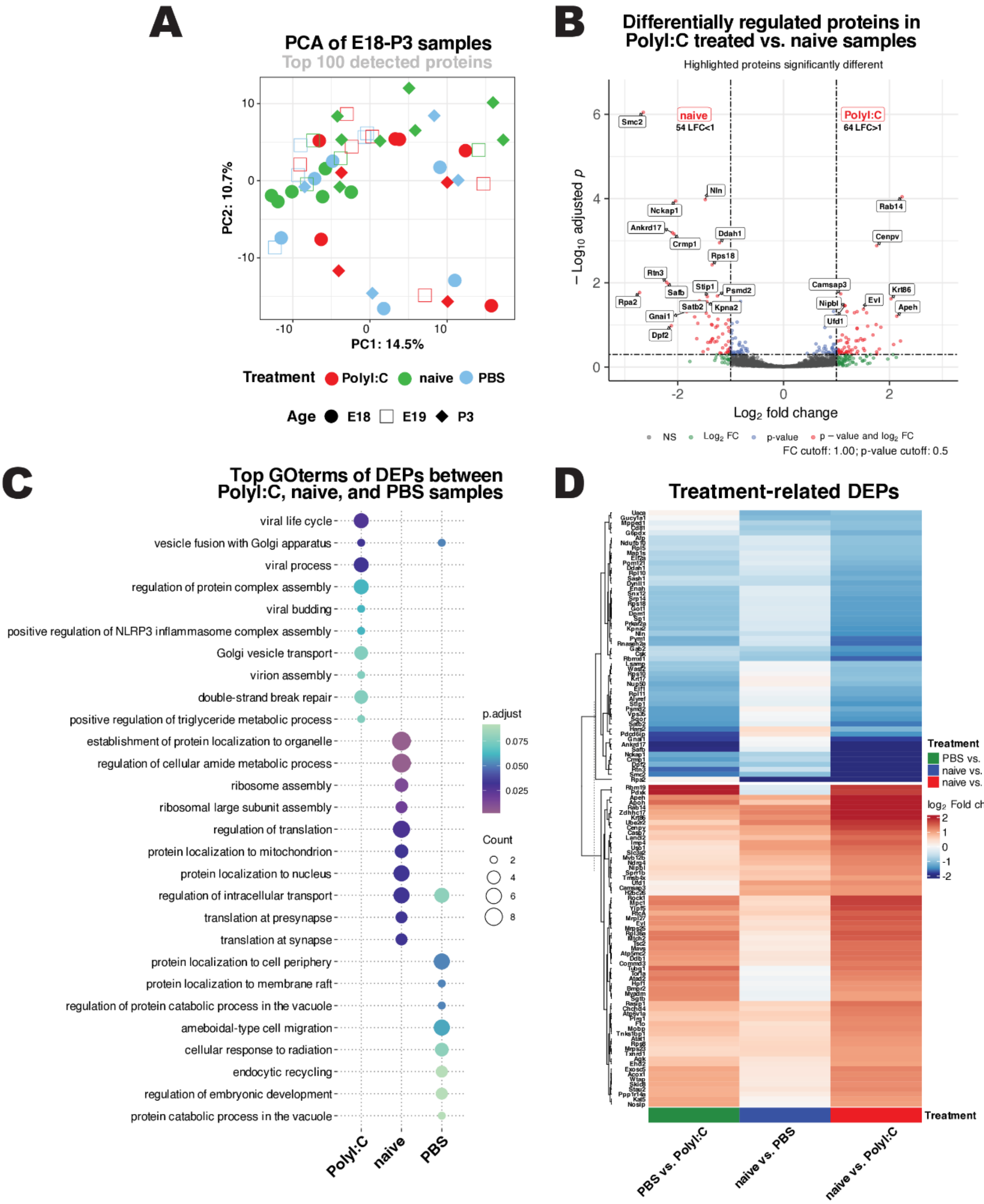

Figure 40: At the proteomic level, PolyI:C treatment reduces synaptic translation

A. PCA of E18, E19, and P3 MIA treated and untreated samples. Some treated (PolyI:C and PBS) samples differ from the large cluster of untreated samples. PC1 and PC2 together account for 25.2% of the total variance.

Caption continued on next page

B. The volcano plot compares the 118 differentially detected proteins for PolyI:C vs. the untreated condition over the three timepoints tested here. With an p.adj. cut-off<0.5 and a log2 fold change cut-off of 1, more (64) proteins are specifically upregulated in the PolyI:C cohort versus the untreated cohort with 54 upregulated proteins. SMC2, SATB2, and GNAI1 are more abundant in the naïve cohort, whereas CENPV, APEH, and CAMSAP3 are upregulated in the PolyI:C condition compared with the naïve samples.

C. The top 10 GO terms of the small set of DEPs show an underrepresentation of the treated samples for synaptic translation (GO:0140241) and “ribosome assembly” (GO:0042255), with an even larger difference in the PolyI:C condition. Centred values served as input to the clusterProfiler::compareCluster function. More details can be found in supplementary Table 9.

D. Heatmap comparing the ratios of the 118 DEPs between the three different conditions with Euclidean clustering. Actin skeleton-associated and centromere proteins such as ROCK1 and CENPV are upregulated in the MIA treated samples.

At the proteomic level, PolyI:C treatment was contrasted with the PBS and the naïve cohort of E18, E19, and P3 timepoints. Although the initial PCA showed variability attributable to differences in treatment, these differences were not as pronounced when the analyses were restricted to the relevant time points tested here (E18, E19 and P3, Fig. 40A). With a p.adj. cutoff <0.5, 118 proteins were differentially detected (Suppl. Table 9).

The underrepresentation of proteins associated with “translation at synapse” (GO:0140241) was prominent in the PolyI:C treated samples. For example, among them, SATB2 was down-regulated in the PolyI:C samples with a centered log2 fold change of -0.433 compared to the untreated cohort with 0.68 (Fig. 40B, D). RNASEH2A, RPL5, RPL10, and RPS10, which were also associated with “translation at presynapse” (GO:0140236) were underrepresented in the PolyI:C condition (Fig. 40C, Suppl. Table 9).

In contrast, ROCK1, CENPV, APOH, and APEH were more abundantly detected in the PolyI:C samples than in the untreated samples (Fig. 40B, D), albeit less significantly. In addition, proteins related to “Golgi vesicle transport” (GO:0048193), such as CSK, USO1, YIPF5, and RAB14, were upregulated in PolyI:C samples compared with their naïve counterparts (Fig. 40C, Suppl. Table 9).

Differences in the DNA methylome

Significantly increased expression of methyl CpG-binding domain protein 2 (*Mbd2*), deacetylase *Sirt1* and several lysine methyltransferases in mice treated with PolyI:C and PBS at E18 prompted subsequent analyses for DNA methylation in these MIA samples (Fig. 41). Without treatment, the expression of DNMT3a, a *de novo* methylase, increased postmigratory in pNeuroD1+ samples (Suppl. Fig. 18).

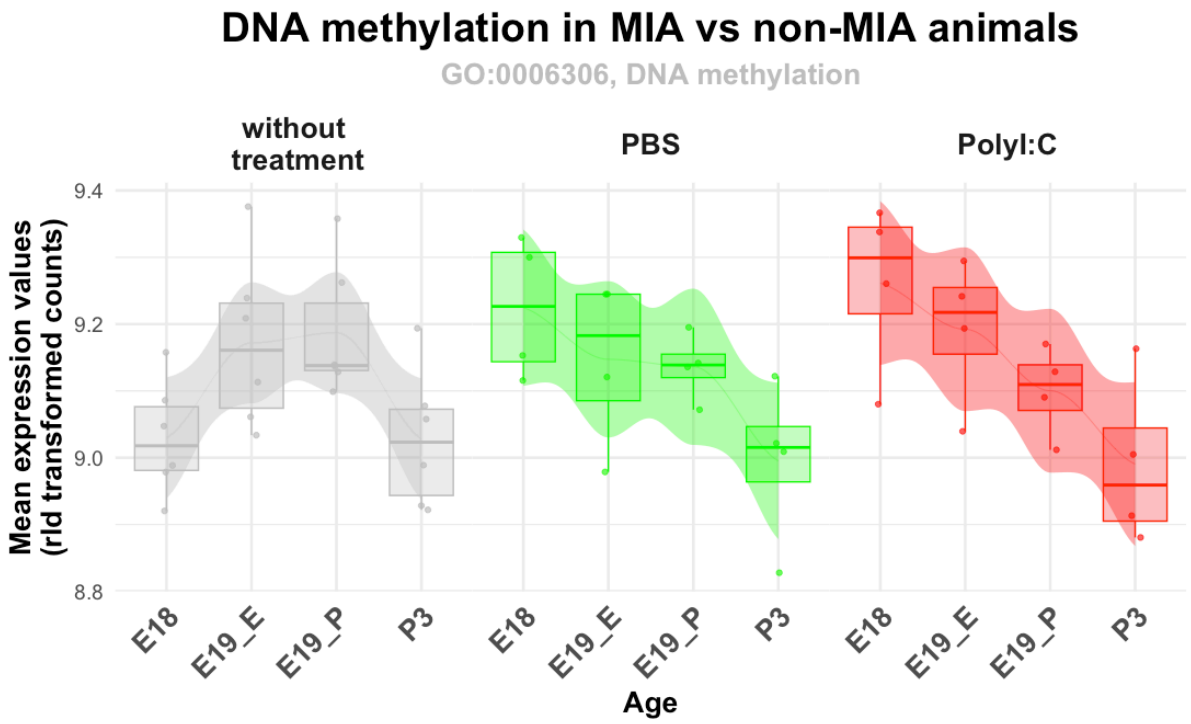

Figure 41: MIA animals have altered gene expression levels associated with "DNA methylation" compared with their untreated counterpart

At the transcriptomic level, genes associated with DNA methylation (GO:0006306), such as *Mbd2*, had higher expression levels in the pNeuroD1+ cell population than their untreated counterparts, particularly at E18.

DNA methylation is a widespread epigenetic modification closely associated with transcriptional repression, making it an important biomarker for developmental processes and disease aetiology [7,332,424–426]. However, it is less clear how DNA methylation relates to the phenotype of immune-activated offspring. Therefore, the cell type-specific DNA methylation response of the pNeuroD1+ cell population upon a maternal immune stress was detected here using an improved DNA methylation protocol called "EM-seq".

Enzymatic **m**ethyl **seq**uencing (**EM-seq**) detects both 5-mC and 5-hmC modifications on DNA at base resolution, which are associated with transcriptional silencing and general developmental processes. Here, EM-seq was performed on DNA from two PolyI:C samples and two PBS samples at E18 together with one fully methylated (pUC19) and one unmethylated (λ-DNA) SpikeIn control. The SpikeIn controls (Fig. 6) and the library QCs (Suppl. Fig. 22) confirmed successful sequencing and that the read depth of 50 million read pairs per sample on average was sufficient to produce meaningful results. Besides, the partly presence of the pNeuroD1-ires-eGFP vector was detected (Fig. 6).

In all samples, ~10% of the CpGs were unmethylated, while ~15% of the CpGs in the samples were fully methylated. Instead of a bimodal distribution, all samples had a local peak at ~25% methylation (Fig. 42A).

Read coverage indicated no PCR duplication bias for all samples (Fig. 42A). Pairwise correlation between PolyI:C and the respective PBS samples yielded coefficients ranging from 0.92 to 0.93 (Fig. 42B). Likewise, the dendrogram of samples and PCA between these samples indicated a batch effect rather than a biological difference between methylated CpGs in this data set (Fig. 42B).

After filtering base pairs with sequencing coverage below 10x and exceeding the 99.9th percentile in each sample and normalisation, 7,878 CpG sites remained for analysis. CpGs with standard deviations larger than 2% were kept. Differential methylation was further assessed with a p.adj. cut-off <0.5 (BH adjusted). Overdispersion was corrected using the proposed GLM of McCullagh and Nelder implemented by the methylKit R package v.1.26.0. Gene parts were annotated with the inferred differentially methylated regions using a GRCm38/mm10 genome as a GRanges/BED file from the UCSC Genome Browser [369].

With the moderate p.adj. cut-off <0.5 applied, six CpG regions were differentially methylated. These were mainly intergenic (Fig. 42C). The IGV lanes showed a broader methylated promoter region of *Shank2* in PolyI:C samples compared with the two PBS samples (Suppl. Fig. 23). *Shank2* was one of the genes that were downregulated in the PolyI:C samples at the transcriptomic level (Fig. 38C).

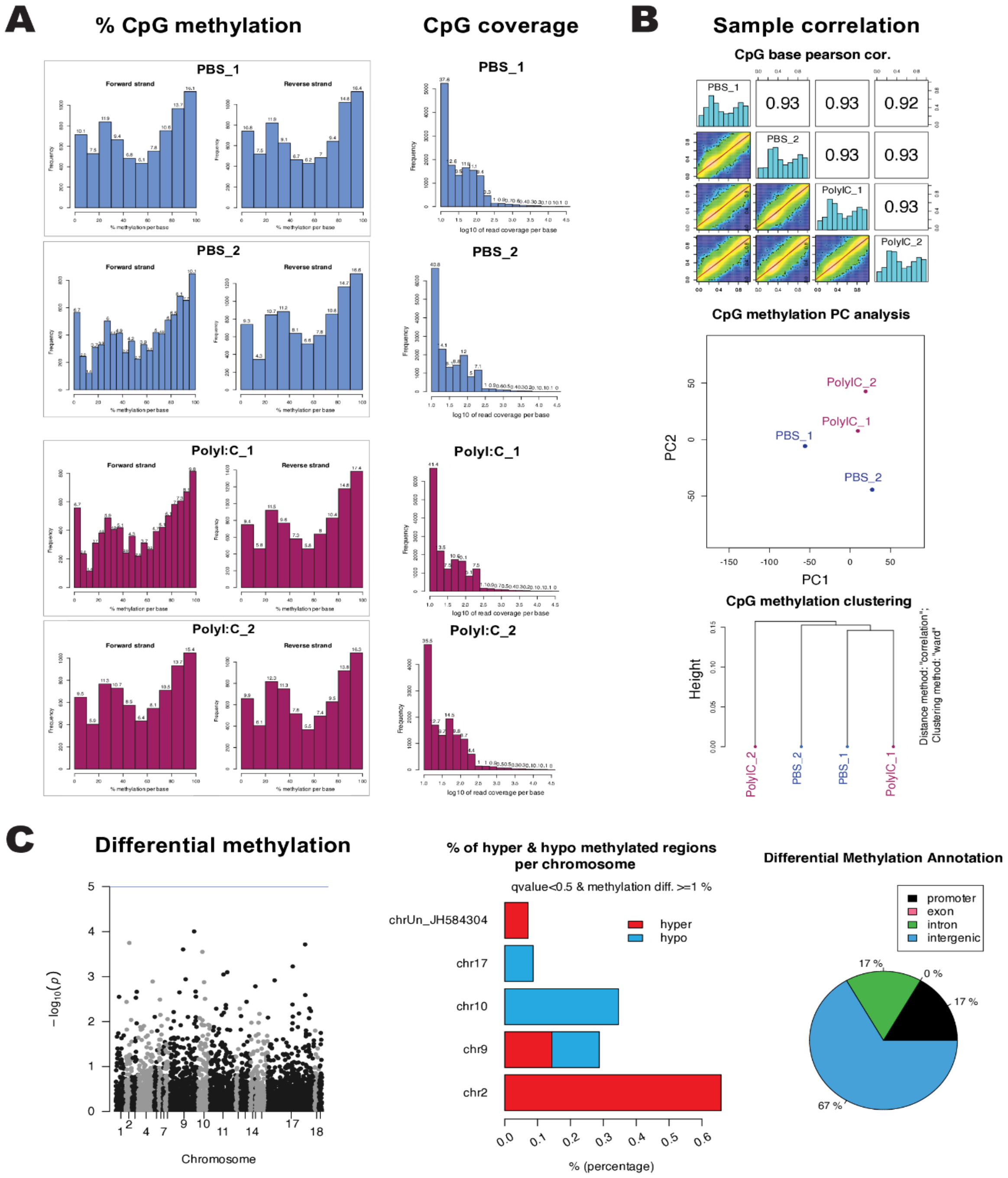

Figure 42: The PolyI:C condition resembles the PBS condition at the DNA methylome level at E18

A. The descriptive methylation analysis shows the fidelity of data collection. The distribution of methylation levels at CpG sites is enriched with fully methylated regions, but unmethylated and partially methylated regions are also detected, indicated by a bimodal distribution with a peak at 25%. In addition, most bases in all samples have uniform coverage, indicating no PCR duplication bias.

B. The Pearson correlation of the CpG bases shows that the samples from both conditions have a high positive correlation coefficient, indicating no differences. PCA and hierarchical clustering also show a higher batch effect than the actual biological difference between the PBS and PolyI:C conditions.

C. DNA methylation changes compared between PolyI:C as treatment condition and PBS as control condition show statistical significance for six DMRs, two of which were part of chromosome 9. These differentially methylated CpGs with significant p-values are highlighted in the Manhattan plot. They are not enriched for either hypo- or hypermethylation and are predominantly associated with intergenic regions.

Discussion

From an evolutionary point of view, **u**pper-**l**ayer **n**eurons (**ULNs**) have created an asset for mammalian species. The axons of the ULNs are the first emergence of two symmetrically connected cortical hemispheres *via* the *corpus callosum*. This complex connection requires a highly orchestrated genesis. Disturbed upper-layer genesis can drive aetiologies such as ASD [4],[5] or schizophrenia [6],[7].

This study sought to uncover the molecular coordination of upper-layer corticogenesis, spanning only a few days in mice. In such a narrow time frame, ULNs transition from a neuronal progenitor cell (E14, E16) through a migratory state (E17, E18) to a differentiated neuron (E19-P7). Bulk analyses were used to track these neurons throughout their cell fate transitions across three different levels of biological complexity. The analysis of this particular cell population – both its untreated and perturbed genesis – clarified our understanding and revealed key patterns for tailored further research.

► Specificities of experimental approach

Single cell POPULATION united the advantages of bulk and scRNA-seq

In this study, bulk analyses of two cell populations were performed across three modalities and their developmental time frame. The bulk approach was particularly advantageous at the transcriptional level: Sorting whole cell populations is more coherent and provides a “purer” method than computational sorting of whole tissue cell populations using marker genes in **s**ingle-**c**ell **RNA seq**uencing (**scRNA-seq**) [427,428]. Targeting single cell populations – in contrast to whole tissues – was possible by taking advantage of the physiological behaviour of the cells (here: inside-out, out-side-last migration into the upper cortical layers). By exploiting this physical dynamic these cells were acutely sorted via flow cytometry (Fig. 10, 11) yielding enough cell population aliquots to cover at least two, if not three bulk analyses. Thus, cell population analyses are thus suitable for deep sequencing and even for mass spectrometry approaches. Additionally, they are advantageous for DNA methylation analyses, as DNA methylation is cell type specific, but requires relatively large amounts of DNA. Since the NeuroD1 promoter was used to specifically target the post-mitotic neuronal cell population, the presence of the "ori" and the "AmpR promoter" of the pNeuroD1-ires-eGFP plasmid was indeed confirmed in EM-seq data (Fig. 4, 6).

The bulk approach required a robust sample size at the transcript level to allow reliable comparisons with upstream and downstream levels of biological complexity. A sample size of six for both cell populations and each time point in the RNA-seq increased statistical power, while a sample size of three allowed equally detailed analysis at the proteome level.

The cell populations were sorted by fluorescent constructs. All constructs used in this study had a similar size of 5-7 kb, guaranteeing that no plasmid was favoured over another in cytoplasmic integration.

The developmentally active promoter pNeuroD1 has already been frequently used to target post-mitotic neurons [80,202,429]. Indeed, the pNeuroD1+ population decreased dramatically in genes related to "DNA replication", while these genes were oscillatorily regulated in the pCAG+ cell population and increased cell cycle activities after birth (Fig. 23, cluster 2; Fig. 43).

The ubiquitously expressed pCAG-driven fluorescent marker was co-transfected to visualise the transfection site and facilitate isolation of the transfected cortical tissue whilst cell preparation. Fluorophores under the control of developmentally active promoters were often weakly expressed in the lower cortical layers where the progenitor cells or immature neurons were. The pCAG+ cell population consisted of mainly neurons, but also astrocytes and oligodendrocytes (Fig. 23, cluster 3; Fig. 13B; Table 4).

Interestingly, the pCAG+ cell population resembled the pNeuroD1+ population more than expected. Similar DEGs were derived when the special population was analysed alone or together with the pCAG+ control population (Fig. 21, 22). At the proteomic level, the distinction between the cell populations was less prominent and mainly showed a progressive, neuronal landscape (Fig. 26, 29). This strengthens the hypothesis [39,101] that neurogenic cell fate determination occurs at the transcriptional level at the precursor stage and leads mainly to a neurogenic fate at E14.

Here, the strong expression of neuronal precursor genes ruled out the identity of mature cells in the pGlast1-dsRed2 precursor samples at E14 (Fig. 14). Note that the marker proteins (pCAG-Venus and pCAG-tDimer) targeted neural progenitor cells that had the capacity to mainly transform into Satb2+ neurons (Fig. 12). Furthermore, the pNeuroD1+ cell population showed critical upregulation of marker genes, indicating a successful sorting and sequencing procedure (Fig. 15, 16; [202]). However, the definition of marker genes needs to be revised as, for example, Satb2 was down-regulated towards birth at the RNA-seq level, but it was one of the up-regulated proteins (Fig. 33).

Given the differences in cell identity, these results demonstrate the importance of considering an experimental design that is focused on cell populations and covers narrow time points when studying developmental processes. Regulatory changes during development are transient and return to baseline levels after dynamic interventions with other biological levels (Fig. 16, 33; Suppl. Fig. 18). Thus, this study has overcome the reliance of transcriptomic analyses on so-called “marker genes” and non-stationary tracking over time, highlighting the importance of considering the multiple biological layers when defining cell types.

Radial glia cell character transcriptomically overlapped with post-mitotic neuronal character

Time point E14 was used here for the IUE of all later collection time points. For reference, cells were also harvested at E14, but with a different, RGC-specific promoter pGlast1 (Fig. 9).

At the transcriptomic level, these E14 samples overlapped with all pCAG+ samples from the other time points, while samples positive for the post-mitotic neuron-specific promoter pNeuroD1 clustered outside the E14 cluster (Fig. 13A). The shared transcriptomic profile might indicate a shared molecular profile and confirmed that RGCs at embryonic age E14 were not yet restricted in their cell fate; they had a mixed character and continued to produce both neuronal and glial outputs.

Additionally, the E16 pNeuroD1+ samples were transcriptionally more similar to the E14 pGlast1+ samples than to the E17 pNeuroD1+ samples, again indicating that the E16 pNeuroD1+ cell population was a direct developmental descendant of the E14 pGlast1+ cell population (Fig. 13A).

This suggests a potential developmental relationship and that this study has hereby overcome the usual limit of cell type-specific resolution in bulk RNA-seq and the limitations of progenitor cell heterogeneity [10,408,409].

► How do neurons gradually enter and maintain the "post-mitotic" state?

In this study, the question arose how neurons gradually transition into this "post-mitotic" state and how they maintain it. As “*elementi perenni*”, ULNs exit the cell cycle very early, shortly before migration (Fig. 43).

In the multicomparison analysis, the second cluster of figure 23 was differentially regulated between the pNeuroD1+ and the pCAG+ population. At E16, the genes of this cluster were associated with “DNA replication” and dropped below average gene expression at the exact time when the cells targeted with the pNeuroD1-ires-eGFP construct were firstly harvested. This supported the usage of the NeuroD1 promoter to target specifically post-mitotic neurons. Corresponding to the decrease in NeuroD transcription factor members (Fig. 16, cluster 1), the initial high mitotic state during progenitor expansion in the pNeuroD1+ cell population transitioned to a cell cycle exit, unlike the population driven by the ubiquitous promoter pCAG (Fig. 43). The pCAG+ cell population continued to cycle, which was accompanied by gene expression typical for “progenitor” transcription factors such as *Pax6* and even *Tbr2* in the pCAG+ population (Suppl. Fig. 18, panel “Transcription factors”).

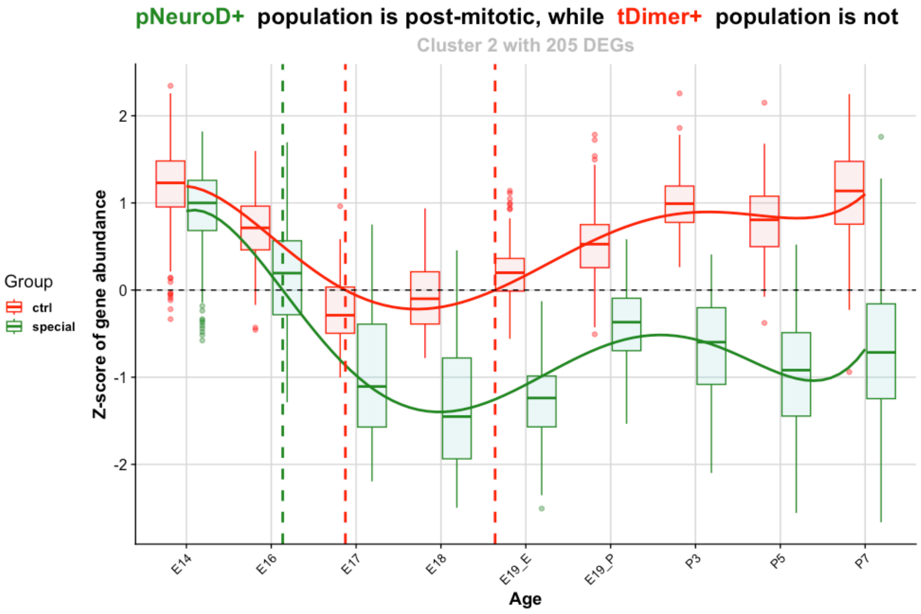

Figure 43: The pNeuroD1-eGFP+ cell population is post-mitotic, while the pCAG-tDimer+ population is not

Zoom on cluster 2 in the DEG analysis of figure 23 with enhanced population contrast. Cell cycle dynamics were actively down-regulated after E16. The pNeuroD1+ population drastically decreases its gene expression associated with "nuclear division" (GO:0000280) and "DNA replication" (GO:0006260) below average gene expression.

As IPCs give rise to ULNs, they undergo another phase of symmetrical mitosis. In general, IPCs undergo 1-3 symmetric progenitor divisions before exiting the cell cycle [11], which they even transiently suppress [392]. Delamination processes trigger the suppression of *Cdkn1c* [339] and the switch from cyclin D1 to D2 during IPC genesis, which links migration events to cell cycle dynamics [116,430]. The timing of cell cycle exit itself has been independent of the determinants of cell fate, implying that pure time spent cycling does not lead to IPC- or RGC-mediated neurogenesis [431, 432]. However, bio-horological experiments on IPC mitoses have shown that the transcriptional landscape of the late-born EOMES+ population correlates with the gene expression of the later upper-layer II/III neuronal population [54,433–435].

IPCs invest more time in G1 phase for quality control of mitotically replicated DNA than RGCs [436,437]. The more the G1 phase was delayed e.g. by calcium induction or by overexpression of *p25* [438], the longer IPCs could increase their cell production [439–442]. IPCs delay the acquisition of laminar fate by resolving poised enhancer states and modulating their cell cycle length and number within the SVZ [10,443]. Here, the IPC marker gene, *Tbr2*, was biphasically regulated (Fig. 33): Its expression was slightly down-regulated just before migration (E17) and then drastically down-regulated after birth (P3), which was also gradually observed at the protein level. This sequential decrease could be an indication of different requirements in these phases. Perhaps, EOMES is part of a feedback loop regarding the exit from the cell cycle that closed completely after birth. In this way, developing neurons gradually lost retrograde fate plasticity during corticogenesis, as shown by many heterochronic transplantation and electroporation studies [100,444,445].

Terminal differentiation in neurons, to which IPCs gradually transition, differs from qui- or senescence. The involvement of signalling pathways such as Notch/Dll, which suppress cell cycle dynamics [446] permanently, makes the terminal cell cycle exit specific. From E14 onwards, neuronal progenitors began to express neogenin [447], which triggered terminal differentiation of the just emerging neurons by downregulating E2F1 [448], thereby impairing CDK5 activity [449]. Acetyl-CoA helped regulate the epigenetic status of neurogenic pioneer factors such as *Ngn1* and *Neurod1*, which had decreased gene expression from E14 to P7, mutually with the p53-inducible TIGAR complex [450]. TIGAR dephosphorylates RB and stabilises its association with E2F1 (part of the DREAM complex [451,452]) during migration, which is downregulated here over time, forcing an exit from the cell cycle [447,453]. However, this does not appear to be unique to the upper-layer population studied here. Both the upper and deep layer neurons go through a multipolar state and eventually exit the cell cycle [123].

Their basic functions, excitability and metabolism seemed to depend on this neuronal "G0" state. For example, the increasing establishment of the membrane potential influences the mitotic index via increased receptor expression and responsiveness to neurotrophic stimuli [197,454–456]. Due to the robustness of neuronal cell identity, the “barrier of no return” is probably not limited to a missing or added factor, but is formed by interdependent, reinforcing parameters at many levels of biological complexity. These levels mutually force progenitor cells into a highly specific neuronal niche, possibly driven by glutamate. The methods used here enabled mapping the entry and the maintenance of this state, but we still lack the “threads" that connect the levels of biological complexity.

► What regulatory landscape mediates the explicit formation of the upper layers?

Upper-layer neurons restrain their developmental competency within a narrow time window of a few days in mice. The ULN cell population exhibits heterogeneous cell identities, not only morphologically/histologically seen [457], but likewise evident in scRNA-seq experiments [408,409]. Their heterogeneous identity is primarily characterised by a catalogue of factors at different levels of biological complexity rather than by individual marker genes, as figure 16 showed. The specific upper layer characterisation of the cluster in the representative meta-analysis was based on individual marker genes that partly overlapped with the here sorted cell population (Fig. 19). Despite the lack of comparison with deep-layer neurons here, cluster analyses performed in this study revealed that important features of upper-layer neurons were overlooked in scRNA-seq data. Key patterns such as the immune activation and the drastic decrease in alternative splicing events in the pNeuroD1+ cell population suggest specific features of upper-layer developing neurons.

Below, only selected, important biological functions are discussed, as this is a rich multi-omic dataset that can be further explored from different perspectives. Comparative consecutive and cluster analyses, such as degPatterns and WGCNA, helped to derive key processes.

The pNeuroD1+ cell population physiologically activated immunogenic factors

In particular, the pNeuroD1+ population appeared to develop in response to environmental cues during untreated neurogenesis. One cluster derived by multicomparison analysis of the transcriptomic dataset was strikingly different with 1,395 out of a total of 5,467 DEGs enriched over time in the pNeuroD1+ compared to the pCAG+ population (Fig. 23, cluster 5; Fig. 44). These genes also represented the top loadings in the PCA that accounted for PC2 variability (Fig. 13A; Table 4).

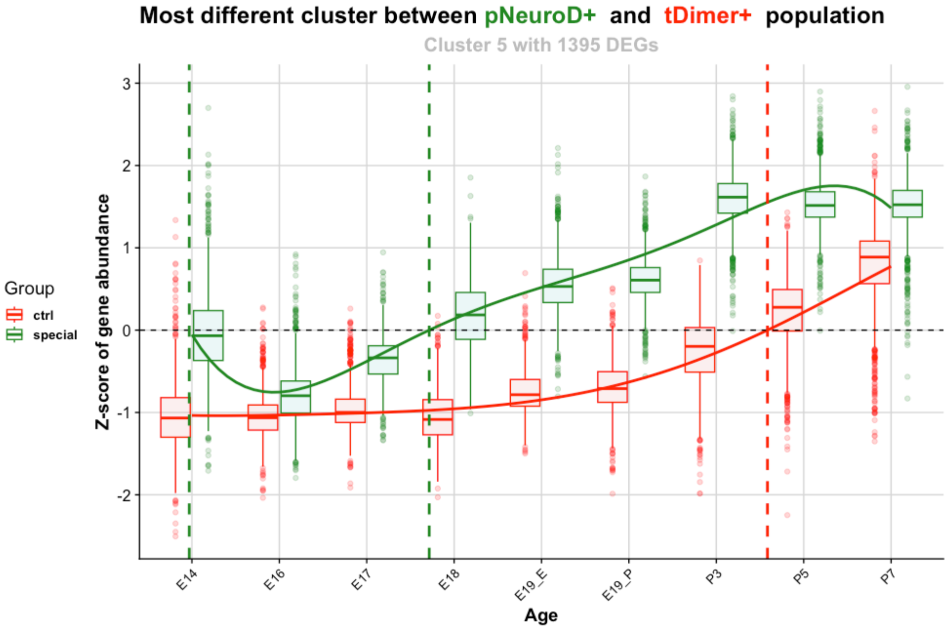

Figure 44: Cluster of most elevated gene expression of pNeuroD1-eGFP+ cell population in comparison with the pCAG-tDimer+ population

Zoom on cluster 5 in the DEG analysis of figure 23 with enhanced population contrast. From E18, when most cells have stopped migrating, the pNeuroD1+ population has steadily increased gene expression, while the pCAG+ population first showed increased expression of these genes over average at P5.

Gene expression in this cluster differed most at time points E18/E19 between the “ctrl” and “special” cell populations. Among these genes were not only those being associated with "activation of immune response" (GO:0002253) but also with an “exclusive” expression by microglia (fractalkine receptor CX3CR1, scavenger receptor FCRL2, purinergic receptor P2RY12, complement factors C3, C1QA, B, C etc.; Suppl. Fig. 7; [300,356,458–460,461]).

Table 4: Genes (loadings in the PCA, Fig. 13A) segregating the untreated transcriptomic landscape along the first two PCs

According to the literature cited, the respective biological function of these genes indicates a microglial character along with known markers for inflammation of the untreated pNeuroD1+ cell population. These genes are marker genes for both homeostatic and disease-associated microglia as well as for microglial chemotaxis for scRNAseq. In contrast, genes associated with the pCAG+ cell population suggest a rather oligodendrocytic or astrocytic character.

Gene	***Description***	***Biological function (literature)***	***References***
Ccl4	C-C motif chemokine 4	Microglial marker, inflammatory signalling, blood-brain barrier disruption, ligand to CCR5, 8	465
Csf1r	Colony stimulating factor 1 receptor	Neurotrophic role during corticogenesis, binds CSF1 and IL-34, **RTK**	146, 304; 302, 303
Cx3cr1	Chemokine (C-X3-C motif) receptor 1	Microglial marker, impacts microglial activation, chemokine **GPCR**, binds Fcrl2	306, 309, 303
Fcrl2	Fc receptor-like 2/S	Microglial cell surface marker, ligand to CX3CR1	460
Gpnmb	Glycoprotein (transmembrane) nmb	Inflammation, improves memory, inhibition of oligodendrogenesis	466, 467
Laptm5	Lysosomal-associated protein transmembrane 5	Microglial marker, inflammation	468
Mrc1	Mannose receptor, C type 1	Microglial marker, cell surface receptor	469
Selenop	Selenoprotein P	Adult hippocampal neurogenesis	470
Spp1	Secreted phosphoprotein 1	Microglial marker, inflammation	
P2ry12	P2Y purinoreceptor 12	Microglial marker, **GPCR**, purinergic junction	313, 312, 471, 311
Gpr17	G protein-coupled receptor 17	Oligodendrocyte progenitors, myelination	472
Bcas1	Brain enriched myelin associated protein 1	Myelinating oligodendrocytes	473
Gpr37l1	G protein-coupled receptor 37-like 1	Oligodendrocyte progenitors, modulates extracellular glutamate concentration	474
Gfap	Glial fibrillary acidic protein	Radial glia cells	403, 17
Olig1	Oligodendrocyte transcription factor 1	Oligodendrocyte precursor cells, represses Dlx1/2	475, 476
Pdgfra	Platelet derived growth factor receptor, alpha	Myelinating oligodendrocytes, RTK	475, 477
Cldn10	Claudin-10	Astrocytes	478
Aqp4	Aquaporin-4	Water channel, Astrocytes	479

Lately, there is more and clearer evidence that the connections between neurons and microglia are complex from the progenitor state onwards. Chemokine-based extrinsic signals, such as the complement [462] and the Cxcr-Cxcl systems [463,464,306] have already been well-defined in the radial glia scaffold. Still, it is unclear how chemokines act on migrating neurons.

However, in this study, there was no evidence that eGFP+ cells had microglial character, as analyses were performed to exclude microglial contamination in pNeuroD1+ samples:

Firstly, these suspicious transcripts (Fig. 23, cluster 5) were highly enriched, with e.g. a log2 fold change of ~20 even in the RT-PCR (Fig. 17C, 18C). Considering the **mass spectrometry** results here, which primarily detected proteins derived from very abundant mRNA transcripts (Fig. 30A), both cell populations were purely neuronal (Fig. 26, 29). Post-transcriptional or post-translational mechanisms could have controlled their protein expression or stability. Additionally, these modifications could have caused transcript degradation, or proteases may also have degraded exactly these proteins immediately after their synthesis. However, as they were not consistently detected in the mass spectrometry experiments (Suppl. Fig. 8), these gene products did not crucially contribute to the pNeuroD1+ cell population identity.

Secondly, an anti-**CD11b flow cytometry** staining (Suppl. Fig. 5, 6) and **immunofluorescent staining** (Suppl. Fig. 3, 4) were performed to rule out a potential microglial contribution to the acquired untreated cell populations. Indeed, a subpopulation positive for the CD11b antibody was observed, mainly within the pNeuroD1-eGFP+ population, but also in the pCAG-tDimer+ population. The minor contribution of Cd11b+ cells to the pNeuroD1+ population (~5-10%, Suppl. Fig. 6) would be congruent, if of real microglial character, with Lawson et al. [480]. However, the former observation does not mirror the immunofluorescence staining results against Iba1/Aif1 (Suppl. Fig. 4). Microglia do not colocalise with the eGFP-transfected cells at this developmental stage. Moreover, the promoter of NeuroD1 to drive the expression of the fluorophore is specific for post-mitotic neurons [80,202,429], and microglia derive from another germ layer, the yolk sac. They physically cannot be hit by electroporation [298]. The minor presence of potential microglia in the pNeuroD1+ population therefore has no significant impact on the study results and does not hinder the efforts made here to improve scRNA-seq methods.

Given that this prominent expression of genes associated with "activation of immune response" (GO:0002253) plays a functional role in the upper-layer post-mitotic neuron population (pNeuroD1+), at least three hypotheses arise that need to be investigated in the future:

1. ‘**Paracrine signalling** orients the migrating neuron pool.’

   Interestingly, **both ligands as well as their receptors** of commonly reported chemoattractants were part of cluster 5 in Fig. 23. For example, the expression patterns of Cx3cr1 and its ligand Cx3cl1 have been extensively characterised between microglia, endothelial cells and neurons [346]. Here, both *Cx3cr1* and *Cx3cl1* were differentially expressed in pNeuroD1+ samples post migration. The same applied to *Tgfb1* and *Tgfbr2*, *Tnf* and *Tnfrsf11a*/*Tnfrsf13b*/*Tnfrsf1a*/*Tnfrsf1b*, and *Csf1* and *Csf1r*. Further experimental validation with **RT-PCR** of some of these signalling interactions, such as of *Csf1* and *Csf1r* and *Cx3cl1*, *Fcrl2*, and *Cx3cr1*, confirmed the relevance of these genes, both ligand and receptor, to pNeuroD1+ population identity (Fig. 17, 18). This could be indicative of paracrine signalling that helps the migrating neuron pool orient and perhaps even send stop signals once the pia is reached.

2. ‘**Neuromodulatory signalling** guides synaptic integration’

   Since 2010, research has particularly focused on microglia-mediated synaptic pruning during the establishment of neuronal circuits in early postnatal life [481]. Microglia phagocytose “overextruded” axon fragments as they preferentially accumulate around axons, called “**synaptic pruning**” [316,482,483]. In particular, the complement cascade components C1q and C3, which otherwise recognise pathogens in the immune system, are secreted by developing neurons to tag synaptic targets for microglia (CR3/CD11b+) [482,484]. Also here, *C1qa*, *C1qb*, and *C1qc* were among those immune-activating genes. Perhaps, synaptic pruning takes place directly once the first synapses are formed (Fig. 21, cluster 3).

   However, the genes upregulated in Fig. 23, cluster 5, are the **receptors** acting reportedly on microglia. They receive cues from e.g. the neurons. It cannot be ruled out that these by gene ontology assigned genes (e.g. to "leukocyte migration") are used for other purposes than described so far. Their implication of those genes with neurogenesis is rising: For example, the metabotropic purinoreceptor P2RY12 [485] was among those “immunomodulatory” genes, which was also validated by RT-PCR (Fig. 17, 18). P2RY12 is activated by ADP and adenosine fragments in the extracellular space. During neurogenesis, early K+ depolarisation evokes ATP, adenosine, and glutamate release [486]. ATP is a common co-transmitter that is degraded soon after secretion in the synaptic cleft. Intracellular targets for P2RY12 are Gαi proteins [487]; thus, they are closely related to non-canonical Wnt-mediated Ca^{2+} signalling via PLC- and subsequent PKC activation. This **purinergic neuromodulation pathway** is relevant for synaptic transmission and plasticity during neuronal development [488]. A crucial function appears to be the inhibitory action of P2Y receptors on presynaptic Ca^{2+} channels, which probably have a general modulatory function to enable the first orchestrated action potentials and to balance excitation versus inhibition from the beginning onwards [489–491].

   Another hint could be the enriched cluster of these DEGs on chromosome 11 (Suppl. Fig. 9): Chromosome 11 of the mm10 genome contains many important genes for **neurogenesis**, such as *Camk2b*, *Gria1*, *Trp53,* and *Igfbp4*, besides the enriched genes in this cluster 5 (Fig. 44). Their spatial proximity on chromosome 11 could indicate a mutual regulatory network or that they were just co-expressed without any functional significance. The other differentially expressed receptors in this cluster were more specialised in chemokine and growth factor ligands, which probably have a pronounced **guidance** function for ULNs.

3. ‘Chemokine receptors trigger **primary cilium** re-establishment’.

   Most of these genes associated with “activation of the immune system" were chemokine **GPCRs and RTKs**, which mediate communication between microglia and neurons (Table 4). During **ciliogenesis**, which was upregulated concomitantly with this gene cluster 5 in Fig. 23 (Fig. 21, cluster 4), GPCRs and RTKs play at least as important a role [492–495]. It is possible that these genes have a novel function in restoring the primary cilium on developing neurons [496,497].

These results suggest an environment-dependent feedback loop crucial for ULNs, which have to migrate the farthest. Given that the gene expression of immunogenic factors in neurons has not been reported to such an extend in the past, and given that past studies were based on whole cortex experiments, I hypothesise that these immunogenic factors are specific for upper-layer neurons.

This novel and unexpected finding expands our understanding of the complex biology of neurogenesis and underscores the importance of analysing specific cell populations physiologically targeted by the study. Since adult neurogenesis has been highly correlated with embryonic neurogenesis [8,23,198,230], the data obtained here may help to advance their approaches. One of the main problems of adult neurogenesis is the migration and subsequent integration of the newly formed neurons. This study shows evidence for chemokine and cytokine receptors that can contribute to the path of e.g. synaptic integration. Further studies are needed to clarify the exact functions and relevance of these molecules in migratory and post-migratory neurons.

Molecular dynamics in developing neurons

Considering that the here used RNA-seq read count summarizer "featureCounts" [370] with build-in reference mm10 genome resulted in 27,179 unique Entrez gene identifiers, and given that the mouse genome encompasses 22,018 protein-coding genes [498], almost half of it was differentially regulated during the here mapped time frame (13,314 DEGs with reduced ~Population contrast). The large amount of DEGs across time indicates a substantial rearrangement of the mRNA transcript abundance, mainly visible at the progenitor stage and at birth. These rearrangements were differently coordinated at mRNA transcript and protein level:

Cluster analyses of RNA-seq counts revealed predominantly synchronised dynamics, but also anticorrelated gene expressions. RNA splicing and protein association with centrosomes/chromosomes were inversely regulated to membrane potential and small molecule catabolic processes (Fig. 21, 22). In addition, axonogenesis was temporally flanked by mitotic processes. During development, various cellular structures, such as members of the actin network, were dynamically reorganised, preceding the actual execution of cellular processes, such as migration (Fig. 21, 22). These preparatory changes facilitate the correct course of development that cannot be captured by a consecutive analysis alone, even if the consecutive analysis already well recapitulated *in vitro* morphological observations [104], both in bipolar and multipolar progenitor cells [79,104]. The migratory state had exceptional effects on the pNeuroD1+ cells. So-called "marker" genes for upper-layer neurons were regulated either before or after migration (Fig. 16), and consecutive analysis (Fig. 20) revealed relatively few genes that changed their mRNA transcript levels during migration.

Mass spectrometry results revealed a typical development from an early neuronal precursor cell to a differentiated neuron (Fig. 27, 28). As with RNA-seq, the largest detected fraction of proteins belonging to "neuron projection development" (GO:0031175), translation at synapse (GO:0140241), and neurotransmitter transport (GO:0006836) were upregulated towards birth, while mitotic cell cycle phase transition (GO:0044772) and RNA splicing (GO:0008380) were downregulated (Fig 28). This generally followed a **time-delayed** trend (Fig. 31, 32). Here, biological processes were prepared. For example, axonogenesis and membrane potential follow a sequential expression pattern. They were first upregulated at the transcriptome level and then, one or two days later, differentially detected at the protein level. This pattern confirms the central dogma of DNA to mRNA to protein expression. The discrepancies between gene and protein levels can be traced back to regulatory mechanisms or post-translational modifications [423]. Overall, the time delay between the transcriptomic and proteomic levels establishes enable regulatory networks to govern developmental processes. All further described rearrangements were subject to the sequential occurrence over time.

Developing upper-layer neurons underwent drastic metabolic, cytoskeletal, and transcriptional rearrangements

The plastic IPC stage enabled ULNs particularly to redefine molecular pathways and to allow for specific environmental guidance: In preparation for radial migration, progenitor cells upregulated disintegrins such as *Adam17* [105] to detach from the early cell context (Fig. 9B) and transiently expressed adhesion molecules such as cadherins, laminin, and vimentin, which then aid in radial fibre attachment and repeated detachment [108–112]. For example, N-cadherin and the ‘piezo-type mechanosensitive ion channel component 1’ (*Piezo1*), which were downregulated after migration, mediated radial glia-driven locomotion and durotaxis of young neurons [15,106,107,124]. Protocadherin-19 [53] and cadherin 11 [115,116], known for their role in neural tube differentiation, are important regulators in mediating radial migration of multipolar cells and were downregulated here after E19. These cadherins also play a crucial role in polarity formation, which happens simultaneously with preparation for migration [396]. Neurogenic transcription factors such as Neurod1 and Tbr2 and morphogenic signalling supported their transient expression and proper laminar formation [108,110,114]. For example, the canonical Wnt signalling pathway played a decisive role in transforming RGCs into IPCs [113,494,495,499–501].

During migration itself and in the postnatal stage, almost no DEG was detected at the statistical thresholds applied here. This does not mean these cells have ceased transcription but have maintained expression levels.

After birth, ULNs further rearranged their ECM (Fig. 22; 34), elongated their axon (Fig. 9B, prominent fluorescence of axons at P3), repositioned their cilium, and established synaptic connections.

These processes have already been described and overlap with the results presented here ([502,503]; Suppl. Fig. 18). However, this study now provides a more detailed picture of how ULNs carry out these processes and at what point they prepare for which process.

Membrane potential-based upper-layer neuronal functionality

ULNs mature not only morphologically but also electrophysiologically: By timely regulation of their ion channel expression and secretion of inhibitory and excitatory neurotransmitters, they build up a membrane potential that is initially spontaneous and eventually becomes activity-dependent [157–159,503]. Prominently shown by cluster analysis, ULNs gradually upregulate their excitatory functions opposite to the downregulation of RNA splicing or cell cycle exit (mRNA: Fig. 22, 23; protein: Fig. 28), which were the main biological functions at the protein level. The glutamatergic fate of the neuronal populations studied here was initiated during migration, during which neurotransmitter expression and regulation of synaptic growth began. Transcription factor activity prompted the sequential expression of transporters that ensured the balance of ionotropic neurotransmitters. First, GABA channels, such as *Gabra2* and *5* were upregulated at the progenitor stage. Interestingly, the kainate family of glutamate receptors, such as *Grik1* and *4,* and AMPA receptors, such as *Gria1* and *2*, which are ionotropic, were upregulated simultaneously. The kainate family expression was then overlaid by the expression of store-operated calcium entry proteins such as the transient receptor potential cation channel Trpc4 and calcium-dependent proteins such as *Camk2b* and phospholipase C, which also promoted axonal outgrowth via activation of non-canonical Wnt signalling [504].

Moreover, the expression of several voltage-gated calcium channels (Cacna family) and sodium chloride-dependent neurotransmitter transporters (Slc family) peaked at this stage, marking the “GABA shift” from excitatory to inhibitory function. Potassium channel expression (Kcn family) was differentially upregulated in the postmigratory phase. At the same time, metabotropic glutamate channels were first differentially regulated (e.g. *Grm5*, *Grm7*). Then, ionotropic glutamate channels such as the NMDA receptors *Grin1* and *Grin2a* followed. Finally, glutamate transporters such as *Glud1* and *Slc1a3* were upregulated (Suppl. Fig. 18). Once settled in their new location, layer II/III, ULNs established connections to the target soma or dendrites in the other hemisphere (Fig. 9B; [133,134,151]). Synaptic connections diversify and start to release neurotransmitters via synaptic vesicles. Synaptogenesis increased towards birth, slightly delayed to axon and dendrite formation (Fig. 20, 21, 22), which mutually account for the characteristic pyramidal shape of projection neurons and their functional activation.

Myelination of the young axons directly occurred by glia cells for which the pCAG+ samples were enriched, such as oligodendrocytes (Fig. 13B; Table 4). Ensheathed and isolated axons are metabolically more stable [505] and propagate the action potential faster, depending on the developmental stage [506,507]. Neuronal crosstalk with oligodendrocytes begins congruently with the onset of axon potential and the synchronisation via ionotropic receptors [90,508].

Metabolic switch to oxidative phosphorylation strengthened neuronal differentiation

The metabolic network fulfils the basic needs of developing neurons. Progenitor cells frequently colocalise with the vasculature to meet their high metabolic demands during differentiation [509]. Angiogenesis ensures the vascular supply of metabolically active transitory cells such as IPCs. IPCs are tightly associated with a honeycomb-like scaffold of blood vessels that invade the SVZ from E12 – paralleling the onset of IPC genesis and microglial invasion [37,76,510,511]. Mature neurons are generally metabolically demanding cells, challenged by the birth process and subsequent oxygen exposition.

Here, the daily changes of key rate-limiting enzymes of the respective metabolic pathways were followed at both the mRNA and protein levels. In general, metabolic factors were differentially regulated between the pNeuroD1+ and pCAG+ populations and opposed to the expression levels of cell cycle genes (Suppl. Fig. 18, panel “metabolism”).

The pNeuroD1+ population showed an integration of mitochondrial oxidative phosphorylation into energy metabolism. NEUROD1, also called BETA2, itself can alter metabolic demands of developing cells as coactivator of the insulin gene [512,513]. NEUROD1 controls the promoter of the insulin gene [512–514]. Neurod1 expression is increased at higher glucose availability [515], which is characteristic of a progenitor state rather than a differentiated state. Here, the insulin-like growth factor 2 mRNA-binding proteins *Igf2bp1* and *Igf2bp2* were among the most downregulated genes across the entire timeframe, suggesting a degradation of target mRNAs [516]. During the migration phase, pNeuroD1+ cells downregulated genes related to both glycolysis and oxidative phosphorylation. The drop in gene expression was explicitly prominent among members of the mitochondrial respiratory complex I and V (*Ndufa2*, *Ndufa7*, *Ndufa3*, *Ndufb2*, *Ndufa5*, *Ndufa1*, *Atp5e*, *Atp5k*, and *Atp5g1*). However, they were increasingly expressed again after the migratory stage.

Moreover, a steady upregulation of genes encoding for enzymes that increase the conversion of glucose to pyruvate promoted the entry of pyruvate into mitochondria, such as *Ldha* [517], pyruvate dehydrogenase kinase *Pdk4*, *Gapdh*, *Atp5c1*, and *Eno1.* Common enzymes sequentially effective in glycolysis such as hexokinase 1 (HK1), phosphofructokinases (PFKL, PFKP), fructose-biphosphate aldolases *Aldoc* and *Aldoa,* and the pyruvate kinase M (PKM) were upregulated. While the input for the mitochondria increased, the input for glycolysis gradually followed this trend.

Besides, fatty acid entry into mitochondria was increasingly enabled through upregulating protein level of the carnitine-palmitoyl transferase-1A (CPT1A) and genes responsible for “fatty acid metabolic process” (GO:0006631; Fig. 21) were increasingly expressed towards birth.

The lipid metabolism here was linked to catabolic processes such as the mitochondrial β-oxidation. β-oxidation serves via lipolysis for energy production and stem cell maintenance [518,519].

Expression levels related to mitochondrial fission (e.g. *Mff*, *Ppargc1a*, and *Esrrg*; Suppl. Fig. 18) peaked at the migratory stage and were upregulated at the protein level at postnatal stage [221,520]. The key modulators of mitochondrial metabolism, PGC-1α and ERRγ, enhanced glycolytic processes as the demand for pyruvate increased. They shift transcriptional control of mitochondrial and metabolic genes from a cell-cycling mode to a post-mitotic neuronal programme – in proliferating IPCs, MYC and E2Fs (here downregulated) activated the transcription of metabolic genes. In contrast, PGC-1α and ERRγ were responsible in differentiated neurons [221].

All these changes in energy supplies over time likely secured the “post-mitotic” state of the pNeuroD1+ cell population.

RNA splicing was downregulated

Factors associated with "RNA splicing" (GO:0008380) were significantly downregulated in both transcriptomics and proteomics (mRNA: Fig. 20, 21; protein: Fig. 28) from E14 to P7. This timely drop was more pronounced in pNeuroD1+ samples than in pCAG+ samples. Remarkably, this crucial downregulated biological process did not appear in the consecutive analysis of the transcriptome (Fig. 20). RNA splicing allows eukaryotic cells to produce many different isoforms of a single mRNA with varying functions by combinatorial removal of introns – so-called “alternative splicing” [540]. Exon skipping is the preferred form of alternative splicing during neurogenesis [541]. These skipped exons have been linked to microtubule cytoskeletal organisation, cell migration, and synaptic proteins [542–544]. RNA splicing factors such as *Ptbp2* and *Rbfox2*, which are constantly downregulated here, mediate balanced isoform expression during axonogenesis [84] and the assembly of the axon initial segment [545].

Furthermore, mature neurons translocate their mRNA to their synapses and dendrites [546] for local protein synthesis, usually with a low copy number [547]. “Transport” processes (GO:0006810) were most abundant in the proteomic dataset. Another effect of alternative splicing is the inherent tendency of neurons to have longer transcripts [548], so that even an R package for classification of neuronal identity has been created based on their characteristic longer RNA transcripts [549].

Suppression of RNA splicing events results in less diversity of translated proteins and promotes stem cell differentiation rather than proliferation. Fewer isoforms of a protein are formed, reducing its potential to be dynamically regulated. This in turn could be another barrier to re-entry into the cell cycle, as dynamic interventions in gene expression are required for cell fate acquisition. Lower alternative splicing events could promote the elimination of developmental transcripts [550–552] and allow for a terminally adapted cell fate. Protein isoforms relevant to neurogenic factors were even more specified to a differentiated state rather than a precursor state. For example, *Rbm4*/RMB4, which plays a crucial role during neurogenesis and neurite outgrowth, was downregulated over time [553]. Furthermore, actin itself was not differentially expressed, unlike actin regulators, such as drebrin 1 (*Dbn1*), which has previously been reported to change its isoform during neurogenesis [554]. Suppression of RNA splicing could lead to alternative splicing patterns, resulting in aberrant functionality or stability of otherwise spliced pre-mRNAs.

Thus, the expression of different isoforms was likely to be more important at the precursor stage. RNA splicing had to be explicitly repressed to develop into a mature ULN. Here, quantification was performed at the gene level, which does not distinguish between isoforms. Instead of using featureCounts, tools such as Salmon, designed explicitly for isoform quantification, could be used to reanalyse the dataset.

In summary, ULNs adjusted RNA splicing mechanisms over time, focussing on the mature neuronal translation.

Birth crucially matured upper-layer neurons accompanied by ciliogenesis

For transcriptomic analyses, the E19 time point was split into *in utero* samples (E19_E) and *ex utero* samples (E19_P), as the pooled samples showed a wide range of variation (Suppl. Fig. 14). With birth, the transcriptomic landscape ceased neurogenesis-related functions and upregulated specific functions for mature neurons (Fig. 20). Interestingly, the organisation of the primary cilium played an important role. “Cilium organisation” and "axoneme assembly" were enhanced in the postnatal, post-mitotic stage (Fig. 21, cluster 4).

A shift at birth also appeared at the protein level. Initially, more proteins were up-regulated than down-regulated, which reversed from birth onwards (Fig. 27). This shift could be attributed to biological functions, such as the absence of “RNA splicing” (GO:0008380, qvalue: 2.70E-10) associated DEPs and the increase in “cytoplasmic translation” (GO:0002181, qvalue: 0.0004) as well as the shift from pre- to postsynaptic organisation (GO:0140238, qvalue: 5.63E-07; GO:0099173, qvalue: 0.0005) (Fig. 28).

Remarkably, cluster gene expression for axonogenesis (e.g., *Robo1* and *2*) and cilium organisation (particularly *Cfap* expression) peaked at opposite levels at E17/E18. Axonogenesis, a process highly dependent on microtubules and actin, was reduced at the transcriptome level after migration, unlike ciliogenesis. At the protein level, axonogenesis-related levels were constantly high.

The neuronal primary cilium has a double role during neurogenesis, representing the intersection between cell cycle dynamics and cytoskeletal reorganisation:

In RGCs, primary cilia serve as intracellular signalling hubs [521] and apical anchorage, which points perpendicular to the ventricles. Primary cilia are longitudinal microtubule-based structures that form the central structure of the centrosome [522–524]. The two centrioles, as part of the centrosomal complex, condensate as the basal body of the primary cilium in interphase RGCs. As a signalling hub, the primary cilium controls 1. proliferation, 2. differentiation, and 3. polarity formation of RGCs, all via GPCR-driven signals transmitted through Shh or Wnt pathways [492–495]. With the help of diverse RTKs and GPCRs that play a crucial role here, especially in the pNeuroD1+ population, the primary cilia sense their environment, maintain the binding of aRGCs to the VZ, and thus prevent delamination.

During S phase (IKNM in RGCs, Fig. 2), the centrioles are duplicated and concentrate as centrosomes at the tip of each spindle pole. The daughter pair of centrioles then re-nucleates microtubules to form a new primary cilium with surrounding PCM of the new cell [525,526], which emerges apically in renewed RGCs or basally in differentiated neurons as a solitary microtubule-based growth process outside the cell soma. How the centrosome segregates and how the PCM surrounding the primary cilium is distributed [526], decides over symmetrical or asymmetrical division and over proliferation or differentiation of the neuronal progenitor cell [526–528]. The motility of the centrosome is therefore crucial for the correct extrusion of axonal growth cones from progenitor cells on their way to becoming neurons: Actin contractility and microtubule mechanodynamics depend on mutual interaction with the centrosome as the MTOC [79]. Here, regulation of cell projection was initiated simultaneously with axoneme assembly and microtubule polymerisation (see e.g. *Tubb3* expression), similar to that proposed *in vitro* [104]. The axoneme is the structural core of the microtubules, which compose the primary cilium.

For mitosis, the primary cilium is retracted for cytokinesis upon RTKs and GPCR signalling [526,529] so that both centrioles are freed from the basal cilium body to form the spindle apparatus. Interestingly, most of these neurotrophic receptors expressed predominantly in the pNeuroD1+ cell population (Fig. 23, cluster 5) were RTKs and GPCRs. Certain neuron-specific GPCRs, such as serotonin receptor 6 (*Htr6*) and somatostatin receptor 3 (*Sstr3*), were downregulated after E14 [492,493]. GPCRs help transfer protein cargos along microtubules through intraflagellar transport (IFT) components and dynein, whose expression was particularly enriched towards birth, such as *Cfap*, *Dnah*, and *Dnai*, encoding ciliary and dynein proteins. They acted via calcium and cAMP signalling and were co-regulated with Wnt signalling processes (Fig. 24).

Thus, the centrioles switch their role during neurogenesis from being the basal body of the primary cilium to a mobile version as part of the spindle apparatus and back to a stationary function. Moreover, in ciliopathies, it is the centrosome motility that is affected, leading to micro- or megalencephaly or even to psychiatric disorders [302,530–532].

In developed projection neurons, the primary cilium is re-established on their soma [79,533]. Ultimately, primary cilia integrate mechano-chemical stimuli into cellular responses, which results in axon formation and subsequent extension. Their role in differentiated neurons is yet unclear. Perhaps, they help secure the location and integration into the cortical circuits, as well as maintain the post-mitotic state [521,534]. It raises the question of whether it additionally plays a role in the maturation of the upper layers of **premature infants**. Further research should focus on the reorganisation of the primary cilium during corticogenesis and its link to the “barrier of no return”. In a mouse model using the Zika virus, a virus particularly affecting the development of Tbr2+ IPCs, ciliopathy was a common aetiology [535,536]. The ciliopathy appeared to originate in immune activation rather than an effect of the birth date. Here, immunogenic activation by PolyI:C was not particularly correlated with ciliogenesis.

An association between neuronal ciliary reorganisation and oxidative stress was observed in postnatal samples, particularly in relation to the termination of neurogenesis. Considering that the main locations of proteins shifted from nuclear to subcellular and membrane regions at the proteomic level (Fig. 28B) and that early neurons ceased their cell cycle (Fig. 23, cluster 2; Fig. 43), this reorganisation of the primary cilium after birth may be characteristic of the post-mitotic state as described in cardiomyocytes [219]. The birth process may reflect a natural, systemic "stress" response that exacerbated the associated oxidative stress (Fig. 24) and, as a result, perhaps reinforced the “point of no return” in ULNs. This is consistent with Qiu et al., 2023 [253] and Castillo-Ruiz et al., 2018 [271], who found birth to be a crucial maturation point for the developmental system. The HPA axis as well as cytokine levels have been proposed to underlie preterm-associated and prenatal stressor-associated defects [7,537,538].

In addition, the postnatal samples had a higher variance in both modalities here. Perhaps, gene expression after the end of neurogenesis and at the beginning of the birth phase is more adapted to the individual organism and follows less of a strict developmental programme. However, this is only a hypothesis and needs to be further tested.

The IPC stage the ULNs undergo includes a second symmetric cell cycle and the subsequent long-distance migration into the upper layers of the CP. During migration, they do not change their transcription (Fig. 20A), but pull their centrosome upwards to the pial surface (Fig. 2; [79]). Perhaps the transcriptional information may be interpreted differently, because the centrosome has to reposition itself and some other polarised organelles, such as the Golgi apparatus. Perhaps this cytoplasmic repositioning of several organelles does not allow re-entry into the cell cycle. This raises the question: **What is the role of the neuronal centrosome and the primary cilium in terminally differentiated cells and, in the opposite case, during carcinogenesis [539]?**

► Do prenatal stressors influence upper-layer corticogenesis?

In utero exposure to e.g. pathogens has multiple effects closely interwoven with “normal” embryonic development, making it challenging to separate acute physiological signatures from altered development. Recent epidemiological events such as the COVID-19 pandemic and the Zika virus epidemic highlight the urgency of understanding the mechanistic aspects of **m**aternal **i**mmune **a**ctivation (**MIA**). This knowledge is critical for predicting and managing future viral challenges and their potential impact on maternal and foetal health.

Here, the focus was on the upper-layer neuronal population (pNeuroD1+) and their susceptibility to immunogenic hits during their development. In particular, these callosal neurons have been associated with histological and behavioural phenotypes in recent pandemics and related studies, such as the incidence of microcephalies upon Zika virus infection [292,305,325,335,536,555,556].

In the present study, the "stressed” ULN population was examined at three levels of biological complexity: RNA-seq, mass spectrometry, and DNA methylation assays, and over the time course from E18 to P3. In this way, the initial settlement of the newly differentiated neurons (E18) in their “destined” location, the upper layers, was recorded from the time of birth (E19) to three days after birth (P3) upon immune activation. As a stressor, two injections of the viral mimic PolyI:C together with PBS as control were administered to the mother mice before surgery. The cells of the offspring were analysed, analogous to the experiments for mapping unstressed genesis (Fig. 9A).

MIA administration was successful

First, **effects on immune activation** were confirmed via cytokine level measurements in the mother mice, which underwent double administration of PolyI:C at the onset of neurogenesis (Fig. 35). Administered PolyI:C binds to the maternal toll-like receptor 3 (TLR3) and thus stimulates an immune response, which is able to cross the placental barrier, the foetal choroid plexus, and the foetal blood-brain barrier. The insults, may they be of artificial or viral nature, reach the foetal brain via a disturbed cytokine balance, affecting the offspring also sustainably until postnatal age [286,332,557,558].

Here, maternal serum levels were indeed elevated, but the trend decreased on the way to the embryonic brain: In the placenta, cytokine levels were already relatively low in the treated conditions (PBS and PolyI:C) compared to the untreated conditions. In the embryonic brains, all cytokines measured were underrepresented in the treated groups, although this should be viewed with caution as only one observation was made in the naïve state. In contrast to other studies ([286,290,557,559]), cytokine levels were not checked a few hours after injection, so an earlier influence on the developmental system cannot be excluded. It is possible that the measured cytokine levels were merely equilibrated a few days later, in particular in peripheral tissues [558].

Still, PolyI:C increased the IL-2 concentration in the maternal serum. IL-2 is the ligand for IL-2R, which activates T-cell responses upon pathogen invasion. Its immunoregulatory role balances the adaptive and innate immune systems, making it a universal mediator of enhanced immune responses [560]. The two proinflammatory cytokines IFN-γ and TNF-α are the first cytokines released during immune activation, and both can cause neural tube defects when elevated during pregnancy [561]. They were not significantly increased in the sera of mother mice treated with PolyI:C and were even significantly decreased in the placenta, as were IL-1β and IL-10 (Fig. 35).

The **PBS condition had a medium effect on cytokine levels**, suggesting neither an effect that was not unique to the PolyI:C cohort nor the expected similarity to the completely untreated group. In fact, the PBS treatment showed an intermediate profile between the untreated and PolyI:C cohorts at all biological levels of complexity. All samples for all conditions were randomly collected between 2021 and 2023 to avoid sampling bias. Certainly, litter-to-litter variability may cause these differences; however, the daily handling of the MIA mice (PBS and PolyI:C) to document the weights likely triggered a general stress response. Both handling and anaesthesia have been reported to affect neurogenesis [562–565].

Interestingly, these differences were observed at E18, **a few days later** than the actual administration of PBS or PolyI:C. Meanwhile, mice of all conditions underwent surgery (*in utero* electroporation) with anaesthesia lasting about half an hour at E14, two and four days after injections. Under non-pregnant circumstances, cytokine levels in the peripheral blood of mice returned to baseline after only 1-3 days following viral infection. The lasting elevated cytokine levels in the peripheral blood sera might have been a pregnancy-specific response to the MIA treatment.

In conclusion, the significantly different serum levels in mother mice treated with PolyI:C report successful administration of the viral analogue PolyI:C. MIA was induced so further results can be reliably evaluated.

The number of **microglia** or their activation mode did not differ from their untreated counterpart (data not shown), not even in acute brain slices (data not shown, [559]). Microglia disappear temporarily from the cortical plate [306] within a specific time window between E17 and E18, precisely during the migration phase of the ULNs, and this did not change with MIA. However, upper layers have been reported to be slightly thickened in PolyI:C offspring [290,335], suggesting that MIA nevertheless had a substantial effect on upper-layer neurogenesis.

Changes in **DNA methylation** were anticipated upon stimulation with PolyI:C, as some DNA and histone methyltransferases that function biologically as epigenetic silencing signals appeared higher expressed in MIA treated animals (Fig. 41). Other studies reported global hypomethylation events in MIA treated C57BL/6J mice [426,566]. DNA methylation often contributes to neuroinflammatory responses reflected by DNA methylation of the *Grm2* [567] or the *Il-1β* promoter region [568]. DNA methylation of pro-inflammatory gene bodies served as an indicator of neurodegenerative diseases [569].
Here, EM-seq was used to reveal these potential effects of maternal immune activation in both PolyI:C- and PBS-treated embryos, along with pUC19 as a fully methylated SpikeIn control and the unmethylated λ-DNA SpikeIn control. In previous studies, EM-seq has outperformed standard bisulphite sequencing methods by preventing DNA depyrimidination and damage to unmethylated cytosines, also covering 5hmC modifications and working at lower DNA concentrations without affecting sequencing results [359]. Here, the sequencing depth of 50 million reads per sample yielded sufficient coverage to draw conclusions on differential methylation (Fig. 42, Suppl. Fig. 23). The unusual peak of 25% CpG methylation (Fig. 42A) should not interfere with the interpretation of the results.

No conclusive difference could be found between the PBS and the PolyI:C cohorts (Fig. 42). This resembles the RNA-seq outcome, where only subtle differences to the PBS group could be detected, whereas the difference to the naïve samples is prominent at E18.

MIA cohort differed in canonical Wnt pathway and synaptic processes

At the **transcriptomic** level, WGCNA was used to explicitly test the impact of MIA on the physiological landscape as it not only assessed DEGs, unlike degPatterns, but incorporated the entire data set (E18-P3) to provide an unbiased analysis. WGCNA tested the effects of MIA on all other conditions tested (e.g. cell population association), allowing for a holistic evaluation. MIA treatment correlated with the pNeuroD1+ cell population, which may be attributed to the unequal ratio of 32 pNeuroD+ to 9 pCAG+ samples within the MIA cohort (Fig. 36A, 37A).

Five modules were mainly associated with MIA. The pink and red modules strongly correlated positively and negatively with MIA treatment. They comprised a small number of a few hundred genes (Fig. 37A), but these genes targeted signalling pathways essential for the function of upper-layer neurons (Fig. 37B). Also, these genes overlapped with markers of ASD (Fig. 38C).

Gene expression of the pink module – related to “Wnt signalling” and “Ras protein signalling” – was enriched in the MIA progeny and even more in the PolyI:C-treated group (Fig. 38). In contrast, the PolyI:C-treated samples were underrepresented in red module genes related to the regulation of synapse organisation and dendritic spine organisation, compared to the untreated group.

Wnt signalling is an evolutionarily conserved signalling cascade that accompanies neuronal differentiation from the initial specification of neuronal progenitors, through their radial migration, to their transition into differentiated neurons [80,499–501]. In unstressed corticogenesis, the Wnt signalling pathway specifically controls the development of callosal layer II/III neurons [570]. Again, in the untreated context, genes of the Wnt signalling pathway were expressed pre- and postnatally, which in turn was related to neuronal maturation (Fig. 24, 37A). At the protein level, only a few signalling factors were detected, and several values were missing for these factors (Fig. 34; Suppl. Fig. 18).

Wnt signalling can be divided into a β-catenin-dependent (canonical) and a β-catenin independent version (non-canonical). During neurogenesis of cortical projection neurons, the canonical pathway is increasingly replaced by the non-canonical pathway to meet different developmental hallmarks [571–573]:

The **canonical** version was mainly responsible for the neuronal progenitor pool’s expansion, migration, and first differentiation due to transcriptional activity triggered by β-catenin [184,495,574,575].

Once secreted, Wnt ligands form a transmembrane heterodimer with a frizzled receptor (here: *Fzd3*. *Fzd1* and *2* were downregulated after the progenitor state) and its co-receptor *Lrp5/6*. Here, *Lrp3* was upregulated in the PolyI:C treated condition instead of *Lrp5/6* [110], together with *Ryk* [504]. They recruit the mediator proteins *Dvl1* (here present: *Dvl1,2,3*, Fig. 38C) and *Axin* (here present: *Axin1*), respectively, which then stabilise the otherwise constantly degraded β-catenin output and enable its translocation into the nucleus [576],[577]. Intranuclearly, β-catenin associates with Tcf transcription factors (here present: *Tcf7*), eventually triggering the transcription of Wnt target genes [500,504,578,579]. The transcription factor NEUROD1, for example, regulates calcium-dependent delamination as a target gene of Wnt [181,183,184]. Other proneural transcription factors are likewise target genes of this canonical Wnt signalling [181],[580] to activate cell cycle dynamics [184,581,582]. Gene expression of δ-catenin (*Ctnnd1*), first expressed in neuronal progenitors and later in dendritic structures [583], was upregulated in the pink module.

In contrast, the **non-canonical** version consists of two β-catenin-independent pathways with different biological implementations: a Wnt pathway with calcium as a second messenger that triggers cell proliferation and the **p**lanar **c**ell **p**olarity (**PCP**) pathway, which is primarily associated with neuronal polarisation and axon guidance.

Already in the untreated state, the pNeuroD1+ population showed unique properties in terms of forming synaptic connections and exploiting the activity of small GTPases (e.g. CDC42, RND2, RYK/Ras proteins) during migration. Interestingly, GTPases and guanine nucleotide exchange factors played an elevated role in the MIA condition (pink module), which can be attributed to enhanced expression of microtubule genes and increased utilisation of G-proteins and GTPases in conjunction with e.g. Wnt and purinergic signalling transductions, which are worth investigating their modulatory function. For example, Ras-related proteins were upregulated in PolyI:C treated samples. These GTPases control vesicle transport and movement within neurons and play a central role in the non-canonical Wnt-PCP pathway. Ras proteins are closely associated with polarised cellular organelles such as the Golgi apparatus, endosomes, and lysosomes [584], and this way ensure that synaptic vesicles reach the presynapse. The PCP proteins disheveled 1-3 (*Dvl1-3*), *Fzd3*, and frizzled coreceptor *Ryk*, modulate axonogenesis [585] and the synaptogenic activity of Wnt [586]. The unphosphorylated version of Dvl binds small GTPases such as the Ras-related proteins, RhoA, Rnd2 and 3, which is typical for emerging projection neurons [587,588] as they in turn are mutually controlled by neurogenic transcription factors such as neurogenin 2 (*Neurog2*) and achaete-scute homolog 1 (*Ascl1*) [340,406,589]. Disruptions in the PCP pathway can lead to impaired distribution of polarised cell organelles such as the Golgi apparatus and have ultimately led to aberrant lamination [590] and have been linked to increased susceptibility to schizophrenia [591].

The relationship between the three major Wnt signalling pathways is fluid and context-dependent [592]. For example, in the physiological context, Wnt manipulates polarity and promotes the multipolar-to-bipolar transition through the association of N-cadherin [500,593] and cortical plate lamination through the stabilisation of β-catenin [9,74,123,570,594]. In addition, Wnt and glutamate receptors also orchestrate asymmetric cell division [456]. The target genes of Wnt signalling differ depending on the stage of development, and the components of the signalling cascade are shared between Wnt signalling pathways.

Here, however, the pink module genes were more associated with canonical rather than with non-canonical Wnt signalling (Fig. 38, 39). Expression levels for Wnt signalling were asynchronously increased after PolyI:C administration compared to the untreated condition. In contrast, gene expression related to synaptic organisation was variable, covering a wide range of expression levels across replicates. These significant changes induced by treatment were pronounced at E18 and then disappeared at birth, suggesting a potentially vulnerable time window at E18. Given that synaptic plasticity seems to be disrupted in MIA offspring at the protein level, impaired connectivity in the postnatal period cannot be ruled out. This is consistent with studies by [325,595–598], which suggest that MIA leads to transient dysregulation in cytoarchitecture when occurring during a crucial window of late gestation.

Here, PolyI:C treatment modulated expression patterns that are likely cumulative for the same biological process: synaptic processes (Suppl. Fig. 20). PolyI:C administration primarily increased gene expression of the Wnt signalling pathway compared to its untreated counterpart (Fig. 37, 38, 39). Conversely, PolyI:C treatment also subtly downregulated synaptic gene expression. These otherwise did not overlap with those genes related to immune activation from cluster 5 (Fig. 23). Instead, they exhibited a different range of log2 fold changes in the transcriptome of PolyI:C treated animals, which deviated from the consistent log2 fold changes of their untreated counterparts.

The applied immunogenic hit also revealed differentially regulated postsynaptic- and dendritic-associated genes, recapitulating previous studies linking these genes to ASD-like behaviour. It is already known that MIA impacts the upper cortical layers [290] and causes the loss of cognitive flexibility [556] measured in the prefrontal cortex of MIA offspring [599]. The influence of MIA on dendritic development is largely unknown [600]. In murine Zika offspring, ciliopathies contributed to microcephaly [535,536], and in a recent collaboration with Prof. Gabriel, we found more basal dendritic spines than the untreated cohort (data not shown).

Together, these results suggest that neurodevelopmental deficits in MIA are not primarily mediated by microglia but are likely mediated by activation of the canonical Wnt pathway of glutamate projection neurons. This had implications for synaptic processes, also at protein level. The effects of PolyI:C treatment on synaptic circuitry are supported by a range of studies, some of which even link it to behavioural abnormalities on this basis.

For example, synaptic Ras GTPase activating protein 1 (*Syngap1*), downregulated or unreliably expressed in the MIA condition, plays a vital role in mediating synaptic connectivity and maintaining excitatory and inhibitory potentials (E/I balance). Mutations of the SYNGAP1 locus have been associated with epilepsy and deficits in working memory and motor function [601].

Members of the Shank genes were likewise downregulated in the PolyI:C cohort compared with their naïve counterparts at the transcriptomic level. Even the EM-seq analysis showed more methylation percentage for the promoter region of Shank2 in PolyI:C than in PBS samples, indicating that the promoter of Shank2 was more silenced and the transcription impaired (Suppl. Fig. 23). Mutations in any of the Shank (**SH3** And Multiple Ankyrin Repeat Domains Protein) genes often caused shankopathies [602,603] – neurodevelopmental disorders closely linked to the postsynaptic NMDAR/glutamate signalling pathway. Thus, Shank genes play a central role in the development and function of the upper layers of the prefrontal cortex. Differential gene expression of previously identified risk factors for ASD, such as Shank 1-3 and Syngap1, may provide a plausible explanation for the subtle ASD-like phenotypic changes, even if the underlying cause was different [597,604]. Thereby, early enrichment measures could counteract this process, which thus seems to be partly reversible. Early life stress in general disrupted E/I balance [162,605] and accelerated neuronal maturation [606].

Rho-associated coiled-coil containing protein kinase (ROCK1) [607] and centromere protein V (CENPV) were among the proteins that were upregulated in the PolyI:C condition at the proteomic level (Fig. 40). CENPVs regulate dendrite development, support microtubule formation through association with **SH3** domains and reflect post-transcriptional stress responses, but also highlight the potential for intervention [609]. In contrast, the upper-layer neuronal marker SATB2 was downregulated (Fig. 40).

Even though the Wnt signalling pathway plays a crucial role in shaping the architecture and functionality of emerging neural circuits, its specific effect during immune stress has not yet been demonstrated. The activity-dependent neuroprotective protein *Adnp* was among the "pink" module genes, whose gene expression were upregulated in the MIA-treated cohort (Fig. 38). Perhaps, the Wnt signalling pathway had a compensatory function to balance the impaired synaptic function, which is essential for the identity of an upper-layer neuron. Here, Wnt signalling could even be one of the drivers of MIA-induced loss of synaptic processes/plasticity. To clarify the role of Wnt signalling in MIA corticogenesis, optogenetic manipulation of this Wnt morphogen gradient can be conclusive [610,611]. It has already been discussed in another context [612] to target Wnt signalling to correct this abnormally upregulated canonical pathway. There, β-catenin is more suitable as a target than Dvl, since the latter is a mediator of all Wnt pathways.

Overall, maternal immune activation triggered subtle changes in pathways critical for cell differentiation and synaptic connectivity in the upper-layer neuronal population. These effects were likely independent of microglial activation, but rather dependent on the neuronal population itself, which subtly shifted its innate developmental programme upon immune activation. Subtle effects of the neurodevelopmental program can have long-term effects manifesting in neuropsychiatric symptoms [597],[604].

Besides, WGCNA showed signatures other than MIA-associated, which were age- and cell population-specific:

Intrinsically, the module clustering was biased to *in utero* vs. *ex utero* samples, highlighting the relevance of birth as a transition point [253]. This transition was even relevant to consider for the MIA treatment (Fig. 37). With respect to the four time points measured (E18, E19_E, E19_P, P3), the expression of genes related to axonogenesis, and Wnt signalling showed a negative correlation over time; initially high and then decreasing with age. Inversely, the gene expression of chromosome segregation showed a positive correlation over time, which was initially low and then increased with age. Among these genes were e.g. several Kif and other mitosis-associated genes. Postnatally, this “recycling" of mitotic factors may be crucial not for nuclear but for subcellular functions such as synaptic plasticity and dendrite formation at the mature stage, as shown by previous studies [613–615]. Genes generally associated with axonal functions often played concomitant roles in cell cycle regulation [616,617]. Considering that these projection neurons are still searching for target cells in the other hemisphere several days after birth, they could re-use these cell cycle genes for this purpose.

The previous prominent annotation of "immune activation" with the progressing age in the untreated cohort was indeed associated with the postnatally biased turquoise module in the WGCNA. This module was likewise strongly associated with the higher pNeuroD1+ sample size compared to the pCAG+ population. Generally, association with cell population was also clearly represented. While the pCAG+ samples showed more of a general biological association (see grey, turquoise, and magenta gene modules, Fig. 37B), the pNeuroD1+ samples contributed to specific neuronal functions, such as neurogenesis and learning.

► Limitations

First, in this study, only the upper layers of the neocortex were examined, while the deep layers could also be of major interest. Perhaps, a bioinformatic subtraction method could be implicated to investigate this further.

Secondly, IUE is an invasive method that can itself affect measurements, and Rosin, J. M. & Kurrasch, D. M. et al. 2018 [618] indeed reported an increase in proinflammatory cytokine and chemokine levels after IUE. IUE was nevertheless used here to express a fluorescent protein foreign to the system reliably. Also, the fluorophores introduced were expressed little to not at all one day after IUE, which is why the time point E15 was omitted in the experiments. This is a well-known conundrum of foreign vector expression, and can be ameliorated by e.g., implementing protocols based on a transposable-mediated gene expression switch [619].

Third, the postnatal samples had varying sample sizes due to difficulties in rearing the mice during the COVID-19 pandemic. This forced me to negotiate some cohorts but could be reassessed in the future. The long-term effects on the stressed offspring could provide new insights into the development of sporadic neurodegenerative diseases. These experiments can be performed in the future, as the fluorophores are stable within the murine brain for at least 4 weeks (Suppl. Fig. 2).

Moreover, flow cytometry can result in impurities, even though the proteomic analysis revealed a rather pure, neuronal cell identity. However, it is strongly recommended to use an anti-staining approach for e.g. microglia in future studies. This will help clarify and further understand these complicated cellular interactions. Furthermore, ATACseq was not possible to implement because the fluorophores were present in the cytoplasm. Thus, the FACS method could not be used, since the cells had to remain complete and healthy. To date, no cell sorter (BD devices) can guarantee neuronal viability during sorting; even the chip-based method (Sony device, SH800) did not work for the purposes of the present study.

MIA **modelled** an external stressor to interrogate the limits of physiological corticogenesis. Generally, the usage of PolyI:C in mouse models is conclusive, but the possible translation to human infection should be further investigated. PolyI:C can indeed mimic dsRNA viral infections. However, it has been found to produce different, not as sustainable phenotypes as, for example, H1N1 infection [286]. No prior baseline immunoreactivity was determined for the MIA experiments; therefore the samples were not selected accordingly as suggested by Estes et al., 2020 [620]. The general high variation of cytokine levels and sample loss in the sera can be attributed to the general detection limit when measuring concentrations in body fluids. Since only half of each sample was actually measured in the assay, the remaining samples could be repeated to enhance the resolution using a more sensitive method, e.g. novel FACS-based cytokine measurements as currently being set up in the RG of Prof. Gabriel.

A comparison between the naïve and PolyI:C conditions would perhaps have been more meaningful for the DNA methylome analyses, as the PBS administration showed an intermediate effect here and in all other assays. New experiments that include the naïve condition are already in preparation. The pooling of samples to achieve the DNA concentration required for EM-seq could have diluted the result due to biological variation. In addition, DMR analyses could in future be performed tile by tile rather than base pair by base pair.

Mass spectrometry presented additional methodological challenges:

- Missing values (dropouts) are common in mass spectrometry data because they imply multiple detection limits. The data cannot be amplified as in the RNA-seq library preparation, although the bead-based method implemented here has already improved the resolution. Furthermore, only half of the proteomics samples came from the same FACS experiment as the RNA-seq sample for the respective condition. The harvest dates of some samples were a year apart. Nevertheless, the correlation ranged from 70-79%, indicating methodological consistency and robustness of the experimental procedures (Fig. 31).
- The chosen threshold for DEP testing here was moderate, but given the limitations of mass spectrometry and the dynamics of the large time frame covered, probably no DEP was missed. Also, the first two principal components could never account for half of the variance in the contrasts tested, so further PCs would be needed to explain the sources of variance.
- Due to pooling problems, which was particularly necessary for the E19 samples, not all samples could be successfully recovered from mass spectrometry. These two groups were based on splitting the embryos from one litter, which reduced the cell count for these samples. Pooling of the samples reduced the total protein concentration, resulting in autotrypsinisation of the samples and thus increased “contamination” with keratin fragments. These samples were excluded from the analysis.

Finally, the samples were not separated by sex. About two-thirds of the postnatal mouse samples were male, based on eye checking of postnatal P3-P7 pups (low black pigment spot on the scrotum). However, sex-dependent effects of MIA at this early stage of development are still discussed ([290] vs. [621]).

These limitations should be considered when interpreting the results of this study.

Conclusion

> *“The property of a developmental process, of being to some extent modifiable, but to some extent resistant to modification, has been referred to as its “canalization” (Waddington, 1940a). This notion can be applied whether the agents which tend to modify the course of development arise from genetic changes or from changes in the environment. […]*
>
> *Embryos tend to regulate, that is to say, to produce their normal end-result in spite of external accidents which may occur to them as their development proceeds. […]*
>
> *One possible mode of approach to the topic would be to draw attention to the fact that development is usually easier to modify at early stages than late. […]*
>
> *The determination of the direction taken by a canalized pathway has been referred to as the “tuning” of it. (Waddington, 1957a)”* [622]

With this background, the question arose whether the developmental system described here can be influenced by external factors to produce alternative “canalized” paths [622,623]. “Stress” during gestation is known to cause neurodevelopmental deficits [624]. It may even affect later life [287], even though embryonal cortices are protected by a placental barrier [625], the choroid plexus [626], and the blood-brain barrier [627].

Here, I have focussed on the indirect neurogenesis of the upper layers, a developmental process that takes place in mice in a very narrow time window of only a few days. Its onset begins at the last third of gestation. During indirect neurogenesis, the upper-layer cell population is already set in an established microenvironment from the deep layers. Yet, it is a system with extended flexibility going through a plastic intermediate stage that includes a migratory event driven by cues from surrounding cells.

I applied a very common stressor on this system that is often not even noticed by the mother but is suspected of contributing to several aetiologies: a (here: artificial) viral infection. This externally applied stressor is an additional factor affecting the **interdependent processes** and can tune/undermine the **buffering** inherent in developmental systems.

Indeed, I have shown that the system of upper-layer corticogenesis has intrinsic capabilities that are subject to external forces. Their at first multipotent nature was “canalised” by the other layers of biological complexity, making it difficult to determine the respective contribution to constrain the spatio-temporal dynamics of the system [19,433]. Immunoregulatory factors were intrinsically key for establishing ULN cell identity, configuring membrane potential, and forming an axon. Especially those late-born neurons that prolong their time to differentiate with a second phase of cell-cycle and that squeeze past older neurons in the outside-last migration into the cortical plate afterwards are particularly prone to be guided by external factors. They must exchange neurotrophic factors with their environment.

This study raises new perspectives: Even if the effects of the external stress upon the physiological system applied here were subtle and were based on an underrepresentation of biological processes that might not have been registered in the absence of the untreated cohort, stress itself is a potent tool to “tune” cell identity. The resulting signatures of immune activation indeed overlapped with markers of ASD. Further research is needed to accurately explore the capacity of progenitor cells to respond appropriately to inductive cues and, generally, the limits of cell fate buffering.

Appendix

Fluorescent images

Constructs tested in embryonic brains

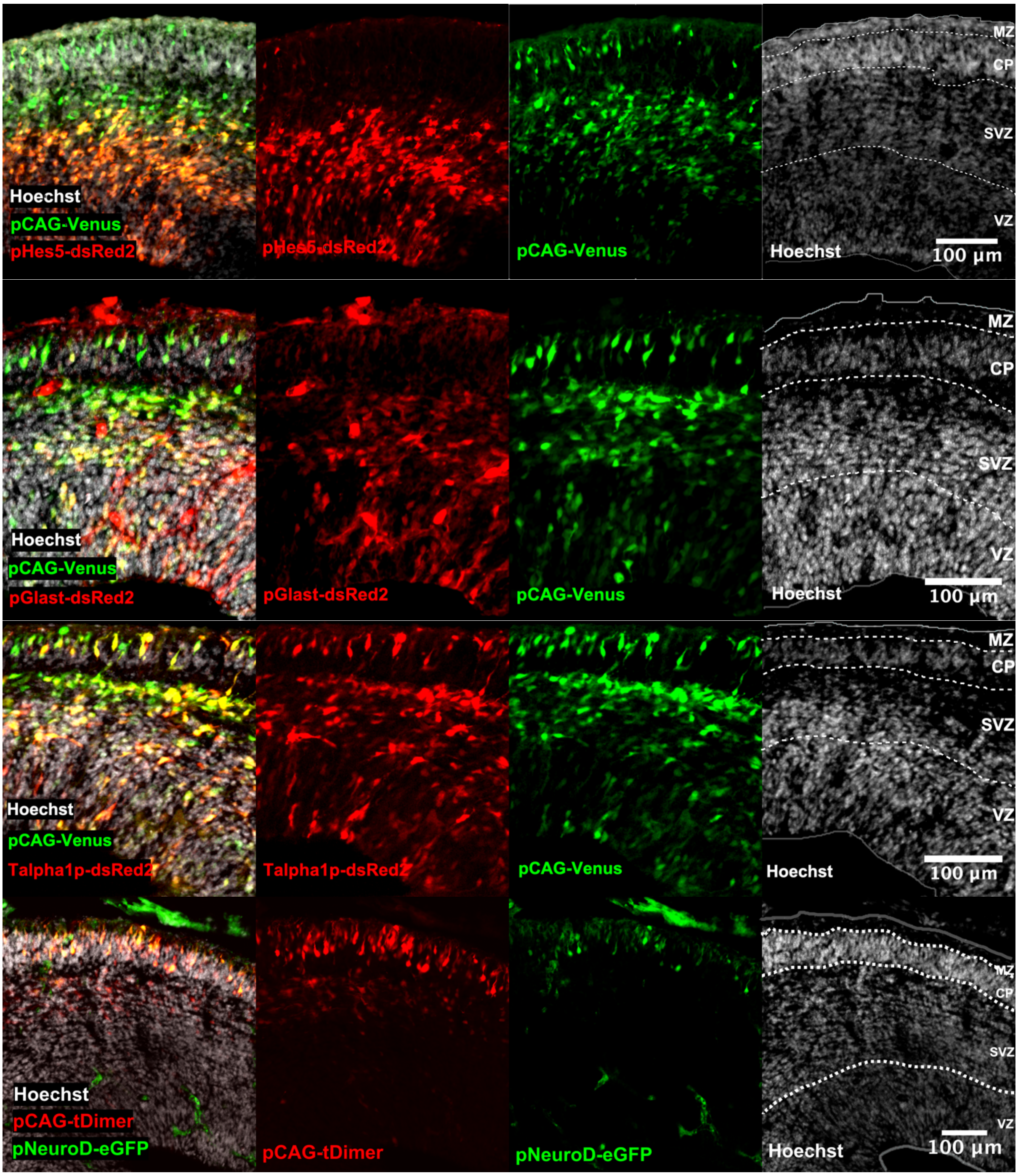

Caption continued on next page

Supplementary Figure 1: Representative coronal murine brain sections show the tested constructs at E14 (IUE at E12)

All constructs contain a developmentally active (pHes5, pGlast1, Talpha1p, pNeuroD1) and a ubiquitously expressed (pCAG) promoter cassette to drive expression of a fluorophore for subsequent flow cytometric detection. pHes5 labels neural progenitor cells with stem cell character, pGlast1 labels radial glia cells, Talpha1p labelled both neural progenitor cells and early neurons, and pNeuroD1 labelled early neurons. The first three plasmids were derived from [82], pNeuroD1 from [330]. For this study, pHes5 had too strong a stem cell character and Talpha1p overlapped too much both intermediate progenitor cell as well as early neuronal character. pNeuroD1 was only used from E14 onwards due to its low transfection rate if electroporated at E12.

Stable detection of fluorophore

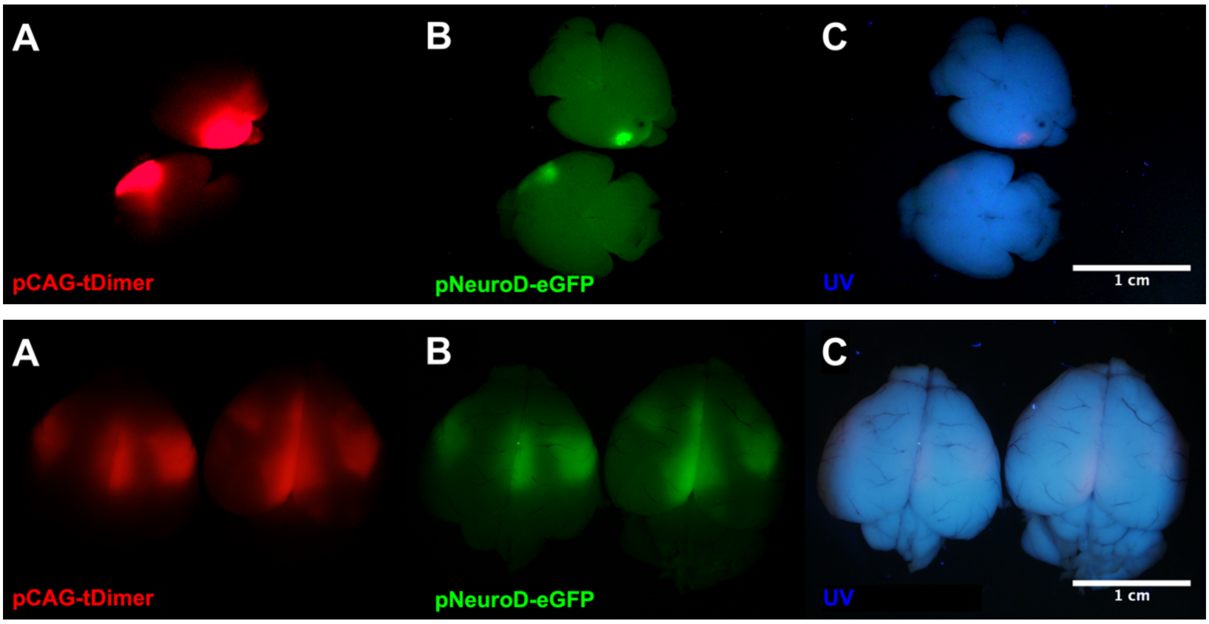

Supplementary Figure 2: The fluorescent signal of eGFP and tDimer is stable for at least four weeks in the murine brain

Even if expression for the particular gene targeted by the promoter of NeuroD1 has long since terminated, fluorescence can still be observed weeks after electroporation at E14. A) tDimer signal, B) eGFP signal, C) UV light. Scale bar: 1 cm.

Upper panel: P3 murine brain (IUE at E14, harvested at postnatal day 3).

Lower panel: One month old murine brain (IUE at E14, harvested four weeks after surgery).

Iba1+ cells in the young murine cortex

Ionised calcium binding adaptor molecule 1 (Iba1, also called Aif1) is expressed on the surface of microglial cells [305,307]. Iba1+ cells begin to invade the mouse brain in early neurogenesis and initially accumulate in the meninges, choroid plexus and ventricular zone (Suppl. Fig. 3), [305,307,626] The same observations were made here. However, they temporarily disappear from the cortical plate at E15/E16 [306] and do not cross the accumulating axonal fibres before E16 (Suppl. Fig. 3).

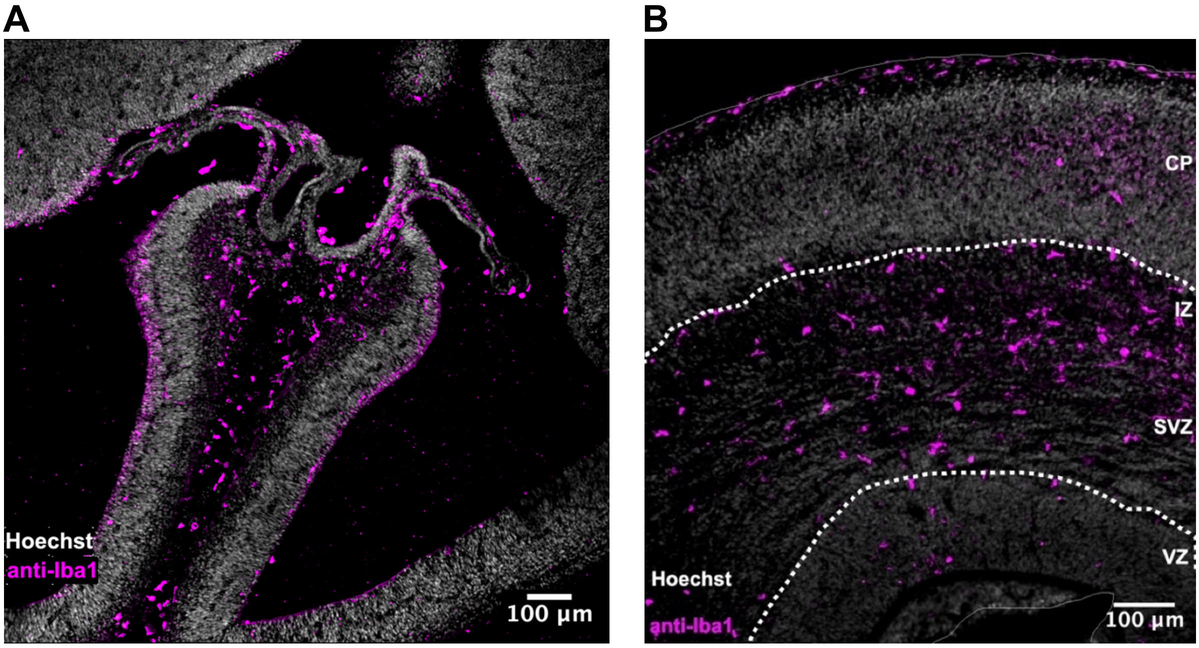

***Supplementary Figure 3:* Iba+ microglial cells localise to the choroid plexus and the subventricular zone in the developing murine cortex**

A. A representative coronal section shows both the cortex and choroid plexus of an E14 brain. Note the accumulation of Iba1+ microglial cells in the choroid plexus, while the cortex is not yet occupied by microglial cells.

B. Representative coronal section of an E16 cortex. Note that Iba1+ cells are localised on the outer surface near the pia, in the ventricular zone, and also mainly in the subventricular zone, but rarely cross the border to the cortical plate. For a comparison with rat cortex, please refer to Cunningham et al., 2013 [305].

Magenta staining represents anti-Iba1 staining, and the nuclei are stained in white with Hoechst. Scale bar: 100 µm.

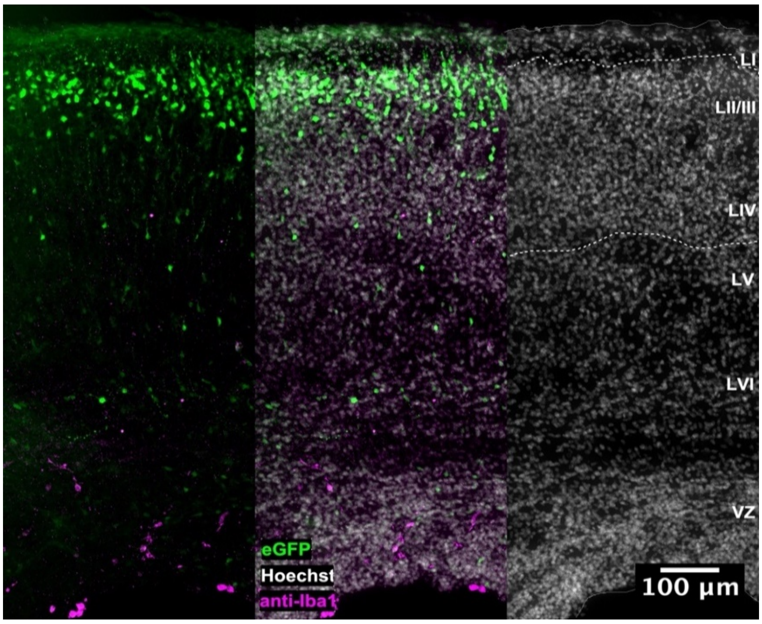

Supplementary Figure 4: pNeuroD1-eGFP+ cells do not stain for microglial marker Iba1

Representative coronal section of a somatosensory cortex of an E18 mouse. The green transfection represents eGFP fluorescence, the white staining shows Hoechst to stain for nuclei and the magenta staining represents anti-Iba1. Most pNeuroD1-eGFP+ cells have already terminated their migration and integrate into their new niche in the upper layers II/III. pNeuroD1-eGFP+ cells are not stained for Iba1, nor do they specifically colocalise with microglial cells at this stage. Scale bar: 100 µm.

Flow cytometry

Workflow for sorting transfected cortical tissue

After harvesting and dissociation of transfected cortical tissue:

- Transfer dissociated cells in 1x HBSS in a 15 mL Falcon tube at 4°C to the FACS facility. Work at 4°C under sterile conditions (also pre-cool the centrifuge).
- Collect the sorted cells in pre-made 1.5 mL Eppendorf tubes containing 0.5 mL FACS buffer (1x DPBS without $CaCl_2$ or $MgCl_2$ but with additional 2 mM EDTA).

Sort the respective cell numbers in the labelled Eppendorf tubes with at least 100 µm nozzle, low flow rate, and preset gates (see below).

1.1	10,000 cells	**Control cells** (positive for **pCAG-Venus** or **pCAG-tDimer**)
1.2	25,000 cells	
1.3	50,000 cells	
1.4	100,000 cells	
1.5	200,000 cells	
1.6	"leftover"	

2.1	10,000 cells	**"Special" cells** (positive for **pGlast1/dsRed2** or **pNeuroD1-eGFP**)
2.2	25,000 cells	
2.3	50,000 cells	
2.4	100,000 cells	
2.5	200,000 cells	
2.6	"leftover"	

Note: 2.x tubes are often cotransfected, and thus double positive (e.g. **eGFP**+ and **tDimer**+)!

- After sorting, centrifuge the Eppendorf tubes at 150xg for 10 minutes at 4°C.
- Remove the supernatant by gently pipetting without disturbing the cell pellet.
  Note: The cell pellet will not be visible –
  leave 10-20 µL FACS buffer at the bottom of the tube; it will contain the cell pellet.
- Immediately freeze the cell pellet on dry ice, transfer them back to the lab, and freeze them at -80°C for long-term storage.

Additional FAC sort identifies a Cd11b+ subpopulation in transfected cells

The purity of the pNeuroD1+ cell population was additionally assessed by anti-CD11b FAC sorting. The antibody was added to the usual transfected cell suspension, with a gating strategy for the transfected cells consistent with the one described in the method section for the conventional FACS experiments.

Staining against CD11b was used to detect potential microglial contamination of the sorted cell population. CD11b is a common surface marker to detect microglia in suspension[354]. The CD11b monoclonal antibody was coupled to APC (M1/70, APC, eBioscience™, CatNo. #17-0112-82) to avoid spill-overs into the filters used for sorting the pCAG-tDimer+ and pNeuroD1-eGFP+ cell populations. The red laser that excites at 633 nm was used to detect the APC, and the emitted light (emission maximum 660 nm, Suppl. Fig. 5) was detected by a band pass filter 660/20. To begin the staining process, 1µg/1mL of antibody was added to the triturated cell suspension and left on ice in the dark for 30 minutes with occasional gentle agitation every 5 minutes. The staining was then stopped by adding 4mL of HBSS buffer, and centrifuging the sample at 150xg for 15 minutes. The supernatant was removed, and the cell pellet was resuspended in 1 mL of 1x HBSS buffer before being transferred to the FACS facility. The sort strategy is shown in Suppl. Fig. 6.

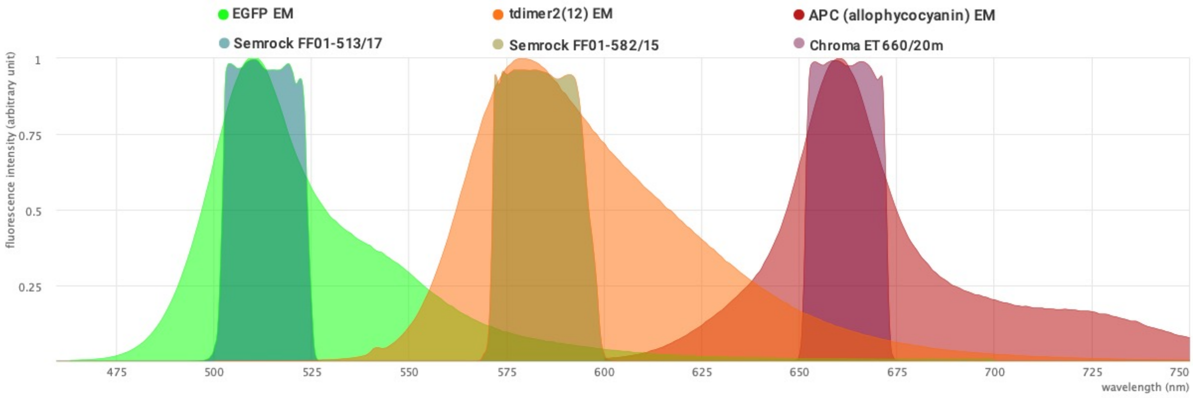

Supplementary Figure 5: The emission spectra of the fluorophores used overlap with the respective band-pass filters

The band-pass filters 660/20, 582/15, and 513/17 cover well the peaks of the emission spectra of the fluorophores used here (APC, tDimer and eGFP, respectively). The plot was generated with FPbase [362].

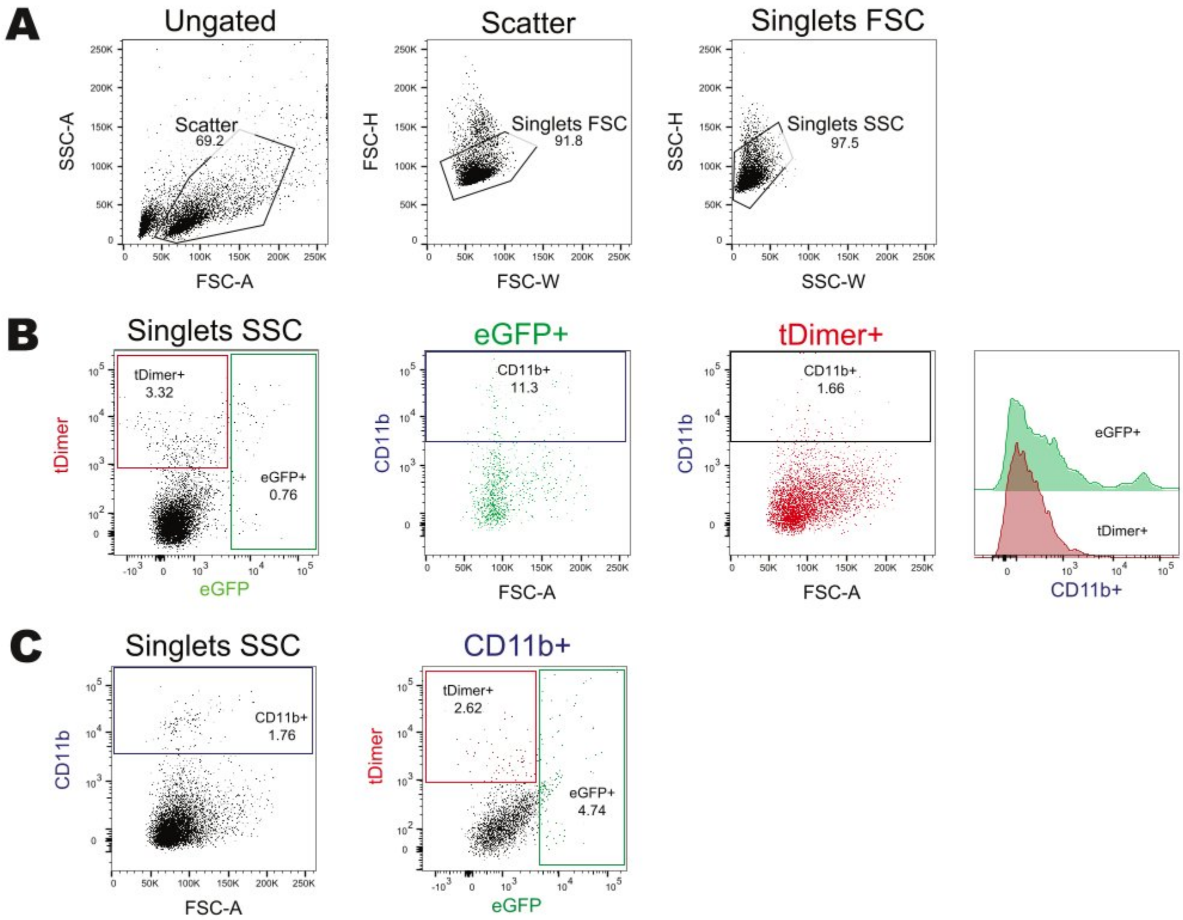

Supplementary Figure 6: Representative FlowJo matrices show the gating strategy for the identification of CD11b+ cells in relation to the transfected cells in E18 cortical tissue

A. Each sort decision begins with identifying the cell population of interest by plotting SSC-area (SSC-A) against FSC-A to compare the size and granularity of the scatter. Second, duplicates in this scatter were excluded by matching the width (W) against the height (H) of the FSC. These gated FSC singlets served as input for the detected cells in the SSC-H versus SSC-W plot. The resulting SSC singlet cell population was the final input for differential fluorescence detection every time the respective transfected areas were sorted and was used for detection of the here used antibody against CD11b. Without considering the addition of the CD11b antibody, the sorting strategy and the compensation is the same as described in Figure 6B.

B. Singlets SSC population of cotransfected samples with the construct pNeuroD1-eGFP/pCAG-tDimer shows the usual gating strategy in the left panel. The middle panels show the APC/Cd11b+ cells within the respective gated fluorophore (tDimer, eGFP). The right-most panel indicates the proportion of CD11b+ cells in the transfected populations as a histogram.

C. The same shown as in B), but with another gating strategy. First, the APC/CD11b+ cells were gated, and from this gate the transfected cells identified. Still, the percentage of CD11b+ cells was doubled in the pNeuroD1-eGFP+ population compared to the pCAG-tDimer+ population.

Both the pNeuroD1-eGFP+ cell population and the pCAG-tDimer+ cell population showed a CD11b+ subpopulation; the eGFP+ cells more (4.74%) than the tDimer+ cells (2.42%) (Suppl. Fig. 6).

Potential contribution of microglia to pNeuroD1+ population limited to transcriptome

In the previous RNA-seq analysis, one cluster was predominant in the pNeuroD1+ population with a total of 1,395 DEGs, while both pCAG+ and pNeuroD1+ populations were otherwise very similar. This cluster was enriched for "activation of immune response" (GO:0002253), suggesting that the immune system fundamentally contributed to the cell identity of the pNeuroD1+ population. Some of these genes have been typically associated with antigen-presenting immune cells, often considered as "exclusively" expressed in microglia [300,323,353], or with the recruitment of inflammatory mediators. However, there is evidence that microglia may also derive from nestin+ neural progenitors, not only through clonal expansion of the myeloid lineage [628]. Here, nestin is highly expressed at the protein level at E14, the time of IUE for the pNeuroD1+ cells, as is Aif1/Iba1 (Fig. 33).

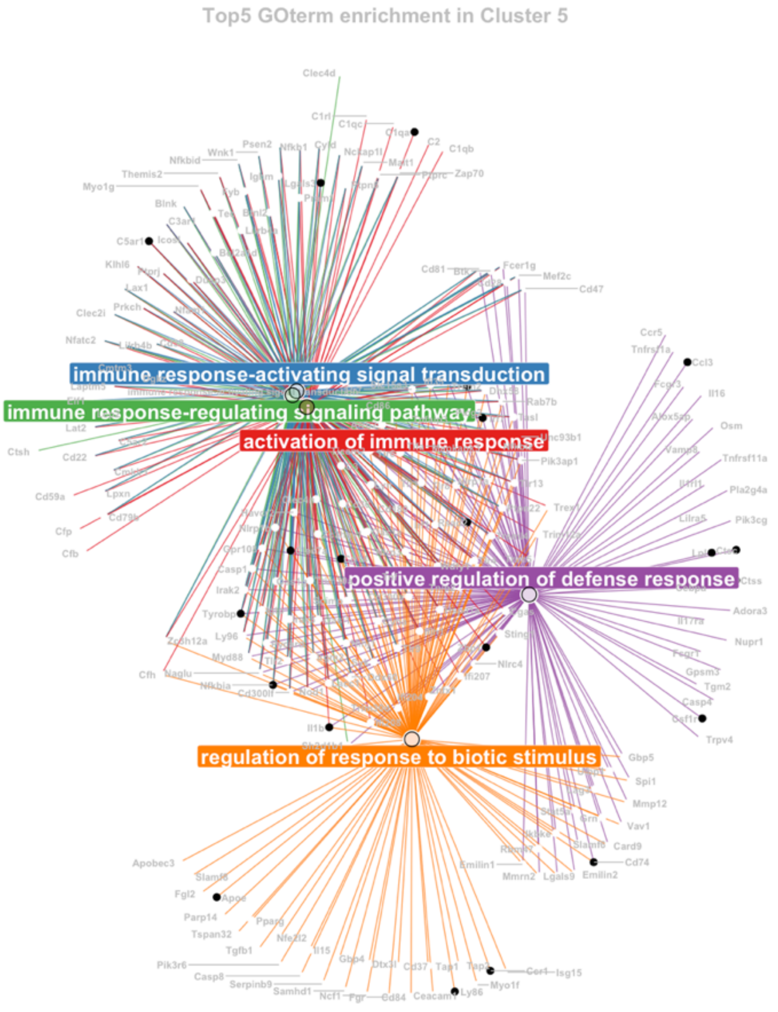

Supplementary Figure 7: Gene expression with functional annotation of cluster 5 in Fig. 23

GO term enrichments for this specific cluster 5 in figure 23 with the five major biological processes (GO). Terms related to the immune system GO, dominate; marker genes specific to microglia are marked in black. Association with microglia-like gene expression according to Pettas et al., 2022 [461].

Here, RNA-seq data was compared with the mass spectrometry data to clarify the cell identity. For this purpose, the entire data sets (non-MIA) were searched for common microglia marker genes from [461] plus Aif1, Cx3cr1, and Itgam, which resulted in 53 proteins as input for the proteomic level and 123 genes as input for the RNA-seq level (Suppl. Fig. 8).

Indeed, the transcriptomic data showed a prevalence for microglial marker genes at postnatal age. However, the 55 proteins had partly a positive l2FC (Ctsd, Ctsb, Apoe, Ctss, Mrc1), and partly a negative one (Aif1, Itgam, Mef2a, C1qa, P2ry12, Ctsc, Mif) with no prevalence for the age (Suppl. Fig. 8). Otherwise, the proteome suggests a neuronal character of the entire dataset (Fig. 26).

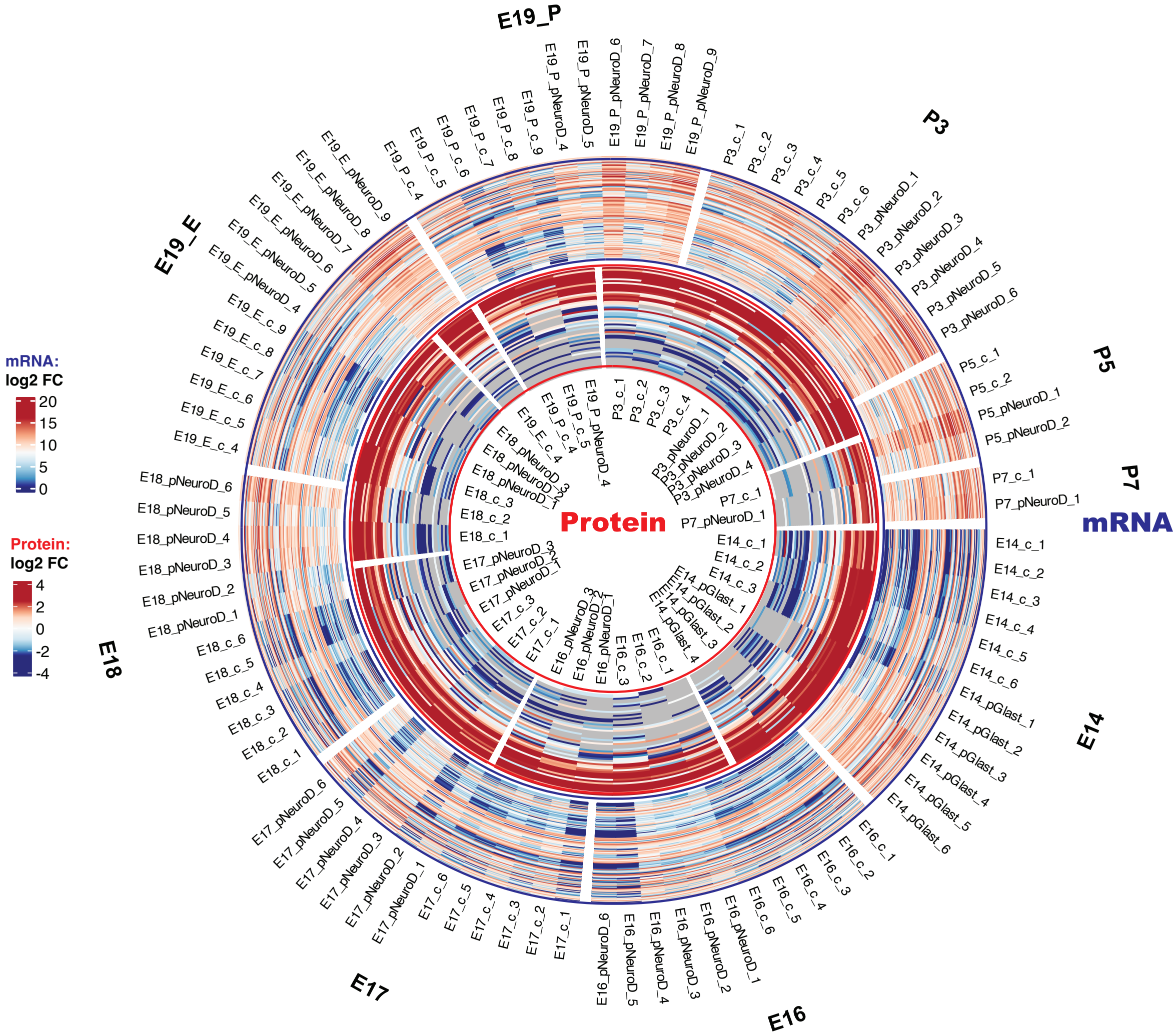

Supplementary Figure 8: Microglia markers are only differentially detectable in the transcriptomic layer

The protein layer shows no differential detection of microglia markers, but one third of the genes tested are consistently upregulated over the time course. The proteins were presented as harmonised and log2-transformed values, the RNA-seq data as DESeq2-normalised and log2-transformed values plus a pseudocount of 0.5.

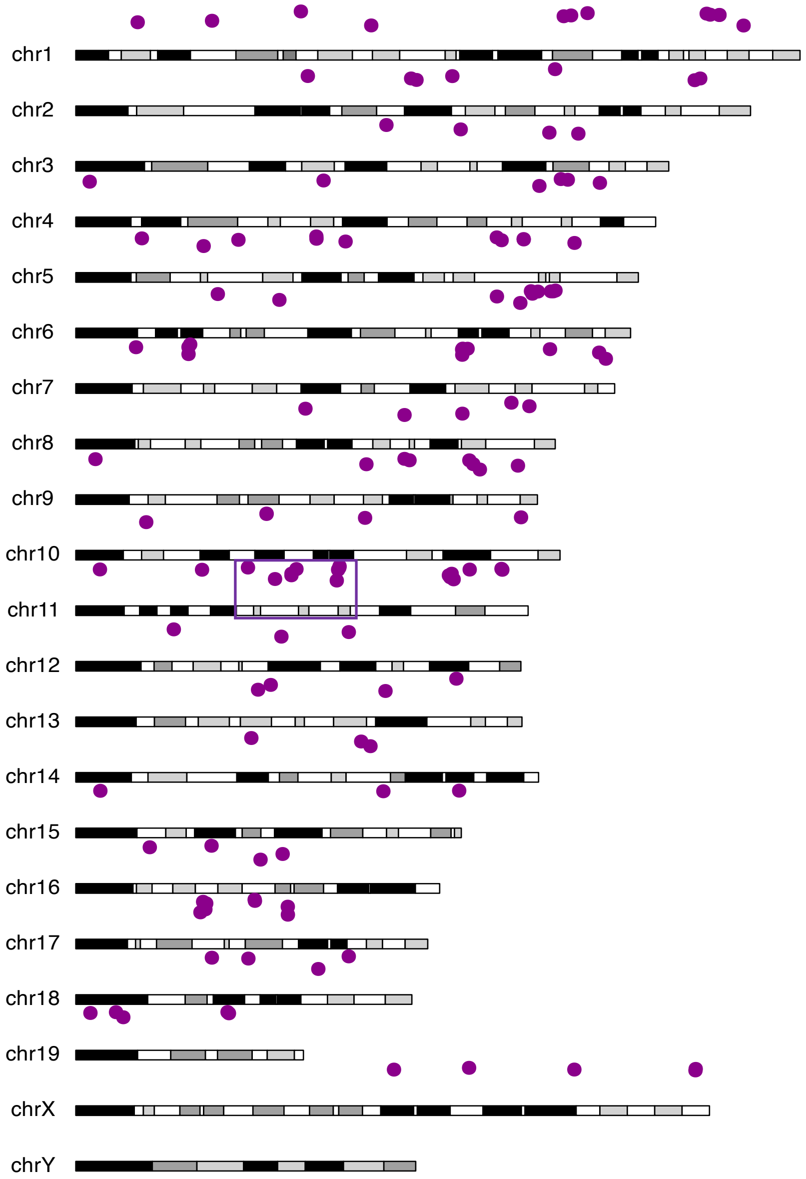

Supplementary Figure 9: Coverage on mm10 chromosomes for DEGs of cluster 5 (Fig. 23) with enhanced cell population contrast

The DEGs of cluster 5 (Fig. 23) are represented by purple dots across the mm10 chromosomes. An enriched region of DEGs ($p<0.01$) was found on chr11 with eighteen genes.

Metrics of MIA animals

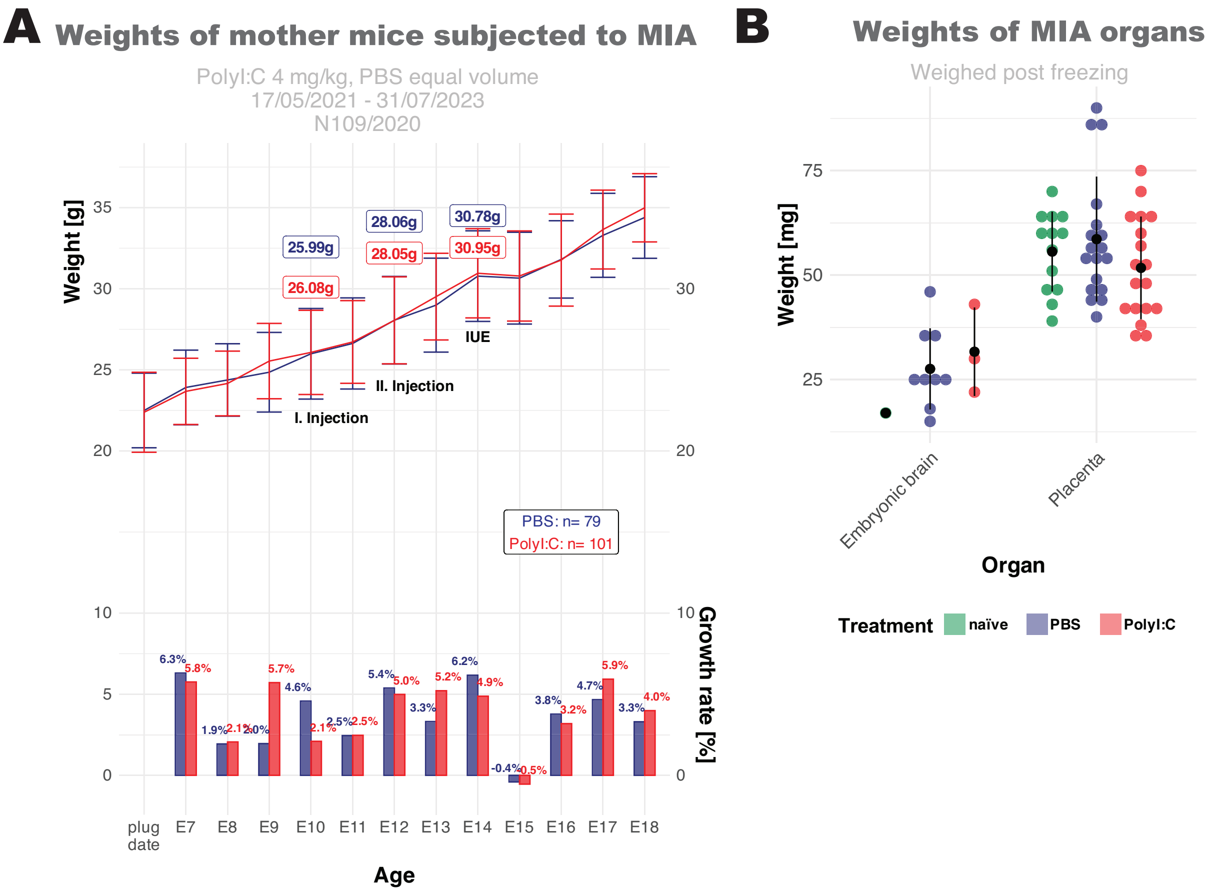

Supplementary Figure 10: The weights of treated and untreated mice are similar

A. The mice of both experimental groups for MIA (PolyI:C and PBS) similarly gained weight until the harvest time point. After the IUE, the weights dropped, but recovered immediately afterwards. Only animals with FACSed offspring were considered in the calculation.

B. Weights post-freezing of embryonic brains and placentae were similar between the tested conditions.

Supplementary Table 1: Metrics of MIA animals, including raw and transformed data for plotting

Preview of the uploaded data, which is available under the name "MIA_TabithaRuecker.xlsx" in the repository on github: https://github.com/TabithaRuecker/NeuroDev.git.

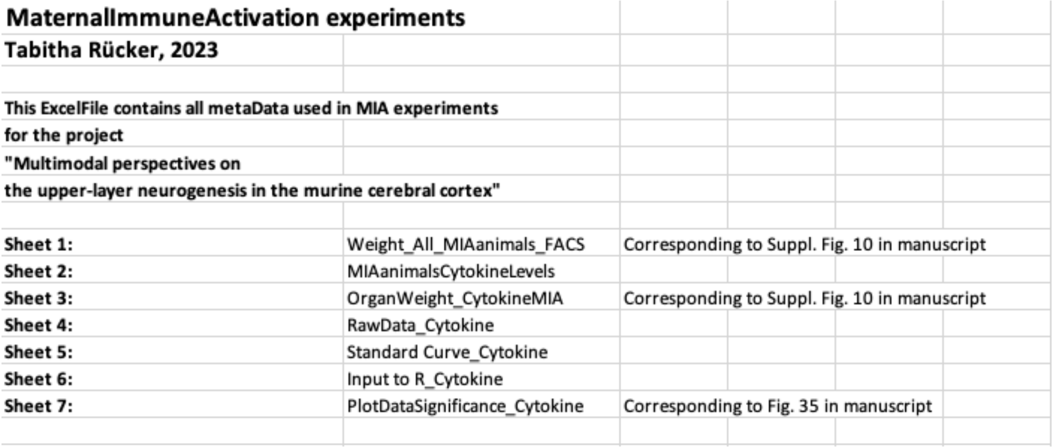

MaternalImmuneActivation experiments		
Tabitha Rücker, 2023		
This ExcelFile contains all metaData used in MIA experiments		
for the project		
"Multimodal perspectives on		
the upper-layer neurogenesis in the murine cerebral cortex"		
Sheet 1:	Weight_All_MIAanimals_FACS	Corresponding to Suppl. Fig. 10 in manuscript
Sheet 2:	MIAanimalsCytokineLevels	
Sheet 3:	OrganWeight_CytokineMIA	Corresponding to Suppl. Fig. 10 in manuscript
Sheet 4:	RawData_Cytokine	
Sheet 5:	Standard Curve_Cytokine	
Sheet 6:	Input to R_Cytokine	
Sheet 7:	PlotDataSignificance_Cytokine	Corresponding to Fig. 35 in manuscript

RNA-seq

RNA extraction[1]

Adapted manual for $<10^5$ cells with RNeasy® Micro Kit (#74004)

1. Remove the tube/eppi with the FACsorted 10,000 cells from dry ice, immediately add 75 µl **Buffer RLT**, and *VORTEX* for 1 min to homogenise the lysate.

2. Add 1 volume of 70% ethanol. Mix well by *PIPETTING*. Do not centrifuge!

3. Transfer the sample to an **RNeasy MinElute spin column** placed in a **2 ml collection tube**.
   ⟳ Centrifuge for 15 s at full speed.
   Discard the **flow through.**
   Place the **spin column** in a **new 2 ml collection tube**.

4. Add 350 µl **Buffer RW1** to the **spin column**. ⟳

5. Add 10 µl **DNase I stock solution** (frozen at -20°C) to 70 µl **Buffer RDD** (kept at 4°C) at RT.
   Mix well by *GENTLY PIPETTING*. Do not vortex!

6. Add the DNase I incubation mix (80 µl each) directly to the **spin column membrane** and place it on the benchtop (at RT) for 15 min.

7. Add 350 µl **Buffer RW1** to the **spin column**. ⟳

8. Add 500 µl **Buffer RPE** to the **spin column**. ⟳

9. Add 500 µl of 80% ethanol to the **spin column**.
   Centrifuge for 2 min at 13,400 rpm.
      Discard the **flow through**.
      Place the **spin column** in a **new 2 ml collection tube**.
   Repeat this step twice.

10. Open the lid of the **spin column**.
    Centrifuge for 5 min at 13,400 rpm.
       Discard the **flow through**.
       Ensure that no ethanol is carried over during RNA elution by drying.
    Place the **spin column** in a **new 1.5 ml collection tube**.

11. Add 14 µl RNase-free water directly to the centre of the spin column membrane and place it on the benchtop (at RT) for 5 min.
    Centrifuge for 1 min at 13,400 rpm to elute the RNA.
    Reelute the flow through.

12. RNA is caught in **1.5 ml collecting tube**! Store at -80ºC.

---

[1] **Before you start**: Prepare DNase I stock solution before using the RNase-Free DNase Set for the first time. Dissolve the lyophilized DNase I (1500 Kunitz units) in 550 µl of the RNase free water provided. To avoid loss of DNase I, do not open the vial. Inject RNase free water into the vial using an RNase-free needle and syringe. Mix gently by inverting the vial. Do not vortex. For long-term storage of reconstituted DNase I, remove the stock solution from the glass vial, divide it into single-use aliquots, and store at –30 to –15° for up to 9 months. Thawed aliquots can be stored at 2–8°C for up to 6 weeks. Do not refreeze the aliquots after thawing. Prepare daily **fresh** 70% & 80% ethanol dilutions with the RNase free water supplied with the kit.

Quality control for RNA-seq

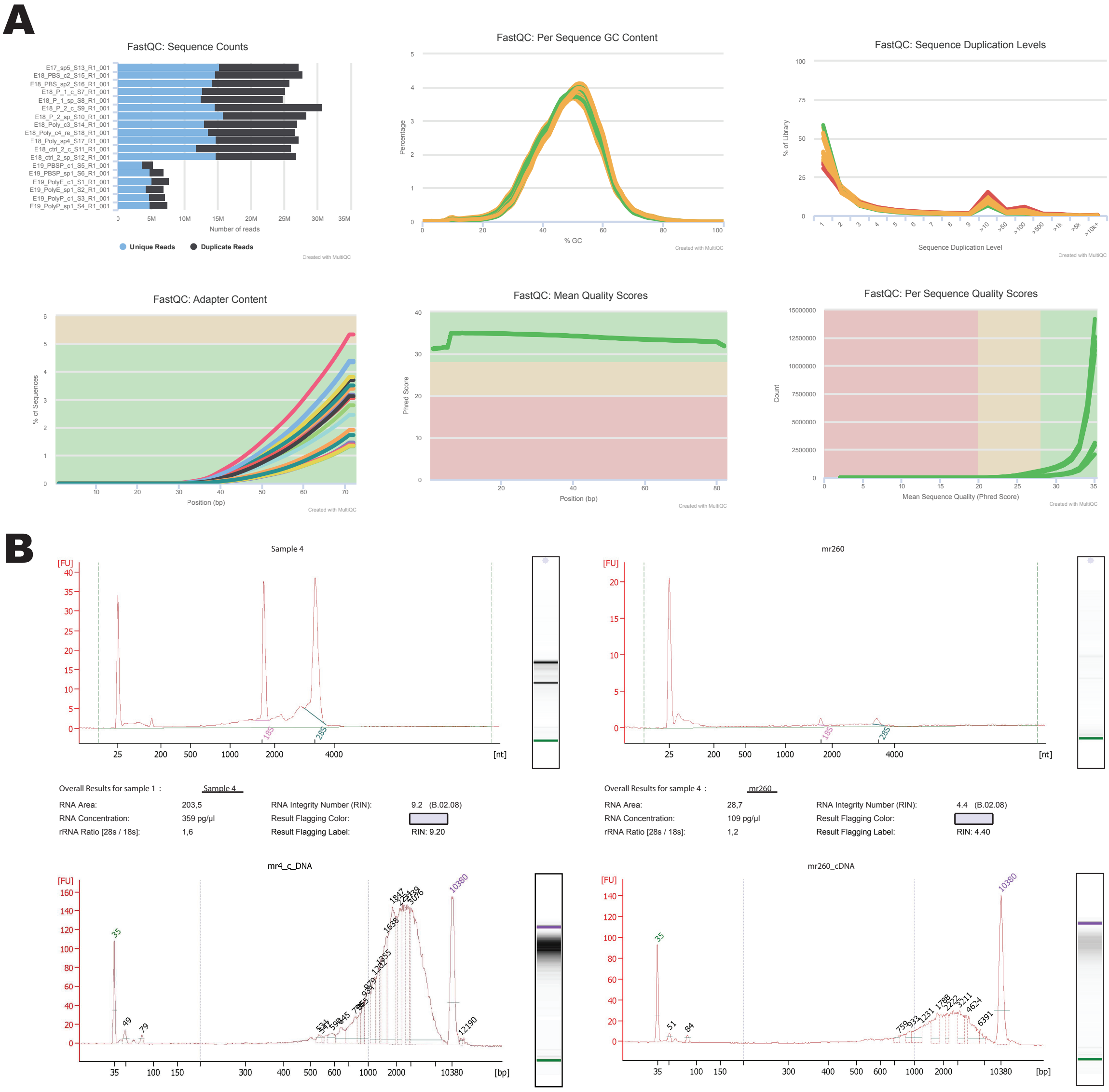

Overall Results for sample 1 : Sample 4

RNA Area: 203,5
RNA Concentration: 359 pg/µl
rRNA Ratio [28s / 18s]: 1,6
RNA Integrity Number (RIN): 9.2 (B.02.08)
Result Flagging Color:
Result Flagging Label: RIN: 9.20

Overall Results for sample 4 : mr260

RNA Area: 28,7
RNA Concentration: 109 pg/µl
rRNA Ratio [28s / 18s]: 1,2
RNA Integrity Number (RIN): 4.4 (B.02.08)
Result Flagging Color:
Result Flagging Label: RIN: 4.40

Supplementary Figure 11: Metrics for RNA-seq quality control

A. Important metrics for evaluation of the base calls are their mean quality scores and their per sequence quality scores (Phred score >30 meant base calling occurred at a correction rate of >99,9%), GC content of ~50% since PCR favours GC rich genomic regions, n content/undetected bases as low as possible, adapter content (Nextera adapter are shown as well as a 3' prime bias due to Poly-A enrichment during library preparation), low duplication rate (on average 25% of sequences are unique, some sequences peak at 10 times duplication due to PCR artifacts, which are not of concern and can be filtered in the next analysis step). Example of fully and partially sequenced RNA samples. Reads from the latter samples were filled up to 20 million reads with the next sequencing run.

B. Representative RNA and cDNA BioAnalyzer tracks of a sample with a high RNA integrity (RIN) value of 9.2 (Sample 4/ E14_pGlast_1), and a sample with a low RIN value of 4.4, that was still sequenced as an exception (mr260/ E19_E_pNeuroD_4).

Evaluation of DEG analyses and annotated GOterms

Supplementary Table 2: Annotated biological processes for the consecutive DEG analysis of the "special" cell population

Only the top five biological processes (GO) for each condition are shown, corresponding to figure 20. Preview of the data available under the name "ConsecutiveAnalysis_special.xlsx" in the repository on github:

https://github.com/TabithaRuecker/NeuroDev.git.

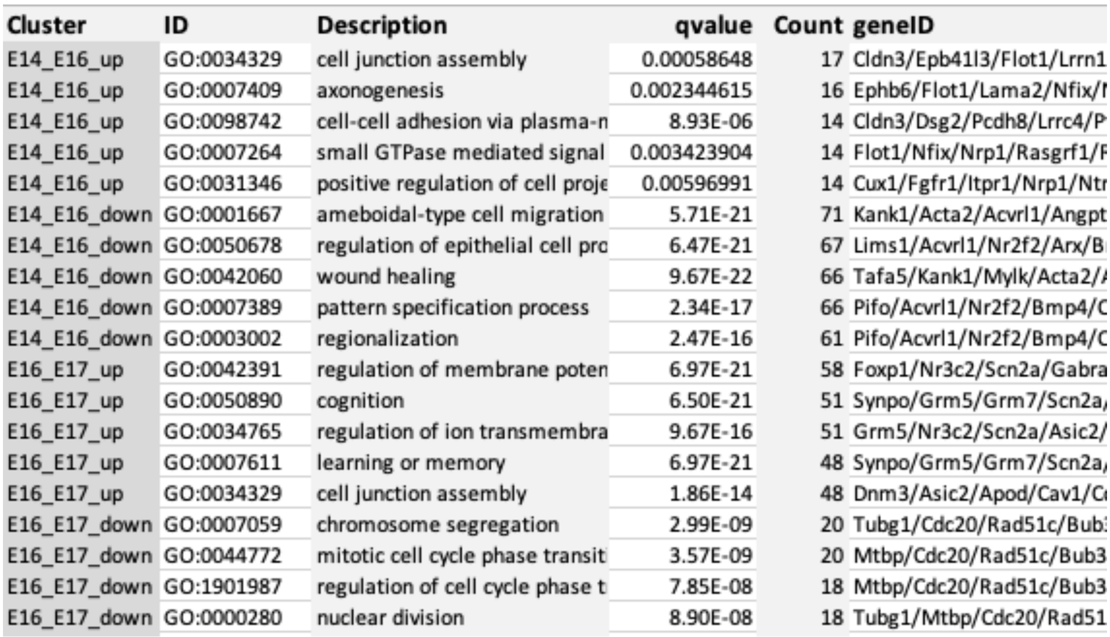

Cluster	ID	Description	qvalue	Count	geneID
E14_E16_up	GO:0034329	cell junction assembly	0.00058648	17	Cldn3/Epb41l3/Flot1/Lrrn1
E14_E16_up	GO:0007409	axonogenesis	0.002344615	16	Ephb6/Flot1/Lama2/Nfix/
E14_E16_up	GO:0098742	cell-cell adhesion via plasma-n	8.93E-06	14	Cldn3/Dsg2/Pcdh8/Lrrc4/P
E14_E16_up	GO:0007264	small GTPase mediated signal	0.003423904	14	Flot1/Nfix/Nrp1/Rasgrf1/
E14_E16_up	GO:0031346	positive regulation of cell proje	0.00596991	14	Cux1/Fgfr1/Itpr1/Nrp1/Ntr
E14_E16_down	GO:0001667	ameboidal-type cell migration	5.71E-21	71	Kank1/Acta2/Acvrl1/Angpt
E14_E16_down	GO:0050678	regulation of epithelial cell pro	6.47E-21	67	Lims1/Acvrl1/Nr2f2/Arx/B
E14_E16_down	GO:0042060	wound healing	9.67E-22	66	Tafa5/Kank1/Mylk/Acta2/
E14_E16_down	GO:0007389	pattern specification process	2.34E-17	66	Pifo/Acvrl1/Nr2f2/Bmp4/C
E14_E16_down	GO:0003002	regionalization	2.47E-16	61	Pifo/Acvrl1/Nr2f2/Bmp4/C
E16_E17_up	GO:0042391	regulation of membrane poten	6.97E-21	58	Foxp1/Nr3c2/Scn2a/Gabra
E16_E17_up	GO:0050890	cognition	6.50E-21	51	Synpo/Grm5/Grm7/Scn2a/
E16_E17_up	GO:0034765	regulation of ion transmembra	9.67E-16	51	Grm5/Nr3c2/Scn2a/Asic2/
E16_E17_up	GO:0007611	learning or memory	6.97E-21	48	Synpo/Grm5/Grm7/Scn2a/
E16_E17_up	GO:0034329	cell junction assembly	1.86E-14	48	Dnm3/Asic2/Apod/Cav1/C
E16_E17_down	GO:0007059	chromosome segregation	2.99E-09	20	Tubg1/Cdc20/Rad51c/Bub
E16_E17_down	GO:0044772	mitotic cell cycle phase transit	3.57E-09	20	Mtbp/Cdc20/Rad51c/Bub3
E16_E17_down	GO:1901987	regulation of cell cycle phase t	7.85E-08	18	Mtbp/Cdc20/Rad51c/Bub3
E16_E17_down	GO:0000280	nuclear division	8.90E-08	18	Tubg1/Mtbp/Cdc20/Rad51

Supplementary Table 3: Cluster membership, their smoothed polynomial function, and annotated biological processes for the "special" population

Preview of the data corresponding to figure 21 available under the name "MulticomparisonAnalysis_special.xlsx" in the repository on github: https://github.com/TabithaRuecker/NeuroDev.git. Here, only one equation is given due to the focus on the "special" population; only the top ten biological processes (GO) for each cluster are shown.

Note: The applied polynomial fit to each gene expression profile marks the time point at which the profiles change dynamics according to scaled gene expression: below or above the average gene expression. I make no claim to optimal fitness or prediction at further times based on these fits. They were only used to derive an estimated time for the biological processes involved.

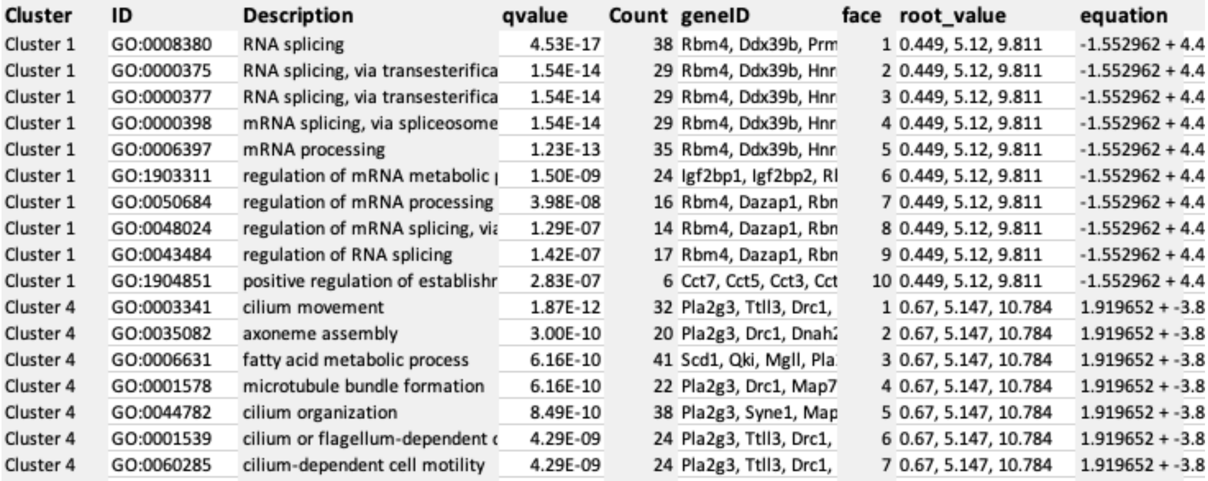

Cluster	ID	Description	qvalue	Count	geneID	face	root_value	equation
Cluster 1	GO:0008380	RNA splicing	4.53E-17	38	Rbm4, Ddx39b, Prm	1	0.449, 5.12, 9.811	-1.552962 + 4.4
Cluster 1	GO:0000375	RNA splicing, via transesterifica	1.54E-14	29	Rbm4, Ddx39b, Hnr	2	0.449, 5.12, 9.811	-1.552962 + 4.4
Cluster 1	GO:0000377	RNA splicing, via transesterifica	1.54E-14	29	Rbm4, Ddx39b, Hnr	3	0.449, 5.12, 9.811	-1.552962 + 4.4
Cluster 1	GO:0000398	mRNA splicing, via spliceosome	1.54E-14	29	Rbm4, Ddx39b, Hnr	4	0.449, 5.12, 9.811	-1.552962 + 4.4
Cluster 1	GO:0006397	mRNA processing	1.23E-13	35	Rbm4, Ddx39b, Hnr	5	0.449, 5.12, 9.811	-1.552962 + 4.4
Cluster 1	GO:1903311	regulation of mRNA metabolic	1.50E-09	24	Igf2bp1, Igf2bp2, Rl	6	0.449, 5.12, 9.811	-1.552962 + 4.4
Cluster 1	GO:0050684	regulation of mRNA processing	3.98E-08	16	Rbm4, Dazap1, Rbn	7	0.449, 5.12, 9.811	-1.552962 + 4.4
Cluster 1	GO:0048024	regulation of mRNA splicing, vi	1.29E-07	14	Rbm4, Dazap1, Rbn	8	0.449, 5.12, 9.811	-1.552962 + 4.4
Cluster 1	GO:0043484	regulation of RNA splicing	1.42E-07	17	Rbm4, Dazap1, Rbn	9	0.449, 5.12, 9.811	-1.552962 + 4.4
Cluster 1	GO:1904851	positive regulation of establishr	2.83E-07	6	Cct7, Cct5, Cct3, Cct	10	0.449, 5.12, 9.811	-1.552962 + 4.4
Cluster 4	GO:0003341	cilium movement	1.87E-12	32	Pla2g3, Ttll3, Drc1,	1	0.67, 5.147, 10.784	1.919652 + -3.8
Cluster 4	GO:0035082	axoneme assembly	3.00E-10	20	Pla2g3, Drc1, Dnah	2	0.67, 5.147, 10.784	1.919652 + -3.8
Cluster 4	GO:0006631	fatty acid metabolic process	6.16E-10	41	Scd1, Qki, Mgll, Pla	3	0.67, 5.147, 10.784	1.919652 + -3.8
Cluster 4	GO:0001578	microtubule bundle formation	6.16E-10	22	Pla2g3, Drc1, Map7	4	0.67, 5.147, 10.784	1.919652 + -3.8
Cluster 4	GO:0044782	cilium organization	8.49E-10	38	Pla2g3, Syne1, Map	5	0.67, 5.147, 10.784	1.919652 + -3.8
Cluster 4	GO:0001539	cilium or flagellum-dependent	4.29E-09	24	Pla2g3, Ttll3, Drc1,	6	0.67, 5.147, 10.784	1.919652 + -3.8
Cluster 4	GO:0060285	cilium-dependent cell motility	4.29E-09	24	Pla2g3, Ttll3, Drc1,	7	0.67, 5.147, 10.784	1.919652 + -3.8

Supplementary Table 4: Cluster membership, their smoothed polynomial function, and annotated biological processes for both "ctrl" and "special" population with enhanced contrast for "Age"

Preview of the data corresponding to figure 22 available under the name "E14toP7_PopulationAge_redPopulation.xlsx" in the repository on github: https://github.com/TabithaRuecker/NeuroDev.git. Here, two equations are given for each cluster, one for the pCAG+/"ctrl" population; one for the "special" population and only the top ten biological processes (GO) for each cluster are shown.

Note: The applied polynomial fit to each gene expression profile marks the time point at which the profiles change dynamics according to scaled gene expression according to the respective cell population ("ctrl" vs "special"). I make no claim to optimal fitness or prediction at further times based on these fits. They were only used to derive an estimated time for the biological processes involved.

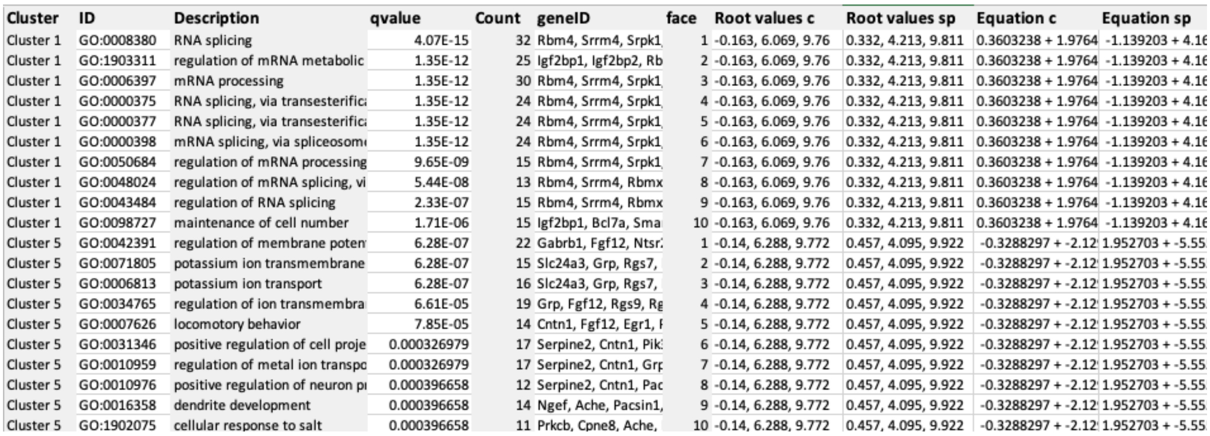

Cluster	ID	Description	qvalue	Count	geneID	face	Root values c	Root values sp	Equation c	Equation sp
Cluster 1	GO:0008380	RNA splicing	4.07E-15	32	Rbm4, Srrm4, Srpk1,	1	-0.163, 6.069, 9.76	0.332, 4.213, 9.811	0.3603238 + 1.9764	-1.139203 + 4.16
Cluster 1	GO:1903311	regulation of mRNA metabolic	1.35E-12	25	Igf2bp1, Igf2bp2, Rb	2	-0.163, 6.069, 9.76	0.332, 4.213, 9.811	0.3603238 + 1.9764	-1.139203 + 4.16
Cluster 1	GO:0006397	mRNA processing	1.35E-12	30	Rbm4, Srrm4, Srpk1,	3	-0.163, 6.069, 9.76	0.332, 4.213, 9.811	0.3603238 + 1.9764	-1.139203 + 4.16
Cluster 1	GO:0000375	RNA splicing, via transesterific	1.35E-12	24	Rbm4, Srrm4, Srpk1,	4	-0.163, 6.069, 9.76	0.332, 4.213, 9.811	0.3603238 + 1.9764	-1.139203 + 4.16
Cluster 1	GO:0000377	RNA splicing, via transesterific	1.35E-12	24	Rbm4, Srrm4, Srpk1,	5	-0.163, 6.069, 9.76	0.332, 4.213, 9.811	0.3603238 + 1.9764	-1.139203 + 4.16
Cluster 1	GO:0000398	mRNA splicing, via spliceosom	1.35E-12	24	Rbm4, Srrm4, Srpk1,	6	-0.163, 6.069, 9.76	0.332, 4.213, 9.811	0.3603238 + 1.9764	-1.139203 + 4.16
Cluster 1	GO:0050684	regulation of mRNA processing	9.65E-09	15	Rbm4, Srrm4, Srpk1,	7	-0.163, 6.069, 9.76	0.332, 4.213, 9.811	0.3603238 + 1.9764	-1.139203 + 4.16
Cluster 1	GO:0048024	regulation of mRNA splicing, vi	5.44E-08	13	Rbm4, Srrm4, Rbmx	8	-0.163, 6.069, 9.76	0.332, 4.213, 9.811	0.3603238 + 1.9764	-1.139203 + 4.16
Cluster 1	GO:0043484	regulation of RNA splicing	2.33E-07	15	Rbm4, Srrm4, Rbmx	9	-0.163, 6.069, 9.76	0.332, 4.213, 9.811	0.3603238 + 1.9764	-1.139203 + 4.16
Cluster 1	GO:0098727	maintenance of cell number	1.71E-06	15	Igf2bp1, Bcl7a, Sma	10	-0.163, 6.069, 9.76	0.332, 4.213, 9.811	0.3603238 + 1.9764	-1.139203 + 4.16
Cluster 5	GO:0042391	regulation of membrane poten	6.28E-07	22	Gabrb1, Fgf12, Ntsr	1	-0.14, 6.288, 9.772	0.457, 4.095, 9.922	-0.3288297 + -2.12	1.952703 + -5.55
Cluster 5	GO:0071805	potassium ion transmembrane	6.28E-07	15	Slc24a3, Grp, Rgs7,	2	-0.14, 6.288, 9.772	0.457, 4.095, 9.922	-0.3288297 + -2.12	1.952703 + -5.55
Cluster 5	GO:0006813	potassium ion transport	6.28E-07	16	Slc24a3, Grp, Rgs7,	3	-0.14, 6.288, 9.772	0.457, 4.095, 9.922	-0.3288297 + -2.12	1.952703 + -5.55
Cluster 5	GO:0034765	regulation of ion transmembra	6.61E-05	19	Grp, Fgf12, Rgs9, Rg	4	-0.14, 6.288, 9.772	0.457, 4.095, 9.922	-0.3288297 + -2.12	1.952703 + -5.55
Cluster 5	GO:0007626	locomotory behavior	7.85E-05	14	Cntn1, Fgf12, Egr1,	5	-0.14, 6.288, 9.772	0.457, 4.095, 9.922	-0.3288297 + -2.12	1.952703 + -5.55
Cluster 5	GO:0031346	positive regulation of cell proje	0.000326979	17	Serpine2, Cntn1, Pik	6	-0.14, 6.288, 9.772	0.457, 4.095, 9.922	-0.3288297 + -2.12	1.952703 + -5.55
Cluster 5	GO:0010959	regulation of metal ion transpo	0.000326979	17	Serpine2, Cntn1, Grp	7	-0.14, 6.288, 9.772	0.457, 4.095, 9.922	-0.3288297 + -2.12	1.952703 + -5.55
Cluster 5	GO:0010976	positive regulation of neuron p	0.000396658	12	Serpine2, Cntn1, Pac	8	-0.14, 6.288, 9.772	0.457, 4.095, 9.922	-0.3288297 + -2.12	1.952703 + -5.55
Cluster 5	GO:0016358	dendrite development	0.000396658	14	Ngef, Ache, Pacsin1,	9	-0.14, 6.288, 9.772	0.457, 4.095, 9.922	-0.3288297 + -2.12	1.952703 + -5.55
Cluster 5	GO:1902075	cellular response to salt	0.000396658	11	Prkcb, Cpne8, Ache,	10	-0.14, 6.288, 9.772	0.457, 4.095, 9.922	-0.3288297 + -2.12	1.952703 + -5.55

.

Supplementary Table 5: Cluster membership, their smoothed polynomial function, and annotated biological processes for both "ctrl" and "special" population with enhanced contrast for "Population"

Preview of the data corresponding to figure 23 available under the name "E14toP7_AgePopulation_redAge.xlsx" in the repository on github: https://github.com/TabithaRuecker/NeuroDev.git. Here, two equations are given for each cluster, one for the pCAG+/"ctrl" population, and one for the "special" population and only the top ten biological processes (GO) for each cluster are shown.

Note: The applied polynomial fit to each gene expression profile marks the time point at which the profiles change dynamics according to scaled gene expression according to the respective cell population ("ctrl" vs "special"). I make no claim to optimal fitness or prediction at further times based on these fits. They were only used to derive an estimated time for the biological processes involved.

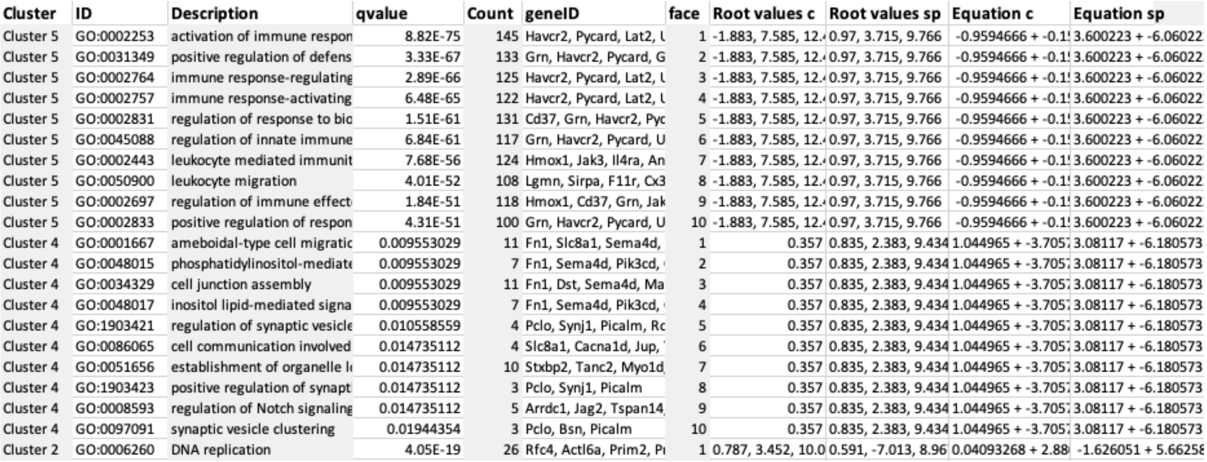

Cluster	ID	Description	qvalue	Count	geneID	face	Root values c	Root values sp	Equation c	Equation sp
Cluster 5	GO:0002253	activation of immune respon	8.82E-75	145	Havcr2, Pycard, Lat2,	1	-1.883, 7.585, 12.4	0.97, 3.715, 9.766	-0.9594666 + -0.1	3.600223 + -6.06022
Cluster 5	GO:0031349	positive regulation of defens	3.33E-67	133	Grn, Havcr2, Pycard, G	2	-1.883, 7.585, 12.4	0.97, 3.715, 9.766	-0.9594666 + -0.1	3.600223 + -6.06022
Cluster 5	GO:0002764	immune response-regulating	2.89E-66	125	Havcr2, Pycard, Lat2,	3	-1.883, 7.585, 12.4	0.97, 3.715, 9.766	-0.9594666 + -0.1	3.600223 + -6.06022
Cluster 5	GO:0002757	immune response-activating	6.48E-65	122	Havcr2, Pycard, Lat2,	4	-1.883, 7.585, 12.4	0.97, 3.715, 9.766	-0.9594666 + -0.1	3.600223 + -6.06022
Cluster 5	GO:0002831	regulation of response to bio	1.51E-61	131	Cd37, Grn, Havcr2, Pyc	5	-1.883, 7.585, 12.4	0.97, 3.715, 9.766	-0.9594666 + -0.1	3.600223 + -6.06022
Cluster 5	GO:0045088	regulation of innate immune	6.84E-61	117	Grn, Havcr2, Pycard, U	6	-1.883, 7.585, 12.4	0.97, 3.715, 9.766	-0.9594666 + -0.1	3.600223 + -6.06022
Cluster 5	GO:0002443	leukocyte mediated immunit	7.68E-56	124	Hmox1, Jak3, Il4ra, An	7	-1.883, 7.585, 12.4	0.97, 3.715, 9.766	-0.9594666 + -0.1	3.600223 + -6.06022
Cluster 5	GO:0050900	leukocyte migration	4.01E-52	108	Lgmn, Sirpa, F11r, Cx3	8	-1.883, 7.585, 12.4	0.97, 3.715, 9.766	-0.9594666 + -0.1	3.600223 + -6.06022
Cluster 5	GO:0002697	regulation of immune effect	1.84E-51	118	Hmox1, Cd37, Grn, Jak	9	-1.883, 7.585, 12.4	0.97, 3.715, 9.766	-0.9594666 + -0.1	3.600223 + -6.06022
Cluster 5	GO:0002833	positive regulation of respon	4.31E-51	100	Grn, Havcr2, Pycard, U	10	-1.883, 7.585, 12.4	0.97, 3.715, 9.766	-0.9594666 + -0.1	3.600223 + -6.06022
Cluster 4	GO:0001667	ameboidal-type cell migratic	0.009553029	11	Fn1, Slc8a1, Sema4d,	1	0.357	0.835, 2.383, 9.434	1.044965 + -3.705	3.08117 + -6.180573
Cluster 4	GO:0048015	phosphatidylinositol-mediate	0.009553029	7	Fn1, Sema4d, Pik3cd,	2	0.357	0.835, 2.383, 9.434	1.044965 + -3.705	3.08117 + -6.180573
Cluster 4	GO:0034329	cell junction assembly	0.009553029	11	Fn1, Dst, Sema4d, Ma	3	0.357	0.835, 2.383, 9.434	1.044965 + -3.705	3.08117 + -6.180573
Cluster 4	GO:0048017	inositol lipid-mediated signa	0.009553029	7	Fn1, Sema4d, Pik3cd,	4	0.357	0.835, 2.383, 9.434	1.044965 + -3.705	3.08117 + -6.180573
Cluster 4	GO:1903421	regulation of synaptic vesicle	0.010558559	4	Pclo, Synj1, Picalm, Rc	5	0.357	0.835, 2.383, 9.434	1.044965 + -3.705	3.08117 + -6.180573
Cluster 4	GO:0086065	cell communication involved	0.014735112	4	Slc8a1, Cacna1d, Jup,	6	0.357	0.835, 2.383, 9.434	1.044965 + -3.705	3.08117 + -6.180573
Cluster 4	GO:0051656	establishment of organelle l	0.014735112	10	Stxbp2, Tanc2, Myo1d,	7	0.357	0.835, 2.383, 9.434	1.044965 + -3.705	3.08117 + -6.180573
Cluster 4	GO:1903423	positive regulation of synapt	0.014735112	3	Pclo, Synj1, Picalm	8	0.357	0.835, 2.383, 9.434	1.044965 + -3.705	3.08117 + -6.180573
Cluster 4	GO:0008593	regulation of Notch signaling	0.014735112	5	Arrdc1, Jag2, Tspan14,	9	0.357	0.835, 2.383, 9.434	1.044965 + -3.705	3.08117 + -6.180573
Cluster 4	GO:0097091	synaptic vesicle clustering	0.01944354	3	Pclo, Bsn, Picalm	10	0.357	0.835, 2.383, 9.434	1.044965 + -3.705	3.08117 + -6.180573
Cluster 2	GO:0006260	DNA replication	4.05E-19	26	Rfc4, Actl6a, Prim2, P	1	0.787, 3.452, 10.0	0.591, -7.013, 8.96	0.04093268 + 2.88	-1.626051 + 5.6625

WGCNA for MIA samples

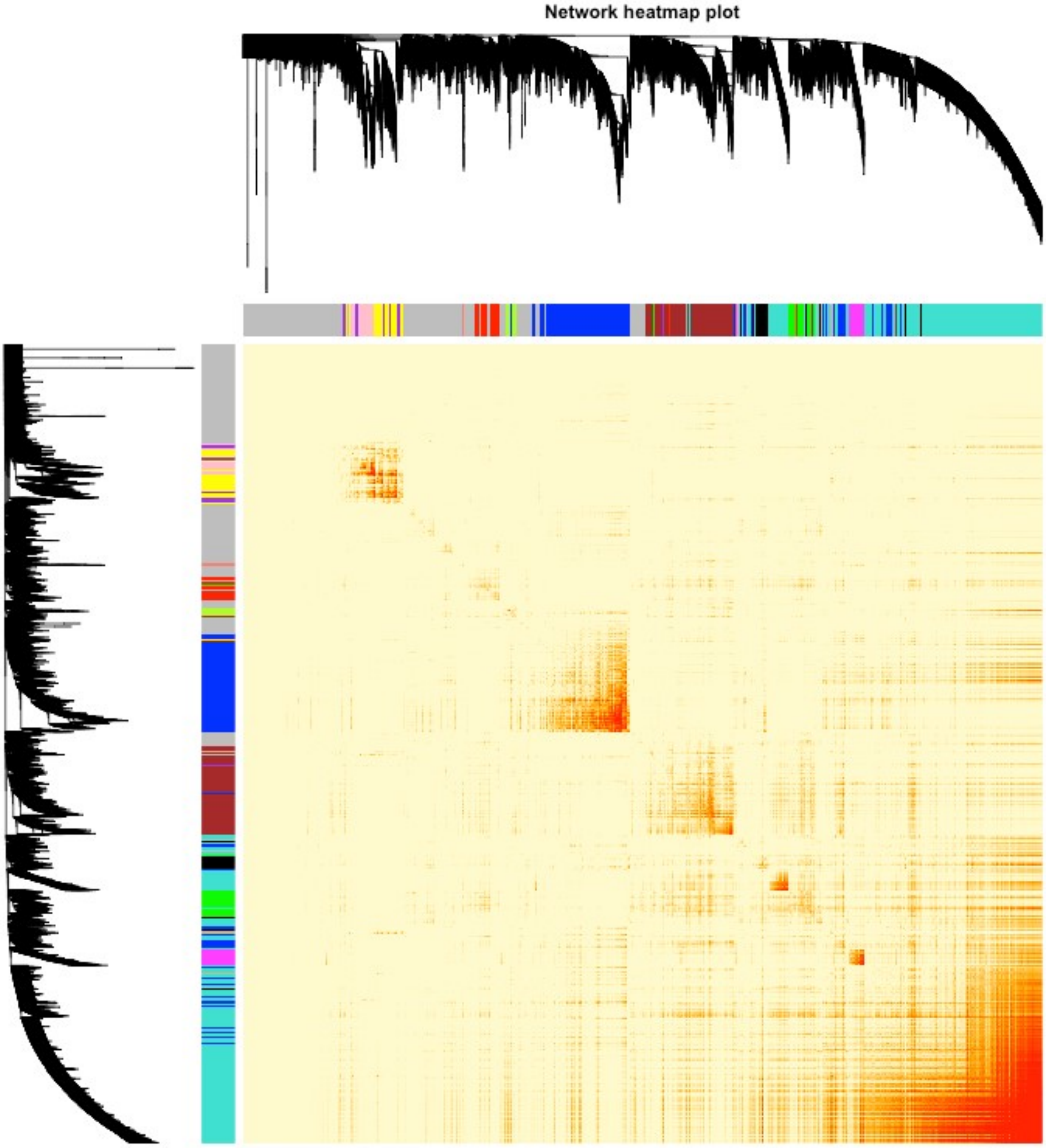

Supplementary Figure 12: Estimation of power threshold from the topology of R^2 and mean connectivity for WGCN construction

Based on consensus topological adjacency/**T**opological **O**verlap **M**easure (**TOM**), the genes are clustered by dissimilarity into fourteen colour-coded gene modules. The dissimilarity is reflected in the intensity of colours: The higher the dissimilarity, the more the connectivity weight turns from yellow to red. Since modules consist of nodes with strong topological overlap, corresponding with higher-order interactions, they are also represented along the diagonal by red squares.

Supplementary Figure 13: Biological functions of significantly enriched gene expression in MIA-associated modules

The ten most important biological functions (GO) associated with the pink and red modules reveal that the functions of the anticorrelating modules partly overlap.

Supplementary Table 6: GO annotation for WGCNA derived DEGs of MIA treatment

Preview of the data available under the name “MIA_DEGs.xlsx” in the repository on github: https://github.com/TabithaRuecker/NeuroDev.git.

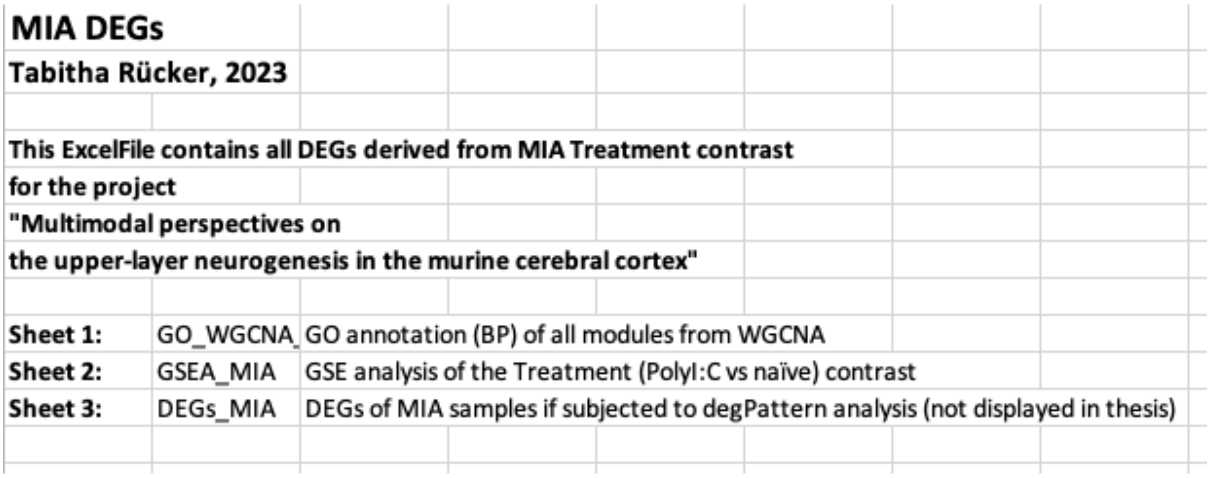

MIA DEGs

Tabitha Rücker, 2023

This ExcelFile contains all DEGs derived from MIA Treatment contrast
for the project
"Multimodal perspectives on
the upper-layer neurogenesis in the murine cerebral cortex"

Sheet 1:	GO_WGCNA_	GO annotation (BP) of all modules from WGCNA
Sheet 2:	GSEA_MIA	GSE analysis of the Treatment (PolyI:C vs naïve) contrast
Sheet 3:	DEGs_MIA	DEGs of MIA samples if subjected to degPattern analysis (not displayed in thesis)

E19 samples vary upon birth

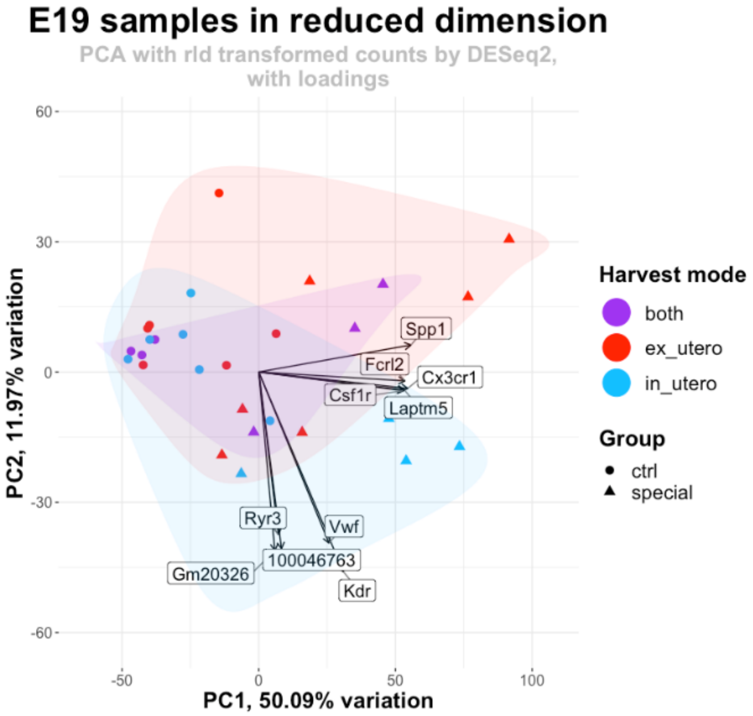

Supplementary Figure 14: Pooled E19 samples can be split by harvesting mode

The PCA, with 50% of the variables removed, shows six pooled samples, twelve *ex utero* samples representing E19_P samples and twelve *in utero* samples designated E19_E in further analysis (all split into half pCAG-tDimer+ and half pNeuroD1-eGFP+ cell populations). The loadings represent approximately the same loadings as in the biplot over the entire period. Again, tDimer+ samples cluster close together, whereas the pNeuroD1+ samples are responsible for most of the variation.

Supplementary Table 7: DEGs and GO annotations for the analyses around the birth time point E19

Preview of the data available under the name “Birth_DEGs.xlsx” in the repository on github: https://github.com/TabithaRuecker/NeuroDev.git.

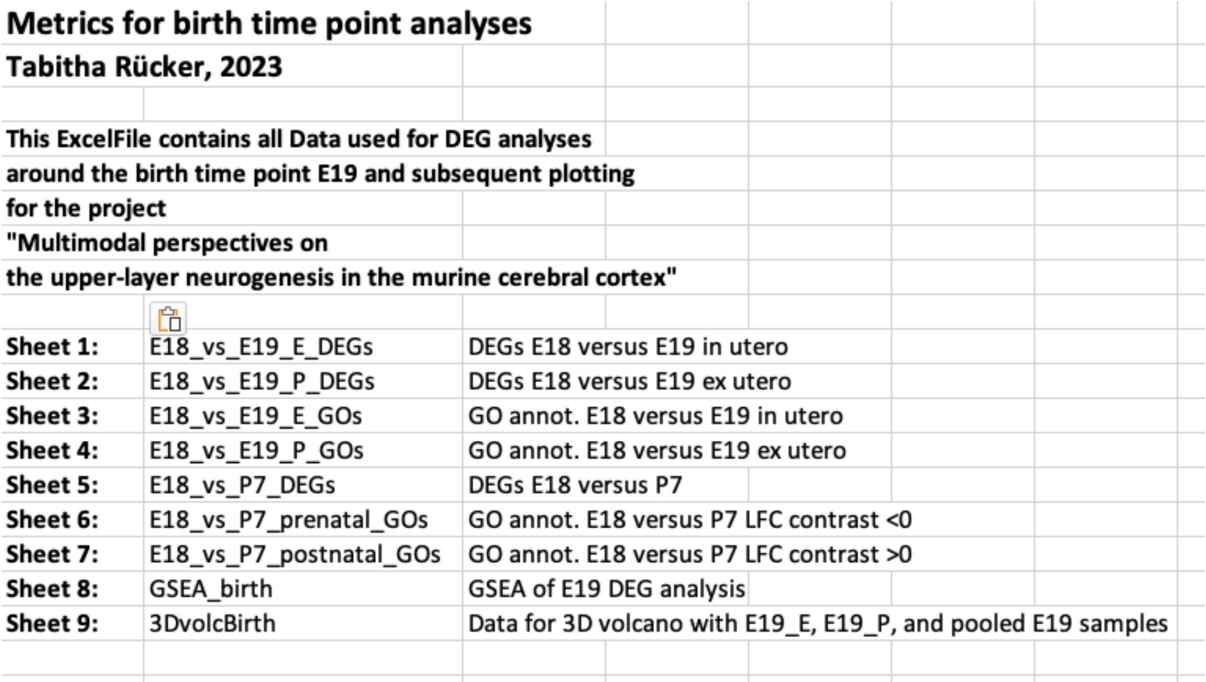

Metrics for birth time point analyses

Tabitha Rücker, 2023

This ExcelFile contains all Data used for DEG analyses
around the birth time point E19 and subsequent plotting
for the project
"Multimodal perspectives on
the upper-layer neurogenesis in the murine cerebral cortex"

Sheet 1:	E18_vs_E19_E_DEGs	DEGs E18 versus E19 in utero
Sheet 2:	E18_vs_E19_P_DEGs	DEGs E18 versus E19 ex utero
Sheet 3:	E18_vs_E19_E_GOs	GO annot. E18 versus E19 in utero
Sheet 4:	E18_vs_E19_P_GOs	GO annot. E18 versus E19 ex utero
Sheet 5:	E18_vs_P7_DEGs	DEGs E18 versus P7
Sheet 6:	E18_vs_P7_prenatal_GOs	GO annot. E18 versus P7 LFC contrast <0
Sheet 7:	E18_vs_P7_postnatal_GOs	GO annot. E18 versus P7 LFC contrast >0
Sheet 8:	GSEA_birth	GSEA of E19 DEG analysis
Sheet 9:	3DvolcBirth	Data for 3D volcano with E19_E, E19_P, and pooled E19 samples

RT-PCR

RT-PCR protocol

cDNA synthesis with SuperScript™ IV CellsDirect™ kit (#11750150) for usage with Thermo Taqman® Array 96-well plate:

1) Pre-set the thermocycler with the following reverse transcription program, then prepare the lysis mix on ice and adapt to the number of samples:

Stage	Temp [°C]	Time [min]
1	25	10
2	50	10
3	85	5
4	4	∞

Reagent	Amount
Lysis Solution (stored at 4°C)	25.61 µL *n
Lysis Enhancer (100x)	0.26 µL *n
DNase (50x)	0.53 µL *n

- Add to each sample 24 µL of lysis mix, prepare samples on ice.
- Remove from ice, incubate at RT for 10min.
- Add 3 µL StopSolution, centrifugation is still possible.
- Incubate at RT for 5min, then place back on ice.
- Add 8 µL of RT-MasterMix to the samples and 8 µL of NoRTctrl to internal plate controls.

2) Start reverse transcription (thermocycler).

3) Use this cDNA for setting up the RT-PCR with Taqman® Array 96-well plates:

Samples to test (per well):	
10 µL	Fast Advanced MasterMix
6 µL	RNase free water
4 µL	cDNA (1:5 dilution)
20 µL	**Total volume**

IPC (split into 6 aliquots & use for all 6 plates)	
30 µL	Fast Advanced MasterMix
18 µL	RNase free water
12 µL	cDNA (1:5 dilution)
60 µL	**Total volume**

Reagent	Catalog number	Company
SuperScript™ IV CellsDirect™ cDNA Synthesis Kit	#11750150	Thermo Fisher Scientific
TaqMan™ Fast Advanced MasterMix	5mL; #4444557	Thermo Fisher Scientific
Taqman® Array 96-well plate	6x16 each; #4413264	Thermo Fisher Scientific

RT-PCR count data

Supplementary Table 8: RT-PCR raw and transformed data for plotting

Preview of the data for figure 17 and 18 available under the name “RTPCR_TabithaRuecker.xlsx” in the repository on github: https://github.com/TabithaRuecker/NeuroDev.git.

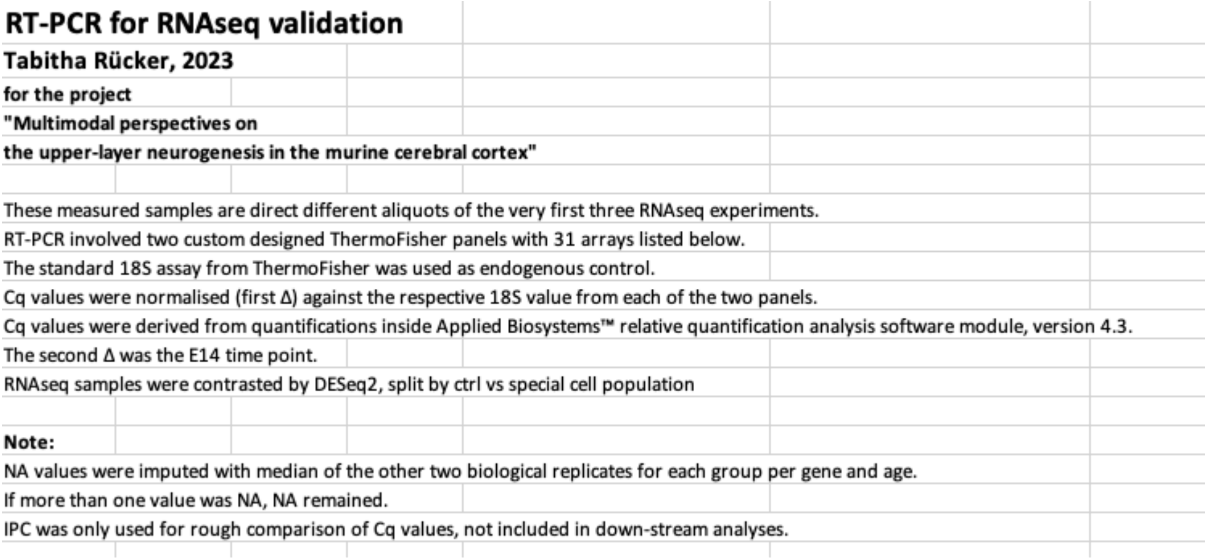

RT-PCR for RNAseq validation

Tabitha Rücker, 2023

for the project

"Multimodal perspectives on

the upper-layer neurogenesis in the murine cerebral cortex"

These measured samples are direct different aliquots of the very first three RNAseq experiments.

RT-PCR involved two custom designed ThermoFisher panels with 31 arrays listed below.

The standard 18S assay from ThermoFisher was used as endogenous control.

Cq values were normalised (first Δ) against the respective 18S value from each of the two panels.

Cq values were derived from quantifications inside Applied Biosystems™ relative quantification analysis software module, version 4.3.

The second Δ was the E14 time point.

RNAseq samples were contrasted by DESeq2, split by ctrl vs special cell population

Note:

NA values were imputed with median of the other two biological replicates for each group per gene and age.

If more than one value was NA, NA remained.

IPC was only used for rough comparison of Cq values, not included in down-stream analyses.

Proteome metrics

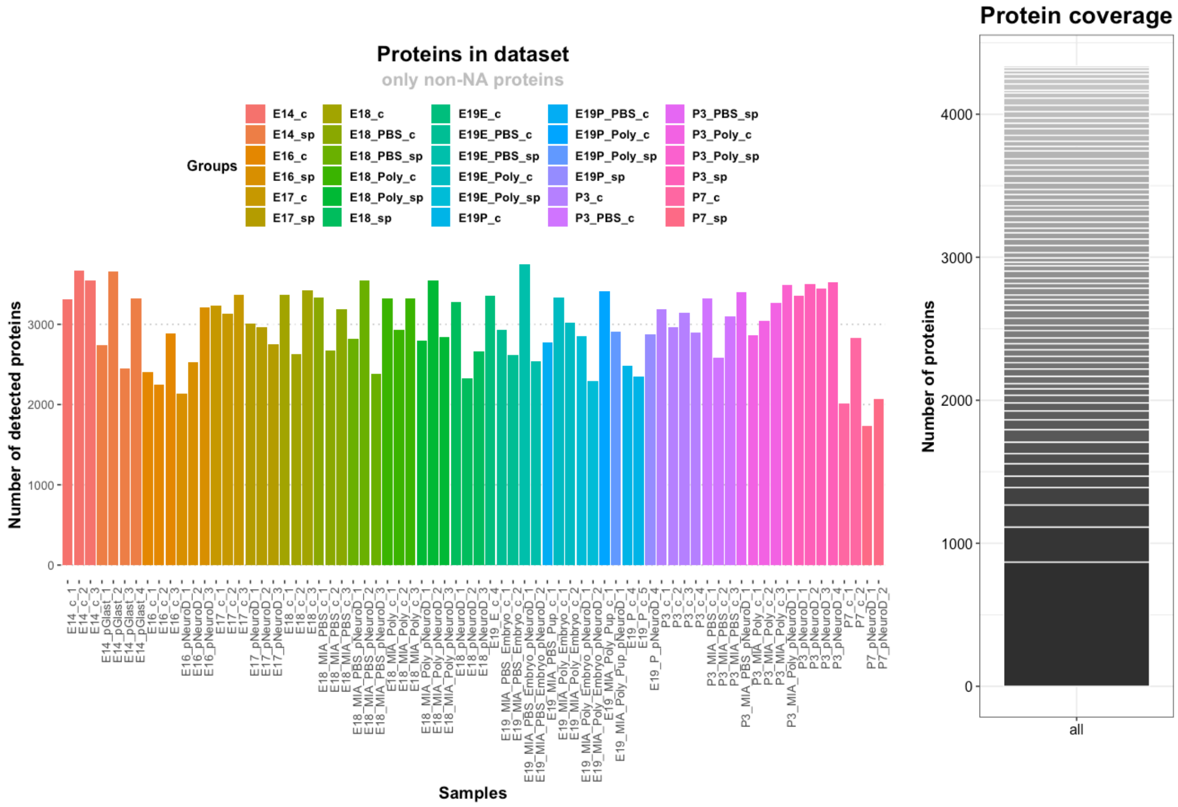

Supplementary Figure 15: Among the 72 samples, the number of detected non-NA proteins was equally distributed

868 proteins were detected in all samples.

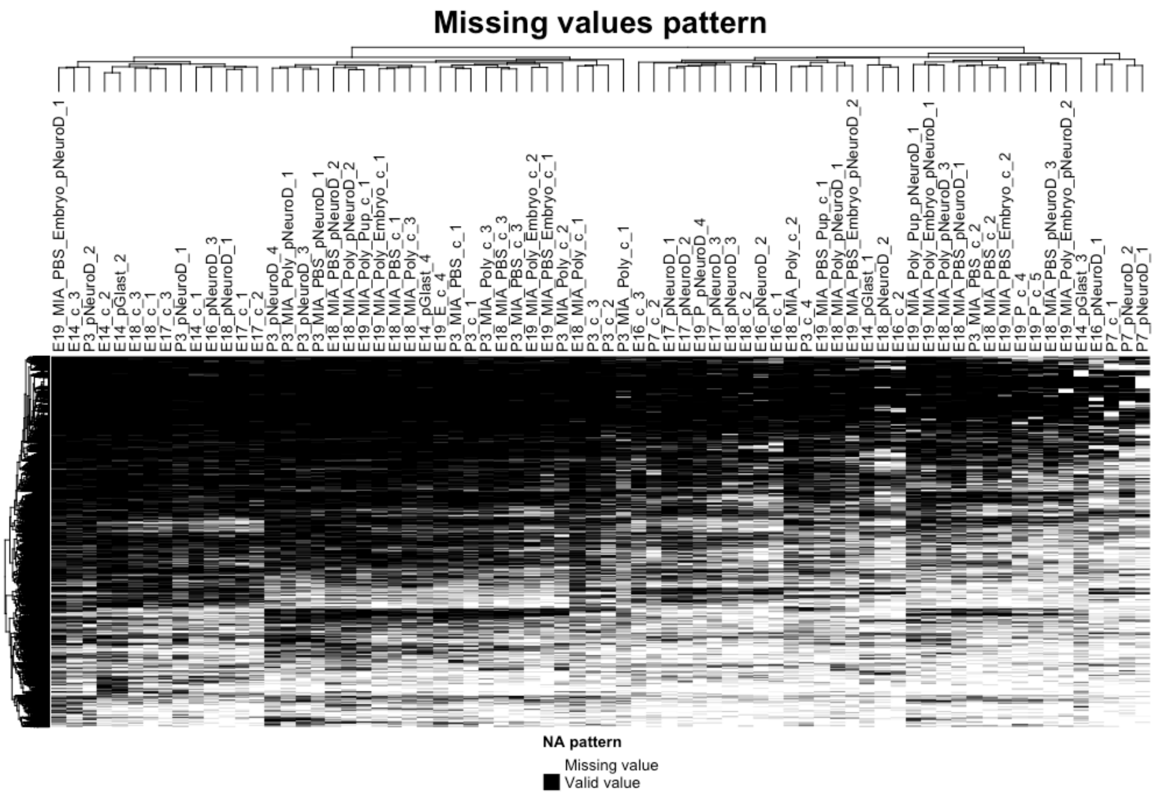

Supplementary Figure 16: Clustering of missing values in the entire dataset

Missing values in the data set predominate in the E19 samples.

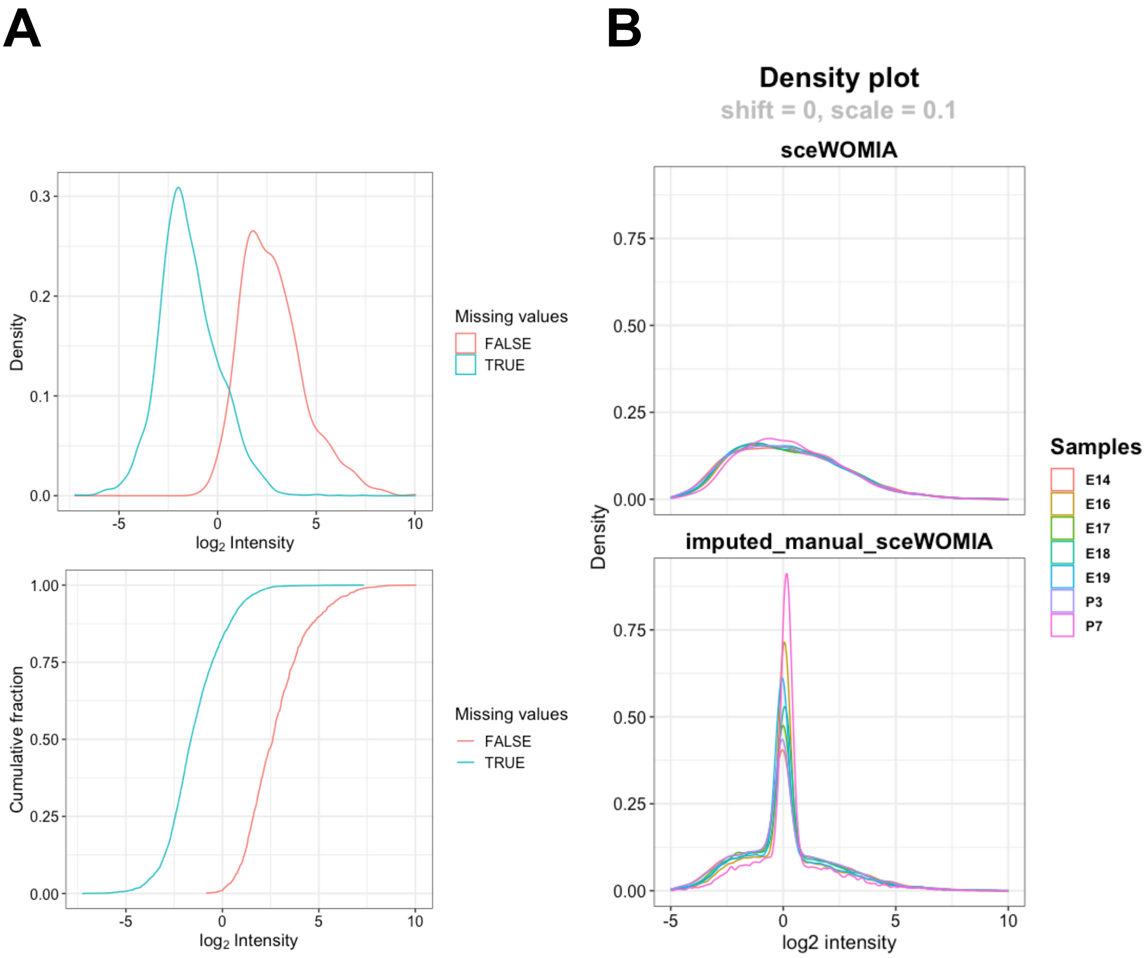

Supplementary Figure 17: Imputation strategy for missing values in the proteomic data set

A. The densities and cumulative fractions for proteins with and without missing values show that the proteins with missing values have low intensities on average.
B. Manual imputation stabilises the MNAR values (Representative example for untreated data set, same for treated data set, shift=0, scale=0.1).

Supplementary Table 9: Overview of DEPs with different contrasts

Preview associated with figures 27, 29, and 40. The uploaded data is available under the name "DEPs.xlsx" in the repository on github: https://github.com/TabithaRuecker/NeuroDev.git.

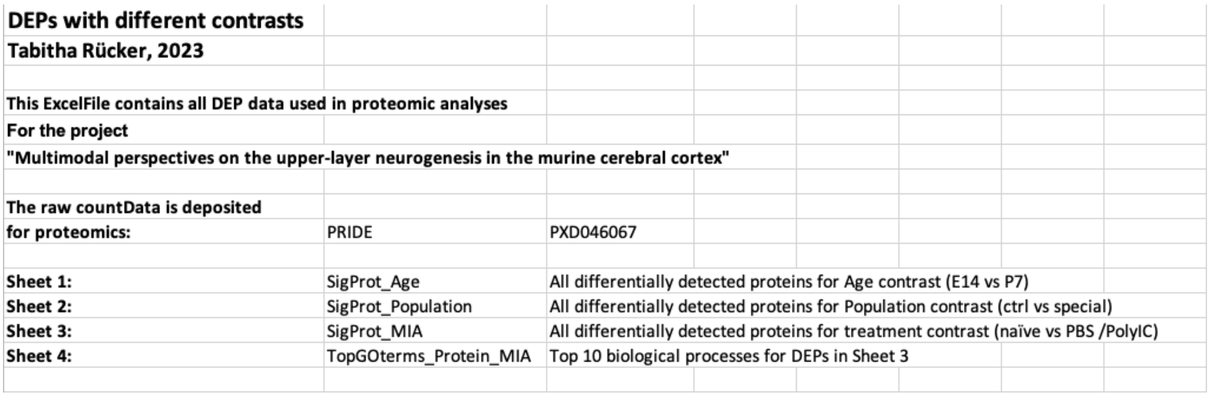

DEPs with different contrasts		
Tabitha Rücker, 2023		
This ExcelFile contains all DEP data used in proteomic analyses		
For the project		
"Multimodal perspectives on the upper-layer neurogenesis in the murine cerebral cortex"		
The raw countData is deposited		
for proteomics:	PRIDE	PXD046067
Sheet 1:	SigProt_Age	All differentially detected proteins for Age contrast (E14 vs P7)
Sheet 2:	SigProt_Population	All differentially detected proteins for Population contrast (ctrl vs special)
Sheet 3:	SigProt_MIA	All differentially detected proteins for treatment contrast (naïve vs PBS /PolyIC)
Sheet 4:	TopGOterms_Protein_MIA	Top 10 biological processes for DEPs in Sheet 3

Supplementary Table 10: ClueGO results for the stably detected proteins from E14 to P7 for both cell populations

Preview associated with figure 26. The uploaded data is available under the name “ClueGOResultTable.xlsx” in the repository on github: https://github.com/TabithaRuecker/NeuroDev.git.

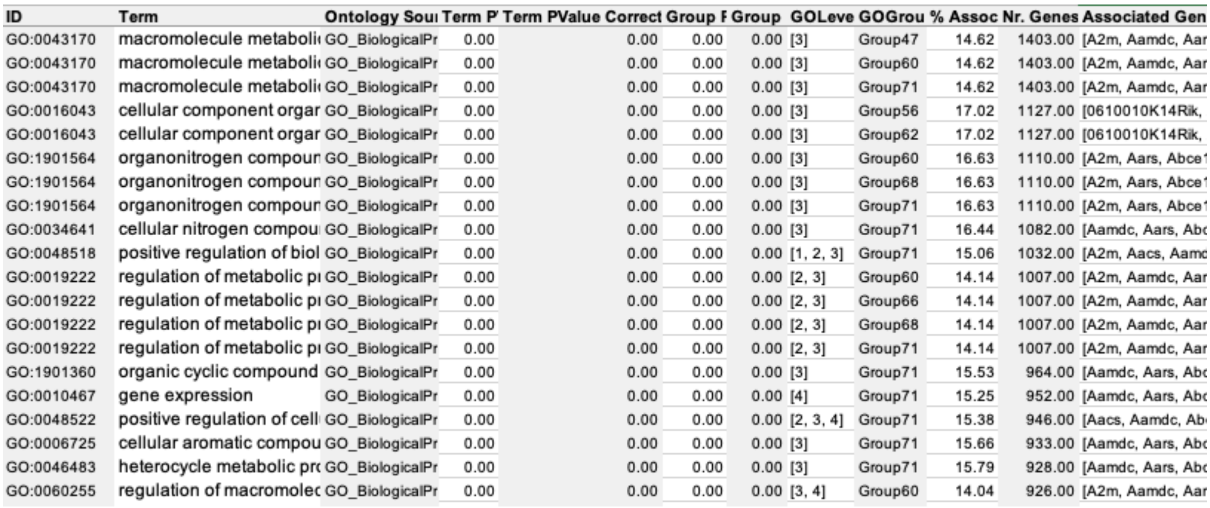

ID	Term	Ontology Sou	Term P	Term PValue Correct	Group F	Group	GOLeve	GOGrou	% Assoc	Nr. Genes	Associated Gen
GO:0043170	macromolecule metaboli	GO_BiologicalPr	0.00	0.00	0.00	0.00	[3]	Group47	14.62	1403.00	[A2m, Aamdc, Aar
GO:0043170	macromolecule metaboli	GO_BiologicalPr	0.00	0.00	0.00	0.00	[3]	Group60	14.62	1403.00	[A2m, Aamdc, Aar
GO:0043170	macromolecule metaboli	GO_BiologicalPr	0.00	0.00	0.00	0.00	[3]	Group71	14.62	1403.00	[A2m, Aamdc, Aar
GO:0016043	cellular component orgar	GO_BiologicalPr	0.00	0.00	0.00	0.00	[3]	Group56	17.02	1127.00	[0610010K14Rik,
GO:0016043	cellular component orgar	GO_BiologicalPr	0.00	0.00	0.00	0.00	[3]	Group62	17.02	1127.00	[0610010K14Rik,
GO:1901564	organonitrogen compour	GO_BiologicalPr	0.00	0.00	0.00	0.00	[3]	Group60	16.63	1110.00	[A2m, Aars, Abce
GO:1901564	organonitrogen compour	GO_BiologicalPr	0.00	0.00	0.00	0.00	[3]	Group68	16.63	1110.00	[A2m, Aars, Abce
GO:1901564	organonitrogen compour	GO_BiologicalPr	0.00	0.00	0.00	0.00	[3]	Group71	16.63	1110.00	[A2m, Aars, Abce
GO:0034641	cellular nitrogen compou	GO_BiologicalPr	0.00	0.00	0.00	0.00	[3]	Group71	16.44	1082.00	[Aamdc, Aars, Abc
GO:0048518	positive regulation of biol	GO_BiologicalPr	0.00	0.00	0.00	0.00	[1, 2, 3]	Group71	15.06	1032.00	[A2m, Aacs, Aamc
GO:0019222	regulation of metabolic pı	GO_BiologicalPr	0.00	0.00	0.00	0.00	[2, 3]	Group60	14.14	1007.00	[A2m, Aamdc, Aar
GO:0019222	regulation of metabolic pı	GO_BiologicalPr	0.00	0.00	0.00	0.00	[2, 3]	Group66	14.14	1007.00	[A2m, Aamdc, Aar
GO:0019222	regulation of metabolic pı	GO_BiologicalPr	0.00	0.00	0.00	0.00	[2, 3]	Group68	14.14	1007.00	[A2m, Aamdc, Aar
GO:0019222	regulation of metabolic pı	GO_BiologicalPr	0.00	0.00	0.00	0.00	[2, 3]	Group71	14.14	1007.00	[A2m, Aamdc, Aar
GO:1901360	organic cyclic compound	GO_BiologicalPr	0.00	0.00	0.00	0.00	[3]	Group71	15.53	964.00	[Aamdc, Aars, Abc
GO:0010467	gene expression	GO_BiologicalPr	0.00	0.00	0.00	0.00	[4]	Group71	15.25	952.00	[Aamdc, Aars, Abc
GO:0048522	positive regulation of cell	GO_BiologicalPr	0.00	0.00	0.00	0.00	[2, 3, 4]	Group71	15.38	946.00	[Aacs, Aamdc, Ab
GO:0006725	cellular aromatic compou	GO_BiologicalPr	0.00	0.00	0.00	0.00	[3]	Group71	15.66	933.00	[Aamdc, Aars, Abc
GO:0046483	heterocycle metabolic prc	GO_BiologicalPr	0.00	0.00	0.00	0.00	[3]	Group71	15.79	928.00	[Aamdc, Aars, Abc
GO:0060255	regulation of macromolec	GO_BiologicalPr	0.00	0.00	0.00	0.00	[3, 4]	Group60	14.04	926.00	[A2m, Aamdc, Aar

Supplementary Table 11: STRING results for the differentially detected proteins from E14 to P7 for both cell populations

Preview associated with figure 28A. The uploaded data is available under the name “STRING_DEP_AgeE14P7.xlsx” in the repository on github: https://github.com/TabithaRuecker/NeuroDev.git.

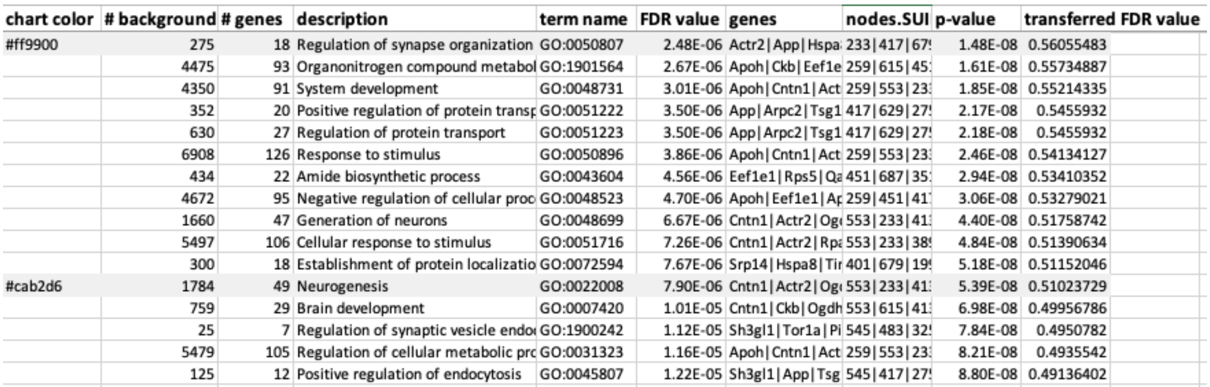

chart color	# background	# genes	description	term name	FDR value	genes	nodes.SUI	p-value	transferred FDR value
#ff9900	275	18	Regulation of synapse organization	GO:0050807	2.48E-06	Actr2|App|Hspa	233|417|67	1.48E-08	0.56055483
	4475	93	Organonitrogen compound metabol	GO:1901564	2.67E-06	Apoh|Ckb|Eef1e	259|615|45	1.61E-08	0.55734887
	4350	91	System development	GO:0048731	3.01E-06	Apoh|Cntn1|Act	259|553|23	1.85E-08	0.55214335
	352	20	Positive regulation of protein transp	GO:0051222	3.50E-06	App|Arpc2|Tsg1	417|629|27	2.17E-08	0.5455932
	630	27	Regulation of protein transport	GO:0051223	3.50E-06	App|Arpc2|Tsg1	417|629|27	2.18E-08	0.5455932
	6908	126	Response to stimulus	GO:0050896	3.86E-06	Apoh|Cntn1|Act	259|553|23	2.46E-08	0.54134127
	434	22	Amide biosynthetic process	GO:0043604	4.56E-06	Eef1e1|Rps5|Q	451|687|35	2.94E-08	0.53410352
	4672	95	Negative regulation of cellular proc	GO:0048523	4.70E-06	Apoh|Eef1e1|A	259|451|41	3.06E-08	0.53279021
	1660	47	Generation of neurons	GO:0048699	6.67E-06	Cntn1|Actr2|Og	553|233|41	4.40E-08	0.51758742
	5497	106	Cellular response to stimulus	GO:0051716	7.26E-06	Cntn1|Actr2|Rp	553|233|38	4.84E-08	0.51390634
	300	18	Establishment of protein localizatio	GO:0072594	7.67E-06	Srp14|Hspa8|Tir	401|679|19	5.18E-08	0.51152046
#cab2d6	1784	49	Neurogenesis	GO:0022008	7.90E-06	Cntn1|Actr2|Og	553|233|41	5.39E-08	0.51023729
	759	29	Brain development	GO:0007420	1.01E-05	Cntn1|Ckb|Ogdh	553|615|41	6.98E-08	0.49956786
	25	7	Regulation of synaptic vesicle endo	GO:1900242	1.12E-05	Sh3gl1|Tor1a|Pi	545|483|32	7.84E-08	0.4950782
	5479	105	Regulation of cellular metabolic prc	GO:0031323	1.16E-05	Apoh|Cntn1|Act	259|553|23	8.21E-08	0.4935542
	125	12	Positive regulation of endocytosis	GO:0045807	1.22E-05	Sh3gl1|App|Tsg	545|417|27	8.80E-08	0.49136402

Integration of modalities

Supplementary Table 12: Metadata matching raw data deposited in public databases

Preview of the data available under the name “MultiOmicsSamples_TabithaRuecker2023.xlsx” in the repository on github: https://github.com/TabithaRuecker/NeuroDev.git.

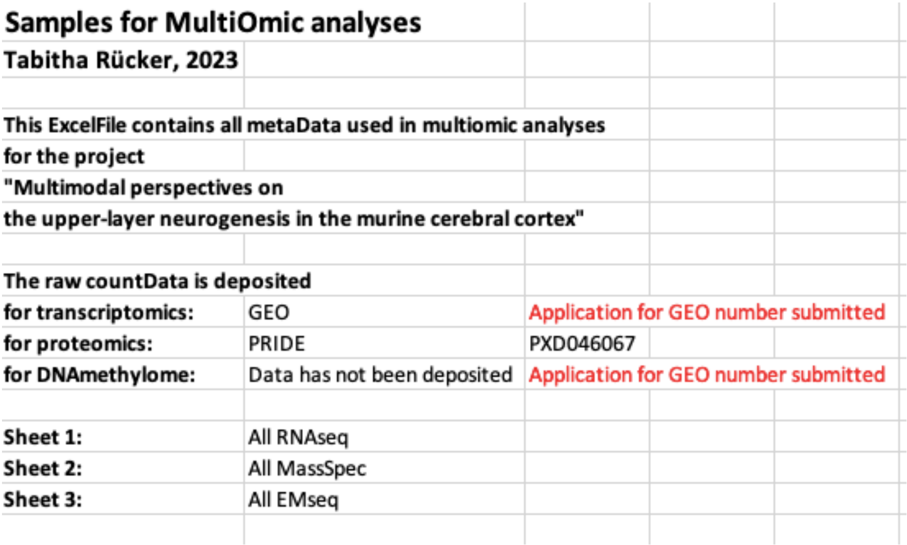

Samples for MultiOmic analyses		
Tabitha Rücker, 2023		
This ExcelFile contains all metaData used in multiomic analyses		
for the project		
"Multimodal perspectives on		
the upper-layer neurogenesis in the murine cerebral cortex"		
The raw countData is deposited		
for transcriptomics:	GEO	Application for GEO number submitted
for proteomics:	PRIDE	PXD046067
for DNAmethylome:	Data has not been deposited	Application for GEO number submitted
Sheet 1:	All RNAseq	
Sheet 2:	All MassSpec	
Sheet 3:	All EMseq	

Reverse panel analysis

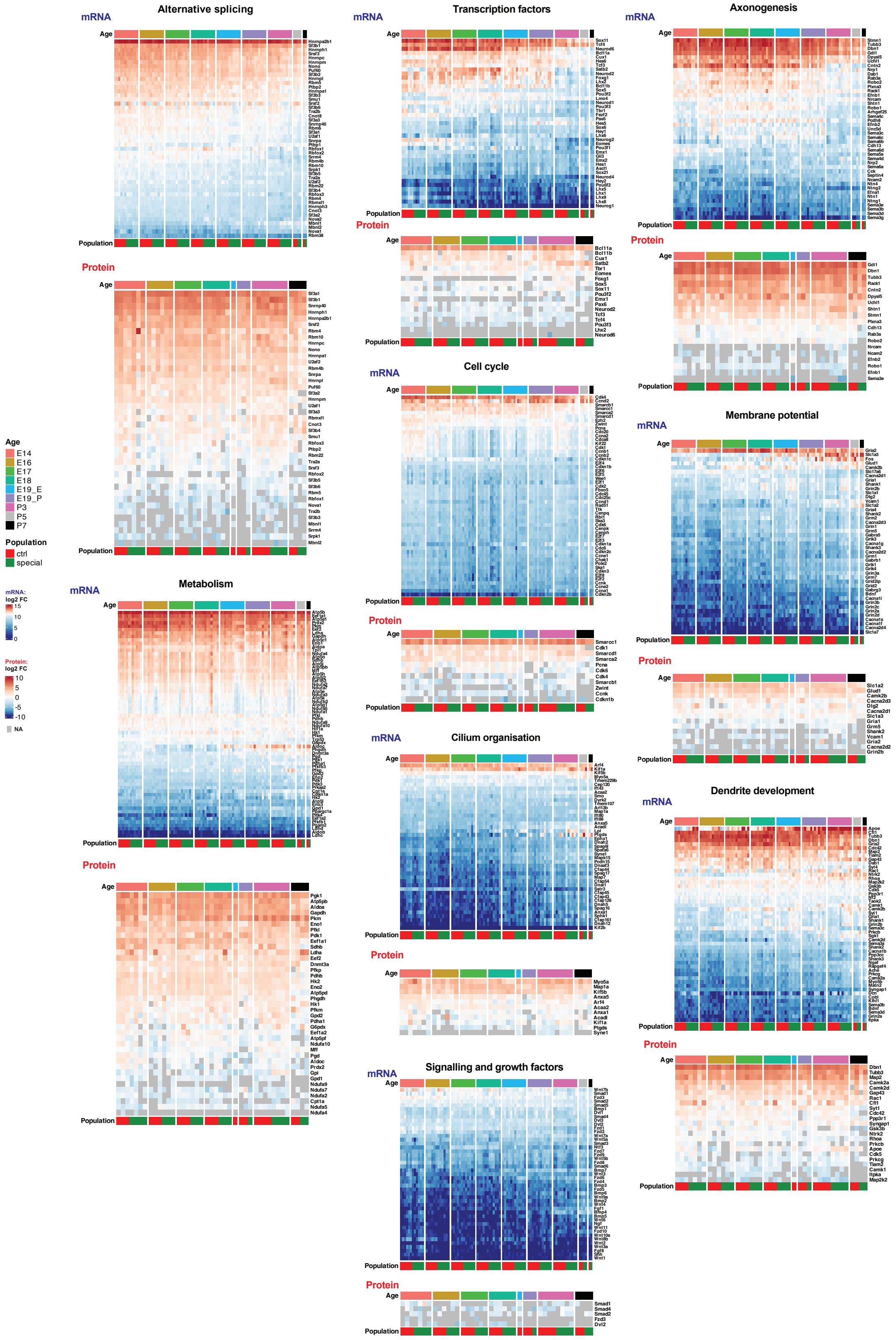

Caption continued on next page

Supplementary Figure 18: Important genes and proteins in selected biological functions

Genes and their respective proteins presented in an unbiased manner, regardless of differential expression or detection. Nevertheless, the same trends as in DEG analysis are evident: Alternative splicing events decrease, metabolism integrates oxidative phosphorylation for energy production, transcription factors and cell cycle activities are down-regulated, while cilium organisation and signalling and growth factors gain importance during upper-layer neurogenesis. Axonogenesis peaked at E16/E17, dendrite development at E18/E19, while membrane potential gradually established by the postnatal stage. RNA and protein levels correlate well, while e.g. secreted factors (see signalling and growth factors) were less detected. One pNeuroD1+ sample at E18 showed extreme gene expression e.g. for metabolism, transcription factors, and cell cycle associated genes. However, this sample was not different at the proteomic level.

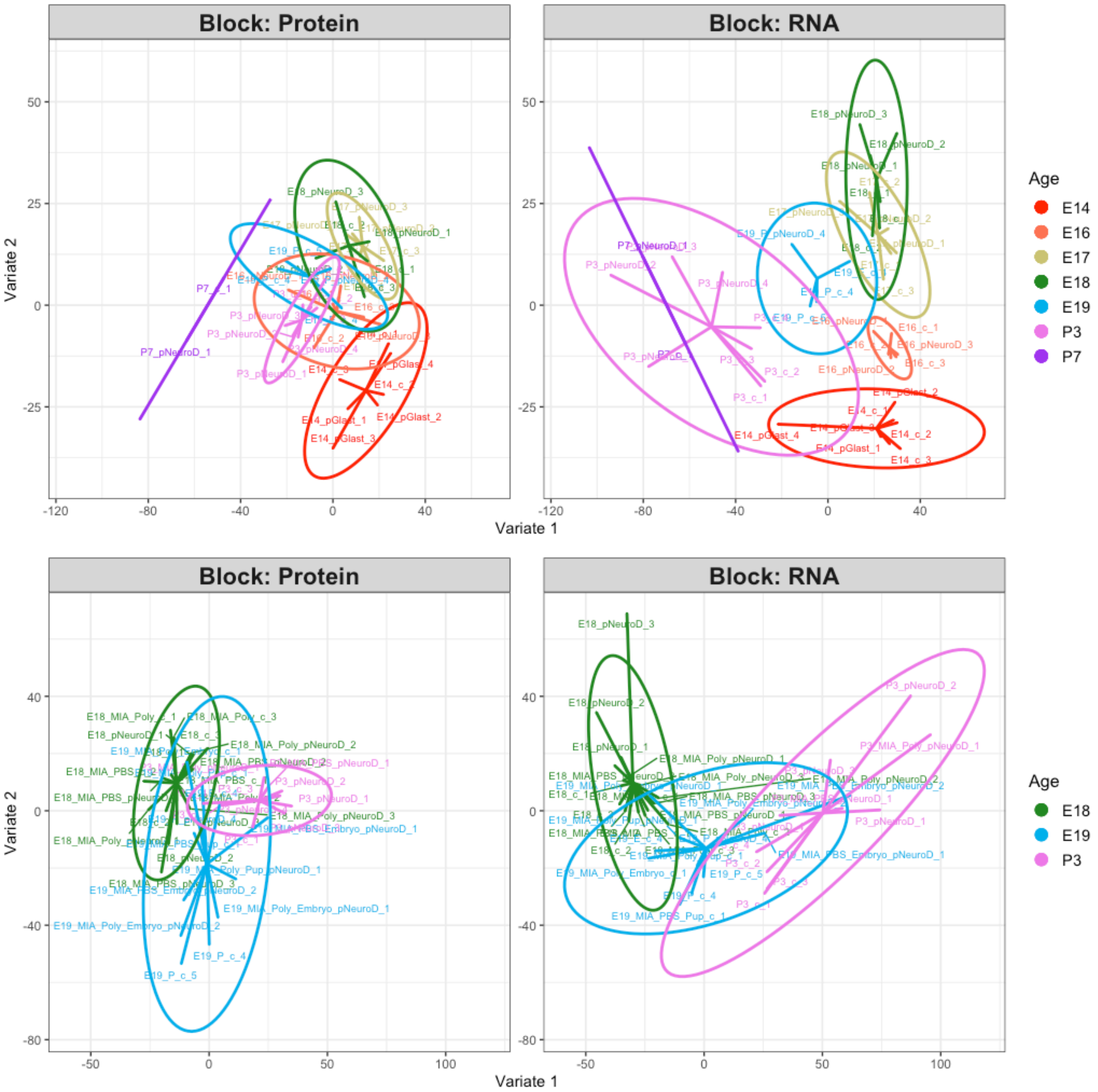

Supplementary Figure 19: Projection of untreated samples (upper panels) and samples focused on E18, E19, and P3 (bottom panels) according to their scores in the first two components for each modality

All detected proteins served as input. The samples differed according to age.

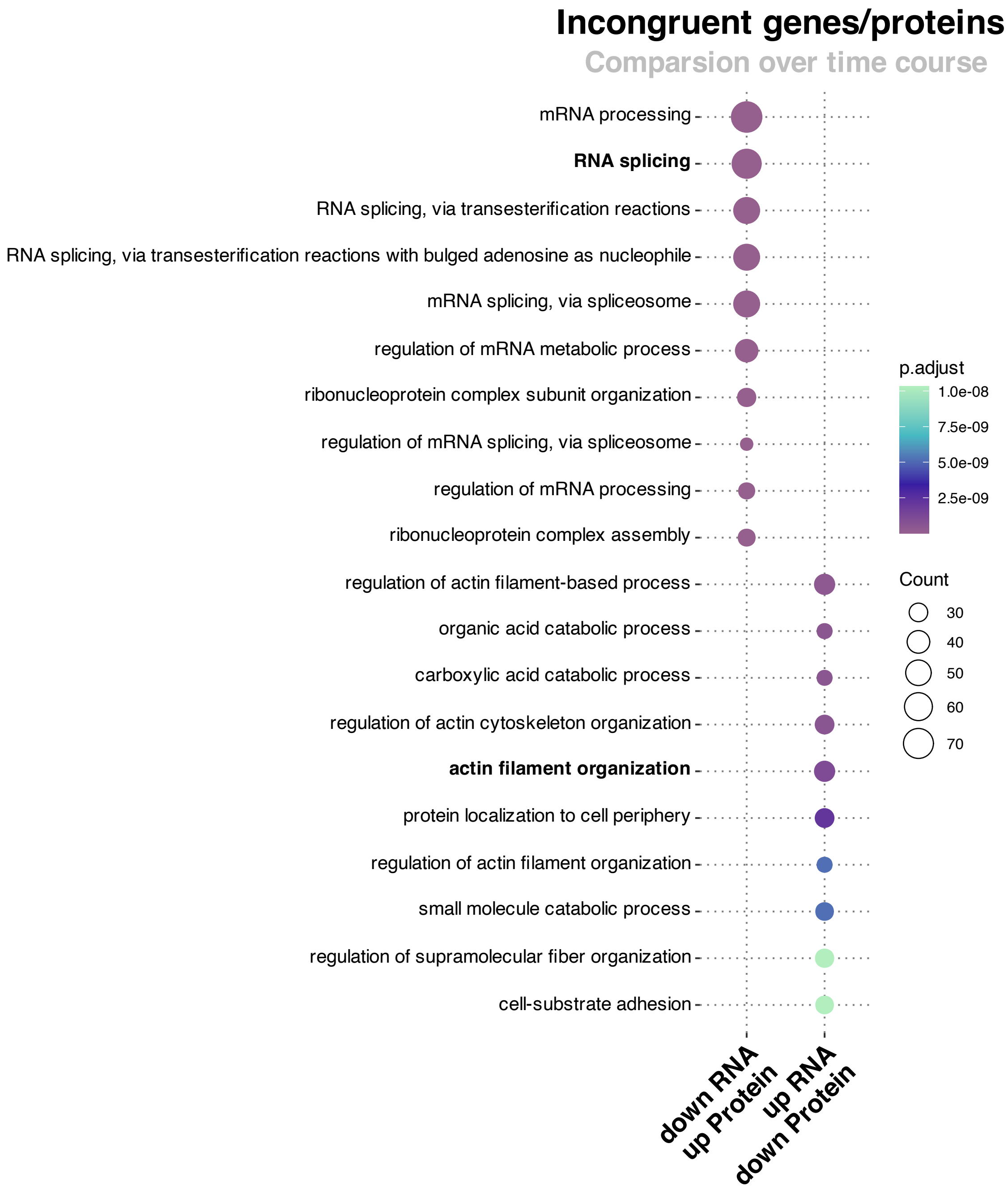

Supplementary Figure 20: Overview of the top ten biological functions (GO) of the incongruently detected genes compared to their respective proteins

Those genes that were down-regulated over measured time but still up-regulated at the protein level were mainly associated with RNA splicing processes (GO:0008380), while those genes that were up-regulated over time but down-regulated as protein were mainly associated with actin filament organisation (GO:0007015).

EM-seq

DNA extraction[2]

Adapted manual for $<10^6$ cells with QIAamp® DNA Micro kit (#56304)

Set up thermoshaker to 56ºC

1. Thaw samples on 4ºC ice.
2. Add 80 µl **Buffer ATL**, ensure that RT has been reached.
   Add 10 µl **proteinase K** and *VORTEX* for 15 sec to homogenise the lysate.
   Add 100 µl **Buffer AL**, ensure that pH<7 has been reached.

3. *VORTEX* the mix for 15 sec and
   incubate for 10 min with 900 rpm in the preheated thermoshaker.
   Briefly centrifuge the sample to conjoin drops.

4. Transfer the sample to a **QIAmp MinElute spin column** placed in a **2 ml collection tube**.
   🔄 Centrifuge for 1 min at 8,000 rpm.
   Discard the **flow through & collection tube**.
   Place the **spin column** in a **new 2 ml collection tube**.

5. Add 500 µl **Buffer AW1** to the **spin column**. 🔄

6. Add 500 µl **Buffer AW2** to the **spin column**.
   Centrifuge for 3 min at 8,000 rpm.
   Discard the **flow through & collection tube**.
   Place the **spin column** in a **new 2 ml collection tube**.

7. Centrifuge for 3 min at 13,400 rpm with closed lid.
   Discard the **flow through and collection tube**. That step ensures that no ethanol is carried over during DNA elution by drying.
   Place the **spin column** in a **new 1.5 ml collection tube**.

8. Add 20 µl **Buffer AE** (10 mM Tris·HCl, 0.5 mM EDTA, pH 9.0) directly to the centre of the spin column membrane and
   place it on the benchtop (at RT) for 5 min.
   Centrifuge for 3 min at 13,400 rpm to elute the DNA.
   Reelute the flow through.

9. DNA is caught in **1.5 ml collecting tube**!
   Store at –20°C.

With this adapted protocol for the QIAamp DNA micro kit (#56304), a proportional increase of DNA concentration can be expected (Suppl. Fig. 21; github repository https://github.com/TabithaRuecker/NeuroDev.git). The extracted DNA was subjected to EM-seq experiments.

---

[2] **Before you start**:
Buffer AW1:
Add 25 ml ethanol (96–100%) to the bottle containing 19 ml Buffer AW1 concentrate. Tick the check box on the bottle label to indicate that ethanol has been added. Reconstituted Buffer AW1 can be stored at room temperature (15–25°C) for up to one year.
Buffer AW2:
Add 30 ml ethanol (96–100%) to the bottle containing 13 ml Buffer AW2 concentrate. Reconstituted Buffer AW2 can be stored at room temperature (15–25°C) for up to one year.

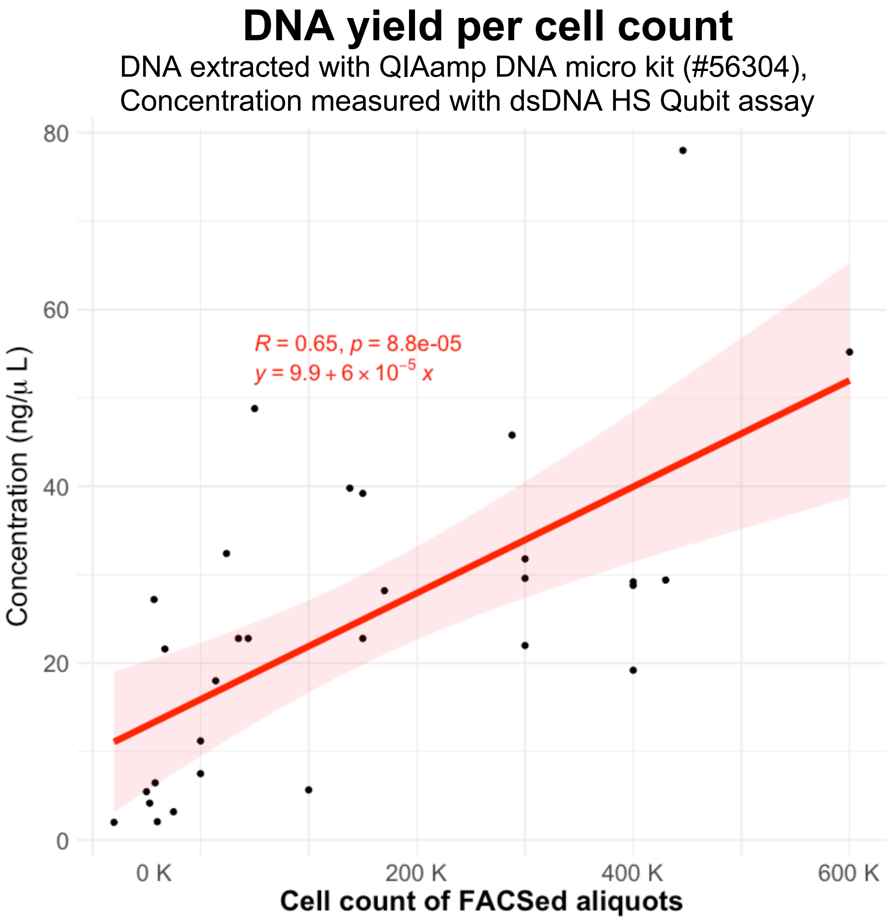

Supplementary Figure 21: DNA yield is predictable at an approximate ratio of 1:10

Quality control for EM-seq libraries

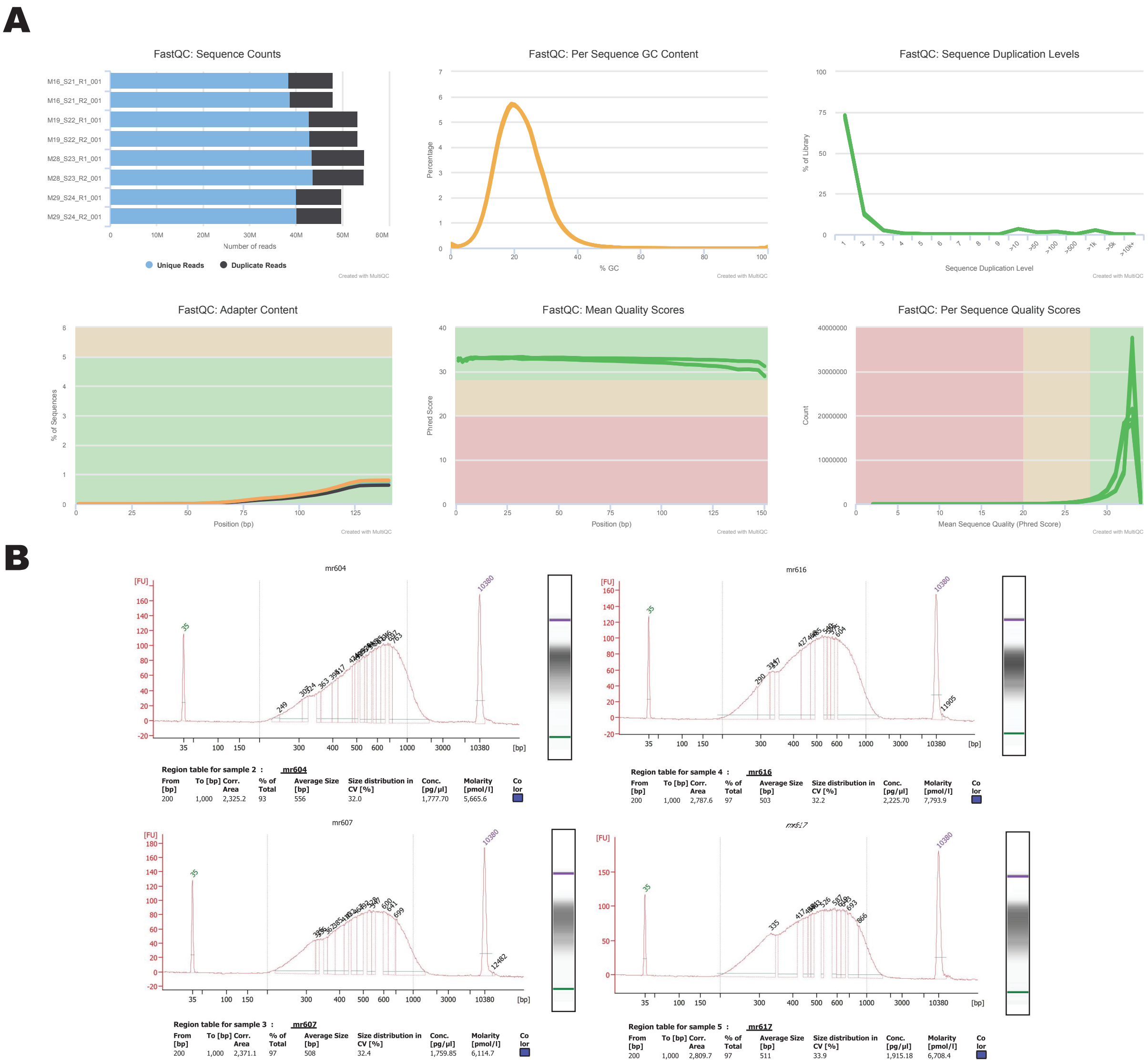

Region table for sample 2 : mr604

From [bp]	To [bp]	Corr. Area	% of Total	Average Size [bp]	Size distribution in CV [%]	Conc. [pg/µl]	Molarity [pmol/l]	Co lor
200	1,000	2,325.2	93	556	32.0	1,777.70	5,665.6	🟦

Region table for sample 4 : mr616

From [bp]	To [bp]	Corr. Area	% of Total	Average Size [bp]	Size distribution in CV [%]	Conc. [pg/µl]	Molarity [pmol/l]	Co lor
200	1,000	2,787.6	97	503	32.2	2,225.70	7,793.9	🟦

Region table for sample 3 : mr607

From [bp]	To [bp]	Corr. Area	% of Total	Average Size [bp]	Size distribution in CV [%]	Conc. [pg/µl]	Molarity [pmol/l]	Co lor
200	1,000	2,371.1	97	508	32.4	1,759.85	6,114.7	🟦

Region table for sample 5 : mr617

From [bp]	To [bp]	Corr. Area	% of Total	Average Size [bp]	Size distribution in CV [%]	Conc. [pg/µl]	Molarity [pmol/l]	Co lor
200	1,000	2,809.7	97	511	33.9	1,915.18	6,708.4	🟦

Supplementary Figure 22: Quality control metrics and Bioanalyzer profiles with an estimation of concentration of the four libraries subjected to EM-seq

A. On average, 40 million read pairs mapped uniquely to the mm10 genome using bwa-meth. GC content averaged 20% after unmethylated cytosines were enzymatically converted by EM-seq. The duplication level was low and adaptor content reported from Illumina universal adaptors. The overall Phred quality scores were all above 30. This applied for most of the read counts.

B. The BioAnalyzer profiles of the EM-seq libraries show comparable quality for all samples. Samples No. 604 and 607 were the PBS-treated samples, while samples No. 616 and 617 were the corresponding PolyI:C-treated samples.

IGV tracks of EM-seq samples

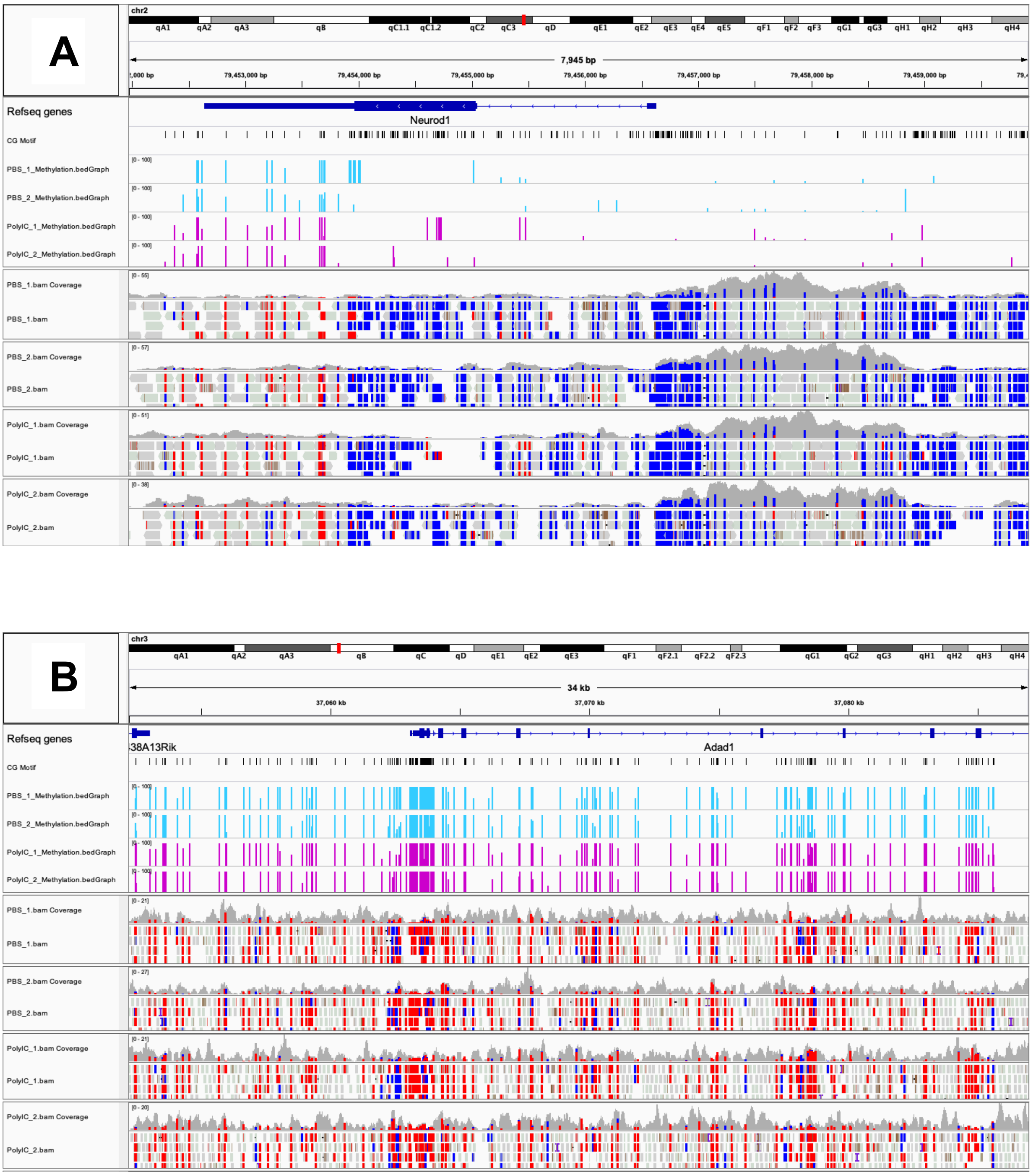

Supplementary Figure 23: IGV tracks of selected genes

The entire mm10 genome was well covered. The Refseq annotation of the mm10 genome is the upper lane, followed by the CG motif for the assumption of CpG islands, followed by the four samples (two PBS samples in turquoise, two PolyI:C samples in magenta) with the percentage methylation per base, and finally the coverage of all samples is shown, with C in blue and G in red. The lanes are arranged so the promoter region, where most CpG islands are expected to be located, is visible.

A. The promoter region of neurogenic differentiation 1 (*NeuroD1*) gene is highly covered and not methylated in all four samples.

B. The promoter region of adenosine deaminase domain containing 1 (*Adad1*) as a testis-specific gene is highly methylated in the promoter region.

Figure and caption continued on next page

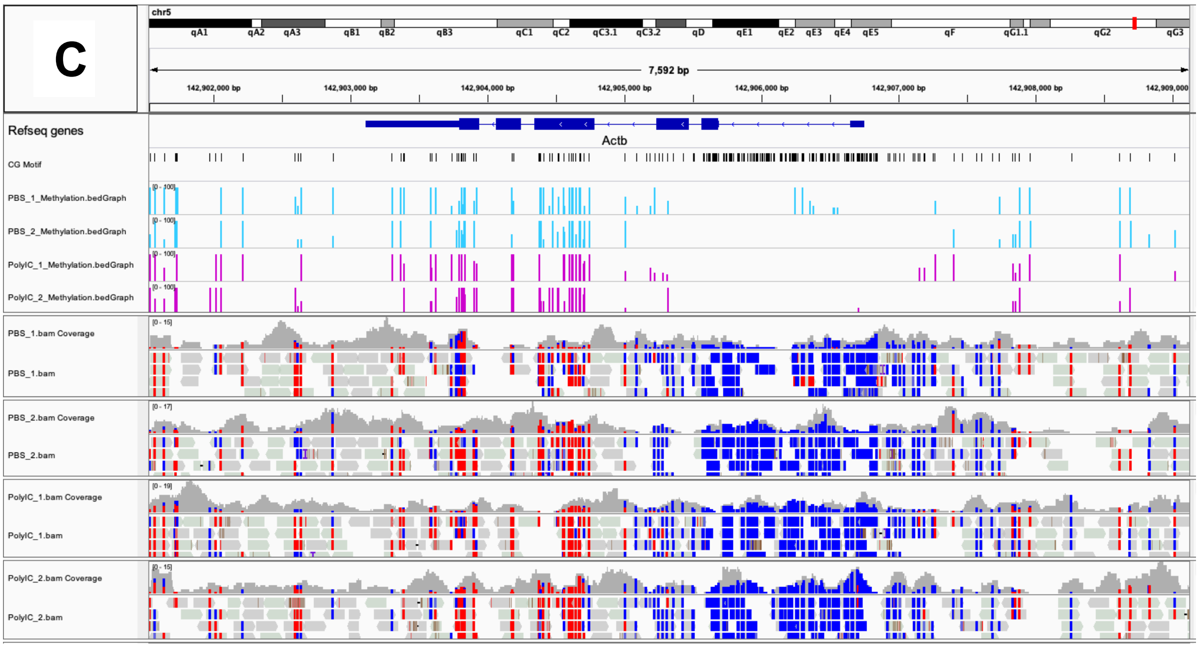

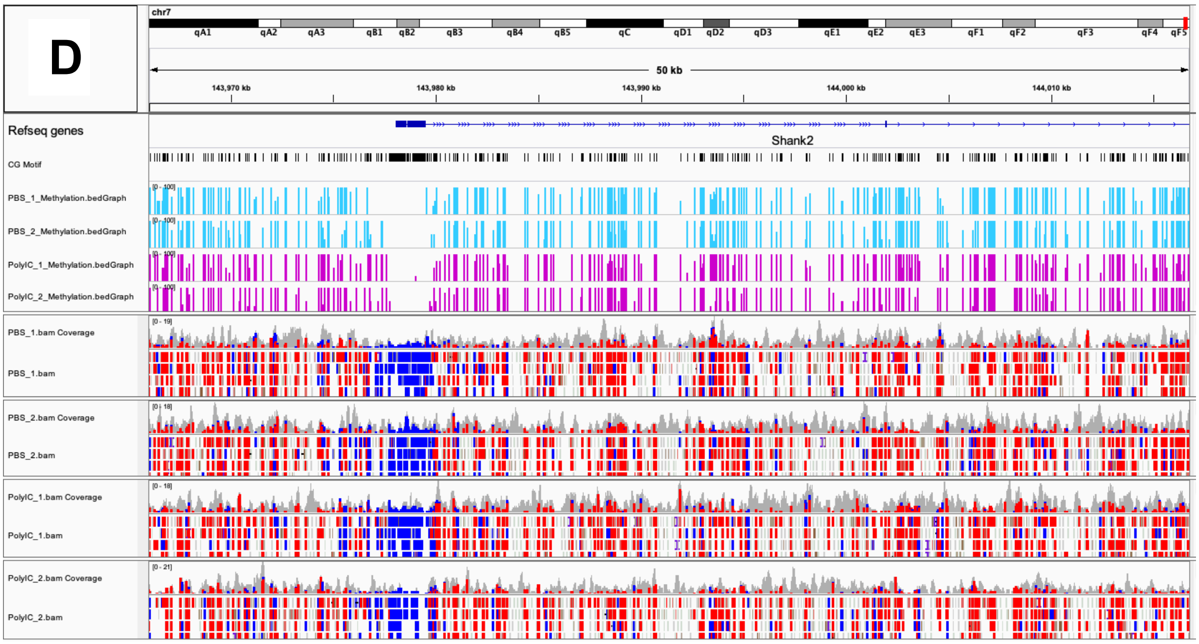

C. The promoter of actin β (*Actb*) as one of the most abundantly expressed genes in neuronal cells, as in the RNA-seq dataset presented, is not expected to be methylated in its promoter region.

D. The promoter of SH3 and multiple ankyrin repeat domains 2 (*Shank2*) was more methylated in the PolyI:C samples than in the PBS samples.

References

1. Rakic, P. Evolution of the neocortex: Perspective from developmental biology. *Nat. Rev. Neurosci.* **10**, 724 (2009).
2. Franchini, L. F. Genetic Mechanisms Underlying Cortical Evolution in Mammals. *Front. Cell Dev. Biol.* **9**, 591017 (2021).
3. Cárdenas, A. *et al.* Evolution of Cortical Neurogenesis in Amniotes Controlled by Robo Signaling Levels. *Cell* **174**, 590-606.e21 (2018).
4. Fang, W. Q. *et al.* Overproduction of Upper-Layer Neurons in the Neocortex Leads to Autism-like Features in Mice. *Cell Rep.* **9**, 1635–1643 (2014).
5. Courchesne, E. *et al.* Neuron number and size in prefrontal cortex of children with autism. *Jama* **306**, 2001–2010 (2011).
6. Batiuk, M. Y. *et al.* Upper cortical layer–driven network impairment in schizophrenia. *Sci. Adv.* **8**, (2022).
7. Dong, E. *et al.* Brain-derived neurotrophic factor epigenetic modifications associated with schizophrenia-like phenotype induced by prenatal stress in mice. **77**, 589–596 (2015).
8. Seuntjens, E. *et al.* Sip1 regulates sequential fate decisions by feedback signaling from postmitotic neurons to progenitors. *Nat. Neurosci.* **12**, 1373–1380 (2009).
9. Sessa, A., Mao, C. an, Hadjantonakis, A. K., Klein, W. H. & Broccoli, V. Tbr2 Directs Conversion of Radial Glia into Basal Precursors and Guides Neuronal Amplification by Indirect Neurogenesis in the Developing Neocortex. *Neuron* **60**, 56–69 (2008).
10. Magrinelli, E. *et al.* Heterogeneous fates of simultaneously-born neurons in the cortical ventricular zone. *Sci. Rep.* **12**, 1–11 (2022).
11. Noctor, S. C., Martinez-Cerdeño, V., Ivic, L. & Kriegstein, A. R. Cortical neurons arise in symmetric and asymmetric division zones and migrate through specific phases. *Nat. Neurosci.* **7**, 136–144 (2004).
12. Iwashita, M., Kataoka, N., Toida, K. & Kosodo, Y. Systematic profiling of spatiotemporal tissue and cellular stiffness in the developing brain. *Dev.* **141**, 3793–3798 (2014).
13. Haydar, T. F., Wang, F., Schwartz, M. L. & Rakic, P. Differential modulation of proliferation in the neocortical ventricular and subventricular zones. *J. Neurosci.* **20**, 5764–5774 (2000).
14. Rakic, P. Radial unit hypothesis of neocortical expansion. *Novartis Found. Symp.* **228**, 30–45 (2000).
15. Jinnou, H. *et al.* Radial Glial Fibers Promote Neuronal Migration and Functional Recovery after Neonatal Brain Injury. *Cell Stem Cell* **22**, 128-137.e9 (2018).
16. Ferent, J., Zaidi, D. & Francis, F. Extracellular Control of Radial Glia Proliferation and Scaffolding During Cortical Development and Pathology. *Front. Cell Dev. Biol.* **8**, 1031 (2020).
17. Miranda-Negrón, Y. & García-Arrarás, J. E. Radial glia and radial glia-like cells: Their role in neurogenesis and regeneration. *Front. Neurosci.* **16**, (2022).
18. Franco, S. J. *et al.* Fate-Restricted Neural Progenitors in the Mammalian Cerebral Cortex. *Science* **337**, 746 (2012).
19. Bonnefont, J. & Vanderhaeghen, P. Neuronal fate acquisition and specification: time for a change. *Curr. Opin. Neurobiol.* **66**, 195–204 (2021).
20. Shibata, T. *et al.* Glutamate transporter GLAST is expressed in the radial glia-astrocyte

lineage of developing mouse spinal cord. *J. Neurosci.* **17**, 9212–9219 (1997).

21. Jansson, L. C. *et al.* Effect of glutamate receptor antagonists on migrating neural progenitor cells. *Eur. J. Neurosci.* **37**, 1369–1382 (2013).

22. Ganor, Y. & Levite, M. The neurotransmitter glutamate and human T cells: Glutamate receptors and glutamate-induced direct and potent effects on normal human T cells, cancerous human leukemia and lymphoma T cells, and autoimmune human T cells. *J. Neural Transm.* **121**, 983–1006 (2014).

23. Schlett, K. Glutamate as a Modulator of Embryonic and Adult Neurogenesis. *Curr. Top. Med. Chem.* **6**, 949–960 (2006).

24. Ikonomidou, C. *et al.* Blockade of NMDA Receptors and Apoptotic Neurodegeneration in the Developing Brain. *Science (80-.).* **283**, 70–74 (1999).

25. Ina, A. *et al.* Cajal-Retzius cells and subplate neurons differentially express vesicular glutamate transporters 1 and 2 during development of mouse cortex. *Eur. J. Neurosci.* **26**, 615–623 (2007).

26. Del Río, J. A., Martinez, A., Fonseca, M., Auladell, C. & Soriano, E. Glutamate-like immunoreactivity and fate of cajal-retzius cells in the murine cortex as identified with calretinin antibody. *Cereb. Cortex* **5**, 13–21 (1995).

27. Ohtaka-Maruyama, C. Subplate Neurons as an Organizer of Mammalian Neocortical Development. *Front. Neuroanat.* **14**, 1–9 (2020).

28. Jansson, L. C. & Åkerman, K. E. The role of glutamate and its receptors in the proliferation, migration, differentiation and survival of neural progenitor cells. *J. Neural Transm.* **121**, 819–836 (2014).

29. Behar, T. N. *et al.* Glutamate Acting at NMDA Receptors Stimulates Embryonic Cortical Neuronal Migration. *J. Neurosci.* **19**, 4449–4461 (1999).

30. Schinder, A. F., Olson, E. C., Spitzer, N. C. & Montal, M. Mitochondrial dysfunction is a primary event in glutamate neurotoxicity. *J. Neurosci.* **16**, 6125–6133 (1996).

31. Aida, T., Ito, Y., Takahashi, Y. K. & Tanaka, K. Overstimulation of NMDA receptors impairs early brain development in vivo. *PLoS One* **7**, 1–8 (2012).

32. Mahmoud, S., Gharagozloo, M., Simard, C. & Gris, D. Astrocytes Maintain Glutamate Homeostasis in the CNS by Controlling the Balance between Glutamate Uptake and Release. *Cells* **8**, (2019).

33. Walsh, T. *et al.* Rare structural variants disrupt multiple genes in neurodevelopmental pathways in schizophrenia. *Science (80-.).* **320**, 539–543 (2008).

34. Karlsson, R. M. *et al.* Assessment of glutamate transporter GLAST (EAAT1)-deficient mice for phenotypes relevant to the negative and executive/cognitive symptoms of schizophrenia. *Neuropsychopharmacology* **34**, 1578–1589 (2009).

35. Matsugami, T. R. *et al.* Indispensability of the glutamate transporters GLAST and GLT1 to brain development. *Proc. Natl. Acad. Sci. U. S. A.* **103**, 12161–12166 (2006).

36. Uchida, M. *et al.* Early postnatal inhibition of GLAST causes abnormalities of psychobehaviors and neuronal morphology in adult mice. *Neurochem. Int.* **150**, 105177 (2021).

37. Tata, M. & Ruhrberg, C. Cross-talk between blood vessels and neural progenitors in the developing brain. *Neuronal Signal.* **2**, 1–13 (2018).

38. Konno, D. *et al.* Neuroepithelial progenitors undergo LGN-dependent planar divisions to maintain self-renewability during mammalian neurogenesis. *Nat. Cell Biol.* **10**, 93–101 (2008).

39. Mihalas, A. B. & Hevner, R. F. Clonal analysis reveals laminar fate multipotency and daughter cell apoptosis of mouse cortical intermediate progenitors. *Dev.* **145**, (2018).

40. Qian, X. *et al.* Timing of CNS Cell Generation: A Programmed Sequence of Neuron and Glial Cell Production from Isolated Murine Cortical Stem Cells. *Neuron* **28**, 69–80 (2000).

41. Kwan, K. Y., Šestan, N. & Anton, E. S. Transcriptional co-regulation of neuronal migration and

laminar identity in the neocortex. *Development* **139**, 1535–1546 (2012).

42. DeFelipe, J. & Fariñas, I. The pyramidal neuron of the cerebral cortex: Morphological and chemical characteristics of the synaptic inputs. *Prog. Neurobiol.* **39**, 563–607 (1992).
43. Tabata, H., Kanatani, S. & Nakajima, K. Differences of migratory behavior between direct progeny of apical progenitors and basal progenitors in the developing cerebral cortex. *Cereb. Cortex* **19**, 2092–2105 (2009).
44. Martínez-Cerdeño, V. *et al.* Evolutionary origin of Tbr2-expressing precursor cells and the subventricular zone in the developing cortex. **524**, 433–447 (2017).
45. Cheung, A. F. P., Pollen, A. A., Tavare, A., Deproto, J. & Molnár, Z. Comparative aspects of cortical neurogenesis in vertebrates. *J. Anat.* **211**, 164–176 (2007).
46. Nomura, T., Gotoh, H. & Ono, K. Changes in the regulation of cortical neurogenesis contribute to encephalization during amniote brain evolution. *Nat. Commun. 2013 41* **4**, 1–12 (2013).
47. Charvet, C. J. & Striedter, G. F. Causes and consequences of expanded subventricular zones. *Eur. J. Neurosci.* **34**, 988–993 (2011).
48. Smart, I. H. M., Dehay, C., Giroud, P., Berland, M. & Kennedy, H. Unique morphological features of the proliferative zones and postmitotic compartments of the neural epithelium giving rise to striate and extrastriate cortex in the monkey. *Cereb. Cortex* **12**, 37–53 (2002).
49. Kriegstein, A., Noctor, S. & Martínez-Cerdeño, V. Patterns of neural stem and progenitor cell division may underlie evolutionary cortical expansion. *Nat. Rev. Neurosci.* **7**, 883–890 (2006).
50. Desai, A. R. & McConnell, S. K. Progressive restriction in fate potential by neural progenitors during cerebral cortical development. *Development* **127**, 2863–2872 (2000).
51. Molyneaux, B. J., Arlotta, P., Menezes, J. R. L. & Macklis, J. D. Neuronal subtype specification in the cerebral cortex. *Nat. Rev. Neurosci.* **8**, 427–437 (2007).
52. Ruan, X. *et al.* Progenitor cell diversity in the developing mouse neocortex. *Proc. Natl. Acad. Sci. U. S. A.* **118**, 10–17 (2021).
53. Lv, X. *et al.* TBR2 coordinates neurogenesis expansion and precise microcircuit organization via Protocadherin 19 in the mammalian cortex. *Nat. Commun.* **10**, 1–15 (2019).
54. Arnold, S. J. *et al.* The T-box transcription factor Eomes/Tbr2 regulates neurogenesis in the cortical subventricular zone. *Genes Dev.* **22**, 2479–2484 (2008).
55. Mihalas, A. B. *et al.* Intermediate Progenitor Cohorts Differentially Generate Cortical Layers and Require Tbr2 for Timely Acquisition of Neuronal Subtype Identity. *Cell Rep.* **16**, 92–105 (2016).
56. Simon, C. S. *et al.* Functional characterisation of cis-regulatory elements governing dynamic Eomes expression in the early mouse embryo. *Development* **144**, 1249 (2017).
57. Pollen, A. A. *et al.* Molecular Identity of Human Outer Radial Glia during Cortical Development. *Cell* **163**, 55–67 (2015).
58. Molnár, Z. *et al.* New insights into the development of the human cerebral cortex. *J. Anat.* **235**, 432–451 (2019).
59. Betizeau, M. *et al.* Precursor Diversity and Complexity of Lineage Relationships in the Outer Subventricular Zone of the Primate. *Neuron* **80**, 442–457 (2013).
60. Lukaszewicz, A. *et al.* G1 phase regulation, area-specific cell cycle control, and cytoarchitectonics in the primate cortex. *Neuron* **47**, 353–364 (2005).
61. Kalebic, N. *et al.* Neocortical Expansion Due to Increased Proliferation of Basal Progenitors Is Linked to Changes in Their Morphology. *Cell Stem Cell* **24**, 535-550.e9 (2019).
62. de la Torre-Ubieta, L. *et al.* The Dynamic Landscape of Open Chromatin during Human Cortical Neurogenesis. *Cell* **172**, 289-304.e18 (2018).
63. Ohtaka-Maruyama, C. & Okado, H. Molecular pathways underlying projection neuron production and migration during cerebral cortical development. *Front. Neurosci.* **9**, 1–24 (2015).

64. Nelson, B. R., Hodge, R. D., Bedogni, F. & Hevner, R. F. Dynamic interactions between intermediate neurogenic progenitors and radial glia in embryonic mouse neocortex: Potential role in Dll1-notch signaling. *J. Neurosci.* **33**, 9122–9139 (2013).

65. Castro, D. S. *et al.* Proneural bHLH and Brn Proteins Coregulate a Neurogenic Program through Cooperative Binding to a Conserved DNA Motif. *Dev. Cell* **11**, 831–844 (2006).

66. Nelson, B. R. *et al.* Intermediate progenitors support migration of neural stem cells into dentate gyrus outer neurogenic niches. *Elife* **9**, 1–30 (2020).

67. Sessa, A. *et al.* The Tbr2 Molecular Network Controls Cortical Neuronal Differentiation Through Complementary Genetic and Epigenetic Pathways. *Cereb. Cortex* **27**, 3378–3396 (2017).

68. Noack, F. *et al.* Multimodal profiling of the transcriptional regulatory landscape of the developing mouse cortex identifies Neurog2 as a key epigenome remodeler. *Nat. Neurosci. 2022* **25**, 1–14 (2022).

69. Elsen, G. E. *et al.* The Epigenetic Factor Landscape of Developing Neocortex Is Regulated by Transcription Factors Pax6→ Tbr2→ Tbr1. *Front. Neurosci.* **12**, (2018).

70. Ochiai, W. *et al.* Periventricular notch activation and asymmetric Ngn2 and Tbr2 expression in pair-generated neocortical daughter cells. *Mol. Cell. Neurosci.* **40**, 225–233 (2009).

71. Kovach, C. *et al.* Neurog2 simultaneously activates and represses alternative gene expression programs in the developing neocortex. *Cereb. Cortex* **23**, 1884–1900 (2013).

72. Arnold, S. J., Hofmann, U. K., Bikoff, E. K. & Robertson, E. J. Pivotal roles for eomesodermin during axis formation, epithelium-to-mesenchyme transition and endoderm specification in the mouse. *Development* **135**, 501–511 (2008).

73. Schulte, J. D. *et al.* Cadherin-11 Regulates Motility in Normal Cortical Neural Precursors and Glioblastoma. *PLoS One* **8**, 1–11 (2013).

74. Ohtaka-Maruyama, C. *et al.* RP58 Regulates the Multipolar-Bipolar Transition of Newborn Neurons in the Developing Cerebral Cortex. *Cell Rep.* **3**, 458–471 (2013).

75. Azzarelli, R., Guillemot, F. & Pacary, E. Function and regulation of Rnd proteins in cortical projection neuron migration. *Front. Neurosci.* **9**, 19 (2015).

76. Komabayashi-Suzuki, M. *et al.* Spatiotemporally Dependent Vascularization Is Differently Utilized among Neural Progenitor Subtypes during Neocortical Development. *Cell Rep.* **29**, 1113-1129.e5 (2019).

77. Itoh, Y. *et al.* Scratch regulates neuronal migration onset via an epithelial-mesenchymal transition-like mechanism. *Nat. Neurosci.* **16**, 416–425 (2013).

78. Tavano, S. *et al.* Insm1 Induces Neural Progenitor Delamination in Developing Neocortex via Downregulation of the Adherens Junction Belt-Specific Protein Plekha7. *Neuron* **97**, 1299-1314.e8 (2018).

79. De Anda, F. C., Meletis, K., Ge, X., Rei, D. & Tsai, L. H. Centrosome Motility Is Essential for Initial Axon Formation in the Neocortex. *J. Neurosci.* **30**, 10391–10406 (2010).

80. Nomura, T. *et al.* Changes in Wnt-Dependent Neuronal Morphology Underlie the Anatomical Diversification of Neocortical Homologs in Amniotes. *Cell Rep.* **31**, 107592 (2020).

81. Bulstrode, H. *et al.* Elevated FOXG1 and SOX2 in glioblastoma enforces neural stem cell identity through transcriptional control of cell cycle and epigenetic regulators. *Genes Dev.* **31**, 757–773 (2017).

82. Mizutani, K. I., Yoon, K., Dang, L., Tokunaga, A. & Gaiano, N. Differential Notch signalling distinguishes neural stem cells from intermediate progenitors. *Nature* **449**, 351–355 (2007).

83. Elsen, G. E. *et al.* The protomap is propagated to cortical plate neurons through an Eomes-dependent intermediate map. *Proc. Natl. Acad. Sci. U. S. A.* **110**, 4081–4086 (2013).

84. Zhang, M. *et al.* Axonogenesis is coordinated by neuron-specific alternative splicing programming and splicing regulator PTBP2. *Neuron* **101**, 690 (2019).

85. Lin, G. *et al.* GCN5/KAT2A contributes to axon growth and neurogenesis. *Neurosci. Lett.* **784**, 136742 (2022).

86. Meka, D. P. *et al.* Centrosome-dependent microtubule modifications set the conditions for axon formation. *Cell Rep.* **39**, 110686 (2022).

87. Leterrier, C. The Axon Initial Segment: An Updated Viewpoint. *J. Neurosci.* **38**, 2135–2145 (2018).

88. Dorrego-Rivas, A. *et al.* The core PCP protein Prickle2 regulates axon number and AIS maturation by binding to AnkG and modulating microtubule bundling. *Sci. Adv.* **8**, (2022).

89. Kole, M. H. P. *et al.* Action potential generation requires a high sodium channel density in the axon initial segment. *Nat. Neurosci.* **11**, 178–186 (2008).

90. Lundgaard, I. *et al.* Neuregulin and BDNF Induce a Switch to NMDA Receptor-Dependent Myelination by Oligodendrocytes. *PLoS Biol.* **11**, 1001743 (2013).

91. Azzarelli, R., Kerloch, T. & Pacary, E. Regulation of cerebral cortex development by Rho GTPases: insights from in vivo studies. *Front. Cell. Neurosci.* **8**, (2014).

92. Ferrer-Vaquer, A., Viotti, M. & Hadjantonakis, A.-K. Transitions between epithelial and mesenchymal states and the morphogenesis of the early mouse embryo. *Cell Adh. Migr.* **4**, 447–457 (2010).

93. Kannan, M. *et al.* WD40-repeat 47, a microtubule-associated protein, is essential for brain development and autophagy. *Proc. Natl. Acad. Sci. U. S. A.* **114**, E9308–E9317 (2017).

94. Hatanaka, Y. & Yamauchi, K. Excitatory Cortical Neurons with Multipolar Shape Establish Neuronal Polarity by Forming a Tangentially Oriented Axon in the Intermediate Zone. *Cereb. Cortex* **23**, 105–113 (2013).

95. Zmuda, J. F. & Rivas, R. J. The Golgi apparatus and the centrosome are localized to the sites of newly emerging axons in cerebellar granule neurons in vitro. *Cell Motil. Cytoskeleton* **41**, 18–38 (1998).

96. Zhao, B. *et al.* Microtubules Modulate F-actin Dynamics during Neuronal Polarization. *Sci. Reports 2017 71* **7**, 1–16 (2017).

97. Solecki, D. J. *et al.* Myosin II Motors and F-Actin Dynamics Drive the Coordinated Movement of the Centrosome and Soma During CNS Glial-Guided Neuronal Migration. *Neuron* **63**, 63 (2009).

98. Hevner, R. F. Intermediate progenitors and Tbr2 in cortical development. *J. Anat.* **235**, 616–625 (2019).

99. Hatanaka, Y., Hisanaga, S. I., Heizmann, C. W. & Murakami, F. Distinct migratory behavior of early- and late-born neurons derived from the cortical ventricular zone. *J. Comp. Neurol.* **479**, 1–14 (2004).

100. Frantz, G. D. & McConnell, S. K. Restriction of late cerebral cortical progenitors to an upper-layer fate. *Neuron* **17**, 55–61 (1996).

101. Pontious, A., Kowalczyk, T., Englund, C. & Hevner, R. F. Role of intermediate progenitor cells in cerebral cortex development. *Dev. Neurosci.* **30**, 24–32 (2007).

102. Toma, K., Kumamoto, T., Hanashima, C., Toma, K. & Hanashima, C. The timing of upper-layer neurogenesis is conferred by sequential derepression and negative feedback from deep-layer neurons. *J. Neurosci.* **34**, 13259–13276 (2014).

103. Oishi, K. *et al.* Identity of neocortical layer 4 neurons is specified through correct positioning into the cortex. *Elife* **5**, (2016).

104. Dotti, C. G., Sullivan, C. A. & Banker, G. A. The establishment of polarity by hippocampal neurons in culture. *J. Neurosci.* **8**, 1454 (1988).

105. Li, Q. *et al.* ADAM17 Is Critical for Multipolar Exit and Radial Migration of Neuronal Intermediate Progenitor Cells in Mice Cerebral Cortex. *PLoS One* **8**, (2013).

106. Shikanai, M., Nakajima, K. & Kawauchi, T. N-cadherin regulates radial glial fiber-dependent

migration of cortical locomoting neurons. *Commun. Integr. Biol.* **4**, 326 (2011).

107. Jossin, Y. & Cooper, J. A. Reelin, Rap1 and N-cadherin orient the migration of multipolar neurons in the developing neocortex. *Nat. Neurosci. 2011 146* **14**, 697–703 (2011).

108. Kadowaki, M. *et al.* N-cadherin mediates cortical organization in the mouse brain. *Dev. Biol.* **304**, 22–33 (2007).

109. Martínez-Martínez, M. Á. *et al.* A restricted period for formation of outer subventricular zone defined by Cdh1 and Trnp1 levels. *Nat. Commun. 2016 71* **7**, 1–15 (2016).

110. Stocker, A. M. & Chenn, A. The role of adherens junctions in the developing neocortex. *http://dx.doi.org/10.1080/19336918.2015.1027478* **9**, 167–174 (2015).

111. Poluch, S. & Juliano, S. L. Populations of radial glial cells respond differently to reelin and neuregulin1 in a ferret model of cortical dysplasia. *PLoS One* **5**, (2010).

112. Morrow, C. S. *et al.* Vimentin coordinates protein turnover at the aggresome during neural stem cell quiescence exit. *Cell Stem Cell.* **26**, 558–568 (2021).

113. Zhang, J. *et al.* Cortical neural precursors inhibit their own differentiation via N- cadherin maintenance of beta-catenin signaling. **18**, 472–479 (2011).

114. Stocker, A. M. & Chenn, A. Differential expression of alpha-E-catenin and alpha-N-catenin in the developing cerebral cortex. *Brain Res.* **1073–1074**, 151–158 (2006).

115. Alimperti, S. & Andreadis, S. T. CDH2 and CDH11 act as regulators of stem cell fate decisions. *Stem Cell Res.* **14**, 270–282 (2015).

116. Thiery, J. P., Acloque, H., Huang, R. Y. J. & Nieto, M. A. Epithelial-Mesenchymal Transitions in Development and Disease. *Cell* **139**, 871–890 (2009).

117. Zander, M. A., Cancino, G. I., Gridley, T., Kaplan, D. R. & Miller, F. D. The Snail Transcription Factor Regulates the Numbers of Neural Precursor Cells and Newborn Neurons throughout Mammalian Life. *PLoS One* **9**, e104767 (2014).

118. Paul, V. *et al.* Scratch2 modulates neurogenesis and cell migration through antagonism of bHLH proteins in the developing neocortex. *Cereb. Cortex* **24**, 754–772 (2014).

119. Schaar, B. T. & McConnell, S. K. Cytoskeletal coordination during neuronal migration. *Proc. Natl. Acad. Sci. U. S. A.* **102**, 13652 (2005).

120. Vallee, R. B., Seale, G. E. & Tsai, J. W. Emerging roles for myosin II and cytoplasmic dynein in migrating neurons and growth cones. *Trends Cell Biol.* **19**, 347 (2009).

121. Thompson, A. J. *et al.* Rapid changes in tissue mechanics regulate cell behaviour in the developing embryonic brain. *Elife* **8**, 1–18 (2019).

122. Koser, D. E. *et al.* Mechanosensing is critical for axon growth in the developing brain. *Nat. Neurosci.* **19**, 1592–1598 (2016).

123. Mizutani, K. I. Physiological significance of multipolar cells generated from neural stem cells and progenitors for the establishment of neocortical cytoarchitecture. *Genes to Cells* **23**, 6–15 (2018).

124. Segel, M. *et al.* Niche stiffness underlies the ageing of central nervous system progenitor cells. *Nature* **573**, 130–134 (2019).

125. Luo, R. *et al.* G protein-coupled receptor 56 and collagen III, a receptor-ligand pair, regulates cortical development and lamination. *Proc. Natl. Acad. Sci. U. S. A.* **108**, 12925–12930 (2011).

126. Jeong, S. J. *et al.* GPR56 functions together with α3β1 integrin in regulating cerebral cortical development. *PLoS One* **8**, (2013).

127. Ohtaka-Maruyama, C. *et al.* Synaptic transmission from subplate neurons controls radial migration of neocortical neurons. *Science (80-.).* **360**, 313–317 (2018).

128. Jingqi Wang, A. *et al.* Organelle mapping in dendrites of human iPSC-derived neurons reveals dynamic functional dendritic Golgi structures. (2023). doi:10.1016/j.celrep.2023.112709

129. Brand, T. Heart development: Molecular insights into cardiac specification and early

morphogenesis. *Dev. Biol.* **258**, 1–19 (2003).

130. Chiapparo, G. *et al.* Mesp1 controls the speed, polarity, and directionality of cardiovascular progenitor migration. *J. Cell Biol.* **213**, 463–477 (2016).

131. Toda, T., Shinmyo, Y., Dinh Duong, T. A., Masuda, K. & Kawasaki, H. An essential role of SVZ progenitors in cortical folding in gyrencephalic mammals. *Sci. Reports 2016 61* **6**, 1–12 (2016).

132. Galakhova, A. A. *et al.* Evolution of cortical neurons supporting human cognition. *Trends Cogn. Sci.* **26**, 909–922 (2022).

133. Petreanu, L., Huber, D., Sobczyk, A. & Svoboda, K. Channelrhodopsin-2–assisted circuit mapping of long-range callosal projections. *Nat. Neurosci. 2007 105* **10**, 663–668 (2007).

134. Fame, R. M., MacDonald, J. L. & Macklis, J. D. Development, Specification, and Diversity of Callosal Projection Neurons. *Trends Neurosci.* **34**, 41 (2011).

135. Kroon, T., van Hugte, E., van Linge, L., Mansvelder, H. D. & Meredith, R. M. Early postnatal development of pyramidal neurons across layers of the mouse medial prefrontal cortex. *Sci. Rep.* **9**, 1–16 (2019).

136. Moradi Chameh, H. *et al.* Diversity amongst human cortical pyramidal neurons revealed via their sag currents and frequency preferences. *Nat. Commun.* **12**, (2021).

137. Larkum, M. E., Petro, L. S., Sachdev, R. N. S. & Muckli, L. A Perspective on Cortical Layering and Layer-Spanning Neuronal Elements. *Front. Neuroanat.* **12**, 1–9 (2018).

138. Epifanova, E. *et al.* Adhesion dynamics in the neocortex determine the start of migration and the post-migratory orientation of neurons. *Sci. Adv.* **7**, (2021).

139. Huszár, R., Zhang, Y., Blockus, H. & Buzsáki, G. Preconfigured dynamics in the hippocampus are guided by embryonic birthdate and rate of neurogenesis. *Nat. Neurosci. 2022* 1–12 (2022). doi:10.1038/s41593-022-01138-x

140. Alcamo, E. A. *et al.* Satb2 Regulates Callosal Projection Neuron Identity in the Developing Cerebral Cortex. *Neuron* **57**, 364–377 (2008).

141. Britanova, O. *et al.* Satb2 is a postmitotic determinant for upper-layer neuron specification in the neocortex. *Neuron* **57**, 378–392 (2008).

142. Johnson, C. A. & Ghashghaei, H. T. Sp2 regulates late neurogenic but not early expansive divisions of neural stem cells underlying population growth in the mouse cortex. *Dev.* **147**, (2020).

143. Petryniak, M. A., Potter, G. B., Rowitch, D. H. & Rubenstein, J. L. R. Dlx1 and Dlx2 Control Neuronal versus Oligodendroglial Cell Fate Acquisition in the Developing Forebrain. *Neuron* **55**, 417–433 (2007).

144. Rodríguez-Tornos, F. M. *et al.* Cux1 Enables Interhemispheric Connections of Layer II/III Neurons by Regulating Kv1-Dependent Firing. *Neuron* **89**, 494–506 (2016).

145. Coquand, L. *et al.* A cell fate decision map reveals abundant direct neurogenesis in the human developing neocortex. (2022). doi:10.1101/2022.02.01.478661

146. Nandi, S. *et al.* The CSF-1 receptor ligands IL-34 and CSF-1 exhibit distinct developmental brain expression patterns and regulate neural progenitor cell maintenance and maturation. *Dev. Biol.* **367**, (2012).

147. Espuny-Camacho, I. *et al.* Human Pluripotent Stem-Cell-Derived Cortical Neurons Integrate Functionally into the Lesioned Adult Murine Visual Cortex in an Area-Specific Way. *Cell Rep.* **23**, 2732 (2018).

148. Richards, S. E. V. *et al.* Experience-Dependent Development of Dendritic Arbors in Mouse Visual Cortex. *J. Neurosci.* **40**, 6536 (2020).

149. Garrett, A. M., Schreiner, D., Lobas, M. A. & Weiner, J. A. Protocadherins Control Cortical Dendrite Arborization by Regulating the Activity of a FAK/PKC/MARCKS Signaling Pathway. *Neuron* **74**, 269–276 (2012).

150. Aizawa, H. *et al.* Dendrite Development Regulated by CREST, a Calcium-Regulated

Transcriptional Activator. *Science (80-.).* **303**, 197–202 (2004).

151. Kalil, K. & Dent, E. W. Branch management: mechanisms of axon branching in the developing vertebrate CNS. *Nat. Rev. Neurosci.* **15**, 7 (2014).

152. Sheu, S. H. *et al.* A serotonergic axon-cilium synapse drives nuclear signaling to alter chromatin accessibility. *Cell* **185**, 3390-3407.e18 (2022).

153. Luo, L. & O'Leary, D. D. M. Axon retraction and degeneration in development and disease. *Annu. Rev. Neurosci.* **28**, 127–156 (2005).

154. Okabe, K. *et al.* Neuron-derived VEGF contributes to cortical and hippocampal development independently of VEGFR1/2-mediated neurotrophism. *Dev. Biol.* **459**, 65–71 (2020).

155. Tyler, W. A., Medalla, M., Guillamon-Vivancos, T., Luebke, J. I. & Haydar, T. F. Neural Precursor Lineages Specify Distinct Neocortical Pyramidal Neuron Types. *J. Neurosci.* **35**, 6142 (2015).

156. Gao, Z. *et al.* Neurod1 is essential for the survival and maturation of adult-born neurons. *Nat. Neurosci.* **12**, 1090 (2009).

157. Andreae, L. C. & Burrone, J. The role of spontaneous neurotransmission in synapse and circuit development. *J. Neurosci. Res.* **96**, 354–359 (2018).

158. Spitzer, N. C. Activity-dependent neuronal differentiation prior to synapse formation: The functions of calcium transients. *J. Physiol. Paris* **96**, 73–80 (2002).

159. Spitzer, N. C. Electrical activity in early neuronal development. *Nat. 2006 4447120* **444**, 707–712 (2006).

160. Kanai, Y. *et al.* The SLC1 high-affinity glutamate and neutral amino acid transporter family. *Mol. Aspects Med.* **34**, 108–120 (2013).

161. Cancedda, L., Fiumelli, H., Chen, K. & Poo, M. M. Excitatory GABA action is essential for morphological maturation of cortical neurons in vivo. *J. Neurosci.* **27**, 5224–5235 (2007).

162. Rakhade, S. N. & Jensen, F. E. Epileptogenesis in the immature brain: emerging mechanisms. *Nat. Rev. Neurol. 2009 57* **5**, 380–391 (2009).

163. Deisseroth, K. *et al.* Excitation-neurogenesis coupling in adult neural stem/progenitor cells. *Neuron* **42**, 535–552 (2004).

164. Cull-Candy, S., Brickley, S. & Farrant, M. NMDA receptor subunits: Diversity, development and disease. *Curr. Opin. Neurobiol.* **11**, 327–335 (2001).

165. Liu, S. Q. J. & Cull-Candy, S. G. Synaptic activity at calcium-permeable AMPA receptors induces a switch in receptor subtype. *Nature* **405**, 454–458 (2000).

166. Tashiro, A., Sandler, V. M., Toni, N., Zhao, C. & Gage, F. H. NMDA-receptor-mediated, cell-specific integration of new neurons in adult dentate gyrus. *Nature* **442**, 929–933 (2006).

167. Range, K., M, D. & Moser, Y. A. A critical period for enhanced synaptic plasticity in newly generated neurons of the adult brain. *Bone* **23**, 1–7 (2012).

168. Silbereis, J. C., Pochareddy, S., Zhu, Y., Li, M. & Sestan, N. The Cellular and Molecular Landscapes of the Developing Human Central Nervous System. *Neuron* **89**, 248 (2016).

169. Cohen, S. & Greenberg, M. E. Communication Between the Synapse and the Nucleus in Neuronal Development, Plasticity, and Disease. *Annu. Rev. Cell Dev. Biol.* **24**, 183 (2008).

170. Li, M., Zhang, D. Q., Wang, X. Z. & Xu, T. J. NR2B-containing NMDA receptors promote neural progenitor cell proliferation through CaMKIV/CREB pathway. *Biochem. Biophys. Res. Commun.* **411**, 667–672 (2011).

171. Sheng, M., McFadden, G. & Greenberg, M. E. Membrane depolarization and calcium induce c-fos transcription via phosphorylation of transcription factor CREB. *Neuron* **4**, 571–582 (1990).

172. Tao, X., Finkbeiner, S., Arnold, D. B., Shaywitz, A. J. & Greenberg, M. E. Ca2+ influx regulates BDNF transcription by a CREB family transcription factor-dependent mechanism. *Neuron* **20**, 709–726 (1998).

173. Ellender, T. J. *et al.* Embryonic progenitor pools generate diversity in fine-scale excitatory cortical subnetworks. *Nat. Commun.* **10**, (2019).

174. Lein, E. S. *et al.* Genome-wide atlas of gene expression in the adult mouse brain. *Nat. 2006 4457124* **445**, 168–176 (2006).

175. Gaudillière, B., Konishi, Y., De La Iglesia, N., Yao, G. L. & Bonni, A. A CaMKII-NeuroD Signaling Pathway Specifies Dendritic Morphogenesis. *Neuron* **41**, 229–241 (2004).

176. Tutukova, S., Tarabykin, V. & Hernandez-Miranda, L. R. The Role of Neurod Genes in Brain Development, Function, and Disease. *Front. Mol. Neurosci.* **14**, 1–13 (2021).

177. Bormuth, I. *et al.* Neuronal Basic Helix–Loop–Helix Proteins Neurod2/6 Regulate Cortical Commissure Formation before Midline Interactions. *J. Neurosci.* **33**, 641 (2013).

178. Boutin, C. *et al.* NeuroD1 induces terminal neuronal differentiation in olfactory neurogenesis. *Proc. Natl. Acad. Sci. U. S. A.* **107**, 1201–1206 (2010).

179. Glahs, A. & Zinzen, R. P. Putting chromatin in its place: the pioneer factor NeuroD1 modulates chromatin state to drive cell fate decisions. *EMBO J.* **35**, 1 (2016).

180. Pataskar, A. *et al.* NeuroD1 reprograms chromatin and transcription factor landscapes to induce the neuronal program. *EMBO J.* **35**, 24–45 (2016).

181. Kuwabara, T. *et al.* Wnt-mediated activation of NeuroD1 and retro-elements during adult neurogenesis. *Nat. Neurosci. 2009 129* **12**, 1097–1105 (2009).

182. Amador-Arjona, A. *et al.* SOX2 primes the epigenetic landscape in neural precursors enabling proper gene activation during hippocampal neurogenesis. *Proc. Natl. Acad. Sci. U. S. A.* **112**, E1936–E1945 (2015).

183. Kuwabara, T. *et al.* Insulin biosynthesis in neuronal progenitors derived from adult hippocampus and the olfactory bulb. *EMBO Mol. Med.* **3**, 742–754 (2011).

184. Silva, F. Da *et al.* Mitotic WNT signalling orchestrates neurogenesis in the developing neocortex. *EMBO J.* **40**, e108041 (2021).

185. Seo, S., Lim, J. W., Yellajoshyula, D., Chang, L. W. & Kroll, K. L. Neurogenin and NeuroD direct transcriptional targets and their regulatory enhancers. *EMBO J.* **26**, 5093–5108 (2007).

186. Adachi, T. *et al.* Notch Signaling between Cerebellar Granule Cell Progenitors. *eNeuro* **8**, (2021).

187. Cherry, T. J. *et al.* Development/Plasticity/Repair NeuroD Factors Regulate Cell Fate and Neurite Stratification in the Developing Retina. (2011). doi:10.1523/JNEUROSCI.2555-10.2011

188. Deneris, E. S. & Hobert, O. Maintenance of postmitotic neuronal cell identity. **17**, (2014).

189. Zhang, X. L., Clay Spencer, W., Tabuchi, N., Kitt, M. M. & Deneris, E. S. Reorganization of postmitotic neuronal chromatin accessibility for maturation of serotonergic identity. *Elife* **11**, (2022).

190. Hobert, O. Regulatory logic of neuronal diversity: Terminal selector genes and selector motifs. *Proc. Natl. Acad. Sci. U. S. A.* **105**, 20067–20071 (2008).

191. Brulet, R. *et al.* NEUROD1 Instructs Neuronal Conversion in Non-Reactive Astrocytes. *Stem Cell Reports* **8**, 1506–1515 (2017).

192. Matsuda, T. *et al.* Pioneer Factor NeuroD1 Rearranges Transcriptional and Epigenetic Profiles to Execute Microglia-Neuron Conversion. *Neuron* **101**, 472-485.e7 (2019).

193. Lee, J. E. *et al.* Conversion of Xenopus ectoderm into neurons by neuroD, a basic helix-loop-helix protein. *Science (80-.).* **268**, 836–844 (1995).

194. Baxter, K. K., Uittenbogaard, M., Yoon, J. & Chiaramello, A. The neurogenic basic helix-loop-helix transcription factor NeuroD6 concomitantly increases mitochondrial mass and regulates cytoskeletal organization in the early stages of neuronal differentiation. *ASN Neuro* **1**, 195–211 (2009).

195. Iwata, R. *et al.* Species-specific mitochondria dynamics and metabolism regulate the timing of

neuronal development. *bioRxiv* 2021.12.27.474246 (2021). doi:10.1101/2021.12.27.474246

196. Lai, M. *et al.* NeuroD1 overexpression in spinal neurons accelerates axonal regeneration after sciatic nerve injury. *Exp. Neurol.* **327**, 113215 (2020).

197. Joo, J. Y. *et al.* Activation of NMDA receptors increases proliferation and differentiation of hippocampal neural progenitor cells. *J. Cell Sci.* **120**, 1358–1370 (2007).

198. Liu, S., Li, C., Xing, Y. & Tao, F. Effect of transplantation of human embryonic stem cell-derived neural progenitor cells on adult neurogenesis in aged hippocampus. *Am. J. Stem Cells* **3**, 21–26 (2014).

199. Richetin, K. *et al.* Amplifying mitochondrial function rescues adult neurogenesis in a mouse model of Alzheimer's disease. *Neurobiol. Dis.* **102**, 113–124 (2017).

200. Bayam, E. *et al.* Genome-wide target analysis of NEUROD2 provides new insights into regulation of cortical projection neuron migration and differentiation. *BMC Genomics* **16**, 1–14 (2015).

201. D'Amico, L. A., Boujard, D. & Coumailleau, P. The neurogenic factor NeuroD1 is expressed in post-mitotic cells during juvenile and adult Xenopus neurogenesis and not in progenitor or radial glial cells. *PLoS One* **8**, (2013).

202. De Anda, F. C. *et al.* Cortical neurons gradually attain a post-mitotic state. *Cell Res.* **26**, 1033–1047 (2016).

203. O'Connor, S. A. *et al.* Neural G0: a quiescent-like state found in neuroepithelial-derived cells and glioma. *Mol. Syst. Biol.* **17**, e9522 (2021).

204. Frade, J. M. & Ovejero-Benito, M. C. Neuronal cell cycle: The neuron itself and its circumstances. *Cell Cycle* **14**, 712–720 (2015).

205. De La Rossa, A. *et al.* In vivo reprogramming of circuit connectivity in postmitotic neocortical neurons. *Nat. Neurosci. 2013 162* **16**, 193–200 (2013).

206. Rouaux, C. & Arlotta, P. Direct lineage reprogramming of post-mitotic callosal neurons into corticofugal neurons in vivo. *Nat. Cell Biol. 2013 152* **15**, 214–221 (2013).

207. Kajstura, J. *et al.* Myocyte proliferation in end-stage cardiac failure in humans. *Proc. Natl. Acad. Sci. U. S. A.* **95**, 8801–8805 (1998).

208. Chen, Y. *et al.* Reversible reprogramming of cardiomyocytes to a fetal state drives heart regeneration in mice. *Science (80-.).* **373**, 1537–1540 (2021).

209. Campa, V. M. *et al.* Notch activates cell cycle reentry and progression in quiescent cardiomyocytes. *J. Cell Biol.* **183**, 129–141 (2008).

210. Gong, R., Jiang, Z., Zagidullin, N., Liu, T. & Cai, B. Regulation of cardiomyocyte fate plasticity: a key strategy for cardiac regeneration. *Signal Transduct. Target. Ther.* **6**, (2021).

211. Venkatesh, I., Mehra, V., Wang, Z., Califf, B. & Blackmore, M. G. Developmental Chromatin Restriction of Pro-Growth Gene Networks Acts as an Epigenetic Barrier to Axon Regeneration in Cortical Neurons. *Dev. Neurobiol.* **78**, 960–977 (2018).

212. Porrello, E. R. *et al.* Transient regenerative potential of the neonatal mouse heart. *Science* **331**, 1078–1080 (2011).

213. Bao N. Puente1, 3,*, Wataru Kimura1,*, Shalini A. Muralidhar1, Jesung Moon3, James F. Amatruda1, 2, 3, Kate L. Phelps4, David Grinsfelder5, Beverly A. Rothermel1, 2, Rui Chen1, Joseph A. Garcia1, Celio X. Santos6, SuWannee Thet1, Eiichiro Mori10, Michael, and H. A. S. The Oxygen Rich Postnatal Environment Induces Cardiomyocyte Cell Cycle Arrest Through DNA Damage Response. *Cell.* **19**, 6218–6221 (2014).

214. Payan, S. M., Hubert, F. & Rochais, F. Cardiomyocyte proliferation, a target for cardiac regeneration. *Biochim. Biophys. Acta - Mol. Cell Res.* **1867**, 118461 (2020).

215. He, L. & Zhou, B. Cardiomyocyte proliferation: Remove brakes and push accelerators. *Cell Res.* **27**, 959–960 (2017).

216. Sharma, G. *et al.* Mitochondrial Substrate Utilization Regulates Cardiomyocyte CellCycle

Progression. **2**, 167–178 (2020).

217. Soonpaa, M. H. & Field, L. J. Assessment of cardiomyocyte DNA synthesis in normal and injured adult mouse hearts. *Am. J. Physiol. - Hear. Circ. Physiol.* **272**, (1997).

218. Scalise, M. *et al. Heterogeneity of Adult Cardiac Stem Cells. Advances in Experimental Medicine and Biology* **1169**, (2019).

219. Zebrowski, D. C. *et al.* Developmental alterations in centrosome integrity contribute to the post-mitotic state of mammalian cardiomyocytes. *Elife* **4**, 1–16 (2015).

220. Sattler, S. & Rosenthal, N. The neonate versus adult mammalian immune system in cardiac repair and regeneration. *Biochim. Biophys. Acta - Mol. Cell Res.* **1863**, 1813–1821 (2016).

221. Zheng, X. *et al.* Metabolic reprogramming during neuronal differentiation from aerobic glycolysis to neuronal oxidative phosphorylation. *Elife* **5**, 1–25 (2016).

222. Herrero-Mendez, A. *et al.* The bioenergetic and antioxidant status of neurons is controlled by continuous degradation of a key glycolytic enzyme by APC/C-Cdh1. *Nat. Cell Biol.* **11**, 747–752 (2009).

223. Bolaños, J. P., Almeida, A. & Moncada, S. Glycolysis: a bioenergetic or a survival pathway? *Trends Biochem. Sci.* **35**, 145–149 (2010).

224. Petrelli, F. *et al.* Mitochondrial pyruvate metabolism regulates the activation of quiescent adult neural stem cells. *bioRxiv* 2022.05.31.494137 (2022). doi:10.1101/2022.05.31.494137

225. Divakaruni, A. S. *et al.* Inhibition of the mitochondrial pyruvate carrier protects from excitotoxic neuronal death. *J. Cell Biol.* **216**, 1091 (2017).

226. Dobolyi, A. *et al.* Exclusive neuronal expression of SUCLA2 in the human brain. *Brain Struct. Funct. 2013 2201* **220**, 135–151 (2013).

227. Kirby, E. D., Kuwahara, A. A., Messer, R. L. & Wyss-Coray, T. Adult hippocampal neural stem and progenitor cells regulate the neurogenic niche by secreting VEGF. *Proc. Natl. Acad. Sci. U. S. A.* **112**, 4128–4133 (2015).

228. Leeson, H. C. *et al.* P2X7 Receptors Regulate Phagocytosis and Proliferation in Adult Hippocampal and SVZ Neural Progenitor Cells: Implications for Inflammation in Neurogenesis. *Stem Cells* **36**, 1764–1777 (2018).

229. Hodge, R. D. *et al.* Intermediate Progenitors in Adult Hippocampal Neurogenesis: Tbr2 Expression and Coordinate Regulation of Neuronal Output. *J. Neurosci.* **28**, 3707–3717 (2008).

230. Borrett, M. J. *et al.* Single-Cell Profiling Shows Murine Forebrain Neural Stem Cells Reacquire a Developmental State when Activated for Adult Neurogenesis. *Cell Rep.* **32**, (2020).

231. Basu, A. & Tiwari, V. K. Epigenetic reprogramming of cell identity: lessons from development for regenerative medicine. *Clin. Epigenetics* **13**, 1–11 (2021).

232. VandenBosch, L. S. & Reh, T. A. Epigenetics in neuronal regeneration. *Semin. Cell Dev. Biol.* **97**, 63–73 (2020).

233. Ponti, G. *et al.* Cell cycle and lineage progression of neural progenitors in the ventricular-subventricular zones of adult mice. *Proc. Natl. Acad. Sci. U. S. A.* **110**, E1045 (2013).

234. Alvarez-Buylla, A. & Lim, D. A. For the Long Run: Maintaining Germinal Niches in the Adult Brain. *Neuron* **41**, 683–686 (2004).

235. Espósito, M. S. *et al.* Neuronal differentiation in the adult hippocampus recapitulates embryonic development. *J. Neurosci.* **25**, 10074–10086 (2005).

236. Mattson, M. P. Glutamate and Neurotrophic Factors in Neuronal Plasticity and Disease. *Ann. N. Y. Acad. Sci.* **1144**, 97–112 (2008).

237. Azim, K. *et al.* Transcriptional profiling of ligand expression in cell specific populations of the adult mouse forebrain that regulates neurogenesis. *Front. Neurosci.* **12**, (2018).

238. Palomer, E., Carretero, J., Benvegnù, S., Dotti, C. G. & Martin, M. G. Neuronal activity controls Bdnf expression via Polycomb de-repression and CREB/CBP/JMJD3 activation in mature

neurons. *Nat. Commun.* **7**, (2016).

239. Lau, D., Bengtson, C. P., Buchthal, B. & Bading, H. BDNF Reduces Toxic Extrasynaptic NMDA Receptor Signaling via Synaptic NMDA Receptors and Nuclear-Calcium-Induced Transcription of inhba/Activin A. *Cell Rep.* **12**, 1353–1366 (2015).

240. Barrio-Alonso, E., Hernández-Vivanco, A., Walton, C. C., Perea, G. & Frade, J. M. Cell cycle reentry triggers hyperploidization and synaptic dysfunction followed by delayed cell death in differentiated cortical neurons. *Sci. Rep.* **8**, 1–14 (2018).

241. Kodis, E. J., Choi, S., Swanson, E., Ferreira, G. & Bloom, G. S. N-methyl-D-aspartate receptor–mediated calcium influx connects amyloid-β oligomers to ectopic neuronal cell cycle reentry in Alzheimer's disease. *Alzheimer's Dement.* **14**, 1302–1312 (2018).

242. Menendez-Montes, I. *et al.* Mitochondrial fatty acid utilization increases chromatin oxidative stress in cardiomyocytes. *Proc. Natl. Acad. Sci. U. S. A.* **118**, 3–5 (2021).

243. Marathe, S., Liu, S., Brai, E., Kaczarowski, M. & Alberi, L. Notch signaling in response to excitotoxicity induces neurodegeneration via erroneous cell cycle reentry. *Cell Death Differ.* **22**, 1775–1784 (2015).

244. Latasa, M. J., Cisneros, E. & Frade, J. M. Cell cycle control of Notch signaling and the functional regionalization of the neuroepithelium during vertebrate neurogenesis. *Int. J. Dev. Biol.* **53**, 895–908 (2009).

245. Barrio-Alonso, E., Fontana, B., Valero, M. & Frade, J. M. Pathological Aspects of Neuronal Hyperploidization in Alzheimer's Disease Evidenced by Computer Simulation. *Front. Genet.* **11**, (2020).

246. Ciceri, G. *et al.* An epigenetic barrier sets the timing of human neuronal maturation. *bioRxiv* 2022.06.02.490114 (2022). doi:10.1101/2022.06.02.490114

247. Gasparoni, G. *et al.* DNA methylation analysis on purified neurons and glia dissects age and Alzheimer's disease-specific changes in the human cortex. *Epigenetics and Chromatin* **11**, 1–19 (2018).

248. Funk, O. H., Qalieh, Y., Doyle, D. Z., Lam, M. M. & Kwan, K. Y. Postmitotic accumulation of histone variant H3.3 in new cortical neurons establishes neuronal chromatin, transcriptome, and identity. *Proc. Natl. Acad. Sci. U. S. A.* **119**, e2116956119 (2022).

249. Zhang, Z. *et al.* Epigenomic diversity of cortical projection neurons in the mouse brain. *Nat.* | **598**, 167 (2021).

250. VandenBosch, L. S. *et al.* Developmental changes in the accessible chromatin, transcriptome and Ascl1-binding correlate with the loss in Müller Glial regenerative potential. *Sci. Rep.* **10**, 1–18 (2020).

251. Fill Malfertheiner, S. *et al.* Vasopressin but Not Oxytocin Responds to Birth Stress in Infants. *Front. Neurosci.* **15**, 1091 (2021).

252. Masuda, T. *et al.* Specification of CNS macrophage subsets occurs postnatally in defined niches. *Nat. 2022 6047907* **604**, 740–748 (2022).

253. Qiu, C. *et al.* A single-cell transcriptional timelapse of mouse embryonic development, from gastrula to pup. *bioRxiv* (2023). doi:10.1101/2023.04.05.535726

254. Lammertink, F., Vinkers, C. H., Tataranno, M. L. & Benders, M. J. N. L. Premature Birth and Developmental Programming: Mechanisms of Resilience and Vulnerability. *Front. Psychiatry* **11**, 531571 (2021).

255. Dammann, O., Leviton, A., Gappa, M. & Dammann, C. E. L. Lung and brain damage in preterm newborns, and their association with gestational age, prematurity subgroup, infection/inflammation and long term outcome. *BJOG An Int. J. Obstet. Gynaecol.* **112**, 4–9 (2005).

256. Constable, R. T. *et al.* Prematurely born children demonstrate white matter microstructural differences at 12 years of age, relative to term control subjects: An investigation of group and gender effects. *Pediatrics* **121**, 306–316 (2008).

257. Kapellou, O. *et al.* Abnormal Cortical Development after Premature Birth Shown by Altered Allometric Scaling of Brain Growth. *PLOS Med.* **3**, e265 (2006).

258. Larroque, B. *et al.* Neurodevelopmental disabilities and special care of 5-year-old children born before 33 weeks of gestation (the EPIPAGE study): a longitudinal cohort study. *Lancet* **371**, 813–820 (2008).

259. Crump, C., Sundquist, J. & Sundquist, K. PRETERM OR EARLY TERM BIRTH AND RISK OF AUTISM. *Pediatrics* **148**, (2021).

260. Wang, C., Geng, H., Liu, W. & Zhang, G. Prenatal, perinatal, and postnatal factors associated with autism: A meta-analysis. *Medicine (Baltimore).* **96**, (2017).

261. Gars, A., Ronczkowski, N. M., Chassaing, B., Castillo-Ruiz, A. & Forger, N. G. First Encounters: Effects of the Microbiota on Neonatal Brain Development. *Front. Cell. Neurosci.* **15**, (2021).

262. Berger, N., Vaillancourt, C. & Boksa, P. Interactive effects of anoxia and general anesthesia during birth on the degree of CNS and systemic hypoxia produced in neonatal rats. *Exp. Brain Res.* **131**, 524–531 (2000).

263. Venerosi, A., Valanzano, A., Cirulli, F., Alleva, E. & Calamandrei, G. Acute global anoxia during C-section birth affects dopamine-mediated behavioural responses and reactivity to stress. *Behav. Brain Res.* **154**, 155–164 (2004).

264. Zhang, T. *et al.* Association of Cesarean Delivery With Risk of Neurodevelopmental and Psychiatric Disorders in the Offspring A Systematic Review and Meta-analysis + Supplemental content. *JAMA Netw. Open* **2**, 1910236 (2019).

265. Deoni, X. S. C. *et al.* Cesarean Delivery Impacts Infant Brain Development. doi:10.3174/ajnr.A5887

266. Mutlu, B., Aksoy, N., Cakir, H., Celik, H. & Erel, O. The effects of the mode of delivery on oxidative-antioxidative balance. *J. Matern. Fetal. Neonatal Med.* **24**, 1367–1370 (2011).

267. Seli, E. & Horvath, T. L. Natural birth-induced UCP2 in brain development. *Rev. Endocr. Metab. Disord. 2013 144* **14**, 347–350 (2013).

268. Taylor-Giorlando, M., Scheinost, D., Ment, L., Rothman, D. & Horvath, T. L. Prefrontal Cortical and Behavioral Adaptations to Surgical Delivery Mediated by Metabolic Principles. doi:10.1093/cercor/bhz

269. Varela, L., Schwartz, M. L. & Horvath, T. L. Mitochondria controlled by UCP2 determine hypoxia-induced synaptic remodeling in the cortex and hippocampus. *Neurobiol. Dis.* **90**, 68–74 (2016).

270. Huang, K. *et al.* Elective caesarean delivery and offspring's cognitive impairment: Implications of methylation alteration in hippocampus glucocorticoid signaling genes. *Brain Res. Bull.* **144**, 108–121 (2019).

271. Castillo-Ruiz, A., Mosley, M., Jacobs, A. J., Hoffiz, Y. C. & Forger, N. G. Birth delivery mode alters perinatal cell death in the mouse brain. *Proc. Natl. Acad. Sci. U. S. A.* **115**, 11826–11831 (2018).

272. Jacobs, A. J., Castillo-Ruiz, A., Cisternas, C. D. & Forger, N. G. Microglial Depletion Causes Region-Specific Changes to Developmental Neuronal Cell Death in the Mouse Brain. *Dev. Neurobiol.* **79**, 769–779 (2019).

273. Lin, M. Y. *et al.* Zika Virus Infects Intermediate Progenitor Cells and Post-mitotic Committed Neurons in Human Fetal Brain Tissues. *Sci. Rep.* **7**, 1–8 (2017).

274. Tarantal, A. F. *et al.* Fetal Rhesus Monkey First Trimester Zika Virus Infection Impacts Cortical Development in the Second and Third Trimesters. *Cereb. Cortex* **31**, 2309–2321 (2021).

275. Kleber de Oliveira, W. *et al.* Increase in Reported Prevalence of Microcephaly in Infants Born to Women Living in Areas with Confirmed Zika Virus Transmission During the First Trimester of Pregnancy — Brazil, 2015. *MMWR. Morb. Mortal. Wkly. Rep.* **65**, (2019).

276. Düsedau, H. P. *et al.* Influenza A Virus (H1N1) Infection Induces Microglial Activation and

Temporal Dysbalance in Glutamatergic Synaptic Transmission. *MBio* **12**, (2021).

277. Fatemi, S. H. *et al.* Prenatal viral infection leads to pyramidal cell atrophy and macrocephaly in adulthood: implications for genesis of autism and schizophrenia. *Cell. Mol. Neurobiol.* **22**, 25–33 (2002).
278. Hosseini, S. *et al.* Long-term neuroinflammation induced by influenza a virus infection and the impact on hippocampal neuron morphology and function. *J. Neurosci.* **38**, 3060–3080 (2018).
279. Cabrera, J. R., Klase, Z., Kaptein, S., King, E. L. & Irigoyen, N. Zika Virus and Neuropathogenesis: The Unanswered Question of Which Strain Is More Prone to Causing Microcephaly and Other Neurological Defects. (2021). doi:10.3389/fncel.2021.695106
280. Miller, V. M. *et al.* Gestational flu exposure induces changes in neurochemicals, affiliative hormones and brainstem inflammation, in addition to autism-like behaviors in mice. *Brain. Behav. Immun.* **33**, 153–163 (2013).
281. Kępińska, A. P. *et al.* Schizophrenia and Influenza at the Centenary of the 1918-1919 Spanish Influenza Pandemic: Mechanisms of Psychosis Risk. *Front. Psychiatry* **11**, (2020).
282. Kara Calkins, MD and Sherin U. Devaskar, M. Fetal Origins of Adult Disease. *Physiol. Behav.* **176**, 139–148 (2017).
283. Barker, D. J. P., Osmond, C., Kajantie, E. & Eriksson, J. G. Growth and chronic disease: Findings in the Helsinki Birth Cohort. *Ann. Hum. Biol.* **36**, 445–458 (2009).
284. de Rooij, S. R., Wouters, H., Yonker, J. E., Painter, R. C. & Roseboom, T. J. Prenatal undernutrition and cognitive function in late adulthood. *Proc. Natl. Acad. Sci.* **107**, 16881–16886 (2010).
285. Roseboom, T., de Rooij, S. & Painter, R. The Dutch famine and its long-term consequences for adult health. *Early Hum. Dev.* **82**, 485–491 (2006).
286. Jacobsen, H. *et al.* Offspring born to influenza A virus infected pregnant mice have increased susceptibility to viral and bacterial infections in early life. *Nat. Commun.* **12**, (2021).
287. Zhu, X., Raina, A. K., Perry, G. & Smith, M. A. Alzheimer’s disease: The two-hit hypothesis. *Lancet Neurol.* **3**, 219–226 (2004).
288. Estes, M. L. & McAllister, A. K. Maternal immune activation: implications for neuropsychiatric disorders. *Science* **353**, 772 (2016).
289. Guma, E. *et al.* Investigating the ‘two-hit hypothesis’: Effects of prenatal maternal immune activation and adolescent cannabis use on neurodevelopment in mice. *Prog. Neuropsychopharmacol. Biol. Psychiatry* **120**, (2023).
290. Canales, C. P. *et al.* Sequential perturbations to mouse corticogenesis following in utero maternal immune activation. *Elife* **10**, (2021).
291. Yim, Y. S. *et al.* Reversing behavioral abnormalities in mice exposed to maternal inflammation. doi:10.1038/nature23909
292. Soumiya, H., Fukumitsu, H. & Furukawa, S. Prenatal immune challenge compromises development of upper-layer but not deeper-layer neurons of the mouse cerebral cortex. *J. Neurosci. Res.* **89**, 1342–1350 (2011).
293. Mehl, L. C., Manjally, A. V., Bouadi, O., Gibson, E. M. & Leng Tay, T. Microglia in brain development and regeneration. *Development* **149**, (2022).
294. Holtman, I. R., Skola, D. & Glass, C. K. Transcriptional control of microglia phenotypes in health and disease. *J. Clin. Invest.* **127**, 3220 (2017).
295. Hashimoto, D. *et al.* Tissue resident macrophages self-maintain locally throughout adult life with minimal contribution from circulating monocytes. *Immunity* **38**, 792–804 (2013).
296. Eglitis, M. A. & Mezey, É. Hematopoietic cells differentiate into both microglia and macroglia in the brains of adult mice. *Proc. Natl. Acad. Sci. U. S. A.* **94**, 4080 (1997).
297. Hoeffel, G. *et al.* C-Myb+ Erythro-Myeloid Progenitor-Derived Fetal Monocytes Give Rise to Adult Tissue-Resident Macrophages. *Immunity* **42**, 665 (2015).

298. Forstreuter, F., Lucius, R. & Mentlein, R. Vascular endothelial growth factor induces chemotaxis and proliferation of microglial cells. *J. Neuroimmunol.* **132**, 93–98 (2002).

299. Casano, A. M. & Peri, F. Microglia: Multitasking specialists of the brain. *Dev. Cell* **32**, 469–477 (2015).

300. Jurga, A. M., Paleczna, M. & Kuter, K. Z. Overview of General and Discriminating Markers of Differential Microglia Phenotypes. *Front. Cell. Neurosci.* **14**, (2020).

301. Schulz, R., Korkut-Demirbaş, M., Venturino, A., Colombo, G. & Siegert, S. Chimeric GPCRs mimic distinct signaling pathways and modulate microglia responses. *Nat. Commun. 2022 131* **13**, 1–26 (2022).

302. Guo, J. *et al.* Developmental disruptions underlying brain abnormalities in ciliopathies. *Nat. Commun.* **6**, 1–13 (2015).

303. Squarzoni, P. *et al.* Microglia Modulate Wiring of the Embryonic Forebrain. *Cell Rep.* **8**, 1271–1279 (2014).

304. Easley-Neal, C., Foreman, O., Sharma, N., Zarrin, A. A. & Weimer, R. M. CSF1R Ligands IL-34 and CSF1 Are Differentially Required for Microglia Development and Maintenance in White and Gray Matter Brain Regions. *Front. Immunol.* **10**, 2199 (2019).

305. Cunningham, C. L., Martínez-Cerdeño, V. & Noctor, S. C. Microglia regulate the number of neural precursor cells in the developing cerebral cortex. *J. Neurosci.* **33**, 4216–4233 (2013).

306. Hattori, Y. *et al.* Transient microglial absence assists postmigratory cortical neurons in proper differentiation. *Nat. Commun.* **11**, (2020).

307. Arnò, B. *et al.* Neural progenitor cells orchestrate microglia migration and positioning into the developing cortex. *Nat. Commun. 2014 51* **5**, 1–13 (2014).

308. Tiveron, M. C. *et al.* Molecular interaction between projection neuron precursors and invading interneurons via stromal-derived factor 1 (CXCL12)/CXCR4 signaling in the cortical subventricular zone/intermediate zone. *J. Neurosci.* **26**, 13273–13278 (2006).

309. Hattori, Y. & Miyata, T. Microglia extensively survey the developing cortex via the CXCL12/CXCR4 system to help neural progenitors to acquire differentiated properties. *Genes to Cells* **23**, 915–922 (2018).

310. Shan, Y., Farmer, S. M. & Wray, S. Drebrin regulates cytoskeleton dynamics in migrating neurons through interaction with CXCR4. *Proc. Natl. Acad. Sci. U. S. A.* **118**, 1–12 (2021).

311. Liu, X., Hashimoto-Torii, K., Torii, M., Haydar, T. F. & Rakic, P. The role of ATP signaling in the migration of intermediate neuronal progenitors to the neocortical subventricular zone. *Proc. Natl. Acad. Sci. U. S. A.* **105**, 11802–11807 (2008).

312. Modeling, L. M. *et al.* Microglia monitor and protect neuronal functions via specialized somatic purinergic junctions. **26**, 1–4 (2019).

313. Haynes, S. E. *et al.* The P2Y12 receptor regulates microglial activation by extracellular nucleotides. *Nat. Neurosci. 2006 912* **9**, 1512–1519 (2006).

314. Joly-Amado, A. *et al.* CCL2 Overexpression in the Brain Promotes Glial Activation and Accelerates Tau Pathology in a Mouse Model of Tauopathy. *Front. Immunol.* **11**, 997 (2020).

315. Selenica, M. L. B. *et al.* Diverse activation of microglia by chemokine (C-C motif) ligand 2 overexpression in brain. *J. Neuroinflammation* **10**, 1–17 (2013).

316. Ueno, M. *et al.* Layer v cortical neurons require microglial support for survival during postnatal development. *Nat. Neurosci.* **16**, 543–551 (2013).

317. Liu, J., Spéder, P. & Brand, A. H. Control of brain development and homeostasis by local and systemic insulin signalling. *Diabetes, Obes. Metab.* **16**, 16–20 (2014).

318. Catapano, L. A., Arnold, M. W., Perez, F. A. & Macklis, J. D. Specific Neurotrophic Factors Support the Survival of Cortical Projection Neurons at Distinct Stages of Development. *J. Neurosci.* **21**, 8863 (2001).

319. Škuljec, J. *et al.* CCL5 induces a pro-inflammatory profile in microglia in vitro. *Cell. Immunol.*

270, 164–171 (2011).

320. Anderson, S. R. *et al.* Neuronal apoptosis drives remodeling states of microglia and shifts in survival pathway dependence. *Elife* **11**, (2022).

321. Stogsdill, J. A. *et al.* Pyramidal neuron subtype diversity governs microglia states in the neocortex. *Nat. 2022* 1–7 (2022). doi:10.1038/s41586-022-05056-7

322. Ronzano, R. *et al.* Microglia-neuron interaction at nodes of Ranvier depends on neuronal activity through potassium release and contributes to remyelination. *Nat. Commun.* doi:10.1038/s41467-021-25486-7

323. Dhandapani, R. *et al.* Sustained Trem2 stabilization accelerates microglia heterogeneity and Ab pathology in a mouse model of Alzheimer's disease ll Sustained Trem2 stabilization accelerates microglia heterogeneity and Ab pathology in a mouse model of Alzheimer's disease. *CellReports* **39**, 110883 (2022).

324. Deczkowska, A. *et al.* Disease-Associated Microglia: A Universal Immune Sensor of Neurodegeneration. *Cell* **173**, 1073–1081 (2018).

325. Shi, L., Fatemi, S. H., Sidwell, R. W. & Patterson, P. H. Maternal Influenza Infection Causes Marked Behavioral and Pharmacological Changes in the Offspring. *J. Neurosci.* **23**, 297 (2003).

326. He, Y., Taylor, N., Yao, X. & Bhattacharya, A. Mouse primary microglia respond differently to LPS and poly(I:C) in vitro. **11**,

327. Cameron, J. S. *et al.* Toll-Like Receptor 3 Is a Potent Negative Regulator of Axonal Growth in Mammals. *J. Neurosci.* **27**, 13033 (2007).

328. Rosshart, S. P. *et al.* Laboratory mice born to wild mice have natural microbiota and model human immune responses. *Science (80-.).* **365**, (2019).

329. Govindan, S., Oberst, P. & Jabaudon, D. In vivo pulse labeling of isochronic cohorts of cells in the central nervous system using FlashTag. *Nat. Protoc.* **13**, 2297–2311 (2018).

330. Guerrier, S. *et al.* The F-BAR domain of srGAP2 induces membrane protrusions required for neuronal migration and morphogenesis. *Cell* **138**, 990 (2009).

331. Niwa, H., Yamamura, K. I. & Miyazaki, J. I. Efficient selection for high-expression transfectants with a novel eukaryotic vector (Recombinant DNA; B-actin promoter; bovine papilloma virus; transfection; interleukin-2; G418 selection; copy number). *Gene* **108**, (1991).

332. Bao, M., Hofsink, N. & Plösch, T. LPS vs. Poly I:C Model: Comparison of Long-Term Effects of Bacterial and Viral Maternal Immune Activation (MIA) on the Offspring. *Am. J. Physiol. - Regul. Integr. Comp. Physiol.* **322**, (2022).

333. Furusawa, A., Reiser, J., Sadashivaiah, K., Simpson, H. & Banerjee, A. Eomesodermin Increases Survival and IL-2 Responsiveness of Tumor-specific CD8 + T Cells in an Adoptive Transfer Model of Cancer Immunotherapy. *J. Immunother.* **41**, 53–63 (2018).

334. Wu, W. L., Hsiao, E. Y., Yan, Z., Mazmanian, S. K. & Patterson, P. H. The placental interleukin-6 signaling controls fetal brain development and behavior. *Brain. Behav. Immun.* **62**, 11–23 (2017).

335. Choi, G. B. *et al.* The maternal interleukin-17a pathway in mice promotes autism-like phenotypes in offspring. *Science (80-.).* **351**, 933–939 (2016).

336. Meberg, P. J. & Miller, M. W. Culturing hippocampal and cortical neurons. *Methods Cell Biol.* **71**, 111–127 (2003).

337. Golan, N. & Cafferty, W. B. Dissociation of intact adult mouse cortical projection neurons for single-cell RNA-seq. *STAR Protoc.* **2**, 100941 (2021).

338. STEPHEN C. NOCTOR1,*, VERÓNICA MARTÍNEZ-CERDEÑO1, and A. R. K. Distinct Behaviors of Neural Stem and Progenitor Cells Underlie Cortical Neurogenesis. *Bone* **23**, 1–7 (2008).

339. Colasante, G. *et al.* ARX regulates cortical intermediate progenitor cell expansion and upper layer neuron formation through repression of Cdkn1c. *Cereb. Cortex* **25**, 322–335 (2015).

340. Heng, J. I. T. *et al.* Neurogenin 2 controls cortical neuron migration through regulation of Rnd2. *Nature* **455**, 114–118 (2008).

341. Englund, C. *et al.* Pax6, Tbr2, and Tbr1 are expressed sequentially by radial glia, intermediate progenitor cells, and postmitotic neurons in developing neocortex. *J. Neurosci.* **25**, 247–251 (2005).

342. Bani-Yaghoub, M. *et al.* Role of Sox2 in the development of the mouse neocortex. **295**, 52–66 (2006).

343. Vaneynde, P., Verbinnen, I. & Janssens, V. The role of serine/threonine phosphatases in human development: Evidence from congenital disorders. *Front. Cell Dev. Biol.* **10**, 1030119 (2022).

344. Schmitt, U., Tanimoto, N., Seeliger, M., Schaeffel, F. & Leube, R. E. Detection of behavioral alterations and learning deficits in mice lacking synaptophysin. *Neuroscience* **162**, 234–243 (2009).

345. Seidenbecher, C. I., Smalla, K. H., Fischer, N., Gundelfinger, E. D. & Kreutz, M. R. Brevican isoforms associate with neural membranes. *J. Neurochem.* **83**, 738–746 (2002).

346. Stuart, M. J., Singhal, G. & Baune, B. T. Systematic Review of the Neurobiological Relevance of Chemokines to Psychiatric Disorders. *Front. Cell. Neurosci.* **9**, 1 (2015).

347. Guo, T. *et al.* Dlx1/2 are Central and Essential Components in the Transcriptional Code for Generating Olfactory Bulb Interneurons. *Cereb. Cortex (New York, NY)* **29**, 4831 (2019).

348. Bell, S. *et al.* Disruption of GRIN2B Impairs Differentiation in Human Neurons. *Stem Cell Reports* **11**, 183 (2018).

349. Leone, D. P. *et al.* Satb2 Regulates the Differentiation of Both Callosal and Subcerebral Projection Neurons in the Developing Cerebral Cortex. *Cereb. Cortex* **25**, 3406–3419 (2015).

350. Pérez-Martínez, L. & Jaworski, D. M. Tissue Inhibitor of Metalloproteinase-2 Promotes Neuronal Differentiation by Acting as an Anti-Mitogenic Signal. *J. Neurosci.* **25**, 4917 (2005).

351. Marsden, K. M., Doll, T., Ferralli, J., Botteri, F. & Matus, A. Transgenic expression of embryonic MAP2 in adult mouse brain: implications for neuronal polarization. *J. Neurosci.* **16**, 3265–3273 (1996).

352. Chithra, Y. *et al.* Mitochondrial Complex I Inhibition in Dopaminergic Neurons Causes Altered Protein Profile and Protein Oxidation: Implications for Parkinson’s disease. *Neurochem. Res.* **48**, (2023).

353. Elmore, M. R. P. *et al.* Colony-stimulating factor 1 receptor signaling is necessary for microglia viability, unmasking a microglia progenitor cell in the adult brain. *Neuron* **82**, 380–397 (2014).

354. Rayaprolu, S. *et al.* Flow-cytometric microglial sorting coupled with quantitative proteomics identifies moesin as a highly-abundant microglial protein with relevance to Alzheimer’s disease. *Mol. Neurodegener.* **15**, 1–22 (2020).

355. Wishart, C. L., Spiteri, A. G., Locatelli, G. & King, N. J. C. Integrating transcriptomic datasets across neurological disease identifies unique myeloid subpopulations driving disease-specific signatures. *Glia* **71**, (2023).

356. Haage, V. *et al.* Comprehensive gene expression meta-analysis identifies signature genes that distinguish microglia from peripheral monocytes/macrophages in health and glioma. *Acta Neuropathol. Commun.* **7**, 1–18 (2019).

357. Schmittgen, T. D. & Livak, K. J. Analyzing real-time PCR data by the comparative C(T) methodSchmittgen, T.D., Livak, K.J., 2008. Analyzing real-time PCR data by the comparative C(T) method. Nat. Protoc. 3, 1101–1108.. *Nat. Protoc.* **3**, (2008).

358. Hughes, C. S. *et al.* Single-pot, solid-phase-enhanced sample preparation for proteomics experiments. *Nat. Protoc. 2018 141* **14**, 68–85 (2018).

359. Vaisvila, R. *et al.* Enzymatic methyl sequencing detects DNA methylation at single-base resolution from picograms of DNA. *Genome Res.* **31**, 1280–1289 (2021).

360. R Core Team (2023). R: A language and environment for statistical computing. *R: A language*

and environment for statistical computing. R Foundation for Statistical Computing, Vienna, Austria (2023).

361. Schindelin, J. *et al.* Fiji: an open-source platform for biological-image analysis. *Nat. Methods 2012 97* **9**, 676–682 (2012).

362. Lambert, T. J. FPbase: a community-editable fluorescent protein database. *Nat. Methods 2019 164* **16**, 277–278 (2019).

363. Shannon, P. *et al.* Cytoscape: A software Environment for integrated models of biomolecular interaction networks. *Genome Res.* **13**, (2003).

364. Wickham, H. Package `ggplot2`: Elegant Graphics for Data Analysis. *Springer-Verlag New York* (2016).

365. Rohart, F., Gautier, B., Singh, A. & Lê Cao, K. A. mixOmics: An R package for 'omics feature selection and multiple data integration. *PLoS Comput. Biol.* **13**, (2017).

366. Andrews, S. & others. FastQC: a quality control tool for high throughput sequence data. 2010. *Https://Www.Bioinformatics.Babraham.Ac.Uk/Projects/Fastqc/* (2019).

367. Martin, M. Cutadapt removes adapter sequences from high-throughput sequencing reads. *EMBnet.journal* **17**, 10–12 (2011).

368. Dobin, A. *et al.* STAR: ultrafast universal RNA-seq aligner. *Bioinformatics* **29**, 15 (2013).

369. Haeussler, M. *et al.* The UCSC Genome Browser database: 2019 update. *Nucleic Acids Res.* **47**, D853–D858 (2019).

370. Liao, Y., Smyth, G. K. & Shi, W. Sequence analysis featureCounts: an efficient general purpose program for assigning sequence reads to genomic features. **30**, 923–930 (2014).

371. Love, M. I., Huber, W. & Anders, S. Moderated estimation of fold change and dispersion for RNA-seq data with DESeq2. *Genome Biol.* **15**, (2014).

372. Pantano, L. DEGreport: Report of DEG analysis. *R package version 1.13.8* (2017).

373. Wu, T. *et al.* clusterProfiler 4.0: A universal enrichment tool for interpreting omics data. *Innovation* **2**, (2021).

374. Langfelder, P. & Horvath, S. WGCNA: An R package for weighted correlation network analysis. *BMC Bioinformatics* **9**, (2008).

375. Ravasz, E., Somera, A. L., Mongru, D. A., Oltvai, Z. N. & Barabási, A. L. Hierarchical organization of modularity in metabolic networks. *Science (80-.).* **297**, 1551–1555 (2002).

376. Voß, H. *et al.* HarmonizR enables data harmonization across independent proteomic datasets with appropriate handling of missing values. *Nat. Commun. 2022 131* **13**, 1–15 (2022).

377. Smits, A. & Wolfgang, H. DEP: Differential Enrichment analysis of Proteomics data. *Bioconductor* (2018).

378. Jensen, L. J. *et al.* STRING 8--a global view on proteins and their functional interactions in 630 organisms. *Nucleic Acids Res.* **37**, (2009).

379. Perez-Riverol, Y. *et al.* The PRIDE database resources in 2022: a hub for mass spectrometry-based proteomics evidences. *Nucleic Acids Res.* **50**, D543–D552 (2022).

380. Pedersen, B. S., Eyring, K., De, S., Yang, I. V & Schwartz, D. A. Fast and accurate alignment of long bisulfite-seq reads. (2014).

381. Akalin, A. *et al.* MethylKit: a comprehensive R package for the analysis of genome-wide DNA methylation profiles. *Genome Biol.* **13**, (2012).

382. Schurch, N. J. *et al.* How many biological replicates are needed in an RNA-seq experiment and which differential expression tool should you use? *RNA* **22**, 839–851 (2016).

383. Ching, T., Huang, S. & Garmire, L. X. Power analysis and sample size estimation for RNA-Seq differential expression. *RNA* **20**, 1684 (2014).

384. Tan, S. S. *et al.* Separate Progenitors for Radial and Tangential Cell Dispersion during Development of the Cerebral Neocortex. *Neuron* **21**, 295–304 (1998).

385. Rakic, P. Specification of cerebral cortical areas. *Science* **241**, 170–176 (1988).

386. Han, S. *et al.* Proneural genes define ground state rules to regulate neurogenic patterning and cortical folding. (2020).

387. Frischknecht, R. & Seidenbecher, C. I. Brevican: A key proteoglycan in the perisynaptic extracellular matrix of the brain. *Int. J. Biochem. Cell Biol.* **44**, 1051–1054 (2012).

388. Nakamura, K. *et al.* In vivo function of Rnd2 in the development of neocortical pyramidal neurons. *Neurosci. Res.* **54**, 149–153 (2006).

389. Farah, M. H. *et al.* Generation of neurons by transient expression of neural bHLH proteins in mammalian cells. *Development* **127**, 693–702 (2000).

390. Velkey, M. M. & O'Shea, K. S. Expression of Neurogenin 1 in mouse embryonic stem cells directs the differentiation of neuronal precursors and identifies unique patterns of down-stream gene expression. *Dev. Dyn.* **242**, 230–253 (2013).

391. Sessa, A. *et al.* Tbr2-positive intermediate (basal) neuronal progenitors safeguard cerebral cortex expansion by controlling amplification of pallial glutamatergic neurons and attraction of subpallial GABAergic interneurons. *Genes Dev.* **24**, 1816–1826 (2010).

392. Alessandro Sessa1, Chai-an Mao, Anna-Katerina Hadjantonakis, William H. Klein, A. & Broccoli, V. Tbr2 Directs Conversion of Radial Glia into Basal Precursors and Guides Neuronal Amplification by Indirect Neurogenesis in the Developing Neocortex. *Bone* **23**, 1–7 (2009).

393. Ferri, A. L. M. *et al.* Sox2 deficiency causes neurodegeneration and impaired neurogenesis in the adult mouse brain. *Development* **131**, 3805–3819 (2004).

394. Mercurio, S., Serra, L. & Nicolis, S. K. More than just Stem Cells: Functional Roles of the Transcription Factor Sox2 in Differentiated Glia and Neurons. *Int. J. Mol. Sci.* **20**, (2019).

395. Bunina, D. *et al.* Genomic Rewiring of SOX2 Chromatin Interaction Network during Differentiation of ESCs to Postmitotic Neurons. *Cell Syst.* **10**, 480 (2020).

396. Andrews, G. L. & Mastick, G. S. R-Cadherin Is a Pax6-Regulated, Growth-Promoting Cue for Pioneer Axons. *J. Neurosci.* **23**, 9873 (2003).

397. Hevner, R. F., Miyashita-Lin, E. & Rubenstein, J. L. R. Cortical and thalamic axon pathfinding defects in Tbr1, Gbx2, and Pax6 mutant mice: evidence that cortical and thalamic axons interact and guide each other. *J. Comp. Neurol.* **447**, 8–17 (2002).

398. Baranek, C. *et al.* Protooncogene Ski cooperates with the chromatin-remodeling factor Satb2 in specifying callosal neurons. *Proc. Natl. Acad. Sci. U. S. A.* **109**, 3546–3551 (2012).

399. Sasaki, S., Tabata, H., Tachikawa, K. & Nakajima, K. The cortical subventricular zone-specific molecule Svet1 is part of the nuclear RNA coded by the putative netrin receptor gene Unc5d and is expressed in multipolar migrating cells. *Mol. Cell. Neurosci.* **38**, 474–483 (2008).

400. Takemoto, M. *et al.* Laminar and Areal Expression of Unc5d and Its Role in Cortical Cell Survival. *Cereb. Cortex* **21**, 1925–1934 (2011).

401. Paonessa, F. *et al.* Microtubules Deform the Nuclear Membrane and Disrupt Nucleocytoplasmic Transport in Tau-Mediated Frontotemporal Dementia. *Cell Rep.* **26**, 582-593.e5 (2019).

402. Watanabe, M., Inoue, Y., Sakimura, K. & Mishina, M. Developmental changes in distribution of nmda receptor channel subunit m rim as. *NeuroReport* **3**, 1138–1140 (1992).

403. Casper, K. B. & McCarthy, K. D. GFAP-positive progenitor cells produce neurons and oligodendrocytes throughout the CNS. *Mol. Cell. Neurosci.* **31**, 676–684 (2006).

404. Raposo, T. P., Alfahed, A., Nateri, A. S. & Ilyas, M. Tensin4 (TNS4) is upregulated by Wnt signalling in adenomas in multiple intestinal neoplasia (Min) mice. *Int. J. Exp. Pathol.* **101**, 80–86 (2020).

405. Liu, J. *et al.* Platelet Activating Factor Receptor Exaggerates Microglia-Mediated Microenvironment by IL10-STAT3 Signaling: A Novel Potential Biomarker and Target for Diagnosis and Treatment of Alzheimer's Disease. *Front. Aging Neurosci.* **14**, 856628 (2022).

406. Dennis, D. J. *et al.* Neurog2 and Ascl1 together regulate a postmitotic derepression circuit to govern laminar fate specification in the murine neocortex. *Proc. Natl. Acad. Sci. U. S. A.* **114**, E4934–E4943 (2017).

407. Núñez, L. *et al.* Tagged actin mRNA dysregulation in IGF2BP1−/− mice. *Proc. Natl. Acad. Sci. U. S. A.* **119**, (2022).

408. Rosenberg, A. B. *et al.* Single-cell profiling of the developing mouse brain and spinal cord with split-pool barcoding. *Science (80-.).* **360**, 176–182 (2018).

409. Tasic, B. *et al.* Shared and distinct transcriptomic cell types across neocortical areas. *Nat. 2018 5637729* **563**, 72–78 (2018).

410. Guo, B. *et al.* Cadherin-12 Regulates Neurite Outgrowth Through the PKA/Rac1/Cdc42 Pathway in Cortical Neurons. *Front. Cell Dev. Biol.* **9**, 3039 (2021).

411. Wu, Q. F. *et al.* Fibroblast growth factor 13 is a microtubule-stabilizing protein regulating neuronal polarization and migration. *Cell* **149**, 1549–1564 (2012).

412. Sun, Z. *et al.* EGR1 recruits TET1 to shape the brain methylome during development and upon neuronal activity. *Nat. Commun.* **10**, 1–12 (2019).

413. D, D., Hung, K.-Y. & Tarn, W.-Y. RBM4 Modulates Radial Migration via Alternative Splicing of Dab1 during Cortex Development. *Mol. Cell. Biol.* **38**, (2018).

414. Liu, X., Zheng, J., Qi, S. & Shen, Q. NONO Regulates Cortical Neuronal Migration and Postnatal Neuronal Maturation. *Neurosci. Bull.* **35**, 1097 (2019).

415. Cappello, S. *et al.* The Rho-GTPase cdc42 regulates neural progenitor fate at the apical surface. *Nat. Neurosci.* **9**, 1099–1107 (2006).

416. Fulcher, L. J. *et al.* FAM83D directs protein kinase CK1α to the mitotic spindle for proper spindle positioning. *EMBO Rep.* **20**, e47495 (2019).

417. Ino, H. & Chiba, T. Expression of proliferating cell nuclear antigen (PCNA) in the adult and developing mouse nervous system. *Mol. Brain Res.* **78**, 163–174 (2000).

418. Zhang, Y. *et al.* Cortical Neural Stem Cell Lineage Progression Is Regulated by Extrinsic Signaling Molecule Sonic Hedgehog. *Cell Rep.* **30**, 4490 (2020).

419. Stevanovic, M. *et al.* SOX Transcription Factors as Important Regulators of Neuronal and Glial Differentiation During Nervous System Development and Adult Neurogenesis. *Front. Mol. Neurosci.* **14**, (2021).

420. Golonzhka, O. *et al.* Pbx regulates patterning of the cerebral cortex in progenitors and postmitotic neurons. *Neuron* **88**, 1192 (2015).

421. Chen, J., Billings, S. E. & Nishimune, H. Calcium channels link the muscle-derived synapse organizer laminin β2 to Bassoon and CAST/Erc2 to organize presynaptic active zones. *J. Neurosci.* **31**, 512–525 (2011).

422. Davydova, D. *et al.* Bassoon specifically controls presynaptic P/Q-type Ca(2+) channels via RIM-binding protein. *Neuron* **82**, 181–194 (2014).

423. Liu, Y., Beyer, A. & Aebersold, R. On the Dependency of Cellular Protein Levels on mRNA Abundance. *Cell* **165**, 535–550 (2016).

424. Price, A. J. *et al.* Divergent neuronal DNA methylation patterns across human cortical development reveal critical periods and a unique role of CpH methylation. *Genome Biol.* **20**, 1–20 (2019).

425. Tremblay, M. W. & Jiang, Y.-H. Annual Review of Medicine DNA Methylation and Susceptibility to Autism Spectrum Disorder. *Annu. Rev. Med. 2019* **70**, 151–66 (2018).

426. Basil, P. *et al.* Prenatal immune activation alters the adult neural epigenome but can be partly stabilised by a n-3 polyunsaturated fatty acid diet. *Transl. Psychiatry 2018 81* **8**, 1–12 (2018).

427. Loo, L. *et al.* Single-cell transcriptomic analysis of mouse neocortical development. *Nat. Commun.* **10**, 1–11 (2019).

428. Lui, J. H. *et al.* Differential encoding in prefrontal cortex projection neuron classes across

cognitive tasks. *Cell* **184**, 489-506.e26 (2021).

429. Inoue, M. *et al.* Correction: Prdm16 is crucial for progression of the multipolar phase during neural differentiation of the developing neocortex (Development 144, (385-399), 10.1242/dev.136382). *Dev.* **144**, 1735 (2017).

430. Glickstein, S. B., Monaghan, J. A., Koeller, H. B., Jones, T. K. & Ross, M. E. Cyclin D2 is critical for intermediate progenitor cell proliferation in the embryonic cortex. *J. Neurosci.* **29**, 9614–9624 (2009).

431. Lobjois, V., Bel-Vialar, S., Trousse, F. & Pituello, F. Forcing neural progenitor cells to cycle is insufficient to alter cell-fate decision and timing of neuronal differentiation in the spinal cord. *Neural Dev.* **3**, (2008).

432. Shitamukai, A., Konno, D. & Matsuzaki, F. Oblique Radial Glial Divisions in the Developing Mouse Neocortex Induce Self-Renewing Progenitors outside the Germinal Zone That Resemble Primate Outer Subventricular Zone Progenitors. *J. Neurosci.* **31**, 3683 (2011).

433. Gaspard, N. *et al.* An intrinsic mechanism of corticogenesis from embryonic stem cells. *Nature* **455**, 351–357 (2008).

434. Shen, Q. *et al.* The timing of cortical neurogenesis is encoded within lineages of individual progenitor cells. *Nat. Neurosci. 2006 96* **9**, 743–751 (2006).

435. Espuny-Camacho, I. *et al.* Pyramidal Neurons Derived from Human Pluripotent Stem Cells Integrate Efficiently into Mouse Brain Circuits In Vivo. *Neuron* **77**, 440–456 (2013).

436. Arai, Y. *et al.* Neural stem and progenitor cells shorten S-phase on commitment to neuron production. *Nat. Commun. 2011 21* **2**, 1–12 (2011).

437. Salomoni, P. & Calegari, F. Cell cycle control of mammalian neural stem cells: putting a speed limit on G1. *Trends Cell Biol.* **20**, 233–243 (2010).

438. Zou, D. *et al.* Transient enhancement of proliferation of neural progenitors and impairment of their long-term survival in p25 transgenic mice. *Oncotarget* **7**, 39148 (2016).

439. Molina, A. *et al.* Single-cell imaging of the cell cycle reveals CDC25B-induced heterogeneity of G1 phase length in neural progenitor cells. *Development* **149**, (2022).

440. García-García, E., Pino-Barrio, M. J., Lopez-Medina, L. & Martińez-Serrano, A. Intermediate progenitors are increased by lengthening of the cell cycle through calcium signaling and p53 expression in human neural progenitors. *Mol. Biol. Cell* **23**, 1167–1180 (2012).

441. Calegari, F. & Huttner, W. B. An inhibition of cyclin-dependent kinases that lengthens, but does not arrest, neuroepithelial cell cycle induces premature neurogenesis. *J. Cell Sci.* **116**, 4947–4955 (2003).

442. Rabia Urun, F., Moore, A. W., During, C. & Lineage, N. Visualizing Cell Cycle Phase Organization and Control During Neural Lineage Elaboration. 1–14 (2020). doi:10.3390/cells9092112

443. Takahashi, T., Nowakowski, R. S. & Caviness, V. S. Early ontogeny of the secondary proliferative population of the embryonic murine cerebral wall. *J. Neurosci.* **15**, 6058–6068 (1995).

444. Oberst, P. *et al.* Temporal plasticity of apical progenitors in the developing mouse neocortex. *Nature* **573**, 370–374 (2019).

445. McConnell, S. K. & Kaznowski, C. E. Cell cycle dependence of laminar determination in developing neocortex. *Science (80-.).* **254**, 282–285 (1991).

446. Gorgoulis, V. *et al.* Cellular Senescence: Defining a Path Forward. *Cell* **179**, 813–827 (2019).

447. Andrusiak, M. G. *et al.* Rb/E2F Regulates Expression of Neogenin during Neuronal Migration. *Mol. Cell. Biol.* **31**, 238–247 (2011).

448. Liu, D. X. & Greene, L. A. Regulation of neuronal survival and death by E2F-dependent gene repression and derepression. *Neuron* **32**, 425–438 (2001).

449. Futatsugi, A. *et al.* Cyclin-dependent kinase 5 regulates E2F transcription factor through

phosphorylation of Rb protein in neurons. *Cell Cycle* **11**, 1603–1610 (2012).

450. Zhou, W. *et al.* TIGAR promotes neural stem cell differentiation through acetyl-CoA-mediated histone acetylation. *Cell Death Dis.* **10**, (2019).

451. Müller, G. A. *et al.* The CHR promoter element controls cell cycle-dependent gene transcription and binds the DREAM and MMB complexes. *Nucleic Acids Res.* **40**, 1561–1578 (2012).

452. Guiley, K. Z. *et al.* Structural mechanisms of DREAM complex assembly and regulation. *Genes Dev.* **29**, 961 (2015).

453. Oshikawa, M., Okada, K., Nakajima, K. & Ajioka, I. Cortical excitatory neurons become protected from cell division during neurogenesis in an Rb family-dependent manner. *Development* **140**, 2310–2320 (2013).

454. Rosendo-Pineda, M. J. *et al.* Phosphorylation of NMDA receptors by cyclin B/CDK1 modulates calcium dynamics and mitosis. *Commun. Biol.* **3**, 1–13 (2020).

455. Hirasawa, T., Wada, H., Kohsaka, S. & Uchino, S. Inhibition of NMDA Receptors Induces Delayed Neuronal Maturation and Sustained Proliferation of Progenitor Cells during Neocortical Development. *J. Neurosci. Res.* **74**, 676–687 (2003).

456. Junyent, S. *et al.* Wnt-and glutamate-receptors orchestrate stem cell dynamics and asymmetric cell division. *Elife* **10**, (2021).

457. Garcia-Lopez, P., Garcia-Marin, V. & Freire, M. The Histological Slides and Drawings of Cajal. *Front. Neuroanat.* **4**, (2010).

458. Gerrits, E., Heng, Y., Boddeke, E. W. G. M. & Eggen, B. J. L. Transcriptional profiling of microglia; current state of the art and future perspectives. *Glia* **68**, 740–755 (2020).

459. Ikezu, S. *et al.* Inhibition of colony stimulating factor 1 receptor corrects maternal inflammation-induced microglial and synaptic dysfunction and behavioral abnormalities. *Mol. Psychiatry* **26**, 1808–1831 (2021).

460. Hammond, T. R. *et al.* Single cell RNA sequencing of microglia throughout the mouse lifespan and in the injured brain reveals complex cell-state changes. *Immunity* **50**, 253 (2019).

461. Pettas, S. *et al.* Profiling Microglia through Single-Cell RNA Sequencing over the Course of Development, Aging, and Disease. *Cells* **11**, (2022).

462. Gurok, U. *et al.* Gene Expression Changes in the Course of Neural Progenitor Cell Differentiation. *J. Neurosci.* **24**, 5982 (2004).

463. Zhu, Y., Matsumoto, T., Nagasawa, T., Mackay, F. & Murakami, F. Chemokine Signaling Controls Integrity of Radial Glial Scaffold in Developing Spinal Cord and Consequential Proper Position of Boundary Cap Cells. (2015). doi:10.1523/JNEUROSCI.0156-15.2015

464. Sánchez-Alcañiz, J. A. *et al.* Cxcr7 Controls Neuronal Migration by Regulating Chemokine Responsiveness. *Neuron* **69**, 77–90 (2011).

465. Estevao, C. *et al.* CCL4 induces inflammatory signalling and barrier disruption in the neurovascular endothelium. *Brain, Behav. Immun. - Heal.* **18**, 100370 (2021).

466. Radecki, D. Z. *et al.* Gpnmb inhibits oligodendrocyte differentiation of adult neural stem cells by amplifying TGFβ1 signaling. *bioRxiv* 2021.08.13.456269 (2021). doi:10.1101/2021.08.13.456269

467. Murata, K. *et al.* The extracellular fragment of GPNMB (Glycoprotein nonmelanosoma protein B, osteoactivin) improves memory and increases hippocampal GluA1 levels in mice. *J. Neurochem.* **132**, 583–594 (2015).

468. Zhang, Z. *et al.* Lysosomal-associated transmembrane protein 5 deficiency exacerbates cerebral ischemia/reperfusion injury. *Front. Mol. Neurosci.* **15**, (2022).

469. von Ehr, A. *et al.* Inhibition of Microglial TGFβ Signaling Increases Expression of Mrc1. *Front. Cell. Neurosci.* **14**, (2020).

470. Leiter, O. *et al.* Selenium mediates exercise-induced adult neurogenesis and reverses learning

deficits induced by hippocampal injury and aging. *Cell Metab.* **34**, 408-423.e8 (2022).

471. Cserép, C. *et al.* Microglial control of neuronal development via somatic purinergic junctions. *Cell Rep.* **40**, (2022).

472. Bonfanti, E. *et al.* The role of oligodendrocyte precursor cells expressing the GPR17 receptor in brain remodeling after stroke. *Cell Death Dis. 2017 86* **8**, e2871–e2871 (2017).

473. Ishimoto, T. *et al.* Mice lacking BCAS1, a novel myelin-associated protein, display hypomyelination, schizophrenia-like abnormal behaviors, and upregulation of inflammatory genes in the brain. *Glia* **65**, 727–739 (2017).

474. Jolly, S. *et al.* G protein-coupled receptor 37-like 1 modulates astrocyte glutamate transporters and neuronal NMDA receptors and is neuroprotective in ischemia. *Glia* **66**, 47–61 (2018).

475. Di Bella, D. J. *et al.* Molecular logic of cellular diversification in the mouse cerebral cortex. *Nature* **595**, 554–559 (2021).

476. Silbereis, J. C. *et al.* Olig1 function is required to repress Dlx1/2 and interneuron production in mammalian brain. *Neuron* **81**, 574 (2014).

477. Hamashima, T. *et al.* Oligodendrogenesis and Myelin Formation in the Forebrain Require Platelet-derived Growth Factor Receptor-alpha. *Neuroscience* **436**, 11–26 (2020).

478. Hasel, P. *et al.* Neurons and neuronal activity control gene expression in astrocytes to regulate their development and metabolism. *Nat. Commun.* **8**, (2017).

479. Szu, J. I. & Binder, D. K. The role of astrocytic aquaporin-4 in synaptic plasticity and learning and memory. *Front. Integr. Neurosci.* **10**, 168999 (2016).

480. Lawson, L. J., Perry, V. H., Dri, P. & Gordon, S. Heterogeneity in the distribution and morphology of microglia in the normal adult mouse brain. *Neuroscience* **39**, 151–170 (1990).

481. Stephan, A. H., Barres, B. A. & Stevens, B. The complement system: An unexpected role in synaptic pruning during development and disease. *Annu. Rev. Neurosci.* **35**, 369–389 (2012).

482. Schafer, D. P. *et al.* Microglia Sculpt Postnatal Neural Circuits in an Activity and Complement-Dependent Manner. *Neuron* **74**, 691 (2012).

483. Hristova, M. *et al.* Activation and deactivation of periventricular white matter phagocytes during postnatal mouse development. *Glia* **58**, 11–28 (2010).

484. Wang, C. *et al.* Microglia mediate forgetting via complement-dependent synaptic elimination. *Science (80-.).* **367**, 688–694 (2020).

485. Burnstock, G. Discovery of purinergic signalling, the initial resistance and current explosion of interest. *Br. J. Pharmacol.* **167**, 238 (2012).

486. Heinrich, A., Andõ, R. D., Túri, G., Rõzsa, B. & Sperlágh, B. K+ depolarization evokes ATP, adenosine and glutamate release from glia in rat hippocampus: a microelectrode biosensor study. *Br. J. Pharmacol.* **167**, 1003–1020 (2012).

487. Abbracchio, M. P. *et al.* International Union of Pharmacology LVIII: Update on the P2Y G Protein-Coupled Nucleotide Receptors: From Molecular Mechanisms and Pathophysiology to Therapy. *Pharmacol. Rev.* **58**, 281 (2006).

488. Sebastião, A. . & Ribeiro, J. . Tuning and Fine-Tuning of Synapses with Adenosine. *Curr. Neuropharmacol.* **7**, 180 (2009).

489. Sperlágh, B., Heinrich, A. & Csölle, C. P2 receptor-mediated modulation of neurotransmitter release—an update. *Purinergic Signal.* **3**, 269 (2007).

490. Guzman, S. J. & Gerevich, Z. P2Y Receptors in Synaptic Transmission and Plasticity: Therapeutic Potential in Cognitive Dysfunction. *Neural Plast.* **2016**, (2016).

491. Zhang, P., Bannon, N. M., Ilin, V., Volgushev, M. & Chistiakova, M. Adenosine effects on inhibitory synaptic transmission and excitation–inhibition balance in the rat neocortex. *J. Physiol.* **593**, 825 (2015).

492. Tereshko, L., Gao, Y., Cary, B. A., Turrigiano, G. G. & Sengupta, P. Ciliary neuropeptidergic signaling dynamically regulates excitatory synapses in postnatal neocortical pyramidal

neurons. *Elife* **10**, (2021).

493. Nager, A. R. *et al.* An actin network dispatches ciliary GPCRs into extracellular vesicles to modulate signaling. *Cell* **168**, 252 (2017).

494. Nozawa, Y. I., Lin, C. & Chuang, P. T. Hedgehog signaling from the primary cilium to the nucleus: an emerging picture of ciliary localization, trafficking and transduction. *Curr. Opin. Genet. Dev.* **23**, 429 (2013).

495. Hirabayashi, Y. *et al.* The Wnt/β-catenin pathway directs neuronal differentiation of cortical neural precursor cells. *Development* **131**, 2791–2801 (2004).

496. Liu, J. *et al.* Chemokine signaling links cell-cycle progression and cilia formation for left–right symmetry breaking. *PLOS Biol.* **17**, e3000203 (2019).

497. Atkins, M., Darmon, M., Roche, F., Nicol, X. & Métin, C. CXCL12 targets the primary cilium cAMP/cGMP ratio to regulate cell polarity during migration. *bioRxiv* 2023.02.07.527463 (2023). doi:10.1101/2023.02.07.527463

498. Breschi, A., Gingeras, T. R. & Guigó, R. Comparative transcriptomics in human and mouse. *Nat. Rev. Genet.* **18**, 425 (2017).

499. Wrobel, C. N., Mutch, C. A., Swaminathan, S., Taketo, M. M. & Chenn, A. Persistent expression of stabilized β-catenin delays maturation of radial glial cells into intermediate progenitors. *Dev. Biol.* **309**, 285 (2007).

500. Mutch, C. A., Schulte, J. D., Olson, E. & Chenn, A. Beta-catenin signaling negatively regulates intermediate progenitor population numbers in the developing cortex. *PLoS One* **5**, 12376 (2010).

501. Munji, R. N., Choe, Y., Li, G., Siegenthaler, J. A. & Pleasure, S. J. Wnt signaling regulates neuronal differentiation of cortical intermediate progenitors. *J. Neurosci.* **31**, 1676–1687 (2011).

502. Ben-Ari, Y. Excitatory actions of GABA during development: The nature of the nurture. *Nat. Rev. Neurosci.* **3**, 728–739 (2002).

503. Medvedeva, V. P. & Pierani, A. How Do Electric Fields Coordinate Neuronal Migration and Maturation in the Developing Cortex? *Front. Cell Dev. Biol.* **8**, 1006 (2020).

504. Li, L., Hutchins, B. I. & Kalil, K. Wnt5a Induces Simultaneous Cortical Axon Outgrowth and Repulsive Axon Guidance through Distinct Signaling Mechanisms. *J. Neurosci.* **29**, 5873–5883 (2009).

505. Saab, A. S. *et al.* Oligodendroglial NMDA Receptors Regulate Glucose Import and Axonal Energy Metabolism. *Neuron* **91**, 119–132 (2016).

506. Hines, J. H., Ravanelli, A. M., Schwindt, R., Scott, E. K. & Appel, B. Neuronal activity biases axon selection for myelination in vivo. *Nat. Neurosci.* **18**, 683–689 (2015).

507. Olsen, A. S. B. & Færgeman, N. J. Sphingolipids: Membrane microdomains in brain development, function and neurological diseases. *Open Biol.* **7**, (2017).

508. Spitzer, S. O. *et al.* Oligodendrocyte Progenitor Cells Become Regionally Diverse and Heterogeneous with Age. *Neuron* **101**, 459-471.e5 (2019).

509. Lange, C. *et al.* Relief of hypoxia by angiogenesis promotes neural stem cell differentiation by targeting glycolysis. *EMBO J.* **35**, 924–941 (2016).

510. Houlihan, S. L., Lanctot, A. A., Guo, Y. & Feng, Y. Upregulation of neurovascular communication through filamin abrogation promotes ectopic periventricular neurogenesis. *Elife* **5**, 1–21 (2016).

511. Javaherian, A. & Kriegstein, A. A stem cell niche for intermediate progenitor cells of the embryonic cortex. *Cereb. Cortex* **19**, (2009).

512. Naya, F. J. *et al.* Diabetes, defective pancreatic morphogenesis, and abnormal enteroendocrine differentiation in BETA2/NeuroD-deficient mice. *Genes Dev.* **11**, 2323–2334 (1997).

513. Hansen, L. *et al.* NeuroD/BETA2. **49**, 31–33 (2000).

514. Lee, J., Kim, K., Yu, S. W. & Kim, E. K. Wnt3a upregulates brain-derived insulin by increasing NeuroD1 via Wnt/β-catenin signaling in the hypothalamus. *Mol. Brain* **9**, 1–12 (2016).

515. Ji, S. *et al.* Maternal hyperglycemia disturbs neocortical neurogenesis via epigenetic regulation in C57BL/6J mice. *Cell Death Dis. 2019 103* **10**, 1–13 (2019).

516. Cao, J., Mu, Q. & Huang, H. The Roles of Insulin-Like Growth Factor 2 mRNA-Binding Protein 2 in Cancer and Cancer Stem Cells. *Stem Cells Int.* **2018**, (2018).

517. Xin Cai, A. *et al.* Lactate activates the mitochondrial electron transport chain independently of its metabolism. *Mol. Cell* **83**, 3904-3920.e7 (2023).

518. Xie, Z., Jones, A., Deeney, J. T., Hur, S. K. & Bankaitis, V. A. Inborn Errors of Long-Chain Fatty Acid β-Oxidation Link Neural Stem Cell Self-Renewal to Autism. *Cell Rep.* **14**, 991–999 (2016).

519. Knobloch, M. *et al.* A Fatty Acid Oxidation-Dependent Metabolic Shift Regulates Adult Neural Stem Cell Activity. *Cell Rep.* **20**, 2144–2155 (2017).

520. Iwata, R., Casimir, P. & Vanderhaeghen, P. Mitochondrial dynamics in postmitotic cells regulate neurogenesis. *Science (80-.).* **369**, 858–862 (2020).

521. Ishii, S. *et al.* Primary cilia safeguard cortical neurons in neonatal mouse forebrain from environmental stress-induced dendritic degeneration. *Proc. Natl. Acad. Sci. U. S. A.* **118**, e2012482118 (2021).

522. Stoufflet, J. & Caillé, I. The Primary Cilium and Neuronal Migration. *Cells* **11**, 3384 (2022).

523. Ding, W., Wu, Q., Sun, L., Pan, N. C. & Wang, X. Cenpj Regulates Cilia Disassembly and Neurogenesis in the Developing Mouse Cortex. *J. Neurosci.* **39**, 1994 (2019).

524. Sarkisian, M. R. & Guadiana, S. M. Influences of primary cilia on cortical morphogenesis and neuronal subtype maturation. *Neuroscientist* **21**, 136–151 (2015).

525. Nigg, E. A. & Stearns, T. The centrosome cycle: Centriole biogenesis, duplication and inherent asymmetries. *Nat. Cell Biol.* **13**, 1154 (2011).

526. Paridaen, J. T. M. L., Wilsch-Bräuninger, M. & Huttner, W. B. Asymmetric inheritance of centrosome-associated primary cilium membrane directs ciliogenesis after cell division. *Cell* **155**, 333 (2013).

527. Kosodo, Y. *et al.* Asymmetric distribution of the apical plasma membrane during neurogenic divisions of mammalian neuroepithelial cells. *EMBO J.* **23**, 2314 (2004).

528. Wang, X. *et al.* Asymmetric centrosome inheritance maintains neural progenitors in neocortex. *Nature* **461**, 947 (2009).

529. Wilsch-Bräuninger, M. & Huttner, W. B. Primary Cilia and Centrosomes in Neocortex Development. *Front. Neurosci.* **15**, 1340 (2021).

530. Reiter, J. F. & Leroux, M. R. Genes and molecular pathways underpinning ciliopathies. *Nat. Rev. Mol. Cell Biol.* **18**, 533 (2017).

531. Shao, W. *et al.* Centrosome anchoring regulates progenitor properties and cortical formation. *Nature* **580**, 106 (2020).

532. Guo, J. *et al.* Primary cilia signaling promotes axonal tract development and is disrupted in Joubert Syndrome Related Disorder models. *Dev. Cell* **51**, 759 (2019).

533. Liu, S., Trupiano, M. X., Simon, J., Guo, J. & Anton, E. S. The essential role of primary cilia in cerebral cortical development and disorders. *Curr. Top. Dev. Biol.* **142**, 99 (2021).

534. Rocha, C. & Prinos, P. Post-transcriptional and Post-translational Modifications of Primary Cilia: How to Fine Tune Your Neuronal Antenna. *Front. Cell. Neurosci.* **16**, (2022).

535. Saade, M. *et al.* Multimerization of Zika Virus-NS5 causes ciliopathy and forces premature neurogenesis. *Cell Stem Cell* **27**, 920 (2020).

536. Gabriel, E. *et al.* Recent Zika Virus Isolates Induce Premature Differentiation of Neural

Progenitors in Human Brain Organoids. *Stem Cell* **20**, 397-406.e5 (2017).

537. Glover, V. Prenatal stress and its effects on the fetus and the child: Possible Underlying biological mechanisms. *Adv. Neurobiol.* **10**, 269–283 (2015).

538. McGowan, P. O. & Matthews, S. G. Prenatal Stress, Glucocorticoids, and Developmental Programming of the Stress Response. *Endocrinology* **159**, 69–82 (2018).

539. Shi, P. *et al.* Hdac6 signaling at primary cilia promotes proliferation and restricts differentiation of glioma cells. *Cancers (Basel).* **13**, 1644 (2021).

540. Graveley, B. R. Alternative splicing: Increasing diversity in the proteomic world. *Trends Genet.* **17**, 100–107 (2001).

541. Feng, H. *et al.* Complexity and graded regulation of neuronal cell-type–specific alternative splicing revealed by single-cell RNA sequencing. *Proc. Natl. Acad. Sci. U. S. A.* **118**, e2013056118 (2021).

542. Liu, J., Geng, A., Wu, X., Lin, R. J. & Lu, Q. Alternative RNA Splicing Associated With Mammalian Neuronal Differentiation. *Cereb. Cortex (New York, NY)* **28**, 2810 (2018).

543. Zhang, X. *et al.* Cell-Type-Specific Alternative Splicing Governs Cell Fate in the Developing Cerebral Cortex. *Cell* **166**, 1147-1162.e15 (2016).

544. Dai, J., Aoto, J. & Südhof, T. C. Alternative Splicing of Presynaptic Neurexins Differentially Controls Postsynaptic NMDA and AMPA Receptor Responses. *Neuron* **102**, 993-1008.e5 (2019).

545. Jacko, M. *et al.* Rbfox Splicing Factors Promote Neuronal Maturation and Axon Initial Segment Assembly. *Neuron* **97**, 853-868.e6 (2018).

546. Perez, J. D. *et al.* Subcellular sequencing of single neurons reveals the dendritic transcriptome of gabaergic interneurons. *Elife* **10**, 1–26 (2021).

547. Kosik, K. S. Life at Low Copy Number: How Dendrites Manage with So Few mRNAs. *Neuron* **92**, 1168–1180 (2016).

548. Zylka, M. J., Simon, J. M. & Philpot, B. D. Gene length matters in neurons. *Neuron* **86**, 353–355 (2015).

549. McCoy, M. J. *et al.* LONGO: An R package for interactive gene length dependent analysis for neuronal identity. *Bioinformatics* **34**, i422–i428 (2018).

550. Anufrieva, K. S. *et al.* Therapy-induced stress response is associated with downregulation of pre-mRNA splicing in cancer cells. *Genome Med. 2018 101* **10**, 1–18 (2018).

551. Su, C. H., Dhananjaya, D. & Tarn, W. Y. Alternative splicing in neurogenesis and brain development. *Front. Mol. Biosci.* **5**, 12 (2018).

552. Weyn-Vanhentenryck, S. M. *et al.* Precise temporal regulation of alternative splicing during neural development. *Nat. Commun.* **9**, (2018).

553. Tarn, W. Y. *et al.* RBM4 promotes neuronal differentiation and neurite outgrowth by modulating Numb isoform expression. *Mol. Biol. Cell* **27**, 1676–1683 (2016).

554. Yasuda, H. *et al.* Drebrin isoforms critically regulate nmdar- and mglur-dependent LTD induction. *Front. Cell. Neurosci.* **12**, 330 (2018).

555. Monteiro, V. R. S. *et al.* Mid-pregnancy poly(I:C) viral mimic disrupts placental ABC transporter expression and leads to long-term offspring motor and cognitive dysfunction. *Sci. Reports 2022 121* **12**, 1–13 (2022).

556. Amodeo, D. A. *et al.* Maternal immune activation impairs cognitive flexibility and alters transcription in frontal cortex. *Neurobiol. Dis.* **125**, 211–218 (2019).

557. Hsiao, E. Y. & Patterson, P. H. Activation of the Maternal Immune System Induces Endocrine Changes in the Placenta via IL-6. *Brain. Behav. Immun.* **25**, 604 (2011).

558. Meyer, U. *et al.* Adult behavioral and pharmacological dysfunctions following disruption of the fetal brain balance between pro-inflammatory and IL-10-mediated anti-inflammatory signaling. *Mol. Psychiatry 2008 132* **13**, 208–221 (2007).

559. Smolders, S. *et al.* Maternal immune activation evoked by polyinosinic:polycytidylic acid does not evoke microglial cell activation in the embryo. *Front. Cell. Neurosci.* **9**, (2015).

560. Bendickova, K. & Fric, J. Roles of IL-2 in bridging adaptive and innate immunity, and as a tool for cellular immunotherapy. *J. Leukoc. Biol.* **108**, 427–437 (2020).

561. Yockey, L. J. & Iwasaki, A. Immunity Review Interferons and Proinflammatory Cytokines in Pregnancy and Fetal Development. *Immunity* **49**, 397–412 (2018).

562. Gaelle, D. *et al.* Sustained corticosterone rise in the prefrontal cortex is a key factor for chronic stress-induced working memory deficits in mice. *Neurobiol. Stress* **10**, 100161 (2019).

563. Kang, E. *et al.* Neurogenesis and Developmental Anesthetic Neurotoxicity. *Neurotoxicol. Teratol.* **60**, 33 (2017).

564. Maloney, S. E. *et al.* Repeated neonatal isoflurane exposures in the mouse induce apoptotic degenerative changes in the brain and relatively mild long-term behavioral deficits. *Sci. Rep.* **9**, (2019).

565. Gluncic, V. *et al.* In utero Exposure to Anesthetics Alters Neuronal Migration Pattern in Developing Cerebral Cortex and Causes Postnatal Behavioral Deficits in Rats. *Cereb. Cortex* **29**, 5285–5301 (2019).

566. Tang, B., Jia, H., Kast, R. J. & Thomas, E. A. Epigenetic changes at gene promoters in response to immune activation in utero. *Brain. Behav. Immun.* **30**, 168–175 (2013).

567. Gerra, M. C. *et al.* DNA methylation changes in genes involved in inflammation and depression in fibromyalgia: A pilot study. *Scand. J. Pain* **21**, 372–383 (2021).

568. Matt, S. M. *et al.* Inhibition of DNA methylation with zebularine alters lipopolysaccharide sickness behavior and neuroinflammation in mice. *Front. Neurosci.* **12**, 1–10 (2018).

569. Conole, E. L. S. *et al.* DNA Methylation and Protein Markers of Chronic Inflammation and Their Associations With Brain and Cognitive Aging. *Neurology* **97**, e2340–e2352 (2021).

570. Bocchi, R. *et al.* Perturbed Wnt signaling leads to neuronal migration delay, altered interhemispheric connections and impaired social behavior. *Nat. Commun. 2017 81* **8**, 1–15 (2017).

571. Boitard, M. *et al.* Wnt signaling regulates multipolar-to-bipolar transition of migrating neurons in the cerebral cortex. *Cell Rep.* **10**, 1349–1361 (2015).

572. Adachi, K. *et al.* Beta-catenin signaling promotes proliferation of progenitor cells in the adult mouse subventricular zone. *Stem Cells* **25**, 2827–2836 (2007).

573. Yu, J. M., Kim, J. H., Song, G. S. & Jung, J. S. Increase in proliferation and differentiation of neural progenitor cells isolated from postnatal and adult mice brain by Wnt-3a and Wnt-5a. *Mol. Cell. Biochem.* **288**, 17–28 (2006).

574. Ma, L. *et al.* WNT/NOTCH Pathway Is Essential for the Maintenance and Expansion of Human MGE Progenitors. *Stem Cell Reports* **12**, 934–949 (2019).

575. Chinnappa, K. *et al.* Secondary loss of miR-3607 reduced cortical progenitor amplification during rodent evolution. **8**, 4010 (2022).

576. Fang, W. Q., Chen, W. W., Fu, A. K. Y. & Ip, N. Y. Axin Directs the Amplification and Differentiation of Intermediate Progenitors in the Developing Cerebral Cortex. *Neuron* **79**, 665–679 (2013).

577. Fang, W. Q. *et al.* Cdk5-Mediated Phosphorylation of Axin Directs Axon Formation during Cerebral Cortex Development. *J. Neurosci.* **31**, 13613–13624 (2011).

578. Bem, J. *et al.* Wnt/β-catenin signaling in brain development and mental disorders: keeping TCF7L2 in mind. *FEBS Lett.* **593**, 1654–1674 (2019).

579. Bertrand, V. β-catenin-driven binary cell fate decisions in animal development. *Wiley Interdiscip. Rev. Dev. Biol.* **5**, 377 (2016).

580. Sun, S. *et al.* WNT signaling represses astrogliogenesis via Ngn2-dependent direct suppression of astrocyte gene expression. *Glia* **67**, 1333–1343 (2019).

581. Arredondo, S. B., Valenzuela-Bezanilla, D., Mardones, M. D. & Varela-Nallar, L. Role of Wnt Signaling in Adult Hippocampal Neurogenesis in Health and Disease. *Front. Cell Dev. Biol.* **8**, 1–15 (2020).

582. Vlad-Fiegen, A., Langerak, A., Eberth, S. & Müller, O. The Wnt pathway destabilizes adherens junctions and promotes cell migration via β-catenin and its target gene cyclin D1. *FEBS Open Bio* **2**, 26–31 (2012).

583. Donta, M. S., Srivastava, Y. & McCrea, P. D. Delta-Catenin as a Modulator of Rho GTPases in Neurons. *Front. Cell. Neurosci.* **16**, (2022).

584. Zhang, L. *et al.* Ras and Rap Signal Bidirectional Synaptic Plasticity via Distinct Subcellular Microdomains. *Neuron* **98**, 783-800.e4 (2018).

585. Zhang, X. *et al.* Dishevelled promotes axon differentiation by regulating atypical protein kinase C. *Nat. Cell Biol. 2007 97* **9**, 743–754 (2007).

586. Ahmad-Annuar, A. *et al.* Signaling across the synapse: a role for Wnt and Dishevelled in presynaptic assembly and neurotransmitter release. *J. Cell Biol.* **174**, 127–139 (2006).

587. Wang, W. *et al.* Feedback regulation of apical progenitor fate by immature neurons through Wnt7–Celsr3–Fzd3 signalling. **7**, 1–11 (2016).

588. Teo, S. & Salinas, P. C. Wnt-Frizzled Signaling Regulates Activity-Mediated Synapse Formation. *Front. Mol. Neurosci.* **14**, 683035 (2021).

589. Pacary, E. *et al.* Proneural transcription factors regulate different steps of cortical neuron migration through Rnd-mediated inhibition of RhoA signaling. *Neuron* **69**, 1069–1084 (2011).

590. Harrison-Uy, S. J. & Pleasure, S. J. Wnt signaling and forebrain development. *Cold Spring Harb. Perspect. Biol.* **4**, 1–11 (2012).

591. Katsu, T. *et al.* The human frizzled-3 (FZD3) gene on chromosome 8p21, a receptor gene for Wnt ligands, is associated with the susceptibility to schizophrenia. *Neurosci. Lett.* **353**, 53–56 (2003).

592. Pierfrancesco Pagella, A. *et al.* The time-resolved genomic impact of Wnt/b-catenin signaling ll The time-resolved genomic impact of Wnt/b-catenin signaling. *Cell Syst.* **14**, 563-581.e7 (2023).

593. Qini Gana, b, Albert Leea, b, Ryusuke Suzukia, b, Takashi Yamagamia, b, Arjun Stokesa, b, Bao Chau Nguyena, David Pleasurea, Junjiang Wangc, Hong–Wu Chenc, and Chengji J. Zhoua, b, C. Pax6 Mediates β-Catenin Signaling for Self-Renewal and Neurogenesis by Neocortical Radial Glial Stem Cells. *Stem Cells.* **23**, 1–7 (2014).

594. Chenn, A. & Walsh, C. A. Regulation of cerebral cortical size by control of cell cycle exit in neural precursors. *Science (80-.).* **297**, 365–369 (2002).

595. Meyer, U., Nyffeler, M., Yee, B. K., Knuesel, I. & Feldon, J. Adult brain and behavioral pathological markers of prenatal immune challenge during early/middle and late fetal development in mice. *Brain. Behav. Immun.* **22**, 469–486 (2008).

596. Tsivion-Visbord, H. *et al.* Increased RNA editing in maternal immune activation model of neurodevelopmental disease. *Nat. Commun. 2020 111* **11**, 1–13 (2020).

597. Smith, S. E. P., Li, J., Garbett, K., Mirnics, K. & Patterson, P. H. Maternal immune activation alters fetal brain development through interleukin-6. *J. Neurosci.* **27**, 10695–10702 (2007).

598. Fatemi, S. H. *et al.* Maternal infection leads to abnormal gene regulation and brain atrophy in mouse offspring: Implications for genesis of neurodevelopmental disorders. *Schizophr. Res.* **99**, 56 (2008).

599. Li, Y. *et al.* Maternal and Early Postnatal Immune Activation Produce Dissociable Effects on Neurotransmission in mPFC–Amygdala Circuits. *J. Neurosci.* **38**, 3358–3372 (2018).

600. Ariza, J. *et al.* Maternal autoimmune antibodies alter the dendritic arbor and spine numbers in the infragranular layers of the cortex. *PLoS One* **12**, e0183443 (2017).

601. Birtele, M. *et al.* The autism-associated gene SYNGAP1 regulates human cortical neurogenesis. *bioRxiv* 2022.05.10.491244 (2023). doi:10.1101/2022.05.10.491244

602. Vyas, Y. *et al.* Shankopathies in the Developing Brain in Autism Spectrum Disorders. *Front. Neurosci.* **15**, (2021).

603. Kim, S. *et al.* Neural circuit pathology driven by Shank3 mutation disrupts social behaviors. *CellReports* **39**, 110906 (2022).

604. Lacaria, M., Spencer, C., Gu, W., Paylor, R. & Lupski, J. R. Enriched rearing improves behavioral responses of an animal model for CNV-based autistic-like traits. *Hum. Mol. Genet.* **21**, 3083 (2012).

605. Karst, H. *et al.* Acceleration of GABA-switch after early life stress changes mouse prefrontal glutamatergic transmission. *Neuropharmacology* **234**, 109543 (2023).

606. Bath, K. G., Manzano-Nieves, G. & Goodwill, H. Early life stress accelerates behavioral and neural maturation of the hippocampus in male mice. *Horm. Behav.* **82**, 64–71 (2016).

607. Swanger, S. A., Mattheyses, A. L., Gentry, E. G. & Herskowitz, J. H. ROCK1 and ROCK2 inhibition alters dendritic spine morphology in hippocampal neurons. *Cell. Logist.* **5**, e1133266 (2015).

608. Klauck, S. M. *et al.* Mutations in the ribosomal protein gene RPL10 suggest a novel modulating disease mechanism for autism. *Mol. Psychiatry 2006 1112* **11**, 1073–1084 (2006).

609. Honda, Z. I., Suzuki, T. & Honda, H. Identification of CENP-V as a novel microtubule-associating molecule that activates Src family kinases through SH3 domain interaction. *Genes Cells* **14**, 1383–1394 (2009).

610. Rosenbloom, A. B. *et al.* β-Catenin signaling dynamics regulate cell fate in differentiating neural stem cells. *Proc. Natl. Acad. Sci. U. S. A.* **117**, 28828–28837 (2020).

611. Repina, N. A. *et al.* Engineered Illumination Devices for Optogenetic Control of Cellular Signaling Dynamics ll Engineered Illumination Devices for Optogenetic Control of Cellular Signaling Dynamics. *CellReports* **31**, 107737 (2020).

612. Kahn, M. Can we safely target the WNT pathway? *Nat. Rev. Drug Discov.* **13**, 513 (2014).

613. Schmetsdorf, S., Gärtner, U. & Arendt, T. Expression of cell cycle-related proteins in developing and adult mouse hippocampus. *Int. J. Dev. Neurosci.* **23**, 101–112 (2005).

614. Akagawa, R., Nabeshima, Y. I. & Kawauchi, T. Alternative Functions of Cell Cycle-Related and DNA Repair Proteins in Post-mitotic Neurons. *Front. Cell Dev. Biol.* **9**, 1–9 (2021).

615. Marlier, Q., D'aes, T., Verteneuil, S., Vandenbosch, R. & Malgrange, B. Core cell cycle machinery is crucially involved in both life and death of post-mitotic neurons. *Cell. Mol. Life Sci.* **77**, 4553–4571 (2020).

616. Karl Herrup. Post-mitotic role of the cell cycle machinery Karl. *Bone* **23**, 1–7 (2014).

617. Christopher L. Frank and Li-Huei Tsai. Alternative functions of core cell cycle regulators in neuronal migration, neuronal maturation, and synaptic plasticity. *Bone* **23**, 1–7 (2013).

618. Rosin, J. M. & Kurrasch, D. M. In utero electroporation induces cell death and alters embryonic microglia morphology and expression signatures in the developing hypothalamus. *J. Neuroinflammation* **15**, 1–15 (2018).

619. Kumamoto, T. *et al.* Direct Readout of Neural Stem Cell Transgenesis with an Integration-Coupled Gene Expression Switch. *Neuron* **107**, 617-630.e6 (2020).

620. Estes, M. L. *et al.* Baseline immunoreactivity before pregnancy and poly(I:C) dose combine to dictate susceptibility and resilience of offspring to maternal immune activation. *Brain. Behav. Immun.* **88**, 619–630 (2020).

621. Barke, T. L. *et al.* Sex modifies placental gene expression in response to metabolic and inflammatory stress. *Placenta* **78**, 1–9 (2019).

622. Waddington, C. H. Genetic Assimilation. *Adv. Genet.* **10**, 257–293 (1961).

623. Waddington. Canalization of development and the inheritence of acquired characters. *Nat. Publ. Gr.* (1942).

624. Zhang, Z. *et al.* Prenatal stress leads to deficits in brain development, mood related behaviors

and gut microbiota in offspring. *Neurobiol. Stress* **15**, 100333 (2021).

625. Gude, N. M., Roberts, C. T., Kalionis, B. & King, R. G. Growth and function of the normal human placenta. *Thromb. Res.* **114**, 397–407 (2004).

626. Cui, J. *et al.* Inflammation of the embryonic choroid plexus barrier following maternal immune activation. *Dev. Cell* **55**, 617 (2020).

627. Goasdoué, K., Miller, S. M., Colditz, P. B. & Björkman, S. T. Review: The blood-brain barrier; protecting the developing fetal brain. *Placenta* **54**, 111–116 (2017).

628. Elmore, M. R. P. *et al.* CSF1 receptor signaling is necessary for microglia viability, which unmasks a cell that rapidly repopulates the microglia-depleted adult brain. *Neuron* **82**, 380 (2014).